UNIVERSITAT AUTONÒMA DE BARCELONA

Nonlinear micro/nano-optomechanical oscillators for energy transduction from IR sources

by

Jordi Agustí Batlle

A thesis submitted in partial fulfillment for the degree
of Doctor of Philosophy in Electronic Engineering

in the
School of Engineering
Department of Electronic Engineering

September 2014

Nonlinear micro/nano-optomechanical oscillators for energy transduction from IR sources

University:

Universitat Autònoma de Barcelona

Department:

Departament d'Enginyeria Electrònica

PhD program:

Enginyeria Electrònica i de Telecomunicació

Author:

Jordi Agustí Batlle

Supervisor:

Gabriel Abadal Berini

September 2014

Dr. Gabriel Abadal Berini, associate professor at the department of Electronic Engineering of the *Universitat Autònoma de Barcelona*

HEREBY CERTIFIES THAT

the thesis entitled **Nonlinear nano-optomechanical oscillators for energy transduction from IR sources** submitted by Jordi Agustí Batlle to fulfill part of the requirements to achieve the degree of Doctor of Philosophy in Electronic Engineering, has been performed under his supervision.

Bellaterra, September the 15$^{\text{th}}$, 2014

Gabriel Abadal Berini

"If we knew what it was we were doing, it would not be called research, would it?"

Albert Einstein

Abstract

In this thesis, a new device merging optical antennas and micro/nano-mechanical structures is proposed with the aim to transform electromagnetic energy into mechanical energy. The study of the involved transduction mechanisms is the main objective of the presented work. The working principle of this new device can be summarized as follows: the antennas acting as absorbers in the infrared spectrum capture the electromagnetic radiation and transform it into a temperature field in the mechanical structure. Due to the thermal properties of the structural material the thermal response is converted to a mechanical deflection which eventually can lead to the self-oscillation of the device.

Given the involved energy transformations, the modeling of the coupled physics becomes a fundamental step in the path of designing, fabricating and characterizing a proof-of-concept device. The energy conversion is shown to be more efficient when the device auto-oscillates. However, due the the highly nonlinear nature of such phenomenon precisely knowing if such oscillation can be achieved using the proof-of-concept device imply its physical characterization in order to apply the developed model.

Resum

En aquesta tesi es proposa un nou dispositiu que combina antenes òptiques i micro/nanoestructures mecàniques amb l'objectiu de transformar energia electromagnètica en energia mecànica. El principal objectiu de la feina realitzada és l'estudi dels mecanismes de transducció implicats. El principi de funcionament d'aquest nou dispositiu es pot resumir de la manera següent: les antenes absorbeixen la radiació electromagnètica en l'espectre infraroig i la transformen en una distribució de temperatura en l'estructura mecànica, a causa de les propietats tèrmiques del material estructural la resposta tèrmica es converteix en una deflexió mecànica que eventualment pot conduir a l'autooscil·lació del dispositiu.

Donades les transformacions d'energia involucrades, el modelatge de les físiques acoblades esdevé un pas fonamental per tal de dissenyar, fabricar i caracteritzar un dispositiu de prova de concepte. La conversió d'energies es demostra que és més eficient quan el dispositiu autooscil·la. No obstant això, a causa de la naturalesa altament no lineal d'aquest fenomen, saber exactament si aquesta oscil·lació es pot aconseguir utilitzant el dispositiu de prova de concepte implica caracteritzarlo físicament per tal d'aplicar el model desenvolupat.

Acknowledgements

I would like to thank all of the following persons in my own language as I feel it is a better way for me to express my gratitude and for them to understand my words.

A la meva família: papa, mama, Anna M. i Núria, gràcies per estar sempre al meu costat tot i la distància, la inevitable i la induïda.

Noelia, expressar tot allò que he viscut i sentit al teu costat al llarg d'aquests anys amb un agraïment és, sincerament, de bojos... M'has fet créixer de manera exponencial com a persona, amb tot el que això implica. A tu, molt especialment, gràcies.

Totes aquelles persones relacionades amb el departament on he passat tots aquests anys han contribuït a fer que la meva llarga estada a l'escola d'enginyeria hagi estat agradable i fructífera. Gràcies als companys que m'han acompanyat durant la meva (nostra) gran travessa: Albert Crespo, Eloi Marigó, Ferran Paredes, Francesc Torres, Gabriel Vidal, Gonzalo Murillo, Joan Giner, Jordi Selga, Jose Luís Muñoz, Miquel López, Pau Aguilà, Xavier Saura, Vanessa Iglesias, Vikas Velayudhan, etc. Agrair també el suport tècnic d'en Javier Hellín i les tasques de secretaria a la Xiomara Maroto, la M. Carmen Mesas i l'Antonia Doroteo.

Compaginar l'escriptura d'una tesi a Sabadell i les quedades amb amics del meu poble, Vilafant, sol ser una tasca difícil, encara més si hi afegim la distància física que separa una cosa de l'altra. Marc i David, espero que a partir d'ara hi sigui més sovint.

No quisiera olvidarme de mis compañeros en Madrid. Alex Cuadrado, has sido un gran compañero de viaje; Fran Arrieta, Javier Muñoz y Manuel Silva, gracias por haber hecho que durante mi estancia me sintiese como en casa. Y, por supuesto, quisiera agradecer a Javier Alda su tiempo y conocimientos.

Per les tasques de micro/nanofabricació dels dispositius, voldria agrair a en Xevi Borrisé, la Libertad Solé, la María José Esplandiu i en Jordi Llobet el temps que m'han dedicat.

Finalment, vull donar les gràcies a en Gabriel Abadal, incansable en el seus esforços per veure les coses de manera positiva i transmetre sempre aquest positivisme.

Contents

List of figures

List of tables

Abbreviations

3D	**Three**-**D**imensional space
AFM	**A**tomic **F**orce **M**icroscope
AR	**A**nti**R**eflective
BC	**B**oundary **C**ondition
BW	**B**and**W**idth
CCD	**C**harge-**C**oupled **D**evice
CIN2	***C**entre d'**I**nvestigació en **N**anociència i **N**anotecnologia*
CMOS	**C**omplementary **M**etal–**O**xide–**S**emiconductor
CNM	***C**entre **N**acional de **M**icroelectrònica*
CW	**C**ontinuous **W**ave
DC	**D**irect **C**urrent
DUT	**D**evice **U**nder **T**est
eBL	**e**lectron-**B**eam **L**ithography
EL	**E**thyl **L**actate
EM	**E**lectro**M**agnetic
EMR	**E**lectro**M**agnetic **R**adiation
FEA	**F**inite **E**lement **A**nalysis
FEM	**F**inite **E**lement **M**ethod
FSS	**F**requency **S**elective **S**urface
GPIB	**G**eneral **P**urpose **I**nterface **B**us
IMB	***I**nstitut de **M**icroelectrònica de **B**arcelona*
IPA	**I**so**P**ropyl **A**lcohol
IR	**I**nfra**R**ed
KOH	Potassium hydroxide

LED	**L**ight-**E**mitting **D**iode
MAA	**M**eth**A**crylic **A**cid
MEMS	**M**icro**E**lectro**M**echanical **S**ystems
MIBK	**M**ethyl **I**so**B**utyl **K**etone
MMA	**M**ethyl **M**eth**A**crylate
MOEMS	**M**icro**O**pto**E**lectro**M**echanical **S**ystems
NEMS	**N**ano**E**lectro**M**echanical **S**ystems
NIR	**N**ear-**I**nfra**R**ed
NOEMS	**N**ano**O**pto**E**lectro**M**echanical **S**ystems
ODE	**O**rdinary **D**ifferential **E**quation
OPACMEMS	**OP**tical **A**ntennas **C**oupled to **MEMS**
PC	**P**ersonal **C**omputer
PCB	**P**rinted **C**ircuit **B**oard
PEC	**P**erfect **E**lectric **C**onductor
PD	**P**hoto**D**etector
PID	**P**roportional-**I**ntegral-**D**erivative
PMC	**P**erfect **M**agnetic **C**onductor
PML	**P**erfectly **M**atched **L**ayer
PMMA	**P**oly**M**ethyl **M**eth**A**crylat
PoF	**P**roof-**o**f-**F**abrication
PoC	**P**roof-**o**f-**C**oncept
PSD	**P**osition **S**ensing **D**etector
PSF	**P**oint **S**pread **F**unction
RAM	**R**andom-**A**ccess **M**emory
RF	**R**adio **F**requency
SB	**S**cattering **B**oundary
SEM	**S**canning **E**lectron **M**icroscope
SMA	**S**ub**M**iniature version **A**
TEC	**T**hermo**E**lectric **C**ooler
TEM	**T**ransverse **E**lectro**M**agnetic
TMM	**T**ransfer **M**atrix **M**ethod

UC	**U**nit **C**ell
UD	**U**nit **D**evice
USB	**U**niversal **S**erial **B**us

Chapter 1

Introduction

1.1 Introduction

There is plenty of room at the bottom, Richard Feynman once said in what must had been an inspiring lecture at the California Institute of Technology; *an invitation to enter a new field of physics* he pointed [1]. As part of this new scientific research line the field of micro/nano-electro-mechanical systems (M/NEMS) has been a hot topic since back in 1967 the results of what is considered the very first MEMS device were published in an international scientific journal [2]. In fact and over the last few decades, researchers over the world have been demonstrating that not only the bottom which Feynman mentioned was full of space but it was also full of uses for it. M/NEMS have broadly open the possibilities of what can be achieved using the micro and nano scale space. By interacting, sensing and actuating in a wide range of physics and magnitudes M/NEMS have become and evolved in essential products of the mankind's modern lifestyle [3].

Within the field of M/NEMS the discipline of energy harvesting has grown a huge interest among the research community due to its promising applications [4, 5]. The fundamental concept behind every energy harvesting device is the transduction mechanisms that enables the energy conversion from one domain to another. The electrical domain is the desirable destination of the harvested energy with the

aim to power ultra low power electronic systems. A direct conversion of the energy produced by vibration [6], fluid flow [7], temperature gradient [8], electromagnetic radiation [9] and radioactive [10] sources can be directly converted to electrical energy by means of a piezoelectric [11], electrostatic [12], electromagnetic [13], thermoelectric [14], photovoltaic [15] or pyroelectric [16] transducer.

The work presented in this thesis is focused on a transduction mechanism used to convert infrared energy to mechanical energy which then can be eventually transformed into electrical energy. However, the M/NEMS device proposed here is only studied from the point of view of the optical, thermal and mechanical domains, leaving for future research the electric domain.

1.2 Motivation: the OPACMEMS project

The framework of the research summarized in this manuscript is the project entitled as OPACMEMS, acronym that stands for Optical Antennas Coupled to MicroElectroMechnical Systems. The objective of this project is to merge two well-known fields or technologies: the optical antennas and the M/NEMS, with the aim to create a new class of micro/nano-opto-electro-mechanical system (M/-NOEMS). As the project proposal manuscript states, these new devices will have novel properties which can be applied to the sensing and transduction of infrared energy. The electromagnetic (EM) resonators (i.e., the optical antennas) will absorb the infrared radiation and transform it into a thermal field on the micro/-nanomechanical structure were they will be engraved on. On the other hand, the mechanical structure will convert the thermal energy into mechanical energy by means of a thermo-mechanical coupling mechanism that will induce the mechanical resonance of the device. Thus, the possibility to transform the produced vibrations into an electrical signal that could be measured, stored and/or used in applications such as infrared detectors and energy harvesting modules for ultra low power applications is opened.

The main tasks that the OPACMEMS project encompasses are:

- Task 1: theoretical analysis and modeling of the involved physics.
- Task 2: design and numerical simulation of a proof-of-concept device.
- Task 3: fabrication of the proposed device.
- Task 4: characterization of the fabricated device.

The research efforts reported in this thesis manuscript deal with all of the above mentioned tasks as it is reflected in the following thesis outline.

1.2.1 Thesis outline

This dissertation is organized following the tasks listed at the end of the previous section. Chapters 2 and 3 are devoted to the understanding and modeling of the physics involved in the OPACMEMS devices behavior (hence diving into task number 1). While in the former chapter the EM and thermal responses of the proposed nanoantennas are described and analyzed, the latter describes the semianalytic model that gathers all the involved and coupled physics (i.e., optical, thermal and mechanical) into a system of nonlinear ordinary differential equations.

Chapter 4 is devoted to the design and numerical simulation of a proof-of-concept OPACMEMS device (which are the main objectives of task number 2). The design process involves the use of a finite element analysis software to numerically solve and optimize the EM response of the designed nanoatennas. Based on latter EM absorbers and on several assumptions, the geometric and material properties of proof-of-concept device are proposed. Finally, the opto-thermo-mechanical model developed in chapter 3 is used to numerically obtain the theoretical behavior of the device.

The third task is covered in chapter 5, where a description of the custom approach used to fabricate the proposed devices is undertaken. Several fabrication results are also reported and analyzed in this chapter.

The objectives of task number 4 are partially fulfilled in chapter 6, where an opto-electrical characterization setup is designed, theoretically analyzed and assembled. In addition, the results obtained from the characterization of non OPACMEMS devices are reported with the aim to show the capabilities of the setup.

Finally, the main conclusions and the future directions of this thesis are collected in chapter 7.

Various appendices are included at the end of the document, including tedious mathematical steps followed during the modeling and other information that regardless of their relative importance have been included as an appendix in order not to extend the heart of the manuscript.

1.3 OPACMEMS background

This section is devoted to present the state-of-the-art of the two main field behind the OPACMEMS project: the optical antennas and the self-oscilation of M/NEMS. Rather than performing a deep study of each field, this section is intended to explain the most important concepts of each field as well as some results reported in the literature.

1.3.1 Opto-thermal coupling: optical antennas

Optical antennas are metallic resonant structures designed to convert the energy of free propagating radiation with visible and infrared wavelengths to localized energy, and vice versa. The big difference between this type of antennas and their radio wave counterpart is that the penetration of the electromagnetic radiation (EMR) into the metals can no longer be neglected. The incident EMR can produce a collective high frequency oscillation of the metal's free electrons, creating what is known as a plasma oscillation[1]. The EM resonance of an optical antenna is

[1]Not to be confused with what in the metallic solid free electron model is called as plasma frequency of the metal itself [17].

produced when this induced current is enhanced by the physical geometry of the antenna, thus producing a globally coherent current in it.

Some of the applications where optical antennas are being used are nanoscale imaging, spectroscopy, photovoltaics, light emission and coherent control [18]. In the field of photovoltaics the rectenna concept [19] (i.e., the rectification of the antenna's induced current to produce a continuous current output) was proposed back in 1972 [20] as a way to convert the solar energy to electrical energy. After the tremendous and continuous advance in the design, optimization and fabrication of the optical antennas the main obstacle still lies on the rectification at visible and infrared frequencies [21–23]. However, more fundamental bounds arise in the concept of harvesting the energy of the sun's radiation [24], such as the coherence of its emitted waves [25, 26]. Keeping in mind the OPACMEMS project it is worth to mention that optical antennas coupled to M/NEMS devices have been proposed as a way to tune the former [27, 28], for applications in local field enhancement [29] and as infrared radiation sensors [30].

One of the most well-known radio frequency antennas is the half-wave dipole. It is made of two metal segments of length $\lambda_0/4$ (being λ_0 the working wavelength) joined to an impedance-matched transmission line through where the electrical signals are sent or received [31]. Thanks to this matching of impedances the physical discontinuity introduced by the feedgap is eliminated. Therefore, a standalone dipole without electrical connectivity can be obtained by simply fabricating one single metal segment of length $\lambda_0/2$, where the aforementioned matching is performed by the metal itself. Accordingly, in the visible and infrared spectra a half-wave dipole antenna can be obtained by fabricating a single metal nanostrip or rod [32].

As its name indicate, a half-wave dipole has a total length equal to half of the wavelength at which it is designed to work [31]. Nevertheless, the fact that the penetration of the EMR at visible and infrared wavelengths can not be neglected causes that a classically designed dipole resonates at a higher wavelength than the one for which it was designed for. The following equation reproduces the simple

linear scaling law for the so-called effective wavelength $\lambda_{0\,eff}$ derived in [33],

$$\lambda_{0\,eff} = n_1 + n_2 \frac{\lambda_0}{\lambda_p} \tag{1.1}$$

where n_1 and n_2 are geometric constants, λ_0 is the EMR wavelength and λ_p the plasma wavelength of the metal of which the antenna is made of [17].

Since the dimensions obtained when designing antennas for applications in the visible and infrared spectra are in the order of the nanomentres, optical antennas are also referred as nanoantennas.

Dipole antennas are the typical example of EM resonant structures acting as absorbers. A different way to construct an absorber is by making use of resonant structures composed by an array of individual antennas. A frequency selective surface (FSS) is a periodic resonant structure that behave like an EM spatial filter by absorbing the incoming EMR [34]. Although the main applications of the FSS are in the radio wave spectrum, several researchers have managed to bring their uses to the infrared [35–38].

1.3.2 Thermo-mechanical coupling: self-oscillations driven by thermoelasticity

Resonant M/NEMS constitute a research field that is continuously under investigation due to its well-known applications (e.g., resonant mass sensors [39], vibratory gyroscopes [40], signal processing devices [41], etc.). The fundamental basis of such applications lie on the characteristics of the vibrational state at which the M/NEMS device is driven to. The device's resonance is often excited by means of an electrostatic [42], piezoelectric [43], thermoresistive [44], magnetic [45] or optical [46] method that require the use of an externally modulated input signal. However and as first reported in 1987 [47], self-oscillation of M/NEMS devices can be induced when the mechanical structure is inserted in the interference field of an unmodulated laser beam. Thus, eliminating the need of a stable periodic drive signal.

The nonlinear nature of the induced auto-oscillation state involves two types of energy conversion: optical to thermal and thermal to mechanical. The optical energy shinned by the laser is transformed to thermal energy through the Joule effect produced by the high frequency currents generated when the M/NEMS material absorb the EMR. Then, the thermal energy is turned to mechanical energy through the thermoelastic properties of the device material. These energy transformation can eventually lead to the self-oscillation of the M/NEMS as a consequence of an abrupt change of the mechanical stability.

Various scientific publications report the self-oscillation behavior of a MEMS device illuminated by a continuous wave (CW) laser. However, several mechanisms are interpreted to be behind the coupling between the optical and the mechanical domains; including the radiation pressure [48–51], the photothermal stress [47, 52–61] or a competition between both [62].

In the literature it can also be found that mechanical self-oscillations have been proposed as an energy harvesting technique in devices presenting an aeroelastic [63–65] and thermoelastic [66] couplings.

1.4 The proposed OPACMEMS device: the fishbone geometry

This section is intended to introduce the proposed OPACMEMS device geometry and its basic characteristics with the aim that the reader grasp the idea behind it so that the forthcoming chapters can be better understood.

To achieve the opto-thermo-mechanical coupling mechanism the geometry shown in figure 1.1 is proposed, which given its similarity to the main bone of a fish is named as fishbone geometry. The clamped-clamped beams (or fishbones) that form the device have a length in the range of the microns, while the nanostrips attached to them are a few hundreds of nanometers long. Therefore, the structure combines micro and nano dimensions.

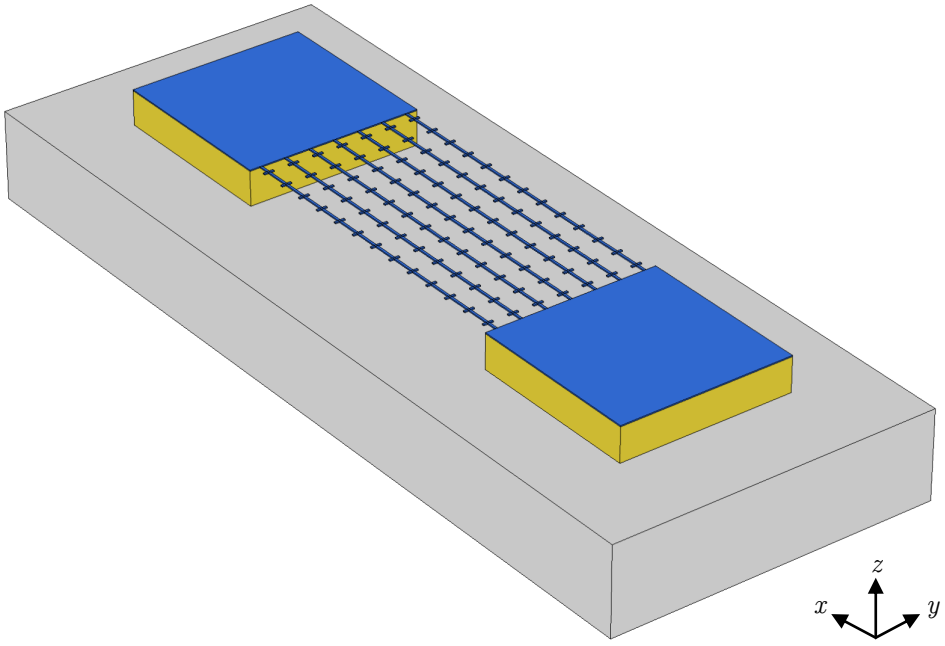

FIGURE 1.1: Fishbone geometry of the proposed OPACMEMS device.

Each of the individual nanostrips act as a dipole antenna and together as a FSS, interacting with the incoming EMR. The FSS will be designed to have its maximum response (i.e., maximum absorbance) at the infrared wavelength of $1.55\,\mu$m. As explained in section 1.3.1, the dimensions of the nanostrips are intimately linked with the working wavelength. Thus, choosing to work at the short-wavelength infrared spectrum range ($\lambda_0 = 1.4 - 3\,\mu$m) results in bigger dimensions when compared with working at the visible range ($\lambda_0 = 380 - 700\,$nm). Such dimensions are the direct cause of other advantages in the context of the OPACMEMS project:

- Electromagnetic FEM simulation: a higher wavelength is translated into less mesh elements for the same volume, hence decreasing the necessary computer memory and computational power.
- Fabrication: although electron beam lithography will be used to fabricate the devices, a better resolution is always obtained for bigger dimensions.
- Characterization setup: a wide range of optical components optimized to work at $1.55\,\mu$m are commercially available due to their applications in fiber-optic communication.

The thermoelasticity properties of the device material come into play due to the fact that the Joule heat produced by the induced high frequency currents on the nanostrips will be dissipated through the anchors of the clamped-clamped beams. Since the mechanical structure is suspended above an air or vacuum gap, it seems reasonable to think that the absorbance of the FSS will be related with the length of this gap (i.e., acting as a Fabry-Pérot cavity). Therefore, the micromechanical structure can be considered to be in the interference field of an incoming radiation perpendicular to its surface. The nonlinear properties of the whole proposed OPACMEMS device can eventually lead to its mechanical self-oscillation for a high enough EM irradiance.

Chapter 2

Modeling the absorption of infrared radiation

This chapter is dedicated to the computer-aided numerical modeling of a proposed FSS. The fishbone unit cell is qualitatively analyzed and compared with a materials and thicknesses equivalent multilayer example. Finally the combination of the studied FSS with a Fabry-Pérot cavity is studied.

2.1 Absorbing the electromagnetic radiation

Matter absorbs EMR by somehow transforming the photons energy into another form of energy, for example thermal energy. Therefore, the term absorption means dissipation of energy into the absorbing material.

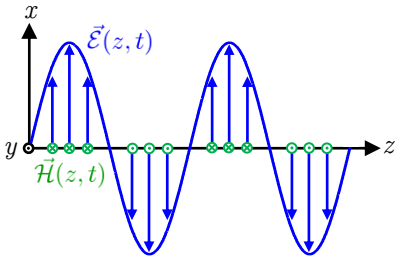

FIGURE 2.1: Illustration of a linearly polarized EM plane wave where $\vec{\mathcal{E}}$ and $\vec{\mathcal{H}}$ are respectively the electric and magnetic fields.

The time-domain expression for the real value of the electric field of a linearly polarized EM plane wave propagating in the positive z-direction (see figure 2.1) inside an absorbing medium can be described by[1] [67]

$$\vec{\mathcal{E}}(z,t) = \mathfrak{Re}\left\{\tilde{\vec{E}}(z)e^{j\omega t}\right\} = \mathfrak{Re}\left\{\hat{x}\tilde{E}(z)e^{j\omega t}\right\} = \hat{x}\,\mathfrak{Re}\left\{E_0 e^{j\left(\omega t - \tilde{k}z\right)}\right\} \tag{2.1}$$

where t is the time variable, $\hat{x}$ the x-direction orientation vector, E_0 a constant real amplitude, ω the angular frequency and $\tilde{k}$ the complex wavenumber of the wave. One way to compute the last term is by using the following definition

$$\tilde{k}(\omega) = \frac{\omega\tilde{n}(\omega)}{c} = \frac{\omega\big(n(\omega) - j\kappa(\omega)\big)}{c} = k(\omega) - j\frac{\omega\kappa}{c} \tag{2.2}$$

where n and κ are the real and imaginary parts of the complex refractive index $\tilde{n}$, and c is the speed of light in vacuum ($2.99792458{\cdot}10^8\,{}^{m}/_{s}$). Therefore, the real part of the complex wavenumber is $k = \frac{\omega n}{c} = \frac{2\pi}{\lambda_m}$, being $\lambda_m = \frac{\lambda_0}{n}$ the wavelength in the propagation material and λ_0 the wavelength in vacuum.

Another way to express the electric field intensity $\vec{\mathcal{E}}$ is by taking into account that during its propagation the wave suffers an attenuation because of the absorption of part of its photons energy by the medium. Defining $\alpha_{abs}(\omega)$ as the electric field absorption coefficient, equation (2.1) can be expressed as

$$\vec{\mathcal{E}} = \hat{x}\,\mathfrak{Re}\left\{E_0 e^{j(\omega t - kz)}\right\} e^{-\alpha_{abs} z} \tag{2.3}$$

Comparing equations (2.1) and (2.3) the following relationships are found

$$\mathfrak{Re}\left\{\tilde{n}\right\} = n = \frac{kc}{\omega} \tag{2.4}$$

$$\mathfrak{Im}\left\{\tilde{n}\right\} = \kappa = \frac{\alpha_{abs} c}{\omega} \tag{2.5}$$

According to (2.5) the extinction coefficient is directly related with the attenuation of the electric field inside the propagating medium.

[1] The convention that vectors are denoted with over-arrows and complex quantities with over-tildes is adopted.

2.1.1 The skin depth

The distance at which the magnitude of the electric field of an EM wave traveling through a medium has decreased to about 37 % of its initial value is called skin depth and it is defined as

$$\delta_{skin}(\omega) = \frac{1}{\alpha_{abs}} = \frac{c}{\omega\, \mathfrak{Im}\{\tilde{n}\}} = \frac{c}{\omega\kappa} \tag{2.6}$$

Figure 2.2 shows the skin depth value for different metals at the near and short-wavelength infrared spectral regions ($\lambda_0 = 0.75 - 3\,\mu$m). Metals are the only type of materials taken into account since the semiconductor or dielectric materials present a very low absorption coefficient in the infrared spectrum (i.e., they have a very low extinction coefficient).

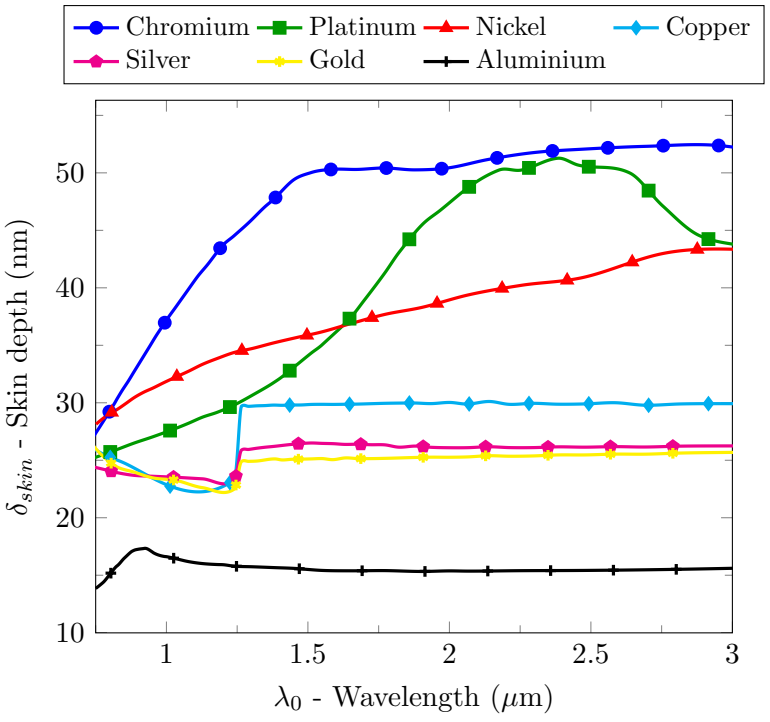

FIGURE 2.2: Skin depth for different metals at the near and short-wavelength infrared spectral regions. The frequency dependent refractive index for each metal was extracted from [68].

Table 2.1 summarizes the skin depth value at a wavelength of 1.55 μm for the metals of figure 2.2.

	Cr	Pt	Ni	Cu	Ag	Au	Al
δ_{skin} @ 1.55 μm (nm)	*50.2*	*35*	*36.2*	*29.9*	*26.5*	*25.1*	*15.4*

TABLE 2.1: Value of δ_{skin} for various metals.

The value of the skin depth when considering a single layer of metal gives information about the metal thickness that will almost block an incident electric field by both reflecting and absorbing it. If the thickness of the layer is equal to the corresponding skin depth, only the 37 % of the nonreflected electric field will be transmitted through it. The thinner, with respect to the skin depth, the layer the greater the transmitted electric field.

2.2 Quantifying the absorption through the Joule heating effect

The to be designed devices must transform the EMR energy into thermal energy, meaning that the absorbed energy is used to heat the device. The Joule induced heat is computed as the time-average resistive power losses,[2]

$$Q_{rpl}\left(\vec{r}\right) = \left\langle \vec{\mathcal{J}}\left(\vec{r},t\right)\vec{\mathcal{E}}\left(\vec{r},t\right)\right\rangle = \frac{1}{2}\,\mathfrak{Re}\left\{\tilde{\vec{J}}\left(\vec{r}\right)\tilde{\vec{E}}^{*}\left(\vec{r}\right)\right\} \tag{2.7}$$

where $\vec{r} = x\hat{x} + y\hat{y} + z\hat{z} = (x,y,z)$ is the position vector, $\vec{\mathcal{J}} = \mathfrak{Re}\left\{\tilde{\vec{J}}e^{j\omega t}\right\}$ the total induced sinusoidal steady state current density in the device, $\vec{\mathcal{E}} = \mathfrak{Re}\left\{\tilde{\vec{E}}e^{j\omega t}\right\}$ the sinusoidal steady state electric field inside it.

Two indistinguishable effects contribute to the total induced current density. The first one is due to the ohmic conduction, which is defined as

$$\vec{\mathcal{J}}_{ohmic}\left(\vec{r},t\right) = \sigma(\omega)\vec{\mathcal{E}} \tag{2.8}$$

[2]The brackets $\langle\,\rangle$ denote the time-average over a complete harmonic cycle (or many cycles) value and * the complex conjugate.

where σ is the conductivity of the device material.

The second contribution is due to the displacement current, which is defined as

$$\vec{\mathcal{J}}_{disp}\left(\vec{r},t\right)=\frac{\partial\vec{\mathcal{D}}\left(\vec{r},t\right)}{\partial t}=\mathfrak{Re}\left\{j\omega\tilde{\vec{D}}\left(\vec{r}\right)e^{j\omega t}\right\} \tag{2.9}$$

where $\vec{\mathcal{D}}=\mathfrak{Re}\left(\tilde{\vec{D}}e^{j\omega t}\right)$ is the sinusoidal steady state displacement field. The complex vector amplitude of the displacement field is given by

$$\tilde{\vec{D}}=\epsilon_0\tilde{\vec{E}}+\tilde{\vec{P}}_v\left(\vec{r}\right) \tag{2.10}$$

where ϵ_0 is the vacuum permittivity ($\approx 8.854187817620\ldots\cdot 10^{-12}\,{}^{F}/_{m}$) and $\tilde{\vec{P}}_v$ the complex vector amplitude of the electric polarization vector. For homogeneous linear and isotropic materials the latter is directly proportional to the amplitude of the electric field,

$$\tilde{\vec{P}}_v=\epsilon_0\tilde{\chi}_e(\omega)\tilde{\vec{E}}=\epsilon_0\big(\tilde{\epsilon}_r(\omega)-1\big)\tilde{\vec{E}} \tag{2.11}$$

where $\tilde{\chi}_e$ is the electric susceptibility of the material and $\tilde{\epsilon}_r$ its relative permittivity.

Thus, for homogeneous linear and isotropic materials equation (2.9) can be re-written as

$$\vec{\mathcal{J}}_{disp}=\epsilon_0\tilde{\epsilon}_r\frac{\partial\vec{\mathcal{E}}}{\partial t}=\mathfrak{Re}\left\{j\omega\epsilon_0\tilde{\epsilon}_r\tilde{\vec{E}}e^{j\omega t}\right\} \tag{2.12}$$

Therefore, the total induced current density for these materials is given by

$$\vec{\mathcal{J}}=\vec{\mathcal{J}}_{ohmic}+\vec{\mathcal{J}}_{disp}=\sigma\vec{\mathcal{E}}+\mathfrak{Re}\left\{j\omega\epsilon_0\tilde{\epsilon}_r\tilde{\vec{E}}e^{j\omega t}\right\} \tag{2.13}$$

When taking into account equations (2.7) and (2.13), the total time-average resistive power losses over the device volume V can be computed as

$$Q_{Trpl}=\frac{1}{2}\int_V|\tilde{\vec{E}}|^2\,\mathfrak{Re}\left\{\sigma+j\omega\epsilon_0\tilde{\epsilon}_r\right\}\,dV \tag{2.14}$$

2.2.1 Optics and photonics applications

In optics and photonics applications the refractive index is used instead of the permittivity. At optical frequencies the relative permeability of common materials is very close to 1 (i.e., $\mu_r \approx 1$), therefore the complex refractive index can be computed as [69]

$$\tilde{\epsilon_r} = \tilde{n}^2 \tag{2.15}$$

where [70]

$$\tilde{\epsilon}_r = \epsilon'_r(\omega) - j\epsilon''_r(\omega) = \epsilon'_r - j\left(\epsilon''_{r.d}(\omega) + \frac{\sigma}{\omega\epsilon_0}\right) \tag{2.16}$$

Note that ϵ''_r takes into account the dielectric (due to $\epsilon''_{r.d}$) and ohmic (due to σ) losses of the material.

As a result of (2.15), the real and imaginary parts of the complex relative permittivity can be computed as

$$\epsilon'_r = n^2 - \kappa^2 \tag{2.17}$$

$$\epsilon''_r = 2n\kappa \tag{2.18}$$

Therefore, and following (2.14), the total time-average resistive power losses over the device volume can be computed as

$$Q_{Trpl} = \frac{1}{2}\int_V |\tilde{\vec{E}}|^2\, \mathfrak{Re}\{j\epsilon_0\tilde{\epsilon}_r\omega\}dV = \frac{\epsilon_0\epsilon''_r\omega}{2}\int_V |\tilde{\vec{E}}|^2\, dV \tag{2.19}$$

2.3 Multilayer absorbers

The simplest way to construct an absorber is by stacking thin layers of different materials backed by a perfect electric conductor. This layered device is designed to minimize the overall reflectivity while maximizing its absorbance in the selected wavelength range. In fact, the most common absorber used in thermal applications is a thin uniform metal layer deposited on a substrate.

In order to establish a comparison in further sections and without the aim to deeply study these type of absorbers, a particular example is shown and analyzed.

There are various methods to theoretically study the reflection, absorption and transmission of EMR through a multilayer absorber. The theoretical results presented in this and the following sections are computed with both the transfer matrix method (TMM) [71] and the finite element method (FEM) [72]. The first method is applied using a custom Matlab code whereas for the second one COMSOL Multiphysics is used.

2.3.1 Multilayer device example

In this section the absorbance at $\lambda_0 = 1.55\,\mu$m of a multilayer composed by a chromium thin film followed by a vacuum gap and ended by a silicon substrate is computed using the FEM and the TMM. The used optical properties of the involved materials are listed in table 2.2. The absorbance is computed for different chromium thicknesses at a constant gap value of $\lambda_0/4 = 387.5\,$nm. Figure 2.3 shows the obtained results.

Material	$n - j\kappa$
Cr	*4.19 − j4.92*
Vacuum	*1*
Si	*3.48 − j1.13e-6*

TABLE 2.2: Complex refractive indexes at $\lambda_0 = 1.55\,\mu$m ($f = 193.4\,$THz). Extracted from [68].

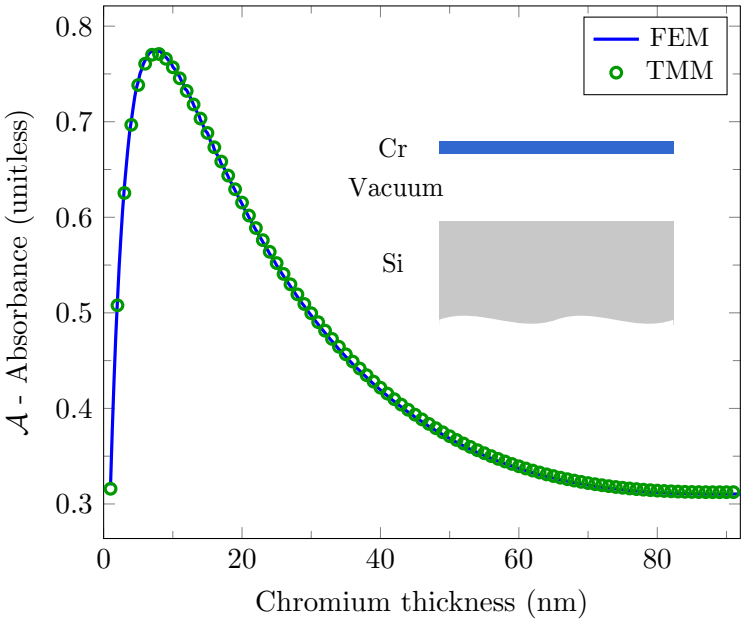

FIGURE 2.3: Evolution of the absorbance at $\lambda_0 = 1.55\,\mu$m with the metal layer thickness.

As shown in table 2.1, the skin depth of chromium at $1.55\,\mu$m is 50.2 nm. Therefore, for thicknesses lower than this value the EM fields can reach the silicon substrate and reflect multiple times. The consequence is that the metal layer, being optically thin, absorbs more energy. For thicknesses higher than the skin depth value, the EM fields are mostly reflected once they reach the chromium surface. For a chromium thickness of about 7.5 nm the absorbance has its maximum, 77.4 %. The regular electron-beam evaporation techniques are in the limit of yielding such uniform and continuous metal thin films. However, thicknesses over 20 nm are feasible with these procedures. Nevertheless, the absorbance drops to less than 61.4 % for these dimensions.

2.4 Infrared frequency selective surface

As explained in section 1.3.1, a properly designed FSS can also be used as an absorber at infrared wavelengths. The fishbone structure is based on a clamped-clamped bridge which geometry has been modified to incorporate several EM

resonant elements. In order to study the proposed geometry, FEM simulations are carried out using the commercial COMSOL Multiphysics software.

To obtain accurate numerical results when solving any harmonic function with the FEM it is necessary for the maximum mesh element to be smaller than half of its wavelength, fulfilling the Nyquist criterion [73]. Following [74], the number of mesh elements per wavelength in free space for the simulations performed in this thesis is chosen to be five. As a consequence of the latter criterion, the simulation of the entire designed FSS requires, what is nowadays considered, a big amount of computer RAM and computing time. Therefore, a full 3D electromagnetic simulation is carried out only using a small portion of each design instead of the entire optically-big geometry. This small periodic portion is called unit cell (UC).

2.4.1 Unit cell simulation: electromagnetic boundary conditions and domain materials

The unit cell of a FSS is the portion of its design that is periodically repeated on both longitudinal and lateral directions. Figure 2.4 shows the unit cell of the proposed OPACMEMS device geometry illustrated in figure 1.1. Although in the proposed geometry these symmetries are broken on the anchor supports of the mechanical structures, their simulation can give a pretty good approximation of the EM behavior of the entire FSS.

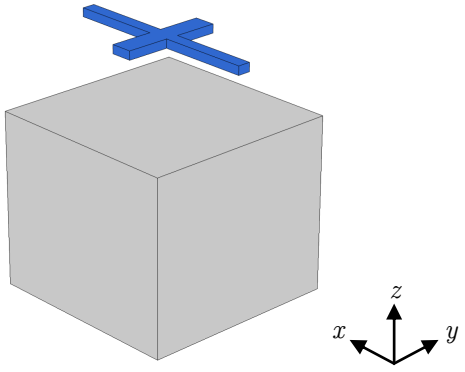

FIGURE 2.4: Fishbone unit cell geometry.

When using an EM simulator to study the unit cell of a FSS the proper boundary conditions (BCs) need to be defined. Two main assumptions were taken into account when choosing the BCs:

- Assumption 1: the excitation of the unit cell is carried out by a uniform transverse electromagnetic (TEM) plane wave normal to its surface.
- Assumption 2: the unit cell has an infinite longitudinal (x-axis) and lateral (y-axis) periodicity, as shown in figure 2.5. Meaning that the unit cell is surrounded by the same exact cell.

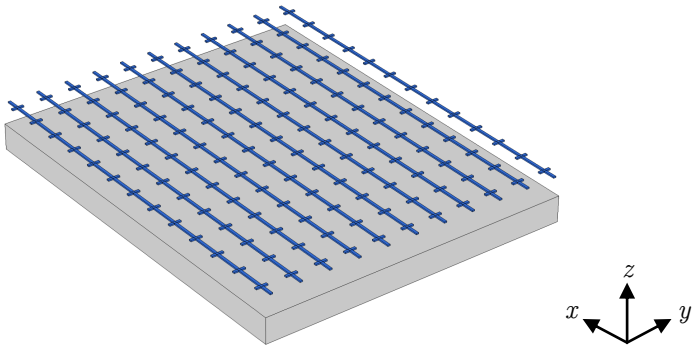

FIGURE 2.5: Illustrative geometry of the fishbone FSS. The unit cell is repeated infinitely along the x and y directions.

From these two assumptions the following EM boundary conditions are applied to the unit cell simulation models:

- BC 1: the unit cell is illuminated with a downward directed uniform TEM plane wave with the electric field along the proper axis. The colored surface of figure 2.6a denote the area from which the plane wave is launched.
- BC 2: perfectly matched layers (PMLs) are defined at the top and bottom of the computational domain to reduce backscatter at these boundaries by absorbing, without reflection, any incoming evanescent or propagating wave. The thickness of these domains are kept constant at $\lambda_0/2$, where λ_0 is the wavelength of the excitation plane wave in vacuum. The colored domains of figure 2.6b denote the PML regions.

- BC 3: the top and bottom surfaces of the computational domain are defined as scattering boundaries (SBs). This boundary condition makes the surface where it is applied perfectly transparent to an incoming plane wave. Using a PML (as defined with the BC 2) backed by a SB reduces any artificial reflections inside the PML domain. The colored surfaces of figure 2.6c denote the scattering boundaries.

- BC 4: the boundaries perpendicular to the electric field are defined as perfect electric conductors (PECs). The colored surfaces of figure 2.6d denote the boundaries where the PEC condition is applied.

- BC 5: the boundaries perpendicular to the magnetic field are defined as perfect magnetic conductors (PMCs). The colored surfaces of figure 2.6e denote the boundaries where the PMC condition is applied.

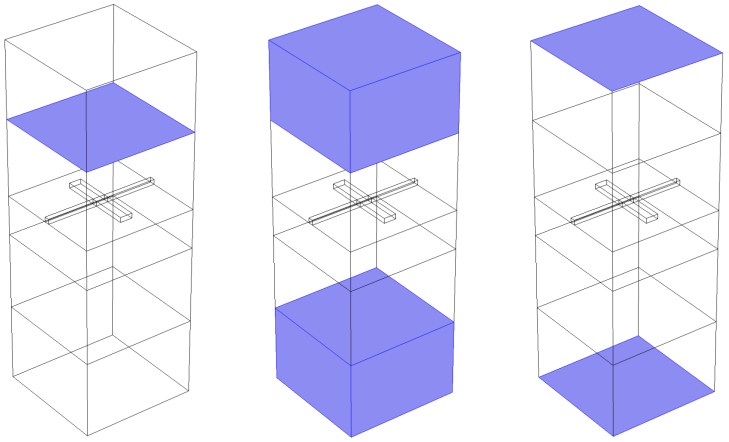

(A) EM BC 1. (B) EM BC 2. (C) EM BC 3.

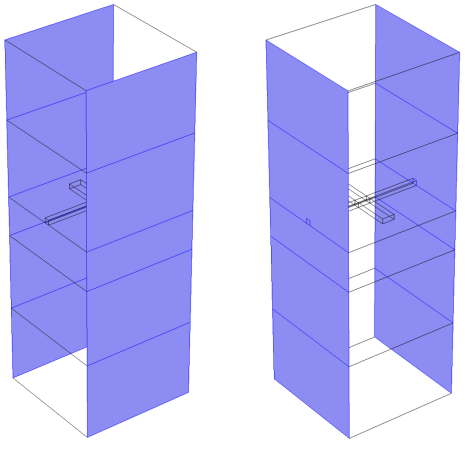

(D) EM BC 4. (E) EM BC 5.

FIGURE 2.6: EM boundary conditions for the unit cell simulation.

The boundary conditions 4 and 5 also ensure normal incidence of the respective fields at the boundaries transverse to the direction of propagation and imply that the solution will be mirror symmetric about those planes. In order to validate the used boundary conditions a simulation where all the domains were set to vacuum was carried out. Figure 2.7 shows the electric field of the generated plane wave, proving the appropriateness of the imposed BCs.

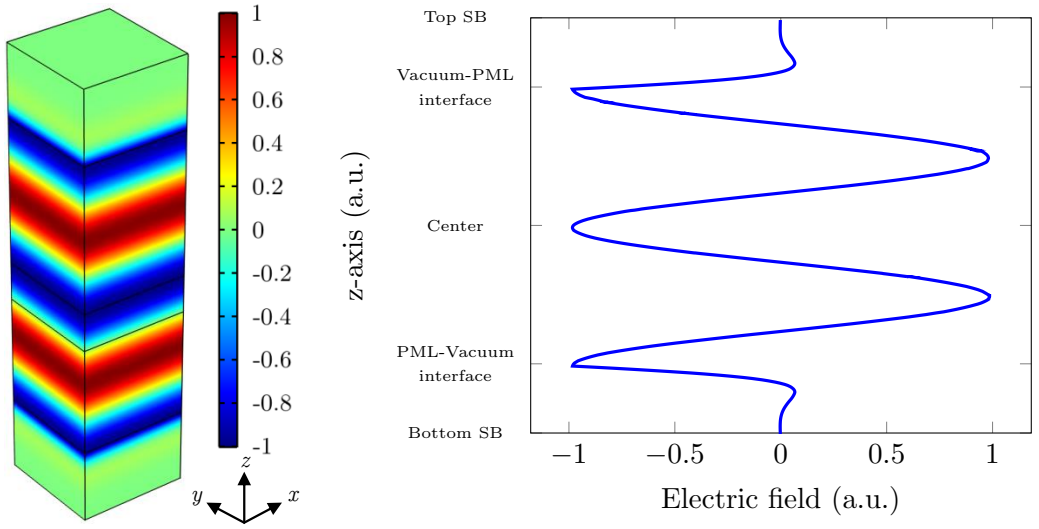

(A) Electric field on the computational domain.

(B) Electric field along the center of the computational domain.

FIGURE 2.7: Electric field of the generated plane wave.

The necessary properties of the different model domains are given by assigning the corresponding material to everyone of them. From an EM simulation point of view, the proposed unit cell is composed by three different materials:

- Metal: all the domains corresponding to the FSS unit cell are described by the appropriate properties of the involved metal. The colored volumes of figure 2.8a are and example of this domains.
- Silicon: the domains beneath the unit cell gap are described as silicon, which simulates the wafer substrate of the device. The colored volumes of figure 2.8b indicates these zones.
- Vacuum: the remaining domains are defined as vacuum, see the colored volumes of figure 2.8c.

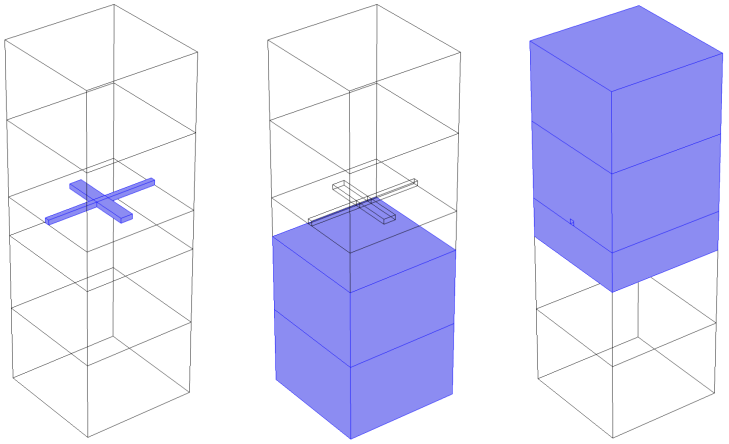

(A) Metal. (B) Silicon. (C) Vacuum.

FIGURE 2.8: Material domains of an example unit cell.

With all the boundary conditions and materials set, a full field simulation is carried out. Once the simulation has ended, the absorbed power converted into heat by the unit cell is computed using equation (2.19).

2.4.2 Unit cell simulation: computing the absorbance

The instantaneous power flow of an EM wave is the so-called Poynting vector, which is given by

$$\vec{\mathcal{P}}(\vec{r},t) = \vec{\mathcal{E}}(\vec{r},t) \times \vec{\mathcal{H}}(\vec{r},t) \tag{2.20}$$

where $\vec{\mathcal{H}} = \mathfrak{Re}\left\{\tilde{\vec{H}}(\vec{r})\, e^{j\omega t}\right\}$ is the sinusoidal steady state magnetic field of the wave. It can be expressed using the electric field of the wave as

$$\vec{\mathcal{H}} = \frac{1}{\eta_0}\hat{k} \times \vec{\mathcal{E}} \tag{2.21}$$

where $\eta_0 = \sqrt{\mu_0/\epsilon_0}$ is the impedance of the free space (being μ_0 the vacuum permeability) and $\hat{k}$ the unitary propagation direction vector of the wave (which for the EM wave defined by (2.1) is $\hat{k} = \hat{z}$).

The time-average power flow of a sinusoidal wave can be computed as

$$\begin{aligned}\vec{P}(\vec{r}) = \langle\vec{\mathcal{P}}\rangle &= \lim_{T\to\infty}\frac{1}{T}\int_{T/2}^{-T/2}\vec{\mathcal{P}}\,dt \\ &= \langle\vec{\mathcal{E}}\times\vec{\mathcal{H}}\rangle = \frac{1}{2}\mathfrak{Re}\left\{\tilde{\vec{E}}\times\tilde{\vec{H}}^{*}\right\}\end{aligned} \tag{2.22}$$

Equation (2.22) can be re-written in terms of the electric field by using (2.21), yielding

$$\vec{P} = \frac{1}{\eta_0}\langle\vec{\mathcal{E}}\times\hat{k}\times\vec{\mathcal{E}}\rangle = \frac{1}{2}\frac{\tilde{\vec{E}}\tilde{\vec{E}}^{*}}{\eta_0}\hat{k} = \frac{1}{2}\frac{\left|\tilde{\vec{E}}\right|^2}{\eta_0}\hat{k} \tag{2.23}$$

The intensity or irradiance of a wave is defined as the amplitude of (2.23),

$$I_{rr} \equiv \left|\langle\vec{\mathcal{P}}\rangle\right| = \frac{1}{2}\frac{\left|\tilde{\vec{E}}\right|^2}{\eta_0} = \frac{1}{2}\frac{\left|\tilde{E}_0\right|^2}{\eta_0} \tag{2.24}$$

where $\tilde{E}_0$ is the constant complex electric field amplitude of the wave. The polarization of the wave is embedded in this complex amplitude. For a linearly polarized plane wave this amplitude is a real number (see (2.1)).

Given the irradiance of a wave its total EM power can be computed as

$$P_{EM.T} = \int_{A_T} I_{rr}\,dA \tag{2.25}$$

where A_T is the total area irradiated by the wave.

The absorbance of a FSS is defined as the ratio between the EM power of the unit cell exciting wave $P_{EM.UC}$ and the heat power produced by the Joule effect in the structure,

$$\mathcal{A} = \frac{Q_{Trpl}}{P_{EM.UC}} \tag{2.26}$$

When simulating a particular unit cell the value of $P_{EM.UC}$ can be computed using (2.25) with $A_T = A_{UC}$ being the xy-area delimited by the UC computational box (see figure 2.7b). Since the irradiance of a plane wave does not depend on the area (2.25) is reduced to

$$P_{EM.UC} = I_{rr}A_{UC} \tag{2.27}$$

A parametric study on the dimensions of the proposed unit cell will be done for each case in order to optimize its absorbance at the working wavelength. These optimization process is shown in chapter 4.

2.4.3 The fishbone unit cell

When simulating the fishbone unit cell, the electric field of the generated plane wave has its linear polarization state along the long axis of the nanostrip (y-axis in figure 2.4). Figure 2.9 shows three magnitude plots for this unit cell when in its EM resonance. The local electric field and induced current density are zero at the extremes of the nanostrip and maximum around its center. Following equation (2.7), the resistive power losses due to the finite conductance of the metal are also maximum around the nanostrip's clamping.

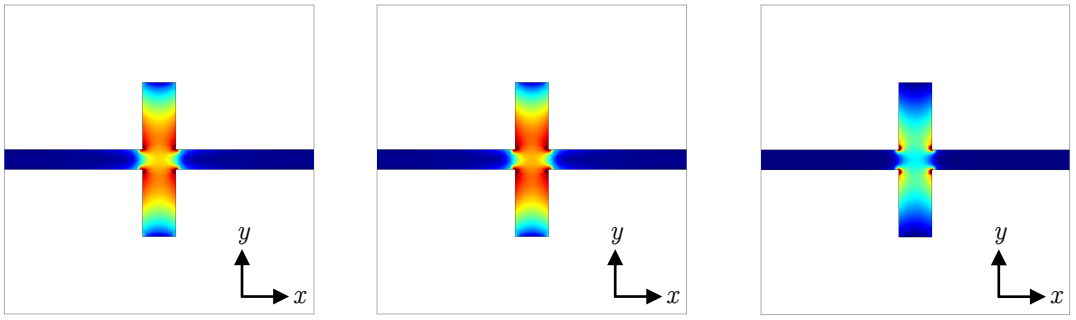

(A) Electric field. (B) Current density. (C) Resistive losses.

FIGURE 2.9: Magnitude plots of a fishbone unit cell. Red (maximum) to blue (minimum) color scale is used.

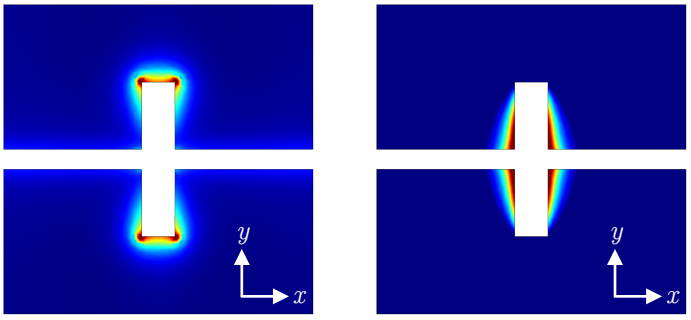

(A) Electric field. (B) Magnetic field.

FIGURE 2.10: Magnitude plots outside the fishbone unit cell domain. Red (maximum) to blue (minimum) color scale is used.

Figure 2.10 shows the electric and magnetic fields outside the nanostrip domain. While the electric field is boosted at the area surrounding the ends of the nanostrip, the magnetic field is enhanced around its center.

2.4.4 Comparison with a multilayer absorber

Figure 2.11 shows a comparison between the multilayer absorber analyzed in section 2.3.1 and the proposed FSS based on the fishbone unit cell when taking into account chromium thicknesses[3] from 20 to 90 nm. For every thickness the corresponding unit cell dimensions are optimized[4] to maximize the absorbance. In all the devices the gap is kept constant at $\lambda_0/4 = 387.5\,\text{nm}$. Thanks to the optimization process the FSS absorbance is managed to be kept approximately constant for any chromium thickness at a roughly the 76 %. The multilayer's maximum absorbance is 77.4 % though it can only be achieved when the metal layer is 7.5 nm thick. Therefore, the use of FSSs as EMR absorbers is clearly justified when the thickness of the metal layer represents a fabrication drawback.

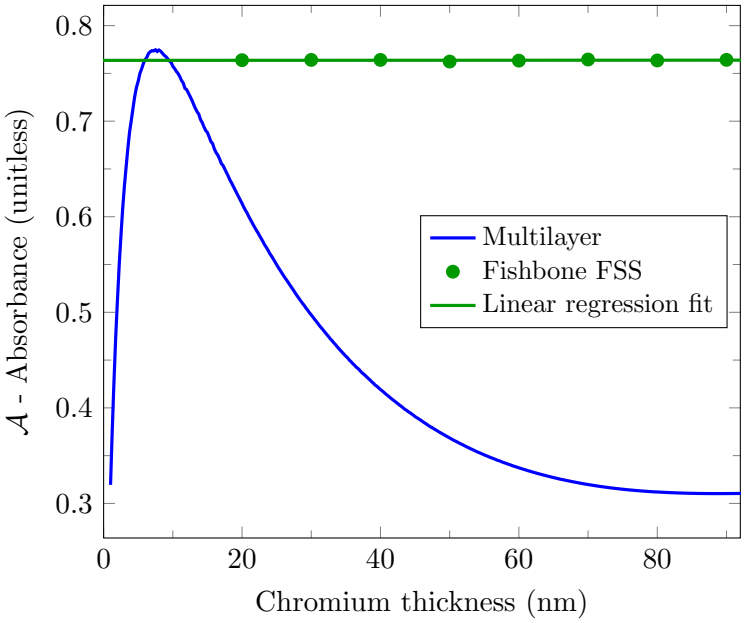

FIGURE 2.11: Evolution of the absorbance at $\lambda_0 = 1.55\,\mu\text{m}$ with the metal layer thickness.

[3]FEM simulations with smaller thicknesses could not be performed due to not having enough RAM memory in the workstation computer (a maximum of 24 GBytes were available)

[4]The optimization process is explained in section 4.1.1.

2.5 Absorbers coupled to a variable Fabry-Pérot cavity

As shown in figure 1.1, the proposed device is suspended above an air or vacuum gap. When the FSS is illuminated, some part of the incident EMR is reflected, some other absorbed by the FSS and the rest of it reaches the air-substrate interface. At this interface a fraction of the downwards traveling wave is transmitted into the substrate and the other fraction is reflected back to the FSS. The same phenomena happens when this reflected wave reaches the bottom air-metal interface. Therefore, multiple waves reflected by the upper and lower boundaries of the cavity interfere with each other and produce a standing wave. Consequently, the equivalent EM wave that interacts with the FSS and eventually leads to the heating of the mechanical structure depends on the thickness and material properties of the cavity. Figure 2.12 shows a schematic of this Fabry-Pérot cavity.

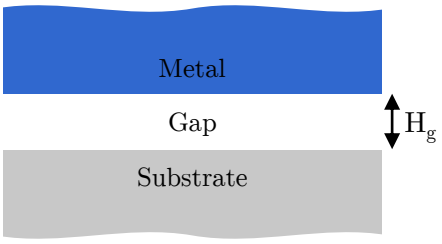

FIGURE 2.12: Schematic of the Fabry-Pérot cavity.

2.5.1 Optimizing the gap thickness: multilayer analysis

The gap thickness that maximizes the absorbance of the metal layer in the multilayer absorber sketched in figure 2.12 is the same one that also maximizes the reflectance of the Fabry-Pérot cavity (i.e., the reflectance (transmittance) of the metal-gap (gap-metal) interface). Assuming that air-substrate and air-metal interfaces are identical flat reflective surfaces that do not absorb any radiation, the reflectance of this ideal Fabry-Pérot cavity is given by [71]

$$\mathcal{R}_{FP} = \frac{4\mathcal{R}_i \sin^2\left(\frac{\delta}{2}\right)}{\left(1-\mathcal{R}_i\right)^2 + 4\mathcal{R}_i \sin^2\left(\frac{\delta}{2}\right)} \tag{2.28}$$

where $\mathcal{R}_i$ is the reflectivity of the interfaces and $\delta = \frac{4\pi n_g}{\lambda_0} H_g$ (being n_g the refraction index of its material and H_g the thickness of the cavity, see figure 2.12).

The derivative of (2.28) as a function of the gap thickness yields

$$\frac{d\mathcal{R}_{FP}}{dH_g} = \frac{2\pi n_g}{\lambda_0} \frac{(1-\mathcal{R}_i)^2 \, 4\mathcal{R}_i \sin(\delta)}{\left[(1-\mathcal{R}_i)^2 + 4\mathcal{R}_i \sin^2\left(\frac{\delta}{2}\right)\right]^2} \tag{2.29}$$

The gap thickness that maximizes the EMR reflected by the cavity can be computed by equaling (2.29) to zero (which is the same as saying that the reflected standing wave comes from a constructive interference), yielding

$$H_{g-max} = (2m+1)\frac{\lambda_0}{4} \tag{2.30}$$

where the consideration of $n_g = 1$ is assumed (since the gap material is air/vacuum) and $m \in \mathbb{Z}$.

Therefore, the minimum gap thickness that maximizes both the EMR reflected into the Fabry-Pérot cavity and the EMR absorbed by the metal layer is $H_g = \lambda_0/4$.

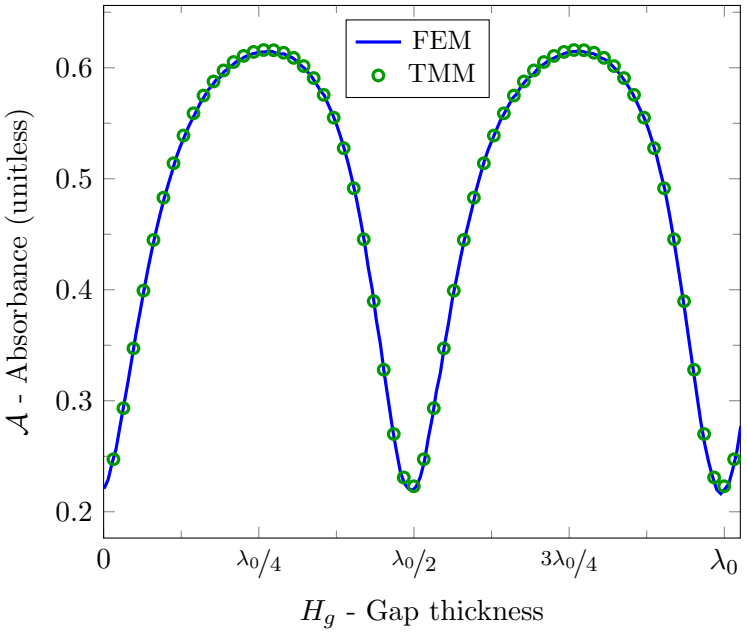

FIGURE 2.13: Evolution of the 20 nm thick chromium layer's absorbance at $\lambda_0 = 1.55\,\mu$m with the Fabry-Pérot cavity thickness.

Figure 2.13 shows the absorbance curve of the multilayer absorber of figure 2.3 for a 20 nm chromium layer as a function of its gap thickness. Although in this analysis the different materials complex refractive indexes (meaning that the cavity interfaces are not equal and the used materials do absorb the EMR) and the finite thickness of the metal layer have been considered, the absorbance's maximums almost follow equation 2.30.

2.5.2 Fishbone unit cell coupled to a variable Fabry-Pérot cavity

When considering that the gap thickness of the fishbone unit cell is going to be somehow modified, the response of the FSS to an incident EM wave is going to be affected by this change. As explained in the previous section, that is because its EM response is linked to the EM alterations of the standing wave generated inside the cavity.

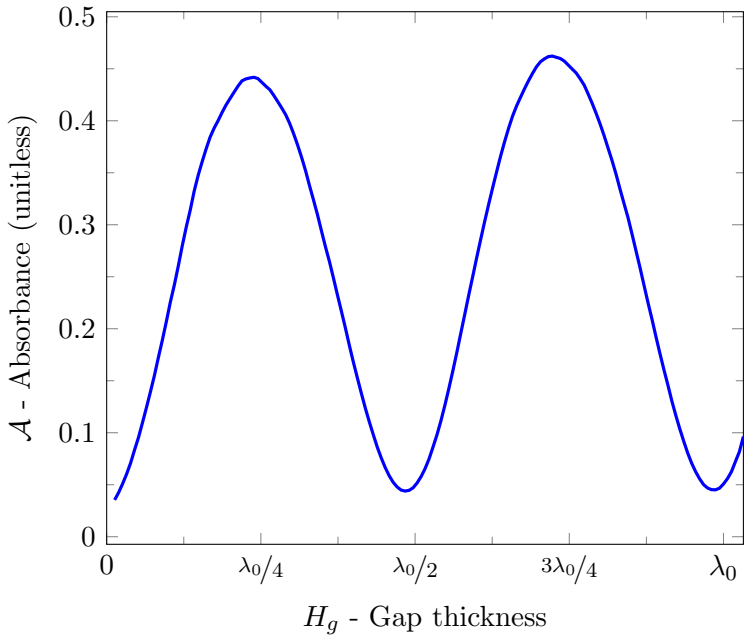

FIGURE 2.14: Evolution of the fishbone FSS absorbance at $\lambda_0 = 1.55\,\mu$m with the gap thickness.

Figure 2.14 shows the absorbance evolution with the gap thickness of a non-optimized FSS example based on the fishbone unit cell (the FEM is used to compute this curve). From the obtained results it can be seen that the gap thicknesses for which the absorbance is maximized closely follow equation 2.30.

2.6 Thermal power per unit volume

In the previous sections different types of absorbers were compared using their characteristic absorbance value at a certain frequency. Since the purpose of the absorbing process is to heat up the mechanical structure, a better way of comparing different absorbers is by analyzing their averaged heat power per unit volume. Given the device dimensions, its value is computed as

$$\mathcal{Q}_{UC} = \frac{Q_{Trpl}}{V_{UC}} \tag{2.31}$$

where Q_{Trpl} is the total time-average resistive power losses over the unit cell volume, V_{UC}.

However, a comparison based on the particular value of $\mathcal{Q}_{UC}$ can only be done when the irradiance of EM source used in the simulation of the different absorbers is the same for each case. That is because the higher the irradiance the higher the amount of EMR energy that contributes to the Joule effect.

Figure 2.15 shows the comparison between the multilayer absorber and the proposed unit cell in terms of their thermal power per unit volume evolution with the thickness of the metal layer. For every thickness the corresponding unit cell dimensions are optimized to maximize the value of $\mathcal{Q}_{UC}$. The simulation results clearly show that the FSS based on the fishbone UC is a better design in terms of the thermal power per unit volume for any chromium thickness, presenting an enhancement up to 20 times with respect to the multilayer absorber.

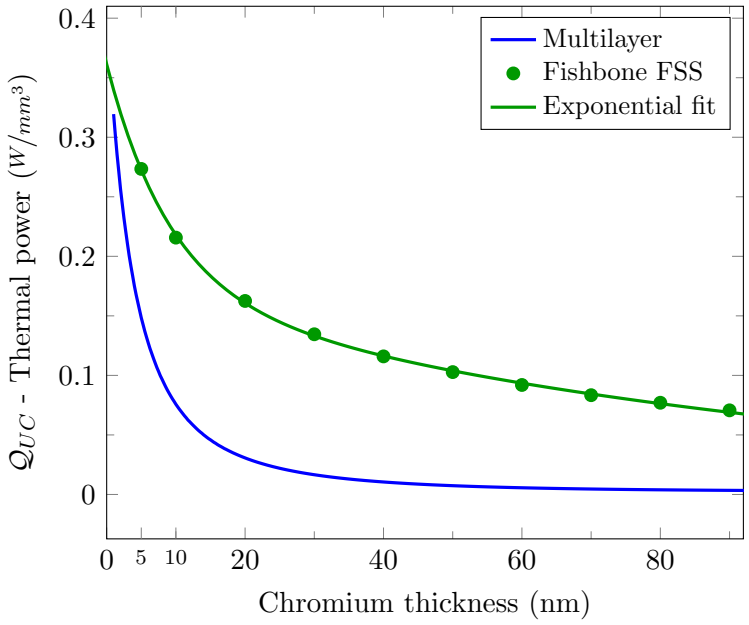

FIGURE 2.15: Evolution of the thermal power per unit volume at $\lambda_0 = 1.55\,\mu$m with the metal layer thickness for various absorbers. Irradiance = $1\,W/m^2$.

2.7 Summary

In this chapter the theoretical background behind the absorption of electromagnetic radiation by matter is presented and analyzed. Thanks to this analysis an equation governing such phenomena is obtained and applied to compute the absorption of both a simple mulilayer device and a more complex one which includes EM resonant structures. These two absorbers are compared in terms of their absorbance parameter and their thermal power per unit volume with the metal layer thickness. In terms of their absorbance, the conclusion of such comparison is that the FSS-based absorber becomes a better option when the thickness of the active layer represents a fabrication drawback. As for the thermal power, the FSS-based absorber also shows a better performance achieving higher values for every metal thickness. Finally, when the absorbers are coupled to a variable Fabry-Pérot cavity their responses become periodic with the thickness of such cavity.

Chapter 3

Modeling the opto-thermo-mechanical coupling mechanism

This chapter is devoted to the analytic modeling of the opto-thermo-mechanical coupling mechanism present in the proposed devices. By order of analysis, the optical, thermal and mechanical parts are studied and later used to finally develop the complete opto-thermo-mechanical model.

3.1 Optical part: modeling the external heat source

As explained in chapter 2, the source from which heat is generated in the proposed devices is the Joule effect produced by the currents induced by the electromagnetic resonance of the device integrated nanoantennas. Therefore, the integrated FSS can be seen as an absorber with a specific absorbance. In order to introduce this effect into the analytic model developed in this chapter, the equivalent absorbance as a function of the FSS vertical position within the gap cavity (which is assumed

to be a function of time) is computed from FEM simulations. The vertical position of FSS, $Z(t)$, can be expressed by its relation with the gap thickness as

$$Z(t) = H_g(t) - H_{g.initial} \tag{3.1}$$

where $H_{g.initial}$ is the gap thickness after the fabrication process.

The latter equation assumes that the deflection of the mechanical structure where the FSS is integrated is parallel to the substrate (i.e., the deflection is the same along the x-axis, see figure 2.4). Therefore, equation (3.1) is only valid for small deflections.

Figure 3.1 reproduces the absorbance values shown in figure 2.14 when plotting them as a function of the FSS vertical position, taking into account equation (3.1).

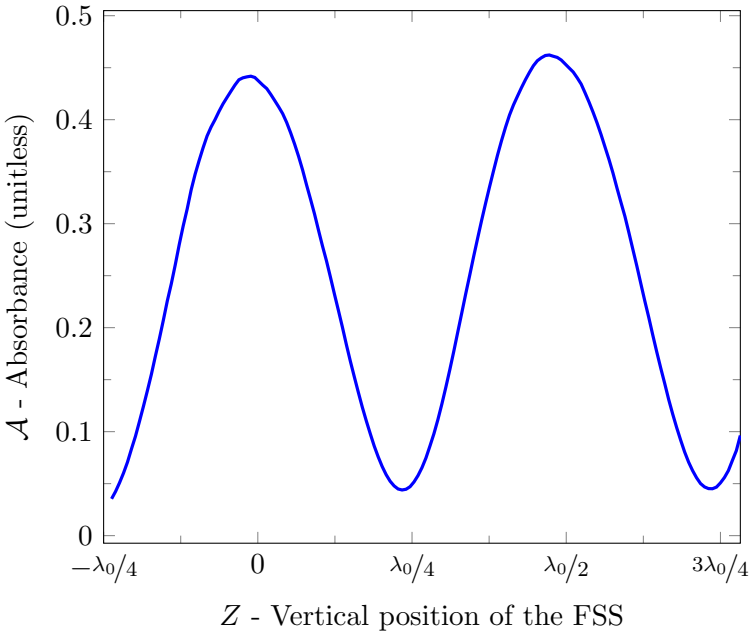

FIGURE 3.1: Evolution of the fishbone unit cell absorbance at $\lambda_0 = 1.55\,\mu$m with its vertical position within the gap. $H_{g-initial} = \lambda_0/4$.

Since the obtained absorbance is periodic the Fourier series approximation can be used to analytically reproduce its shape,

$$\mathcal{A}\big[Z(t)\big] \approx \mathcal{F}\Big\{\mathcal{A}\big[Z(t)\big]\Big\} \equiv \mathcal{F}\big[Z(t)\big] \tag{3.2}$$

where

$$\mathcal{F} = \frac{a_0}{2} + \sum_{r=1}^{R}\left(a_r \cos\left(\frac{2\pi r Z}{T_p}\right) + b_r \sin\left(\frac{2\pi r Z}{T_p}\right)\right) \tag{3.3}$$

being T_p the period of $\mathcal{A}$, $R > 0 \in \mathbb{Z}$ the order of the series and a_r and b_r are given by

$$a_r = \frac{2}{T_p}\int_{Z(t=0)}^{Z(t=0)+T_p} \mathcal{A}\cos\left(\frac{2\pi r Z}{T_p}\right) dZ \tag{3.4}$$

$$b_r = \frac{2}{T_p}\int_{Z(t=0)}^{Z(t=0)+T_p} \mathcal{A}\sin\left(\frac{2\pi r Z}{T_p}\right) dZ \tag{3.5}$$

Therefore, the external heat source can be expressed as

$$\mathcal{Q}\big[Z(t)\big] = P_V \mathcal{F} \approx P_V \mathcal{A} \tag{3.6}$$

where P_V is the total available thermal power per unit volume of the source that induces heat to the FSS. The simulated absorbance is defined as the ratio between the EM power of the UC exciting wave and the heat power produced by the Joule effect in the structure (see (2.26)),

$$\mathcal{A} = \frac{Q_{Trpl}}{P_{EM.UC}} \tag{3.7}$$

When simulating a particular UC the value of $P_{EM.UC}$ can be computed using (see (2.27))

$$P_{EM.UC} = I_{rr} A_{UC} \tag{3.8}$$

where A_{UC} is the xy-area delimited by the UC computational box (see figure 2.7b). However, when the opto-thermo-mechanical model is used to simulate the whole designed device, this same total area must be multiplied by the number of UC forming the entire structure (see figure 4.5). Therefore, if the total number of UC forming the designed device is n_{UC}, the EM power of the FSS exciting wave must be computed as

$$P_{EM.FSS} = I_{rr} n_{UC} A_{UC} \tag{3.9}$$

Given the above definitions, the total available thermal power per unit volume P_V can be computed as

$$P_V = \frac{P_{EM.FSS}}{V_T} = \frac{I_{rr} n_{UC} A_{UC}}{V_T} \tag{3.10}$$

where V_T is the total volume of the FSS structure.

The following temporal and spatial variables are defined when adimensionalizing the time by an elastic frequency scale $\left(\omega_s^2 = \frac{EI}{\rho A L^4}\right)$ and the vertical position of the FSS by the wavelength at which it is designed (i.e., $\lambda_w = 1.55\,\mu$m)

$$\hat{t} = t\omega_s\,, \quad \hat{Z} = \frac{Z}{\lambda_w} \tag{3.11}$$

When using the new temporal and spatial variables equation (3.6) is transformed into

$$Q\left[\hat{Z}(\hat{t})\right] = P_V \hat{\mathcal{F}} \approx P_V \hat{\mathcal{A}} \tag{3.12}$$

Figure 3.2 shows the comparison between the adimensionalized values of figure 3.1 and the computed Fourier series approximation of their evolution with the vertical position of the FSS when the order of the series is $R = 6$.

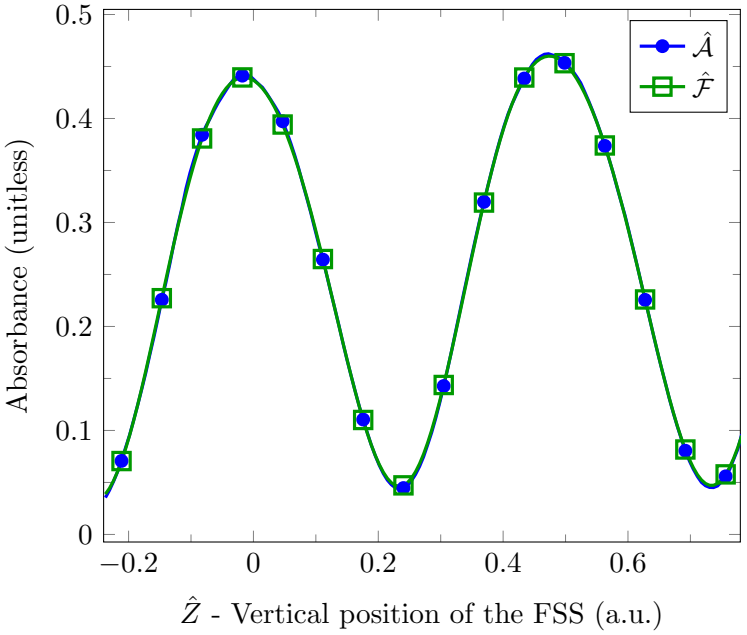

FIGURE 3.2: Evolution of the fishbone unit cell absorbance at $\lambda_w = 1.55\,\mu$m with its adimensionalized vertical position within the gap.

3.2 Thermal part: heat transfer equation

The relative[1] temperature field $\theta(x,t)$ of the modeled beam subjected to the external heat source defined by (3.6) is governed by the heat transfer equation (3.13). Where c_p is the specific heat capacity of the structural material, ρ its density and $\phi(x,t)$ the energy flux within the beam.

$$c_p \rho \frac{\partial \theta}{\partial t} = -\nabla \phi + \mathcal{Q} \tag{3.13}$$

In equation (3.13) θ has been defined as

$$\theta = T_a(x,t) - T_0 \tag{3.14}$$

where T_a is the absolute temperature field of the beam and T_0 the ambient temperature.

The following assumptions have been taken into account when deriving the above equation:

- Assumption 1: due to the small area of the device it can be considered that there is no heat transfer due to convection.
- Assumption 2: heat losses by radiation are negligible, inasmuch that the structure is going to have small temperatures above ambient.
- Assumption 3: there is no energy input or output due to mechanical work. The thermoelastic damping can be neglected since its effect is masked by the external heat source.
- Assumption 4: the structural material is homogeneous and isotropic. The material properties are uniform in all directions within the material.
- Assumption 5: the material properties are a function of neither pressure nor temperature.

[1] For the sake of simplicity, the text refers to $\theta(x,t)$ as temperature field instead of relative temperature field.

- Assumption 6: the beam is heated up by an external heat source.
- Assumption 7: the external source will only cause an horizontal thermal gradient throughout the beam length (x-direction). The clamped ends are assumed to be in perfect thermal contact with the rigid supports (i.e., isothermal). Since the beam is going to be narrow, thin and made from one single material with a high thermal conductivity, the thermal gradient along the y-direction and the z-direction is considered to be non-existent.

From the seventh assumption, the Dirichlet boundary conditions for (3.13) are

$$\theta = 0 \ \text{ at } \ x = 0 \ \text{ and } \ L \tag{3.15}$$

Fourier's law of heat conduction states that the energy flux within the beam is directly proportional to its temperature gradient

$$\phi = -k\nabla\theta \tag{3.16}$$

being k the thermal conductivity of the material.

Introducing the heat conduction equation into (3.13) yields

$$\dot{\theta} = \chi\theta^{II} + \frac{\mathcal{Q}}{C} \tag{3.17}$$

where dots and roman numerals denote respectively the partial differentiation with respect to t and to x, $C = c_p\rho$ and $\chi = \frac{k}{c_p\rho}$ is the thermal diffusivity.

The following spatial, temporal and thermal variables are defined when adimensionalizing the longitudinal coordinate by the beam length, time by an elastic frequency scale $\left(\omega_s^2 = \frac{EI}{\rho AL^4}\right)$, the temperature field by the ambient value and the vertical position of the FSS by the wavelength at which it is designed

$$\hat{x} = \frac{x}{L}\,, \ \ \hat{t} = t\omega_s\,, \ \ \hat{\theta} = \frac{\theta}{T_0}\,, \ \ \hat{Z} = \frac{Z}{\lambda_w} \tag{3.18}$$

Rescaling (3.17) using these new variables yields the following nondimensional equation

$$\dot{\hat{\theta}} = \mathcal{C}_1 \hat{\theta}^{II} + \hat{Q} \tag{3.19}$$

where dots and roman numerals denote respectively the partial differentiation with respect to $\hat{t}$ and to $\hat{x}$ and the following dimensionless parameters have been defined

$$\mathcal{C}_1 = \frac{\chi}{L^2 \omega_s} \ , \ \ \hat{Q} = \frac{Q}{T_0 C \omega_s} \tag{3.20}$$

Notice that in (3.20) Q is defined by (3.12).

The boundary conditions of (3.19) when taking into account (3.18) are

$$\hat{\theta} = 0 \ \text{ at } \ \hat{x} = 0 \ \text{ and } \ 1 \tag{3.21}$$

3.2.1 First linear temperature field mode profile

When the beam is not subjected to any external heat source, the heat transfer equation (3.19) becomes

$$\dot{\hat{\theta}} - \mathcal{C}_1 \hat{\theta}^{II} = 0 \tag{3.22}$$

Using the separation of variables technique, the temperature field of the beam can be split into a position and a time dependent components as

$$\hat{\theta}(\hat{x}, \hat{t}) = \psi(\hat{x}) G(\hat{t}) \tag{3.23}$$

[2]The solution of G for the first temperature field mode is given by

$$G_1(\hat{t}) = A_1 e^{-\hat{t}/\tau_1} \tag{3.24}$$

[2]In section A.1 of appendix A the reader can find a description of the involved mathematics.

where A_1 is determined by the initial temporal conditions and the first dimensionless time constant τ_1 has been defined as

$$\tau_1 = \frac{1}{\mathcal{C}_1 \pi^2} \tag{3.25}$$

[3]The solution for the first temperature field mode profile $\psi_1(\hat{x})$ is given by

$$\psi_1 = B_1 \sin(\kappa_1 \hat{x}) \tag{3.26}$$

where B_1 remains as an undetermined value.

The first temperature field mode profile is plotted in figure 3.3. In order to give a value to B_1, the eigenfunction ψ_1 has been normalized so that

$$\int_0^1 \psi_1^2 \, d\hat{x} = 1 \tag{3.27}$$

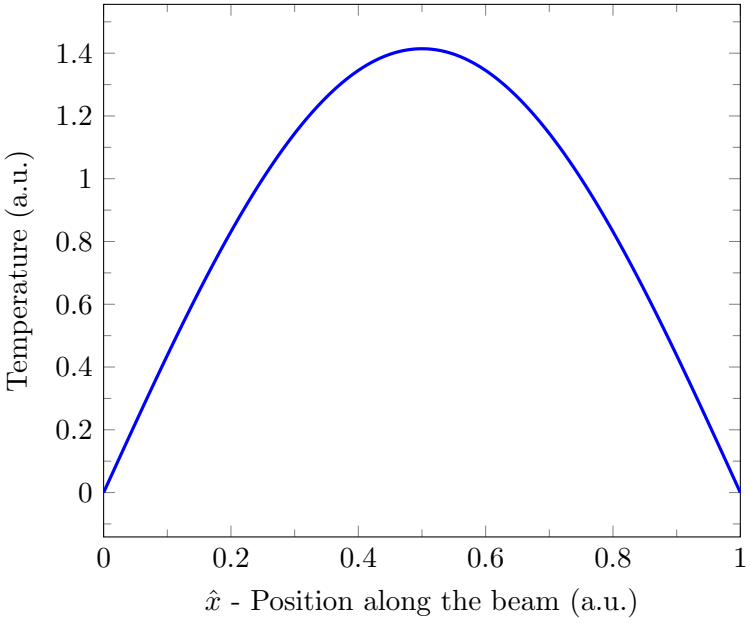

FIGURE 3.3: First temperature field mode profile of the modeled clamped-clamped beam.

[3]In section A.1 of appendix A the reader can find a description of the involved mathematics.

3.2.2 Lumped thermal model

The temperature field $\hat{\theta}$ of the modeled clamped-clamped beam when taking into account the external heat source $\hat{Q}$ is governed by equation (3.19); that is,

$$\dot{\hat{\theta}} = \mathcal{C}_1 \hat{\theta}^{II} + \hat{Q} \tag{3.28}$$

In order to transform the above partial differential equation to an ordinary one the Galerkin space discreatization method is used. Using this procedure, the temperature field of the beam can be expressed as

$$\hat{\theta}(\hat{x}, \hat{t}) = \sum_{m=1}^{M} \hat{g}_m(\hat{t}) \psi_m(\hat{x}) \tag{3.29}$$

Assuming that the only physically real temperature field mode profile is the first one (i.e., single-mode space discreatization: $M = 1$), equation (3.29) is reduced to

$$\hat{\theta} \approx \hat{g}_1(\hat{t}) \psi_1 = \hat{T}_l(\hat{t}) \psi_1 \tag{3.30}$$

[4]The lumped dimensionless temperature $\hat{T}_l$ is governed by the following ordinary differential equation

$$\dot{\hat{T}}_l + \mathcal{C}_1 \hat{T}_l \kappa_1^2 = \hat{Q} J_1 \tag{3.31}$$

where the constant J_1 has been defined as

$$J_1 = \int_0^1 \psi_1 \, d\hat{x} \tag{3.32}$$

Equation (3.31) can be rewritten as

$$\dot{\hat{T}}_l + c_1 \hat{T}_l = c_2 \big[\hat{Z}(\hat{t})\big] \tag{3.33}$$

where

$$c_1 = \mathcal{C}_1 \kappa_1^2 \,, \quad c_2 = \hat{Q} J_1 \tag{3.34}$$

[4]In section A.2 of appendix A the reader can find a description of the involved mathematics.

Notice that while c_1 is a constant parameter, c_2 depends on the dimensionless vertical position $\hat{Z}$ of the FSS within the gap. The latter can be written as a sum of a static or equilibrium position $\hat{Z}_e$ and a dynamic or time-varying position $\hat{Z}_d(\hat{t})$,

$$\hat{Z} = \hat{Z}_e + \hat{Z}_d \tag{3.35}$$

3.2.3 The static and dynamic temperatures of the lumped thermal model

The lumped temperature $\hat{T}_l$ can be written as a sum of a static or equilibrium temperature $\hat{T}_{l.e}$ and a dynamic or time-varying temperature $\hat{T}_{l.d}(\hat{t})$,

$$\hat{T}_l = \hat{T}_{l.e} + \hat{T}_{l.d} \tag{3.36}$$

The lumped equilibrium temperature can be computed setting to zero all the time dependent variables and time derivatives of (3.33),

$$\hat{T}_{l.e} = \frac{c_2\big(\hat{Z} = \hat{Z}_e\big)}{c_1} \tag{3.37}$$

where $\hat{Z}_e$ is the vertical equilibrium position of the FSS within the gap.

Hence, the lumped dynamic temperature can be computed as

$$\hat{T}_{l.d} = \hat{T}_l - \hat{T}_{l.e} \tag{3.38}$$

3.3 Mechanical part: the Euler-Bernoulli equation

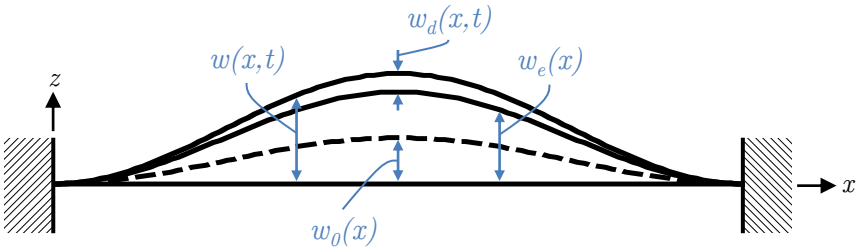

FIGURE 3.4: Schematic of a clamped-clamped beam. All the deformations defined in this section are depicted.

The transverse vibrations $w(x,t)$ of a beam subjected to an axial load S are governed by the large deformation Euler-Bernoulli equation (3.39)[75]. Where A is the cross-sectional area, I the moment of inertia, D the distributed damping[5] and E the modulus of elasticity of the beam material. Figure 3.4 shows a schematic of the beam.

$$\rho A\frac{\partial^2 w}{\partial t^2} + D\frac{\partial w}{\partial t} + EI\frac{\partial^4 w}{\partial x^4} + S\frac{\partial^2 w}{\partial x^2} = 0 \tag{3.39}$$

When both ends of this beam are clamped, the deflection and slope at these points must be zero. Equation (3.40) groups these Dirichlet boundary conditions, where L is the length of the beam.

$$w = 0 \text{ and } \frac{\partial w}{\partial x} = 0 \text{ at } x = 0 \text{ and } L \tag{3.40}$$

The following assumptions have been taken into account when deriving (3.39):

- Assumption 1: the beam is subjected to pure bending. The cross-section of the beam is plane and normal to the longitudinal axis and remains plane and normal to it after deformation (the cross-section is constant along the length of the beam). Meaning that the beam does not suffer from in-plane deformations, transverse shear strains nor transverse normal strains (the

[5]The distributed damping D can be related with the quality factor Q_f of the beam as shown in section A.8 of appendix A.

material from which the beam is made is incompressible, it is linearly elastic and will not deform plastically).

- Assumption 2: the beam is symmetric with respect to the plane of bending.
- Assumption 3: the structural material is homogeneous and isotropic. The material properties are uniform in all directions within the material.
- Assumption 4: the material properties are a function of neither pressure nor temperature.

For a rectangular cross sectional beam with centroid at the origin,

$$A = BH \tag{3.41}$$

$$I = \int_A z^2 \, dA = \frac{BH^3}{12} \tag{3.42}$$

where B is the width of the beam and H its thickness, as illustrated in figure 3.5

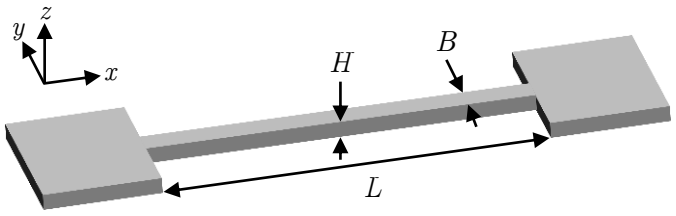

FIGURE 3.5: Diagram of a clamped-clamped beam with a rectangular cross section.

Notice that the geometric discontinuities introduced by the EM resonant elements of the actual fishbone structure (see figure 1.1) are neglected in the latter and in the following modeling. Taking into account such characteristic would require a much more complicated modeling.

3.3.1 Imperfections on a beam

In the case of the studied clamped-clamped beams the most important sources of imperfections are:

- Source 1: geometric defects introduced during the fabrication process can cause minor changes in a beam cross-section along its length (e.g., produced by tiny cracks or bumps in the beam).

- Source 2: the structural layer will have its top and bottom surfaces surrounded by air (or vacuum if it is placed in a vacuum chamber), except the bottom surface on its anchors supports which are bonded to the underlying oxide layer. Assuming that the clamped-clamped beam has a residual compressive stress and noticing that the anchor regions have its top surface free, shear stresses will develop along the bottom surface of these regions in order to counteract the residual stress. Since these shear stresses act below the beam center line, the beam will be statically arched up away from the substrate [61]. This same phenomena happens when the axial compressive force is caused by the thermal stress produced when there is an increase in the overall beam's temperature.

- Source 3: the geometric asymmetry described before is also the cause of another effect produced when the device is heated above its ambient temperature. The metal device layer has a thermal conductivity one or two orders of magnitude higher than the silicon dioxide sacrificial layer. Consequently, heat propagates faster in the device metal layer than in the oxide one. This phenomena causes a large through the thickness temperature gradient in the anchor supports, where heat flows from the metal to the oxide. Because of the difference between the thermal expansion coefficients of the metal and the oxide, a bending moment that tends to statically rotate the beam up away from the substrate is going to be created [61].

All these imperfections can be grouped into a net imperfection which accounts for their physical effect on the beam. Therefore, a beam with a net imperfection can be renamed as an imperfect beam. When an imperfect beam is subjected to a compressive axial stress it statically arches downwards or upwards, even if the corresponding force is lower than the first critical buckling load. Experimentally this means that if a residual compressive stress develops along the structural layer

during the fabrication process (e.g., due to thermal processes) the beam will suffer a static deflection as soon as it is released. To account for this effect the net imperfection can be modeled as a geometric imperfection of the beam in its natural unstressed state [76]. Notice that this predeformation is just a way to model the effect of the net imperfection, a physical unstressed imperfect beam is straight.

It can be assumed that the predeformation $w_0(x)$ has the same shape as the first symmetric buckling mode[6] of the beam,

$$w_0 = A_0 \left[1 - \cos\left(\frac{2\pi x}{L}\right)\right] \tag{3.43}$$

where A_0 is the clamped-clamped imperfect beam's central point predeformation. Following [76], its value can be expressed as proportional to the beam's length L with the dimensionless parameter δ_0 as the proportionality factor:

$$A_0 = \frac{1}{2}\delta_0 L \tag{3.44}$$

Figure 3.6 shows the normalized predeformation shape of a clamped-clamped beam.

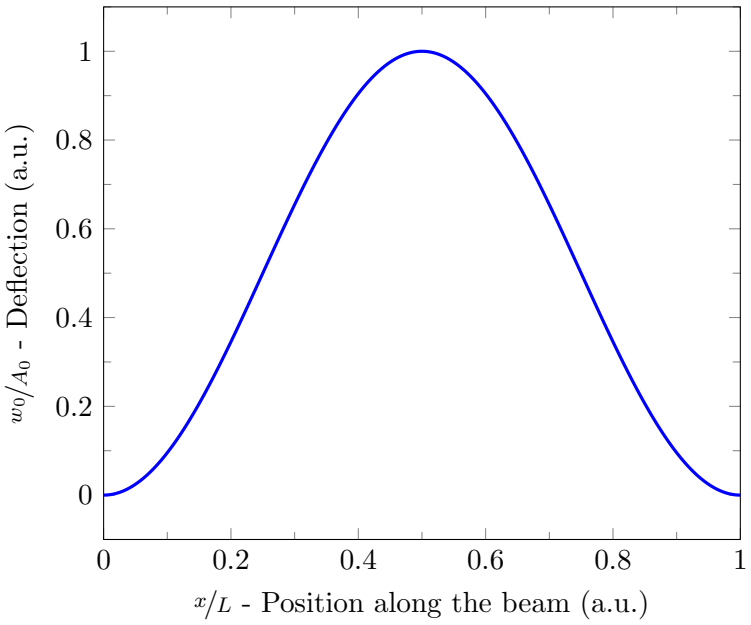

FIGURE 3.6: Normalized predeformation shape of a clamped-clamped beam.

[6] In section A.3 of appendix A the reader can find a description of the mathematics involved when deriving (3.43).

3.3.2 The Euler-Bernoulli equation of a clamped-clamped imperfect beam

The transverse vibrations of a clamped-clamped imperfect beam are governed by the Euler-Bernoulli equation (3.45) with the boundary conditions described by (3.46) [76].

$$\rho A\frac{\partial^2 w}{\partial t^2} + D\frac{\partial w}{\partial t} + EI\left(\frac{\partial^4 w}{\partial x^4} - \frac{\partial^4 w_0}{\partial x^4}\right) + S\frac{\partial^2 w}{\partial x^2} = 0 \tag{3.45}$$

$$w = 0 \;\text{ and }\; \frac{\partial w}{\partial x} = 0 \;\text{ at }\; x = 0 \;\text{ and }\; L \tag{3.46}$$

For the modeled clamped-clamped beam the axial load S groups three terms[7],

$$S(t) = \sigma_r A - \frac{EA}{2L}\int_0^L \left[\left(\frac{\partial w}{\partial x}\right)^2 - \left(\frac{\partial w_0}{\partial x}\right)^2\right] dx + F_\theta(t) \tag{3.47}$$

The first term linearly models the load produced by an axial residual or post-fabrication stress σ_r. The second one accounts, to first order, for the midplane stretching effects induced by bending. Finally, F_θ represents the restraining compressive axial load that cancels out the tensile thermal load caused by a beam temperature field in the form of $\theta(x,t) > 0$[8] (no temperature gradient in the y and z directions). Considering a beam without a predeformation ($w_0 = 0$) and as long as this thermal load is smaller than the buckling load, the beam is not going to suffer any deflection due to its action. That is because the thermal load is canceled out by the restraining load, which is equal in amplitude an opposite in direction to the thermal one. Being the temperature field higher than the ambient temperature, the thermal force is tensile. Hence the restraining force is compressive. Using linear thermoelasticity, the restraining temperature dependent axial force is given by

$$F_\theta = A\alpha_{th}E\frac{1}{L}\int_0^L \theta\, dx \tag{3.48}$$

[7] The sign convention used is that positive loads are compressive and negative loads are tensile.

[8] See the seventh assumption made in section 3.2 to understand the x and t only dependencies of the temperature field.

where α_{th} is the coefficient of thermal expansion and θ the temperature field of the beam governed by equation (3.17).

Taking into account that the dimensionless temperature field can be expressed by (3.30), equation (3.48) can be rewritten as follows by carefully taking into consideration the admiensionalized variables of (3.18)

$$F_\theta = A\alpha_{th}EJ_1T_0\hat{T}_l \tag{3.49}$$

where J_1 is computed as equation (3.32) states.

Incorporating (3.49) into (3.47), the Euler-Bernoulli equation (3.45) is rewritten as

$$\begin{aligned}\rho A\ddot{w} + D\dot{w} + EI\left(w^{IV} - w_0^{IV}\right) + \Big\{\sigma_r A + A\alpha_{th}EJ_1T_0\hat{T}_l \\ -\frac{EA}{2L}\int_0^L \left[\left(w^I\right)^2 - \left(w_0^I\right)^2\right]dx\Big\}w^{II} = 0\end{aligned} \tag{3.50}$$

where dots and roman numerals denote respectively the partial differentiation with respect to t and to x.

The transverse vibrations w can be written as a sum of a static or equilibrium deflection $w_e(x)$ and a dynamic or time-varying deflection $w_d(x,t)$ (as depicted in figure 3.4),

$$w = w_e + w_d \tag{3.51}$$

The nonlinear equilibrium deflection of the beam w_e can be computed setting to zero all the time dependent variables and time derivatives of (3.50) when introducing (3.51); that is,

$$EIw_e^{IV} + \left\{\sigma_r A + A\alpha_{th}EJ_1T_0\hat{T}_{l.e} - \frac{EA}{2L}\int_0^L \left[\left(w_e^I\right)^2 - \left(w_0^I\right)^2\right]dx\right\}w_e^{II} = EIw_0^{IV} \tag{3.52}$$

where w_e satisfies the following boundary conditions

$$w_e = 0 \;\text{ and }\; w_e^I = 0 \;\text{ at }\; x = 0 \;\text{ and }\; L \tag{3.53}$$

Taking into account (3.52) when substituting (3.51) into (3.50) yields a nonlinear partial differential equation governing the dynamic deflection of the beam; that is,

$$\begin{aligned} \rho A\ddot{w}_d + D\dot{w}_d + EIw_d^{IV} + \Big\{\sigma_r A + A\alpha_{th}EJ_1T_0\hat{T}_l \\ -\frac{EA}{2L}\int_0^L \left[\left(w_e^I\right)^2 - \left(w_0^I\right)^2\right] dx\Big\} w_d^{II} - \frac{EA}{2L}w_d^{II}\int_0^L \left[\left(w_d^I\right)^2 + 2w_e^I w_d^I\right] dx \\ -\frac{EA}{2L}w_e^{II}\int_0^L \left[\left(w_d^I\right)^2 + 2w_e^I w_d^I\right] dx = -A\alpha_{th}EJ_1T_0\hat{T}_{l.d}w_e^{II} \end{aligned} \tag{3.54}$$

where w_d satisfies the following boundary conditions

$$w_d = 0 \;\text{ and }\; w_d^I = 0 \;\text{ at }\; x = 0 \;\text{ and }\; L \tag{3.55}$$

The following spatial and temporal variables are defined when adimensionalizing the longitudinal coordinate by the beam length, time by an elastic frequency scale $\left(\omega_s^2 = \frac{EI}{\rho AL^4}\right)$ and the beam deflections by the wavelength at which the FSS has been designed

$$\hat{x} = \frac{x}{L}\,,\;\; \hat{t} = t\omega_s\,,\;\; \hat{w}_0 = \frac{w_0}{\lambda_w}\,,\;\; \hat{w}_e = \frac{w_e}{\lambda_w}\,,\;\; \hat{w}_d = \frac{w_d}{\lambda_w} \tag{3.56}$$

Rescaling (3.52) and (3.54) using these new variables yields the following nondimensional equations

$$\hat{w}_e^{IV} + \left\{\mathcal{C}_3 + \mathcal{C}_4\hat{T}_{l.e} - \mathcal{C}_5\int_0^1 \left[\left(\hat{w}_e^I\right)^2 - \left(\hat{w}_0^I\right)^2\right] d\hat{x}\right\}\hat{w}_e^{II} = \hat{w}_0^{IV} \tag{3.57}$$

$$\begin{aligned} \ddot{\hat{w}}_d + \mathcal{C}_2\dot{\hat{w}}_d + \hat{w}_d^{IV} + \left\{\mathcal{C}_3 + \mathcal{C}_4\hat{T}_l - \mathcal{C}_5\int_0^1 \left[\left(\hat{w}_e^I\right)^2 - \left(\hat{w}_0^I\right)^2\right] d\hat{x}\right\}\hat{w}_d^{II} \\ -\mathcal{C}_5\hat{w}_d^{II}\int_0^1 \left[\left(\hat{w}_d^I\right)^2 + 2\hat{w}_e^I\hat{w}_d^I\right] d\hat{x} - \mathcal{C}_5\hat{w}_e^{II}\int_0^1 \left[\left(\hat{w}_d^I\right)^2 + 2\hat{w}_e^I\hat{w}_d^I\right] d\hat{x} = -\mathcal{C}_4\hat{w}_e^{II}\hat{T}_{l.d} \end{aligned} \tag{3.58}$$

where dots and roman numerals denote respectively the partial differentiation with respect to $\hat{t}$ and to $\hat{x}$ and the following dimensionless parameters have been defined

$$^{9}\mathcal{C}_2 = \frac{D}{\rho A\omega_s}\,,\;\; \mathcal{C}_3 = \frac{\sigma_r}{\rho L^2\omega_s^2}\,,\;\; \mathcal{C}_4 = \frac{\alpha_{th}EJ_1T_0}{\rho L^2\omega_s^2}\,,\;\; \mathcal{C}_5 = \frac{E\lambda_w^2}{2\rho L^4\omega_s^2} \tag{3.59}$$

The boundary conditions of (3.57) and (3.58) when taking into account (3.51) and (3.56) are, respectively,

$$\hat{w}_e = 0 \;\text{ and }\; \hat{w}_e^I = 0 \;\text{ at }\; \hat{x} = 0 \;\text{ and }\; 1 \tag{3.60}$$

$$\hat{w}_d = 0 \;\text{ and }\; \hat{w}_d^I = 0 \;\text{ at }\; \hat{x} = 0 \;\text{ and }\; 1 \tag{3.61}$$

Notice that the nondimensional form of the predeformation w_0 (see (3.43)) after the nondimensionalization process becomes

$$\hat{w}_0 = \frac{1}{2}\delta_0 \frac{L}{\lambda_w}\left[1 - \cos(2\pi\hat{x})\right] \tag{3.62}$$

3.3.3 Analysis of the nonlinear equilibrium and the buckling load

The equilibrium deflection $\hat{w}_e$ of the modeled clamped-clamped imperfect beam with respect to the inertial frame of reference (see figure 3.4) is governed by the static nondimensional Euler-Bernoulli equation (3.57); that is,

$$\hat{w}_e^{IV} + \left\{ P_0 - \mathcal{C}_5 \int_0^1 \left[\left(\hat{w}_e^I\right)^2 - \left(\hat{w}_0^I\right)^2 \right] d\hat{x} \right\} \hat{w}_e^{II} = \hat{w}_0^{IV} \tag{3.63}$$

where $P_0 = \mathcal{C}_3 + \mathcal{C}_4 \hat{T}_{l.e}$.

Since the integral of (3.63) is constant for a given $\hat{w}_0$ and $\hat{w}_e$, (3.63) can be rewritten as

$$\hat{w}_e^{IV} + \lambda^2 \hat{w}_e^{II} = \hat{w}_0^{IV} \tag{3.64}$$

where $\lambda^2 = P_0 - \mathcal{C}_5 \int_0^1 \left[\left(\hat{w}_e^I\right)^2 - \left(\hat{w}_0^I\right)^2 \right] d\hat{x}$.

[9] The dimensionless distributed damping $\mathcal{C}_2$ can be related with the quality factor Q_f of the beam as shown in section A.8 of appendix A.

[10]Considering that the predeformation w_0 can be described by (3.62), the solution of (3.64) is given by

$$\hat{w}_e = \frac{2\pi^2 \delta_0 L}{\lambda_w \left(4\pi^2 - \lambda^2\right)} \left[1 - cos(2\pi\hat{x})\right] \tag{3.65}$$

Observing (3.65) it can be seen that $\hat{w}_e$ has the same form as the predeformation $\hat{w}_0$,

$$\hat{w}_e = \frac{1}{2} W_e \left[1 - cos(2\pi\hat{x})\right] \tag{3.66}$$

where the maximum static deflection is defined as $W_e = \frac{4\pi^2 \delta_0 L}{\lambda_w (4\pi^2 - \lambda^2)}$. Notice that this maximum is given at the beam's central point (i.e., at $\hat{x} = 1/2$).

The following equation is found when $\hat{w}_e$ is replaced by (3.66) in equation (3.63),

$$W_e^3 - \left(\frac{2P_0}{\pi^2 \mathcal{C}_5} - \frac{8}{\mathcal{C}_5} + \delta_0^2 \frac{L^2}{\lambda_w^2} \right) W_e - \delta_0 \frac{8L}{\mathcal{C}_5 \lambda_w} = 0 \tag{3.67}$$

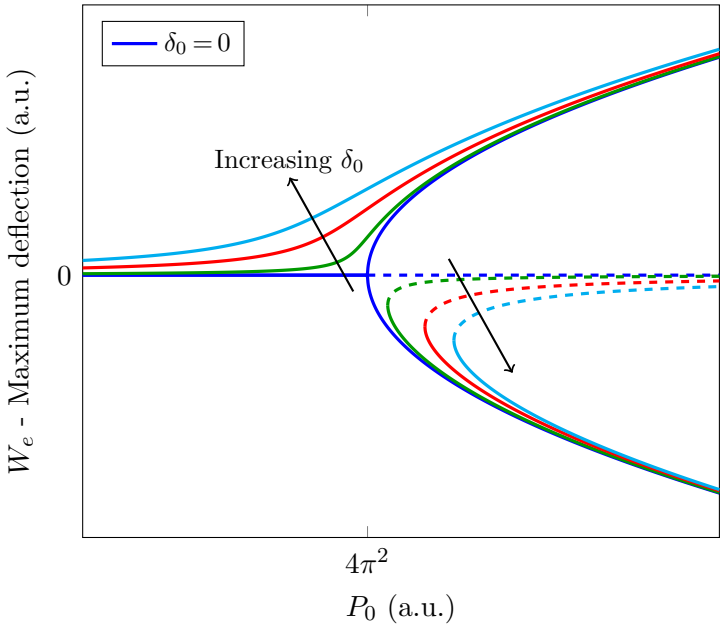

FIGURE 3.7: Bifurcation diagram: evolution of the maximum equilibrium deflection W_e with the P_0 load for various δ_0 values. Solutions: stable (solid lines) and unstable (dashed lines).

[10]In section A.4 of appendix A the reader can find a description of the involved mathematics.

Figure 3.7 shows the qualitative evolution of W_e as a function of the applied load P_0 for various δ_0 values. For a constant residual stress (i.e., $\mathcal{C}_3 = \text{constant}$) and since the axial load P_0 directly depends on the lumped equilibrium temperature $\hat{T}_{l.e}$, figure 3.7 graphically illustrates that the beam can suffer modification of its deflection state due and only to the effect of a thermo-mechanical coupling mechanism.

The static buckling of the modeled beam occurs when two solutions of (3.67) coalesce. This condition is given when the discriminant of (3.67) is zero,

$$\Delta = \left(\frac{8}{\mathcal{C}_5} - \delta_0^2 \frac{L^2}{\lambda_w^2} - \frac{2P_b}{\mathcal{C}_5 \pi^2}\right)^3 + 432 \frac{\delta_0^2 L^2}{\mathcal{C}_5^2 \lambda_w^2} = 0 \tag{3.68}$$

where P_b is the value of P_0 when the beam buckles, the buckling load.

Solving equation (3.68) for P_b gives

$$P_b = \frac{\mathcal{C}_5 \pi^2}{2} \left[\frac{8}{\mathcal{C}_5} - \delta_0^2 \frac{L^2}{\lambda_w^2} + \frac{432^{\frac{1}{3}} \left(\delta_0 \frac{L}{\lambda_w}\right)^{\frac{2}{3}}}{\mathcal{C}_5^{\frac{2}{3}}}\right] \tag{3.69}$$

When the beam is perfect, meaning that $\delta_0 = 0$, the buckling load becomes: $P_b = 4\pi^2$. For this case, and as shown in figure 3.7, the variation of the maximum deflection W_e as a function of P_0 is symmetric through a pitchfork bifurcation originated when $P_0 = P_b$. Otherwise, when $\delta_0 \neq 0$, this variation is not symmetric and the beam gets buckled through a saddle-node bifurcation[11].

The parameter P_0 of (3.63) depends on the lumped equilibrium temperature $\hat{T}_{l.e}$, which value can be determined by solving equation (3.37). In order to do such computation the vertical equilibrium position of the FSS within the gap $\hat{Z}_e$ is considered to be equal to the beam's central point equilibrium deflection,

$$\hat{Z}_e = \hat{w}_e(\hat{x} = 1/2) = W_e \tag{3.70}$$

[11] In section A.5 of appendix A the reader can find more information on these equilibrium ranges.

Notice that the latter consideration neglects the actual nonflat deflection of the beam (see the analysis done in the paragraph following equation (3.1) in page 34).

Taking into account (3.70), the lumped equilibrium temperature is given by

$$\hat{T}_{l.e} = \frac{c_2\big(\hat{Z}_e = W_e\big)}{c_1} \tag{3.71}$$

Using (3.71) when replacing the parameter P_0 by its definition in equation (3.67) develops the latter into the following transcendental equation

$$W_e^3 - \left[\frac{2}{\pi^2 \mathcal{C}_5}\left(\mathcal{C}_3 + \mathcal{C}_4 \frac{c_2\big(\hat{Z}_e = W_e\big)}{c_1}\right) - \frac{8}{\mathcal{C}_5} + \delta_0^2 \frac{L^2}{\lambda_w^2}\right] W_e - \delta_0 \frac{8L}{\mathcal{C}_5 \lambda_w} = 0 \tag{3.72}$$

Notice that the function c_2 has the Fourier series function $\hat{\mathcal{F}}$ embedded in it.

3.3.4 First natural frequency and linear undamped mode shape around the nonlinear equilibrium

In order to obtain the differential equation governing the linear vibrations around the nonlinear equilibrium $\hat{w}_e$, the nonlinear, damping and nonhomogeneous terms plus the dynamic thermal load of equation (3.58) must be removed; yielding,

$$\ddot{\hat{w}}_{d.lu} + \hat{w}^{IV}_{d.lu} + K\hat{w}^{II}_{d.lu} - 2\mathcal{C}_5 \hat{w}^{II}_e \int_0^1 \hat{w}^I_e \hat{w}^I_{d.lu}\, d\hat{x} = 0 \tag{3.73}$$

where $K = P_0 - \mathcal{C}_5 \displaystyle\int_0^1 \left[\left(\hat{w}^I_e\right)^2 - \left(\hat{w}^I_0\right)^2\right] d\hat{x}$ and $\hat{w}_{d.lu}$ satisfies the following boundary conditions

$$\hat{w}_{d.lu} = 0 \;\text{ and }\; \hat{w}^I_{d.lu} = 0 \;\text{ at }\; \hat{x} = 0 \;\text{ and }\; 1 \tag{3.74}$$

[12]Considering that the static predeformation $\hat{w}_0$ can be described by (3.62) and the equilibrium $\hat{w}_e$ by (3.66), the first mode shape of (3.73) is given by

$$\varphi_1(\hat{x}) = A_1 \sin(r_5\hat{x}) + B_1 \cos(r_5\hat{x}) + C_1 \sinh(r_1\hat{x}) + D_1 \cosh(r_1\hat{x}) + E_1 \cos(2\pi\hat{x}) \tag{3.75}$$

The eigenvalue problem yielding ω_1 and the coefficients A_1, B_1, C_1, D_1 and E_1 is described by the following linear system of equations

$$\begin{aligned}
B_1 + D_1 + E_1 &= 0 \\
A_1 r_5 + C_1 r_1 &= 0 \\
A_1 \sin(r_5) + B_1 \cos(r_5) + C_1 \sinh(r_1) + D_1 \cosh(r_1) + E_1 &= 0 \\
A_1 r_5 \cos(r_5) - B_1 r_5 \sin(r_5) + C_1 r_1 \cosh(r_1) + D_1 r_1 \sinh(r_1) &= 0 \\
-A_1 r_5 \frac{\cos(r_5) - 1}{4\pi^2 - r_5^2} + B_1 r_5 \frac{\sin(r_5)}{4\pi^2 - r_5^2} - C_1 r_1 \frac{\cosh(r_1) - 1}{4\pi^2 + r_1^2} & \\
-D_1 r_1 \frac{\sinh(r_1)}{4\pi^2 + r_1^2} - E_1 \left(\frac{1}{2} + \frac{16\pi^4 \frac{\delta_0 L}{W_e \lambda_w} - \omega_1^2}{8\pi^4 \mathcal{C}_5 W_e^2} \right) &= 0
\end{aligned} \tag{3.76}$$

where $r_1 = \sqrt{-\frac{K}{2} + \sqrt{\omega_1^2 + \frac{K^2}{4}}}$, $r_5 = \sqrt{\frac{K}{2} + \sqrt{\omega_1^2 + \frac{K^2}{4}}}$ and ω_1 is the first natural frequency of the beam.

The value of ω_1 is the first solution of the transcendental characteristic equation resulting from equaling to zero the determinant of the coefficient matrix of the linear system (3.76).

One more equation is needed to particularly obtain the values of A_1, B_1, C_1, D_1 and E_1. This sixth equation is obtained by imposing the following normalization to φ_1,

$$\int_0^1 \varphi_1^2 \, d\hat{x} = 1 \tag{3.77}$$

Figure 3.8 shows an example of the first linear undamped mode shape for a clamped-clamped imperfect beam

[12]In section A.6 of appendix A the reader can find a description of the involved mathematics.

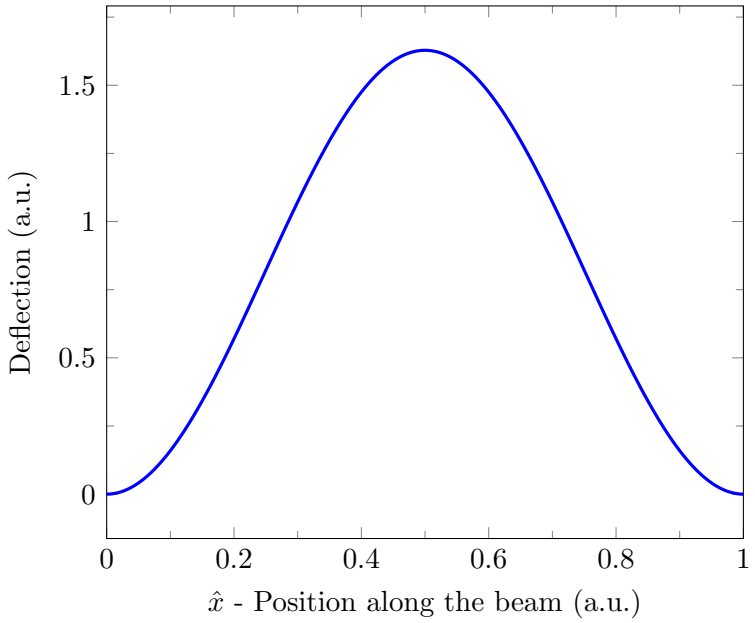

FIGURE 3.8: First linear undamped mode shape φ_1 of a clamped-clamped imperfect beam.

3.3.5 Dynamic lumped mechanical model

The dynamic deflection $\hat{w}_d$ of the modeled clamped-clamped imperfect beam is governed by equation (3.58); that is,

$$\ddot{\hat{w}}_d + \mathcal{C}_2\dot{\hat{w}}_d + \hat{w}_d^{IV} + \left\{\mathcal{C}_3 + \mathcal{C}_4\hat{T}_l - \mathcal{C}_5\int_0^1 \left[\left(\hat{w}_e^I\right)^2 - \left(\hat{w}_0^I\right)^2\right] d\hat{x}\right\}\hat{w}_d^{II}$$
$$-\mathcal{C}_5\hat{w}_d^{II}\int_0^1 \left[\left(\hat{w}_d^I\right)^2 + 2\hat{w}_e^I\hat{w}_d^I\right] d\hat{x} - \mathcal{C}_5\hat{w}_e^{II}\int_0^1 \left[\left(\hat{w}_d^I\right)^2 + 2\hat{w}_e^I\hat{w}_d^I\right] d\hat{x} = -\mathcal{C}_4\hat{w}_e^{II}\hat{T}_{l.d} \tag{3.78}$$

In order to transform the above partial differential equation to an ordinary one the Galerkin space discreatization method is used. Using this procedure, the mechanical vibrations of the beam can be expressed as

$$\hat{w}_d(\hat{x},\hat{t}) = \sum_{n=1}^{N} \hat{q}_n(\hat{t})\varphi_n(\hat{x}) \tag{3.79}$$

Assuming that the first vibration mode shape is the dominant one (i.e., single-mode discreatization: $N=1$), equation (3.79) is reduced to

$$\hat{w}_d \approx \hat{q}_1(\hat{t})\varphi_1 = \hat{W}_{l.d}(\hat{t})\varphi_1 \tag{3.80}$$

[13]The lumped dimensionless mechanical vibrations $\hat{W}_{l.d}$ around the nonlinear equilibrium $\hat{w}_e$ are governed by the following ordinary differential equation

$$\begin{aligned}\ddot{\hat{W}}_{l.d} + \mathcal{C}_2\dot{\hat{W}}_{l.d} + \left(I_1 + \mathcal{C}_3 I_2 - \mathcal{C}_5 I_2 K_1 - 2\mathcal{C}_5 I_3 K_3 + \mathcal{C}_4 I_2 \hat{T}_l\right)\hat{W}_{l.d} \\ -\mathcal{C}_5\left(2I_2K_3 + I_3K_2\right)\hat{W}_{l.d}^2 - \mathcal{C}_5 I_2 K_2 \hat{W}_{l.d}^3 = -\mathcal{C}_4 I_3 \hat{T}_{l.d}\end{aligned} \tag{3.81}$$

where

$$\begin{aligned}I_1 = \int_0^1 \varphi_1^{IV}\varphi_1\, d\hat{x}\ ,\ \ I_2 = \int_0^1 \varphi_1^{II}\varphi_1\, d\hat{x}\ ,\ \ I_3 = \int_0^1 \hat{w}_e^{II}\varphi_1\, d\hat{x}\ , \\ K_1 = \int_0^1 \left(\left(\hat{w}_e^I\right)^2 - \left(\hat{w}_0^I\right)^2\right) d\hat{x}\ ,\ \ K_2 = \int_0^1 \left(\varphi_1^I\right)^2 d\hat{x}\ ,\ \ K_3 = \int_0^1 \varphi_1^I \hat{w}_e^I\, d\hat{x}\end{aligned} \tag{3.82}$$

Following the nomenclature of (3.33), equation (3.81) can be rewritten as

$$\ddot{\hat{W}}_{l.d} + c_3\dot{\hat{W}}_{l.d} + \left(c_4 + c_5\hat{T}_l\right)\hat{W}_{l.d} - c_6\hat{W}_{l.d}^2 - c_7\hat{W}_{l.d}^3 = -c_8\hat{T}_{l.d} \tag{3.83}$$

where

$$\begin{aligned}c_3 = \mathcal{C}_2\ ,\ \ c_4 = I_1 + \mathcal{C}_3 I_2 - \mathcal{C}_5 I_2 K_1 - 2\mathcal{C}_5 I_3 K_3\ ,\ \ c_5 = \mathcal{C}_4 I_2\ , \\ c_6 = \mathcal{C}_5\left(2I_2K_3 + I_3K_2\right)\ ,\ \ c_7 = \mathcal{C}_5 I_2 K_2\ ,\ \ c_8 = \mathcal{C}_4 I_3\end{aligned} \tag{3.84}$$

3.4 The opto-thermo-mechanical model

The outputs of the opto-thermo-mechnical model developed throughout this chapter should be the deflection shape $\hat{w}$ and the temperature field θ of the modeled clamped-clamped imperfect beam. With the aim to analyze the temporal behavior of these functions they can be particularized at the central point along the beam's length (i.e., $\hat{x} = 1/2$).

[13]In section A.7 of appendix A the reader can find a description of the involved mathematics.

The deflection $\hat{w}(\hat{x}=1/2,\hat{t})$ (see (3.51)) is the sum of the equilbrium deflection $\hat{w}_e(\hat{x}=1/2)$ (see (3.66)) and the dynamic deflection $\hat{w}_d(\hat{x}=1/2,\hat{t})$. Since the dynamic part has been space discreatized (see (3.80)), the total deflection can be expressed as

$$\hat{w}(\hat{x}=1/2,\hat{t})=\hat{w}_e(\hat{x}=1/2)+\hat{w}_d(\hat{x}=1/2,\hat{t})\approx W_e+\hat{W}_{l.d}\varphi_1(\hat{x}=1/2) \tag{3.85}$$

The temperature field $\theta(\hat{x}=1/2,\hat{t})$ has also been space discreatized (see (3.30) and (3.36)). Therefore, it can be expressed as

$$\theta(\hat{x}=1/2,\hat{t})\approx\hat{T}_l\psi_1(\hat{x}=1/2)=\left(\hat{T}_{l.e}+\hat{T}_{l.d}\right)\psi_1(\hat{x}=1/2) \tag{3.86}$$

In order to solve for the variables in (3.85) and (3.86) equations (3.71), (3.33), (3.72) and (3.83) must be firstly addressed. These equations are listed below with the aim to summarize the complete opto-thermo-mechanical model,

$$\hat{T}_{l.e}=\frac{c_2\left(\hat{Z}=W_e\right)}{c_1} \tag{3.87}$$

$$\dot{\hat{T}}_l+c_1\hat{T}_l-c_2\left[\hat{Z}\right]=0 \tag{3.88}$$

$$W_e^3-\left[\frac{2}{\pi^2\mathcal{C}_5}\left(\mathcal{C}_3+\mathcal{C}_4\hat{T}_{l.e}\right)-\frac{8}{\mathcal{C}_5}+\delta_0^2\frac{L^2}{\lambda_w^2}\right]W_e-\delta_0\frac{8L}{\mathcal{C}_5\lambda_w}=0 \tag{3.89}$$

$$\ddot{\hat{W}}_{l.d}+c_3\dot{\hat{W}}_{l.d}+\left(c_4+c_5\hat{T}_l\right)\hat{W}_{l.d}-c_6\hat{W}_{l.d}^2-c_7\hat{W}_{l.d}^3+c_8\hat{T}_{l.d}=0 \tag{3.90}$$

where the relations between $\hat{Z}$ and $\hat{W}_{l.d}$, and $\hat{T}_l$, $\hat{T}_{l.e}$ and $\hat{T}_{l.d}$ are as follows

$$\hat{Z}=W_e+\hat{W}_{l.d}\varphi_1(\hat{x}=1/2) \tag{3.91}$$

$$\hat{T}_l=\hat{T}_{l.e}+\hat{T}_{l.d} \tag{3.92}$$

Noticing that equations (3.85) and (3.91) are the same, a lumped deflection $\hat{W}_l(\hat{t})$ can be defined by

$$\hat{W}_{l.d}=\frac{\hat{Z}-W_e}{\varphi_1(\hat{x}=1/2)}=\hat{W}_l(\hat{t})-W_{l.e} \tag{3.93}$$

where

$$\hat{W}_l = \frac{\hat{Z}}{\varphi_1(\hat{x} = 1/2)} \approx \frac{\hat{w}(\hat{x} = 1/2, \hat{t})}{\varphi_1(\hat{x} = 1/2)} \tag{3.94}$$

$$W_{l.e} = \frac{W_e}{\varphi_1(\hat{x} = 1/2)} \tag{3.95}$$

A system of nonlinear ordinary differential equations in the dimensionless time $\hat{t}$ for the lumped temperature $\hat{T}_l$ and the lumped deflection $\hat{W}_l$ can be defined by substituting $\hat{W}_{l.d}$ for (3.93) in (3.90) and grouping the outcome equation with (3.88) ; that is,

$$\begin{aligned} \dot{\hat{T}}_l + c_1\hat{T}_l - c_2\left[\hat{W}_l\,\varphi_1(\hat{x} = 1/2)\right] = 0 \\ \ddot{\hat{W}}_l + c_3\dot{\hat{W}}_l + \left(c_4 + c_5\hat{T}_l\right)\left(\hat{W}_l - W_{l.e}\right) - c_6\left(\hat{W}_l - W_{l.e}\right)^2 \\ -c_7\left(\hat{W}_l - W_{l.e}\right)^3 + c_8\left(\hat{T}_l - \hat{T}_{l.e}\right) = 0 \end{aligned} \tag{3.96}$$

3.4.1 About the analysis of the opto-thermo-mechanical model

The system (3.96) can be numerically solved for a given set of parameters c_1 - c_8, $W_{l.e}$ and $\hat{T}_{l.e}$, obtaining the temporal evolution of $\hat{T}_l$ and $\hat{W}_l$. However, if the irradiance value for which the system self-oscillates wants to be found, another type of analysis has to be performed.

To examine the structure of solutions to a system of ODEs a bifurcation analysis must be performed. A bifurcation is a qualitative change in the asymptotic structure of a dynamical system. Stationary and periodic bifurcations involve respectively changes in the number and/or stability of steady states and periodic solutions (or limit cycle) [77]. The transition to self-oscillation in M/NEMS devices illuminated by a CW laser has been shown to happen in a Hopf bifurcation [58, 59]. To simplify the explanation that follows the latter statement the following nonlinear differential autonomous system is considered

$$\frac{d\vec{X}}{dt} = \vec{F}(\vec{X}; \mu) \tag{3.97}$$

where $\vec{X}$ is a 3-dimensional vector, μ is a parameter, and $\vec{F} : \mathbb{R}^3 \to \mathbb{R}^3$ is a nonlinear function (which takes as input real 3-tuples and produces as output real 3-tuples).

The roots of $\vec{F}$ are steady states and their stability can be determined by linearizing the system about these points. Let $\vec{P} = (p_1, p_2, p_3)$ be a steady state of the planar system, then the linearization about $\vec{P}$ is

$$\frac{d\vec{X}}{dt} = \mathbf{J}\vec{X} = \begin{pmatrix} \frac{\partial F_1}{\partial x_1} & \frac{\partial F_1}{\partial x_2} & \frac{\partial F_1}{\partial x_3} \\ \frac{\partial F_2}{\partial x_1} & \frac{\partial F_2}{\partial x_2} & \frac{\partial F_2}{\partial x_3} \\ \frac{\partial F_3}{\partial x_1} & \frac{\partial F_3}{\partial x_2} & \frac{\partial F_3}{\partial x_3} \end{pmatrix} \vec{X} \tag{3.98}$$

where $\mathbf{J}$ is the 3×3 Jacobian matrix evaluated at $\vec{P}$.

A Hopf bifurcation is a periodic bifurcation in which a new limit cycle is born from a steady state. Suppose that two of the eigenvalues of the linearization about the steady state $\vec{p}$ are purely imaginary when $\mu = \mu_c$, but for some neighborhood to the left of μ_c and some neighborhood to the right of μ_c the eigenvalues are complex with non-zero real part (i.e., the eigenvalues have crossed the imaginary axis.). Then, there is a Hopf bifurcation at $\mu = \mu_c$. The two most important types of Hopf bifurcations are:

- Supercritical: the born limit cycle is stable, meaning that its amplitude will undergo a sustained oscillation about the steady state.
- Subcritical: the born limit cycle is unstable, meaning that its amplitude will eventually shrink to zero about the steady state.

To check for the stability of the born limit cycle the first Lyapunov coefficient must be computed [77]. If its value is negative the Hopf bifurcation is supercritical. On the contrary, if positive it is subcritical.

The system (3.96) can be written as a 3-dimensional system of first order ODEs as

$$\begin{aligned}
\dot{X}_1 &= -c_1 X_1 + c_2\left[X_2 \varphi_1(\hat{x} = 1/2)\right] \\
\dot{X}_2 &= X_3 \\
\dot{X}_3 &= -c_3 X_3 - \left(c_4 + c_5 X_1\right)\left(X_2 - W_{l.e}\right) + c_6\left(X_2 - W_{l.e}\right)^2 \\
&\quad + c_7\left(X_2 - W_{l.e}\right)^3 - c_8\left(X_1 - \hat{T}_{l.e}\right)
\end{aligned} \tag{3.99}$$

where the steady state of the system is: $(\hat{T}_{l.e}, W_{l.e}, 0)$.

The auto-oscillation of an OPACMEMS device would mean that for a given irradiance the above system has undergone a supercritical Hopf bifurcation that raised an stable vibration of the clamped-clamped beam. In order to find for what irradiance the system self-oscillates, the steady state lumped deflection and lumped temperature as a function of the irradiance is computed. Next, the system is linearlized about this equilibrium solution, and then the linear system is checked for a pair of pure imaginary eigenvalues.

3.5 Summary

In this chapter the complete opto-thermo-mechnical model was developed starting from the thermal and mechanical equations. The electromagnetic behavior of the device was added to the model through an equivalent absorbance that contributes to an applied external heat source. The thermal and the mechanical physics were coupled through the inclusion of a temperature induced axial force in the total axial compressive load of the Euler-Bernoulli equation governing the transverse vibrations of the device. Taking into account the imperfections that a fabricated device will have, the effect of the aforementioned total axial load would be the deflection of the beam even if such load is smaller than the buckling load. That is the reason why an imperfection factor was used to define an initial deformation shape that was added to the mechanical modeling with the aim to correctly account for this effect. Therefore, modeling a thermo-mechanical coupling mechanism.

The nonlinear partial differential equations governing the opto-themo-mechanical model were transformed to nonlinear ordinary differential equations by using the Galerkin space discreatization method. Therefore, the complete model was expressed as a system of nonlinear coupled ODEs. At the end of the chapter the necessary steps to theoretically verify if it exists an irradiance value at which the system suddenly starts to auto-oscillate were described.

Chapter 4

Design and analysis of a proof-of-concept device

This chapter is dedicated to the design and analysis of a proof-of-concept (PoC) device based on the concepts outlined in chapter 2. The first design step is the optimization of the proposed FSS unit cell with the aim to maximize its absorbance at a wavelength of 1.55μm. Once the prototype is designed the analyzing process entails the use of the model developed in chapter 3.

4.1 Frequency selective surface optimization

The first step on designing a complete PoC OPACMEMS device is the optimization of its FSS unit cell. This optimization process is carried out through FEM simulations using COMSOL Multiphysics. The hypothesis that the more generated heat per unit volume the better device response is assumed. Therefore, the unit cell dimensions are defined by maximizing its value for the initial gap thickness.

The elements mostly responsible of the generated heat are the periodic nanostrips disposed along the microbridge. Therefore, the microbridge volume essentially contributes to the overall device volume hence lowering the final value of generated heat per unit volume. Meaning that from the thermal point of view, the lower the

microbridge volume the higher the volumetric thermal power. Nevertheless, the best dimensions chosen when only taking into account the thermal behavior might not be the best ones from a mechanical point of view. Thus, there is a trade-off between the best thermal dimensions and the most adequate mechanical ones.

Figure 4.1 shows the characteristic dimensions of the fishbone UC. The overall thickness (t_{sb}) and the supporting beam width (w_b) are fixed before the optimization process. Consequently, the only dimensions left to determine are the width (w_s) and length (l_s) of the nanostrip and the length of the supporting beam. The thickness of the structure is chosen by taking into account the results shown in figure 2.15 and the available fabrication capabilities able to deposit the selected metal. The supporting beam width is fixed at a reasonable small value in order to keep the volume low. Whereas the beam length of the UC is equal to the lateral period (P_x) of the FSS, which together with the longitudinal period (P_y) and the nanostrip dimensions are chosen from an optimization process that will be described in the next subsections.

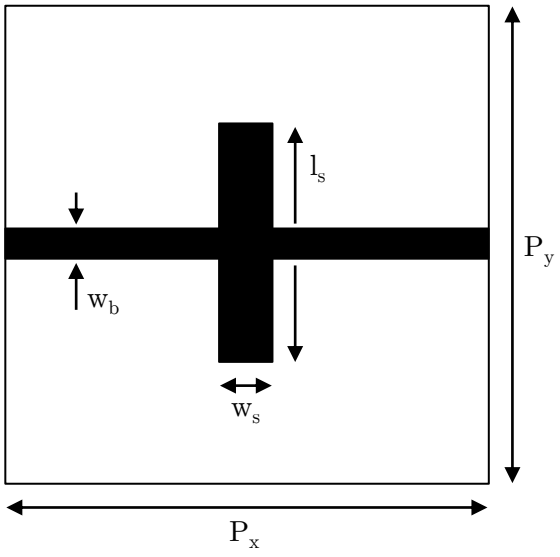

FIGURE 4.1: Characteristic dimensions of the fishbone unit cell. The thickness of the structure t_{sb} is not annotated.

4.1.1 Nanostrip width and length optimization

The nanostrip width and length are set by performing a series of simulations where the best dimensions are found by choosing the ones that give the higher thermal power per unit volume value.

Once the unit cell geometry has been drawn, the nanostrip dimensions are parameterized with the intention of performing a geometry parametric simulation. The optimum dimensions are found by sweeping the value of both the width and length of the nanostrip and plotting the resulting thermal power per unit volume. Figure 4.2 shows the first coarse parametric simulation on the nanostrip dimensions of a fishbone unit cell made of chromium where $t_{sb} = 50\,\text{nm}$, $w_b = 100\,\text{nm}$ and $P_x = P_y = 0.85\,\lambda_w = 1317.5\,\text{nm}$. For an specific width, the length is swept and the thermal power per unit volume computed. This process is done for several widths in order to coarsely determine the best one, which for this particular example is $w_s = 175\,\text{nm}$.

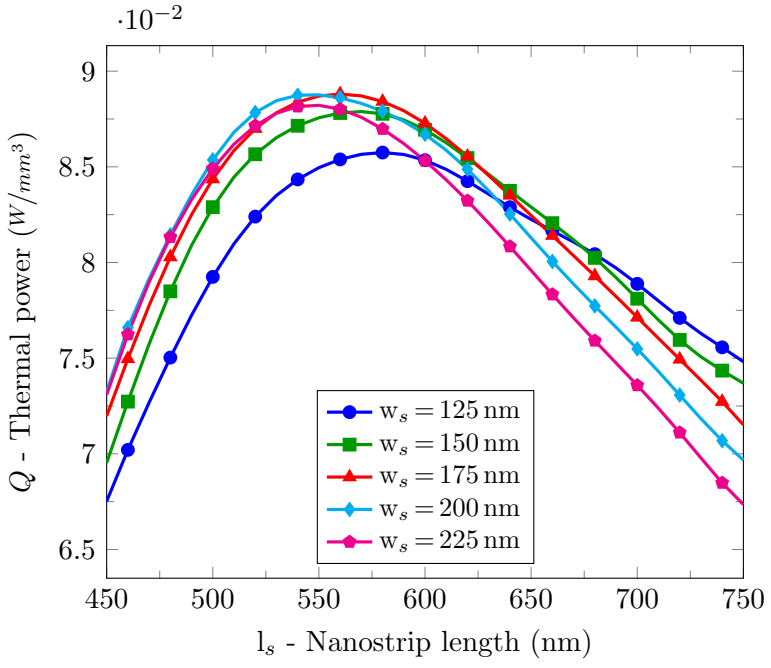

FIGURE 4.2: Evolution of the averaged heat per unit volume of a fishbone unit cell at $\lambda_w = 1.55\,\mu\text{m}$ with the length of the nanostrip for different widths. Irradiance $= 1\,W/m^2$.

A finer adjustment on the dimensions is done by performing several simulations where the width of the nanostrip is swept around its previously found value. Figure 4.3 shows these parametric simulations where the width of the nanostrip has been swept ±10 nm from the initial value. Since the curve that gives the best thermal power per unit volume (i.e., $w_s = 180\,\text{nm}$) is in the middle of two other curves there is no need to increase or decrease the swept range of widths. In order to find an even better value for the nanostrip dimensions a finer swept could be made. However, and given the obtained results, there is no need to do so since the enhancement would be very small.

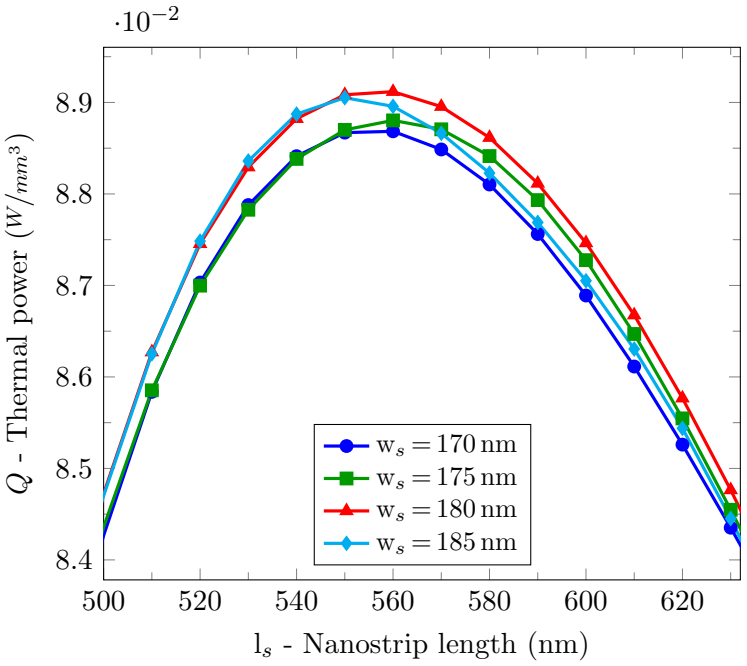

FIGURE 4.3: Evolution of the averaged heat per unit volume of a fishbone unit cell at $\lambda_w = 1.55\,\mu$m with the length of the nanostrip for different widths. Irradiance $= 1\,W/m^2$.

As a result of the previous optimization process and for this particular unit cell, the nanostrip dimension would have been set to $w_s = 180$ nm and $l_s = 560$ nm.

4.1.2 Longitudinal and lateral periods of the FSS

Part of the EM energy absorbed by the unit cells is re-emitted by the same resonant structure. This re-emission is partially absorbed by the neighboring unit cells,

giving rise to a new absorbing/reemitting process. Including the effect of the interference field created by the Fabry-Pérot cavity (see section 2.5), the resonant elements of the FSS receive an equivalent EM field that depends on the interaction of all the surrounding EM fields.

With the aim to study the effect of the longitudinal and lateral periods of the FSS on its EM response, a parametric simulation on these dimensions is done. For each period value, being both equal to simplify the analysis, the unit cell dimensions are determined by the optimization process described in section 4.1.1. The obtained results, shown in figure 4.4, predict that the best thermal power per unit volume is obtained when the periods have a value between $0.8\,\lambda_w$ and $0.9\,\lambda_w$.

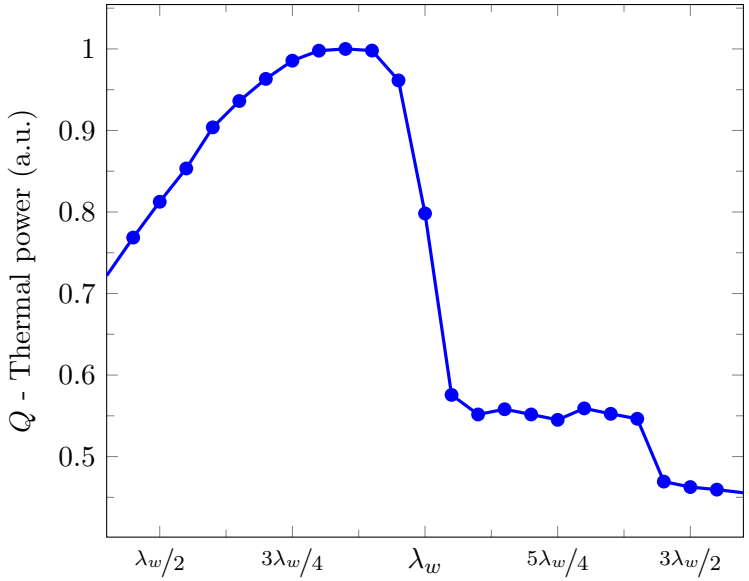

FIGURE 4.4: Evolution of the normalized averaged heat per unit volume of the fishbone unit cell at $\lambda_w = 1.55\,\mu$m with the longitudinal and lateral periods of the FSS. Irradiance $= 1\,{}^{W}/_{m^2}$.

4.2 The unit device

The simulated EM unit cell response is obtained by imposing, through the boundary conditions, that it belongs to an infinite array formed by that same exact

cell (see figure 2.5). Therefore, an OPACMEMS device must have a similar arrangement in order to obtain a fabricated device where its unit cells have an EM response close to the simulated one. To accomplish such layout, a unit device (UD) based on an optimized unit cell is designed and replicated. Such architecture is shown in figure 4.5. The length of the UDs (l_b) and the quantity of them establish the total number of unit cells per device.

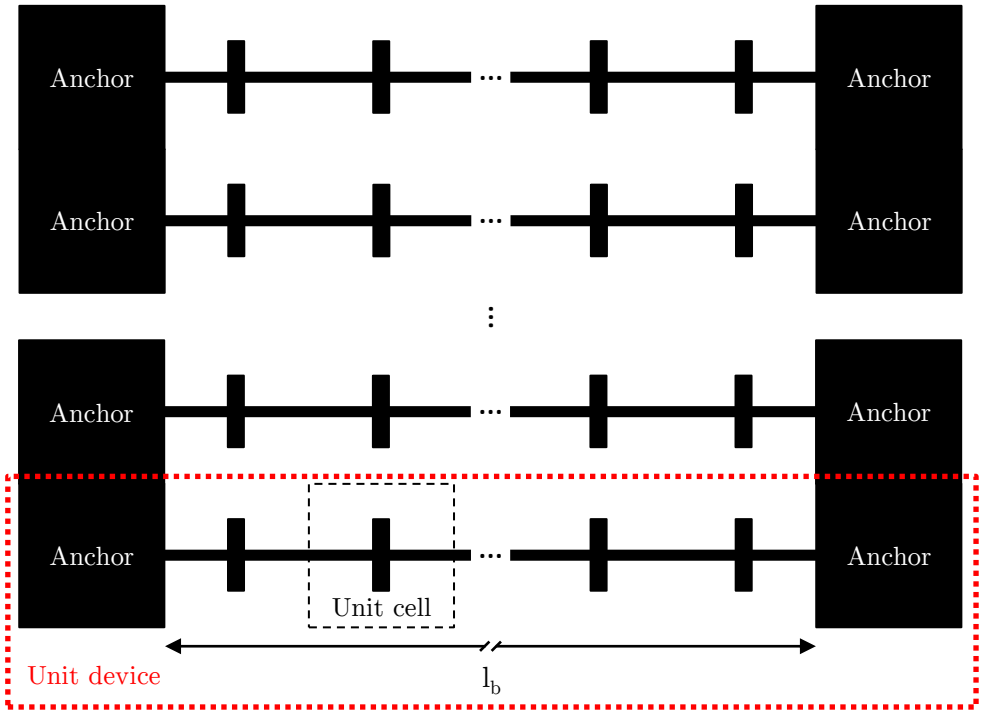

FIGURE 4.5: Schematic geometry of the fishbone OPACMEMS device.

The proposed design breaks its FSS periodicity at its limits, either by the anchors of the UDs or by both ending UDs. Nevertheless, the possible implications of such characteristic can be neglected when characterizing the central UD.

4.3 Geometry and materials of the PoC device

The optimized unit cell of section 4.1.1 is used to design and analyze a theoretical fishbone OPACMEMS prototype. In order to geometrically define the UD the only dimension left to determine is its length, l_b. Choosing its value fixes the number of unit cells forming the UD and also some of its mechanical properties (e.g., its

stiffness, total mass and volume, resonant frequency, etc.). Since from the point of view of the device operation (i.e., accomplish the self-oscillation regime) there is not a strategy to determine the best length value[1], other constrains related with the fabrication and characterization processes serve as the limiting factors. Such constrains are explained in chapters 5 and 6. Therefore, and in order not to jump a step forward into the text, in this section a length value is set and assumed to be feasible.

Characteristic	Value	Defined by...
Material	*Cr*	the fabrication process (see chapter 5)
Thickness - t_{sb} (nm)	*50*	taking into account the results shown in figure 2.15 and the capabilities of the deposition process (see chapter 5)
Beam width - w_b (nm)	*100*	taking into account the nanostrip length and the rigidity of the final structure
Beam length - l_b (μm)	*14.5*	the number of unit cells
Nanostrip width - w_s (nm)	*180*	optimization (see section 4.1.1)
Nanostrip length - l_s (nm)	*560*	optimization (see section 4.1.1)
Lateral period - P_x	$0.85\,\lambda_w$	optimization (see section 4.1.2)
Longitudinal period - P_y	$0.85\,\lambda_w$	optimization (see section 4.1.2)
# of unit cells	*11*	the FSS periodicity and the rigidity of the final structure
Gap	$\lambda_w/4$	optimization (see section 2.5.1)

TABLE 4.1: Characteristics of the PoC unit device where $\lambda_w = 1.55\mu$m.

Table 4.1 summarizes the chosen characteristics of the proof-of-concept unit device, whereas table 4.2 lists the mechanical and thermal properties of the involved

[1]The impossibility to overcome this restriction is due to the nonlinear nature of the model.

materials in addition to the optical ones of table 2.2.

Material	ρ (kg/m^3)	E (GPa)	ν	α_{th} (K^{-1})	k (W/mK)	c (J/kgK)
Cr	*7150*	*279*	*0.21*	$4.9 \cdot 10^{-6}$	*93.7*	*448*
Si	*2330*	*170*	*0.28*	$2.6 \cdot 10^{-6}$	*130*	*700*
SiO_2	*2200*	*70*	*0.17*	$0.5 \cdot 10^{-6}$	*1.4*	*730*

TABLE 4.2: Mechanical and thermal properties of the PoC device materials. Listed from left to right are the density (ρ), Young's modulus (E), Poisson ratio (ν), coefficient of thermal expansion (α_{th}), thermal conductivity (k) and specific heat capacity (c). All the properties where extracted from [78].

4.4 Thermal finite element analysis of the PoC device

The thermal model developed in section 3.2 assumes that the external heat source only cause an horizontal thermal gradient along the UD length (x-direction). Therefore, the thermal gradient either in the direction along its with (y-direction) or its thickness (z-direction) is assumed to be null. This assumptions have a huge implication in the mechanical modeling, since they allow to model the beam's temperature variations as a change on its stress (see (3.47)). Otherwise the mechanical modeling would become over complicated and much more difficult to solve. Therefore, the verification of these assumptions becomes mandatory before considering that the developed opto-thermo-mechanical model is valid.

The following thermal boundary conditions are added to the unit cell FEM model developed in section 2.4.1 with the aim to link the electromagnetic and the thermal physics:

- Boundary condition 1: the resistive power losses computed by the EM physics are included as an external heat flux to the metal volumes highlighted in figure 4.6a.

- Boundary condition 2: the supporting beam ending boundaries (colored in figure 4.6b) are set to be at a constant temperature, modeling the heat flow effect produced by the UD anchors acting as a heat sink.

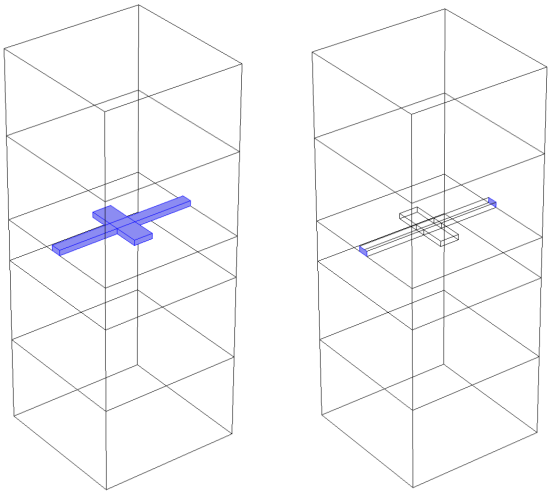

(A) Thermal BC 1. (B) Thermal BC 2.

FIGURE 4.6: Thermal boundary conditions for the unit cell multiphyisics simulation.

Figure 4.7 shows several isothermal surfaces revealing that there is neither a y-direction nor z-direction thermal gradient in the supporting unit cell beam as a consequence of the heat flow. Therefore, the seventh assumption made in section 3.2 can be considered accurate.

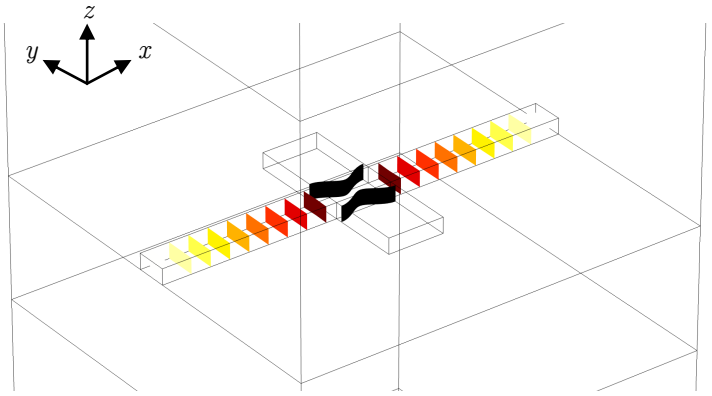

FIGURE 4.7: Isothermal surfaces where black represents the highest temperature and withe the lowest (arbitrary units are used).

4.5 Analysis of the PoC device opto-thermo-mechanical model

In this section the opto-thermo-mechanical model developed in chapter 2 is used to describe the behavior of the designed PoC OPACMEMS device. The first thing that needs to be addressed is the analytic description of the corresponding unit cell absorbance with its normalized position within the gap (see (3.12)). Figure 4.8 shows the obtained UC absorbance curve and its Fourier series fitting.

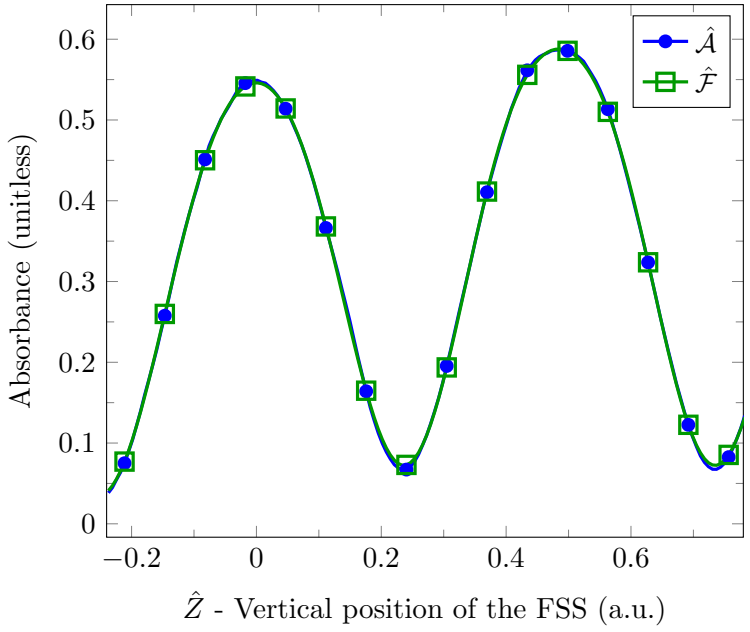

FIGURE 4.8: Evolution of the PoC unit cell absorbance at $\lambda_w = 1.55\,\mu$m with its vertical position within the gap.

In addition to the data shown in tables 4.1 and 4.2, the device's residual stress (σ_r in (3.47)) and its imperfection level (δ_0 in (3.44)) need to be known in order to apply the model. Since PoC device is designed and analyzed from a theoretical point of view two assumptions must be made in order to assign a value to these parameters:

- First: the value of the initial static deflection of the beam's central point is assumed.

- Second: the value of the residual stress is chosen so it is lower than the first buckling load.

Equation (3.67) can be dimensionalized by undoing the rescalation process summarized in (3.56), yielding

$$W_i^3 - \left(\frac{4L^2}{\pi^2 E}\sigma_r - 16\frac{I}{A} + \delta_0^2 L^2\right) W_i - 16\frac{I}{A}\delta_0 L = 0 \tag{4.1}$$

where W_i is the initial beam's central point deflection when it is not being heated.

When taking into account the above listed assumptions and the data shown in tables 4.1 and 4.2, equation (4.1) can be solved for σ_r and δ_0. Table 4.3 summarizes the chosen parameters value for the PoC device.

W_i (nm)	σ_r (MPa)	δ_0 (unitless)
50	*5*	*0.00278*

TABLE 4.3: Initial beam's central point deflection, residual stress and imperfection level of the PoC device.

The last parameter needed to be able to compute all the involved coefficients of the model is the quality factor Q_f of the resonator (or the equivalent distributed damping D). Since this parameter can only be obtained experimentally[2] its value must be also assumed. For the PoC device it is assumed that $Q_f = 1000$.

As explained and sketched in section 3.4.1 a bifurcation analysis of the differential equations that describe the lumped opto-thermo-mechnical model needs to be performed in order to examine the structure of its solutions. A custom MATLAB [79] script was used to numerically carry out such study.

The inputs of the developed script are the unit cell absorbance data obtained by FEM simulation (i.e., the $\hat{\mathcal{A}}$ values in figure 4.8), the data of tables 4.1, 4.2 and 4.3

[2] In section A.9 of appendix A the reader can find an explanation of how to extract the quality factor from the frequency spectrum of a resonator.

plus the assumed quality factor. The major computations performed by the script for a given irradiance are summarized in the following list by order of execution:

- Fit the absorbance data to a Fourier Series, an example of the obtained output would be the analytic expression for the $\hat{\mathcal{F}}$ values shown in figure 4.8.
- Compute the equilibrium solution following the steps described in section 3.3.3. Thus, obtaining the values of $W_{l.e}$ and $\hat{T}_{l.e}$.
- Calculate the first natural frequency and the associated linear undamped mode shape around the previously found equilibrium following the steps described in section 3.3.4. As a result, the value of ω_1 and the expression for ϕ_1 are obtained.
- Compute the $c_1 - c_8$ coefficients of the complete opto-thermo-mechanical model described by the system of nonlinear differential equations (3.96).
- Solve the system of nonlinear differential equations (3.96).

4.5.1 Analysis of the model parameters

When the irradinace value is changed some of the model parameter must be recomputed inasmuch that their value or expression depend upon it. Table 4.4 classifies the model parameters between those that depend on the irradiance and those that do not.

Irradiance dependent	c_2, c_4, c_5, c_6, c_7, c_8, φ_1, $W_{l.e}$, $T_{l.e}$
Irradiance independent	c_1, c_3

TABLE 4.4: Irradiance dependent and independent model parameters.

Figure 4.9 graphically illustrates the evolution of the irradiance dependent model parameters, the P_0 parameter (see (3.63)) and the buckling load P_b are also included. The first included graph shows that there is a thermo-mechanical coupling

mechanism between the irradiance and the lumped equilibrium deflection of the beam's central point. Such effect is the outcome of having included a thermal force in the axial load of the beam (see (3.47)), which is reflected in the $\mathcal{C}_4\hat{T}_{l.e}$ term of equation (3.63). However and as shown in figure 3.7, this effect only exists if the clamped-clamped beam is imperfect (i.e., $\delta_0 \neq 0$)[3].

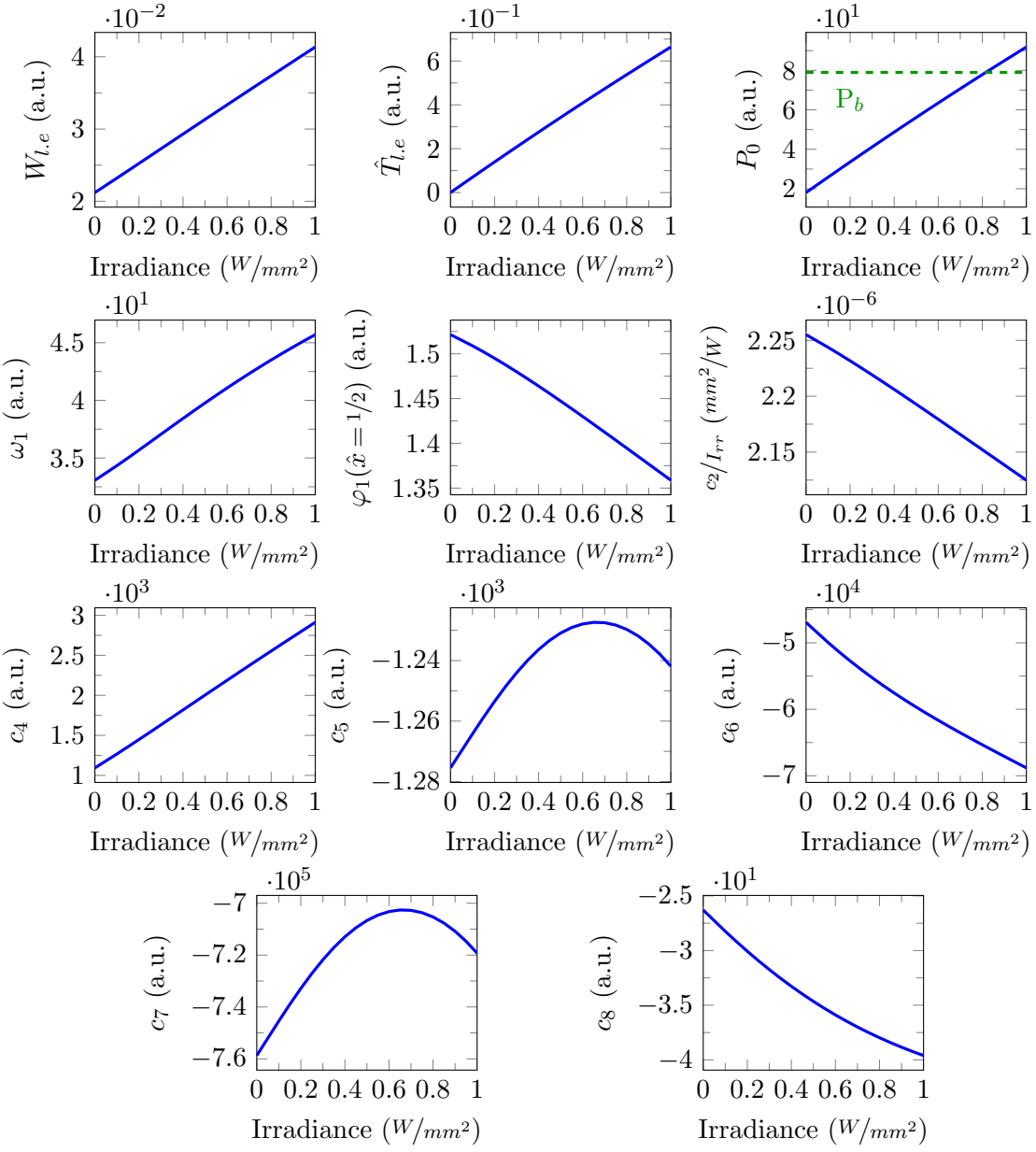

FIGURE 4.9: Evolution of the irradiance dependent opto-thermo-mechanical model parameters of the PoC device.

[3]In appendix B the reader can find a deeper analysis of the irradiance dependent parameters.

4.5.2 Numerical analysis: tracking the auto-oscillations

Has explained in section 3.4.1 the equilibrium solutions of the opto-thermo-mechanical model (3.96) must be calculated and analyzed with the aim to determine if it exists an irradiance at which the system of nonlinear differential equations self-oscillates.

The first step of this analysis begins by monitoring the eigenvalues of the Jacobian of the dynamical system linearitzed about the equilibrium solution while increasing the irradiance. The equilibrium solution loses stability in a Hopf bifurcation when the pair of eigenvalues coming from the mechanical equation cross the imaginary axis.

Once it is determined that a Hopf bifurcation occurs for a particular irradiance, its stability must be studied. Rather than computing the first Lyapunov coefficient, the stability is studied by analyzing the temporal solution at a higher irradiance value than the one at which the bifurcation occurred. If this temporal solution exhibits a limit cycle, it is then established that the Hopf bifurcation is supercritical. On the contrary, if no limit cycle exist at a higher irradiance it is subcritical.

The final step of this numerical analysis is the tracking of the auto-oscillation amplitude while the irradiance is increased beyond the bifurcation point.

Figure 4.10 depicts the auto-oscillation amplitude of the PoC beam's central point obtained by performing the above described numerical analysis. As it can be seen, the steady state of the dynamical system suffers a transition to periodic motion at an irradiance value of $I_{rr} = H = 210\,{}^{mW}/_{mm^2}$.

Figure 4.11 shows the temporal oscillating behavior of the PoC beam's central point displacement for $I_{rr} = 400\,{}^{mW}/_{mm^2}$. For this particular irradiance value, the transverse vibration of the beam has a frequency of 2.14 MHz. During this self-oscillation state the absorbance values of the PoC device are located and oscillate along the region enclosed by the vertical dashed lines of figure 4.12. Due to the initial deflection of the beam, this absorbance region is not symmetric about the vertical position $\hat{Z} = 0$.

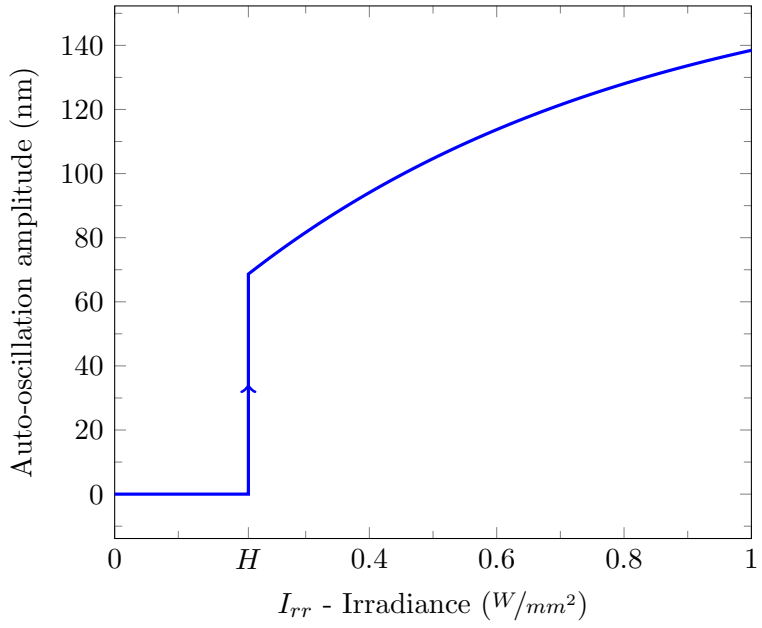

FIGURE 4.10: Evolution of the auto-oscillation amplitude as a function of the irradiance for the theoretical PoC device. The Hopf bifurcation is produced at $I_{rr} = H = 210\,{}^{mW}/_{mm^2}$.

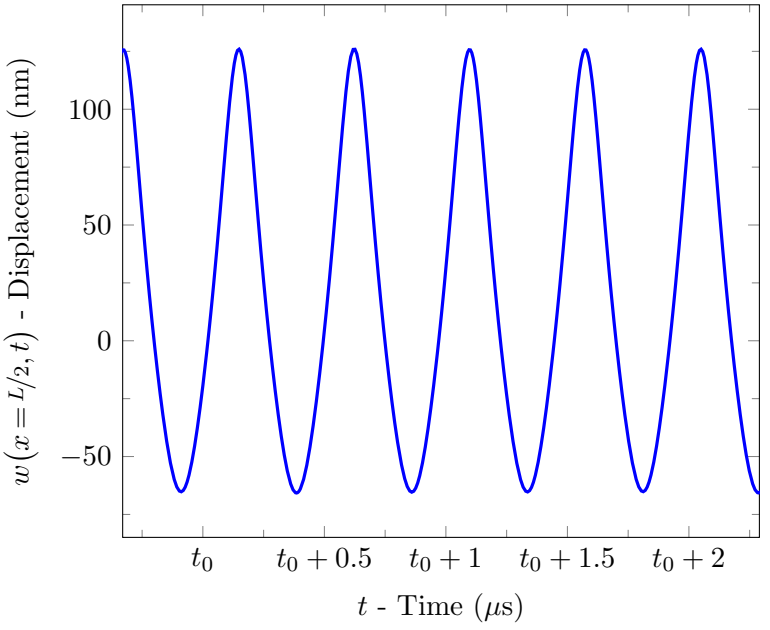

FIGURE 4.11: Temporal evolution of the PoC beam's central point displacement for $I_{rr} = 400\,{}^{mW}/_{mm^2}$. The frequency of oscillation is 2.14 MHz.

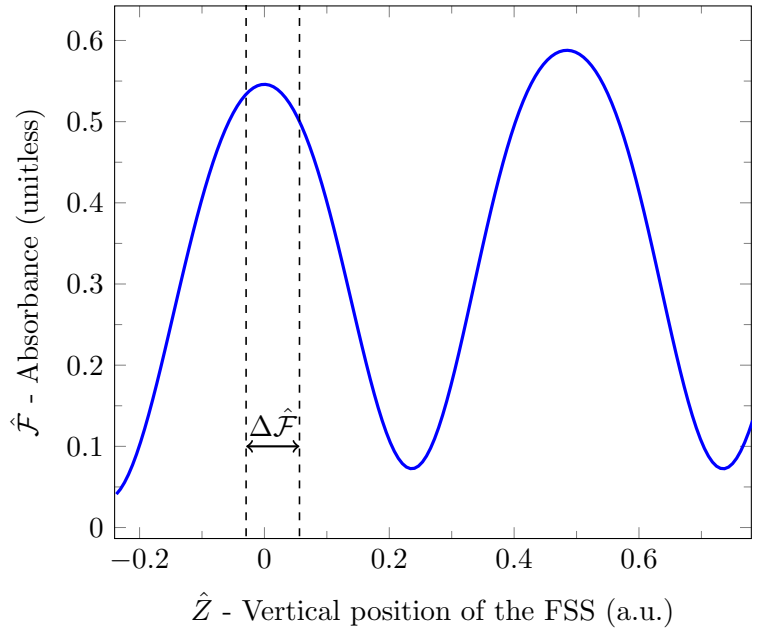

FIGURE 4.12: Evolution of the PoC unit cell absorbance at $\lambda_w = 1.55\,\mu$m with its vertical position within the gap. The absorbance values for $I_{rr} = 400\,{}^{mW}/_{mm^2}$ oscillate along the region enclosed by the vertical dashed lines. $\Delta\hat{\mathcal{F}} = 0.0855$.

Figure 4.13 depicts the temporal oscillating behavior of the PoC beam's average temperature above T_0 for $I_{rr} = 400\,{}^{mW}/_{mm^2}$. Since the average temperature directly depends on the absorbance of PoC device (see (3.33)), its temporal evolution can be attributed to the fact that the absorbance region of figure 4.12 is highly nonlinear.

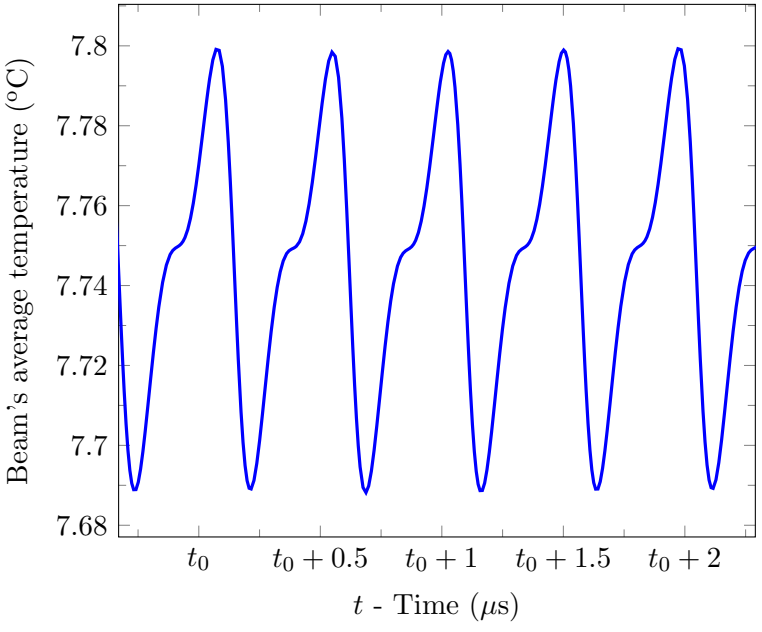

FIGURE 4.13: Temporal evolution of the PoC beam's average temperature above T_0 for $I_{rr} = 400\,{}^{mW}/_{mm^2}$.

Figures 4.14 and 4.15 respectively depict the displacement versus velocity of the beam's central point and the beam's central point displacement versus the beam's average temperature phase planes. The closed trajectories displayed in both of the phase planes are the representation of the stable limit cycle born after the Hopf bifurcation transition.

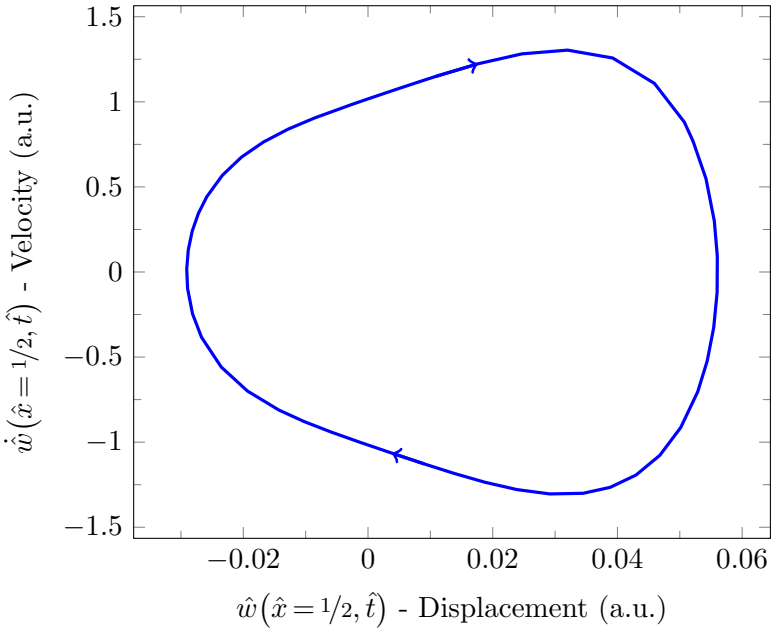

FIGURE 4.14: Phase plane: displacement versus velocity of the beam's central point for $I_{rr} = 400\,{}^{mW}/_{mm^2}$.

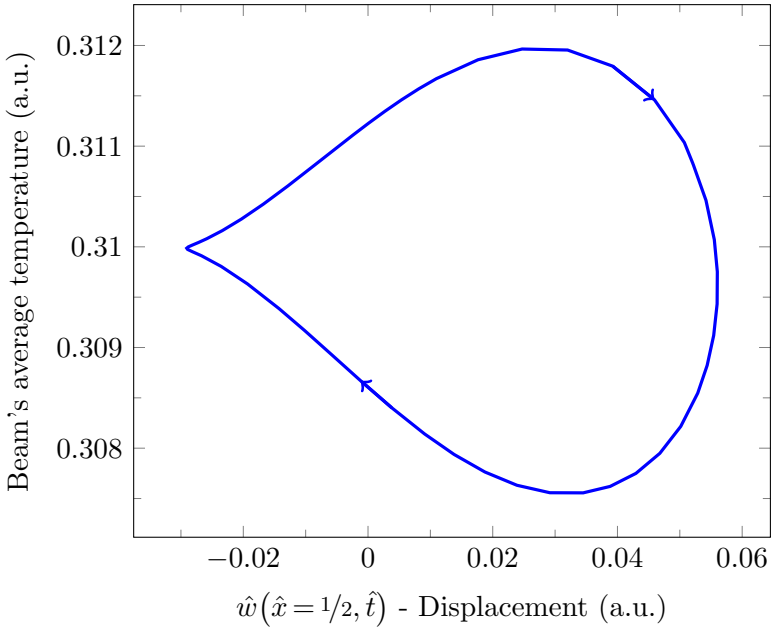

FIGURE 4.15: Phase plane: beam's central point displacement versus beam's average temperature above T_0 for $I_{rr} = 400\,{}^{mW}/_{mm^2}$.

4.6 Numerical analysis: changing the gap and the quality factor of the PoC device

During the design of the theoretical proof-of-concept device analyzed in the previous section several assumptions were made in order to obtain a device with feasible dimensions, common materials and reasonable characteristics. The only parameter obtained after an optimization process was the absorbance of the device's EM resonators. However, the goal of such process was not the optimization of the irradiance value at which the device would self-oscillate. Its goal was to maximize the absorbance at a particular wavelength and using a unit cell with a particular cavity length, assuming that a higher absorbance would decrease the irradiance value at which the system starts to auto-oscillate. Nevertheless and after the analysis of the PoC device model, it can not be asserted that such assumption is valid.

The opto-thermo-mechanical model was developed with the aim to theoretically understand and characterize the behavior of an ideally fabricated OPACMEMS device. However and inevitably, the fabrication process will introduce changes to all of the assumed properties and dimensions (e.g., the optical properties of the structural metal, its thickness, its mechanical properties, etc). The nonlinear nature of the opto-thermo-mechanical model added to the factor that during the modeling process a FEM simulator is needed, a theoretical analysis of the variability of all the involved properties and dimensions in order to optimize the irradiance value at which the system starts to auto-oscillate turns out to be cumbersome if not impossible. Therefore and rather than being a tool to optimize the theoretical OPACMEMS devices, the model is a tool to explain their physical behavior. Consequently, the inputs of the model must be obtained by performing the pertinent measurements on the fabricated device.

The following sections include the results of several numerical analysis with the aim to obtain some insight about what happens when the gap length and the quality factor of the proof-of-concept device are changed.

4.6.1 Gap length

The length of the PoC device gap was set at 387.5 nm as a result of the analysis performed in section 2.5.1. It seems logical that if this value changes, the dynamic behavior of the UD it is also going to change. Figure 4.16 depicts the PoC device absorbance when the gap value is 587.5 nm (i.e., a $Z_0 = 200$ nm increase with respect to the initially designed value). Comparing this graph with the one in figure 4.8 and as expected, the absorbance evolution has been shifted towards the left and now the maximum absorbance is not accomplished at $\hat{Z} = 0$.

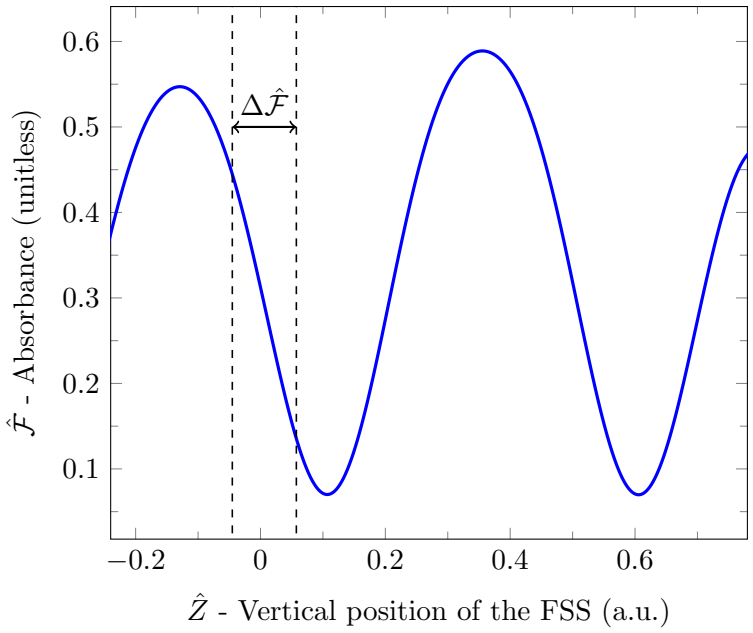

FIGURE 4.16: Evolution of the PoC unit cell absorbance at $\lambda_w = 1.55\,\mu$m with its vertical position within the gap when its initially designed value is 587.5 nm. The absorbance values for $I_{rr} = 400\,{}^{mW}/_{mm^2}$ oscillate along the region enclosed by the vertical dashed lines. $\Delta\hat{\mathcal{F}} = 0.103$.

Figure 4.17 depicts the obtained auto-oscillation amplitude when $\hat{Z}_0 = 0.129$. As it can be seen, the steady state of the dynamical system suffers a transition to periodic motion at lower irradiance value than for the initial designed PoC device (i.e., for $\hat{Z}_0 = 0$). Additionally, the amplitudes of the self-sustained mechanical oscillations are higher than the ones plotted in 4.10.

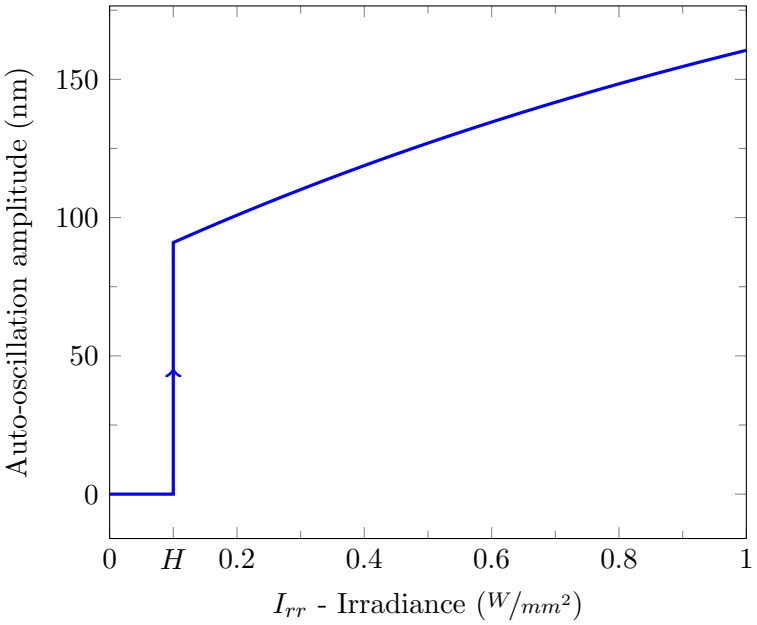

FIGURE 4.17: Evolution of the auto-oscillation amplitude as a function of the irradiance when $Z_0 = 200\,\text{nm}$. The Hopf bifurcation is produced at $I_{rr} = H = 100\,{}^{mW}/_{mm^2}$.

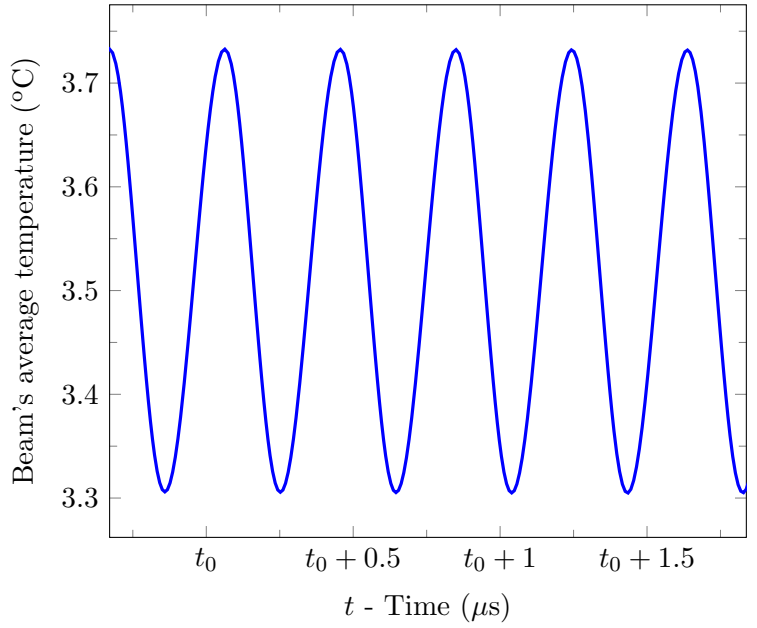

FIGURE 4.18: Temporal evolution of the PoC beam's average temperature above T_0 for $I_{rr} = 400\,{}^{mW}/_{mm^2}$ when $\hat{Z}_0 = 0.129$.

Figure 4.18 shows the temporal oscillating behavior of the beam's average temperature above T_0 for $I_{rr} = 400\,{}^{mW}/_{mm^2}$ when $\hat{Z}_0 = 0.129$. Unlike the data shown in figure 4.13, its temporal evolution has an almost sinusoidal shape that can be

attributed to the fact that the absorbance region of figure 4.16 can be considered to be almost linear.

4.6.2 Quality factor

Figure 4.19 depicts the auto-oscillation amplitude of the PoC beam central point when the quality factor is assumed to be $Q_f = 10000$ and the initial gap 387.5 nm. As it can be seen, the steady state of the dynamical system suffers a transition to periodic motion at an irradiance value of $I_{rr} = H = 180\,{}^{mW}/_{mm^2}$. Thus, increasing the quality factor (i.e., decreasing the damping) decreases the irradiance at which auto-oscillation begins. Although, the amplitude of oscillation for a given irradiance value slightly decreases.

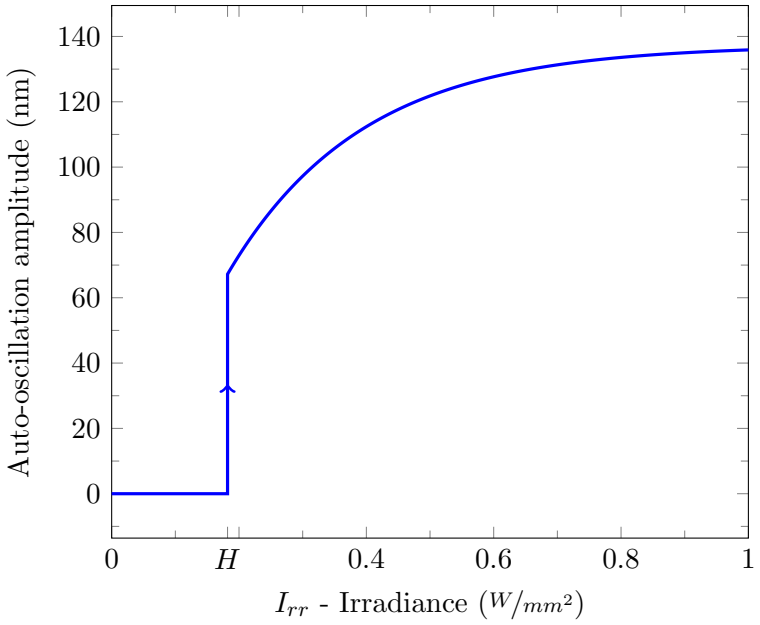

FIGURE 4.19: Evolution of the auto-oscillation amplitude as a function of the irradiance when $Q_f = 10000$. The Hopf bifurcation is produced at $I_{rr} = H = 180\,{}^{mW}/_{mm^2}$.

4.7 Summary

In this chapter a proof-of-concept device featuring both micro and nanometric dimensions is designed and analyzed. The device's EM resonators acting as an

absorber were optimized using a finite element analysis (FEA) software. Due to the nonlinear nature of the devices auto-oscillation principle, some of the PoC device dimensions and characteristic had to be assumed in order to theoretically analyze its dynamic behavior. Making use of the opto-thermo-mechanical model developed in chapter 3 an irradiance of $210\,{}^{mW}/_{m^2}$ was predicted to induce the device self-oscillation. Finally, two studies were performed in order to qualitatively show how does the irradiance value for which the device suffers a transition to a periodic motion depend on both the device's gap length and its quality factor.

Chapter 5

Fabrication

In this chapter the custom approach for the OPACMEMS devices fabrication is described and used to process several chips. The results obtained are also included and analyzed.

5.1 Fabrication process

A custom process was developed in order to fabricate the OPACMEMS devices. Figure 5.1 shows the sequential steps of this microfabrication approach.

The process starts from a silicon wafer[1] (step #0) where a layer of $\approx 387.5\,\text{nm}$ ($\lambda_w/4$ with $\lambda_w = 1.55\,\mu\text{m}$) silicon dioxide is thermally grown (step #1). A precise SiO_2 thickness can be obtained by controlling the temperature and the duration of the oxidation process. Then the Si/SiO_2 wafer is diced into $1.5\,\text{cm} \times 1.5\,\text{cm}$ pieces. The next steps are done using one of the cleaved chips.

Electron beam lithography (eBL) is used to pattern the designed submicron geometry on top of the SiO_2 layer. The eBL writing process begins by performing a dehydration bake on the chip in a hotplate[2]. The next step is the deposition

[1] The used wafer had a diameter of 100 mm and a thickness of 525 μm. Its impurity doping was bulk P-type and its crystallographic orientation was (100).

[2] This process was done at 150 °C for 30 sec.

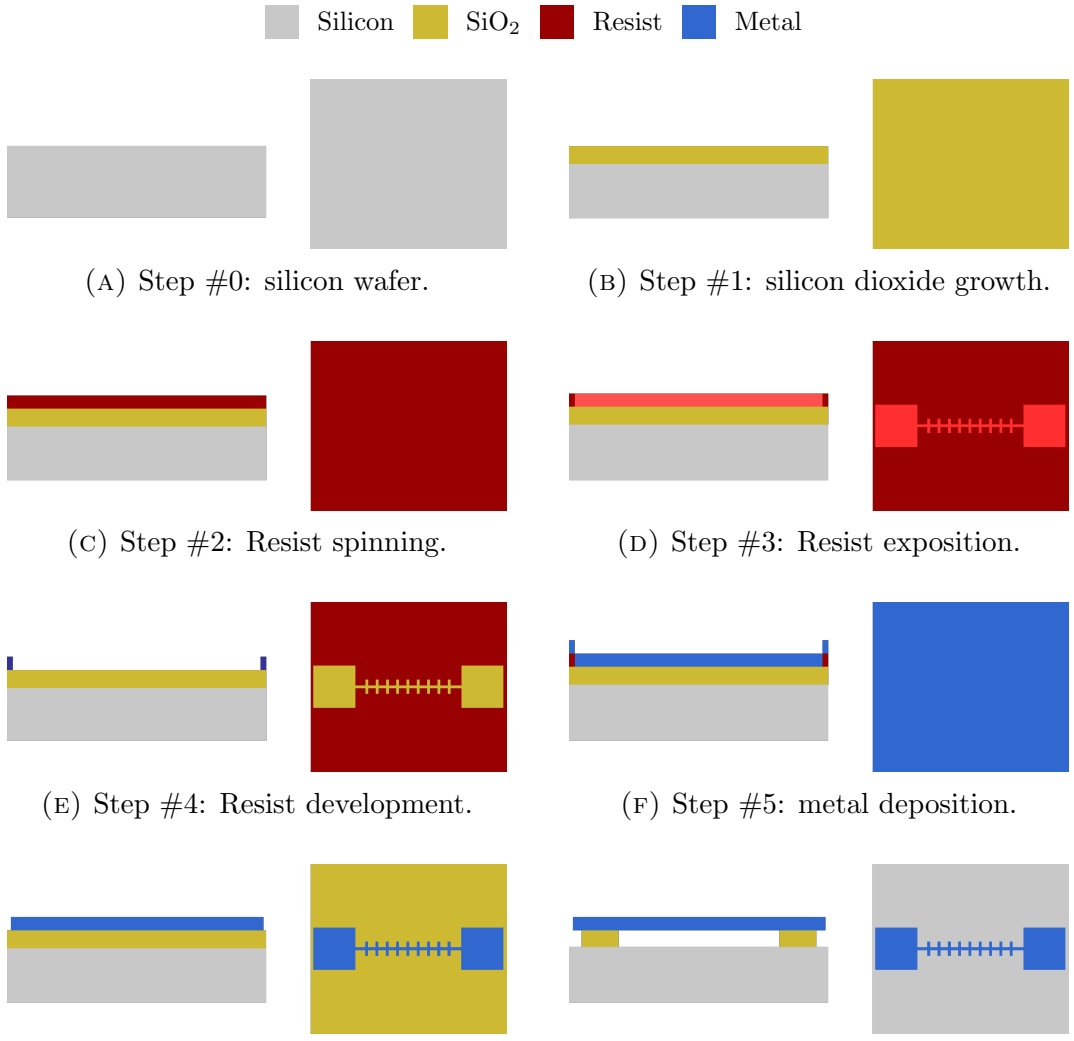

(A) Step #0: silicon wafer.

(B) Step #1: silicon dioxide growth.

(C) Step #2: Resist spinning.

(D) Step #3: Resist exposition.

(E) Step #4: Resist development.

(F) Step #5: metal deposition.

(G) Step #6: metal lift-off.

(H) Step #7: silicon dioxide etching.

FIGURE 5.1: Steps of the fabrication process. For each step, cross-section (left) and top view (right) are shown.

of a bilayer of positive resists by spinning (step #2). The first layer, made of a copolymer [3], helps during the metal lift-off process due to its high solubility when developed. While the second one, made of PMMA[4], provides a better resolution when defining the submicron features. Both spinning processes were followed by a soft-bake[5].

The desired geometry is written onto the sensitive resist by a focused beam of

[3]The used copolymer resist was based on a mixture of methyl methacrylate (MMA) and 8.5% of methacrylic acid (MAA) formulated in ethyl lactate with a 6-11% of solid contents (EL6). It was spunt at 1500 rpm for 1 min, giving a 200-300 nm thick layer.

[4]The used resist was PMMA with a molecular weight of 950 K and a 2-7% in anisole of solid contents (A2). It was spunt at 1500 rpm for 1 min, giving a 100 nm thick layer.

[5]This process was done at 150 °C for 30 sec.

high energy electrons[6]. A voltage of 10 kV, an aperture of 20 μm, a current of 80 pA and an area dose of 100 $\mu C/cm^2$ are the typical used microscope values when transferring the pattern (step #3). The exposed areas are then developed[7] (step #4).

The next fabrication step is the deposition of the desired metal (step #5). The metal that is not directly adhered to the SiO_2 surface is removed using a standard lift-off procedure in acetone (step #6). Etching[8] the sacrificial SiO_2 layer (step #7) releases the structure and completes the fabrication process.

From the fabrication point of view, chromium[9] is chosen to be the device material because, unlike standard metals used in nanotechnology such as Au, Al or Pt, it withstands the SiO_2 wet etching process.

5.2 Fabrication results

The OPACMEMS devices fabrication process was mostly carried out at the nanofabrication facilities of the IMB-CNM (*Institut de Microelectrònica de Barcelona - Centre Nacional de Microelectrònica*), except the metal deposition that was performed at the CIN2 (*Centre d'Investigació en Nanociència i Nanotecnologia*).

This section is divided in two subsections where the remarkable results obtained from different chips are described.

[6] The used electron beam microscope was a Raith 150-TWO.

[7] This process was done by immersing the chip in a mixture of 1 part of methyl isobutyl ketone (MIBK) and 1 part isopropyl alcohol (IPA) during 30 sec. The development procedure was stopped by rinsing the sample with IPA for 30 sec and drying it with nitrogen.

[8] The commercially available SiOetch etchant was used to etch the SiO_2 layer at an approximate rate of 1000 Å per minute.

[9] It was electron beam evaporated using an evaporator (AJA International) working at 8 kV. The deposited thicknesses were between 50 and 100 nm.

5.2.1 Proof-of-fabrication chip

Prior to the design of the proof-of-concept device analyzed in chapter 4, several OPACMEMS devices with non-optimized EM resonators were fabricated with the aim to validate the proposed fabrication process. The design include unit devices with lengths between 1 and 15 μm (l_b) and a width of 100 nm (w_b). While the nanostrips have a length of 450 nm (l_s) and a width of 100 nm (w_s). The deposited chromium layer was approximately 90 nm thick. Figure 5.2 shows various SEM images of these proof-of-fabrication (PoF) devices after their releasing process.

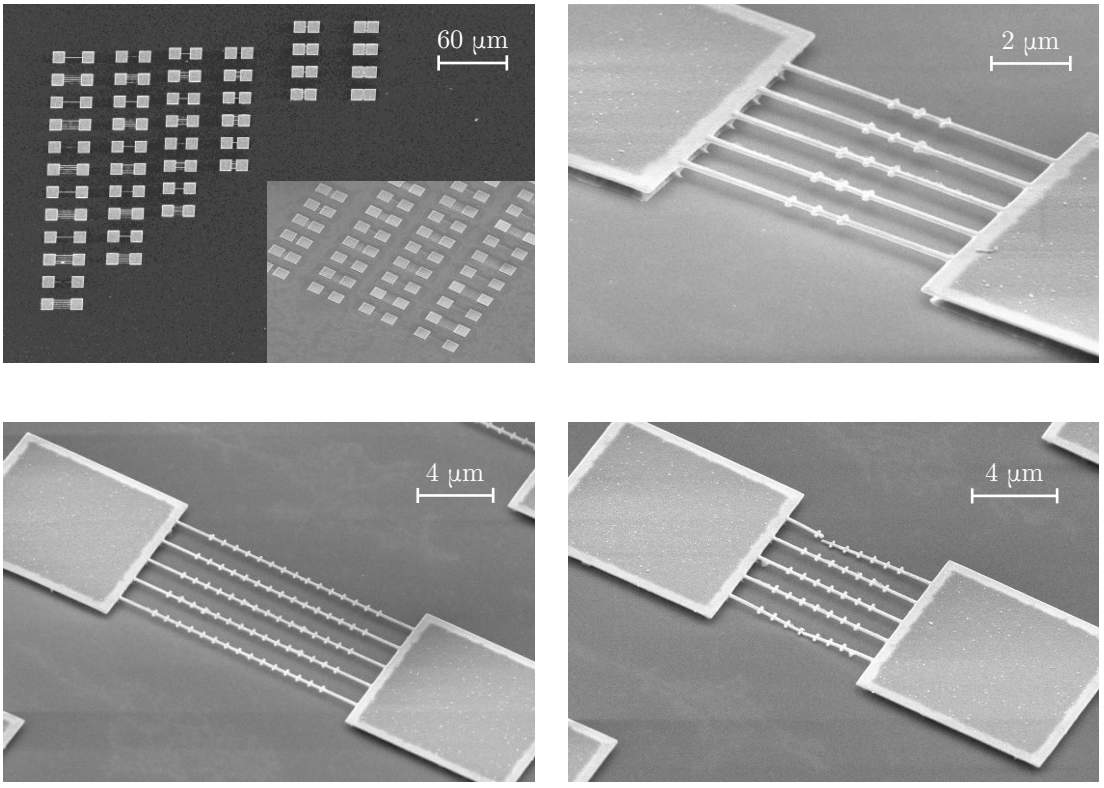

FIGURE 5.2: SEM images of several OPACMEMS PoF devices.

From the SEM images of the PoF chip it can be point out that if the chromium layer has a residual stress it has to be tensile inasmuch that they do not seem to be deflected upwards or downwards (shape that could be attributed to a residual compressive stress, as explained in section 3.3.1). It also can be seen that several unit devices are broken. This can be attributed to the combined effect of the non-uniform chromium layer and the residual tensile stress.

5.2.2 Fabrication of the proof-of-concept device

In this section the results obtained by the fabrication of various OPACMEMS devices are shown and analyzed. In contrast with the previous section, all of the fabricated devices are designed using the optimized unit cell of the PoC device studied in chapter 4. The dimensions of this UC can be found in table 4.1.

Figure 5.3 shows four SEM images corresponding to four different processed chips. As it can be seen, all of the shown devices were unsuccessfully fabricated. The following list comments each of the images:

- Figure 5.3a: as a consequence of the chromium layer being too thin (less than 50 nm) the only parts of the unit devices that remained after the SiO_2 etch are their clamped ends and, stuck to the silicon substrate, the regions where the nanostrips were defined.

- Figures 5.3b and 5.3c: this images show OPACMEMS devices where the chromium lift-off process was not able to remove the metal between adjacent unit devices. After a series of fabrication tests, it was determined that the time between the metal deposition and its lift-off should be as short as possible in order to successfully pull out the chromium of these zones. This problem was not encountered during the fabrication of the PoF devices because the separation between adjacent unit devices was 432 nm larger.

- Figure 5.3d: as a consequence of the previously described unsuccessful metal lift-off, some of the processed chips had all their unit devices ripped off the anchor pads after the SiO_2 etch.

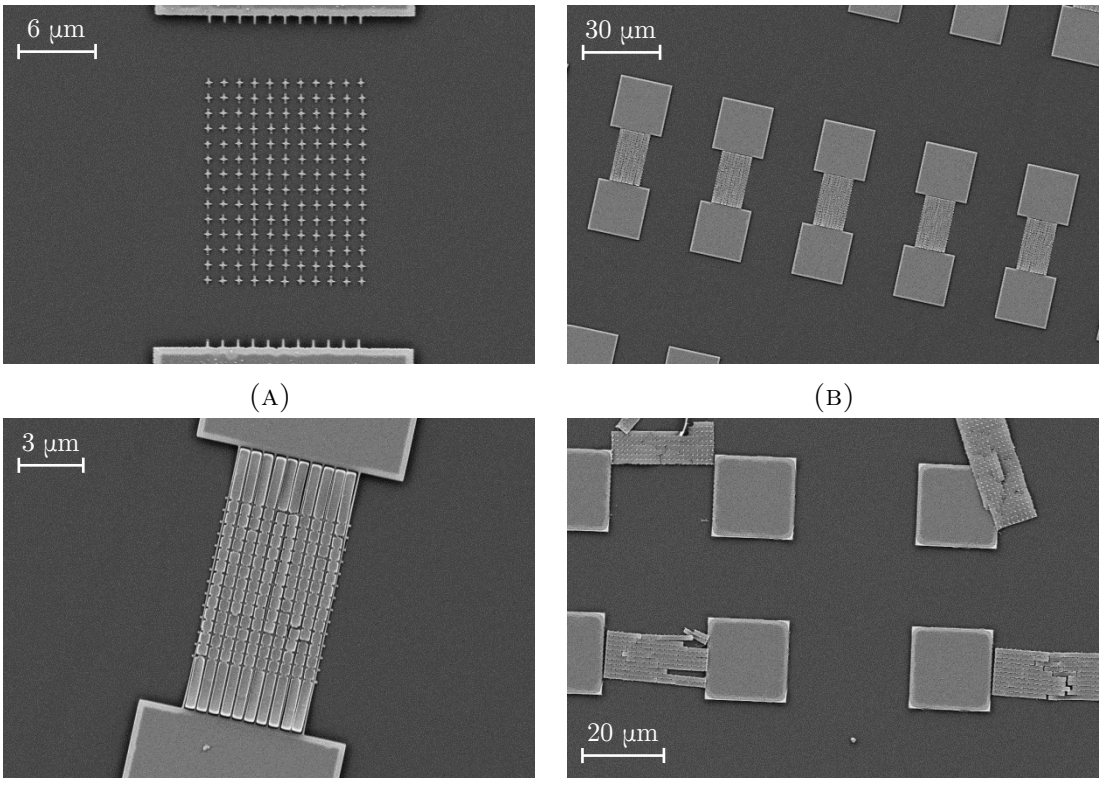

(A) (B) (C) (D)

FIGURE 5.3: SEM images of several unsuccessfully fabricated OPACMEMS devices.

After improving the fabrication process new chips were processed using the PoC device design. Figures 5.4a and 5.4b correspond to two different PoC OPACMEMS devices. As it can be seen, only two or three UDs per sample were successfully fabricated. To further illustrate this yield, figure 5.4c shows a tilted image of a PoC device where the electronic shadow reveals which of the UDs are properly suspended and which ones are resting on the silicon substrate due to their breakage. In order to study the effect of the UDs length, shorter devices were also fabricated. Figure 5.4d shows the tilted image of an OPACMEMS device having seven unit cells and a total length of 9.22 μm (the UDs length of the PoC device were 14.5 μm). It can be appreciated that six of the eleven UDs were successfully fabricated.

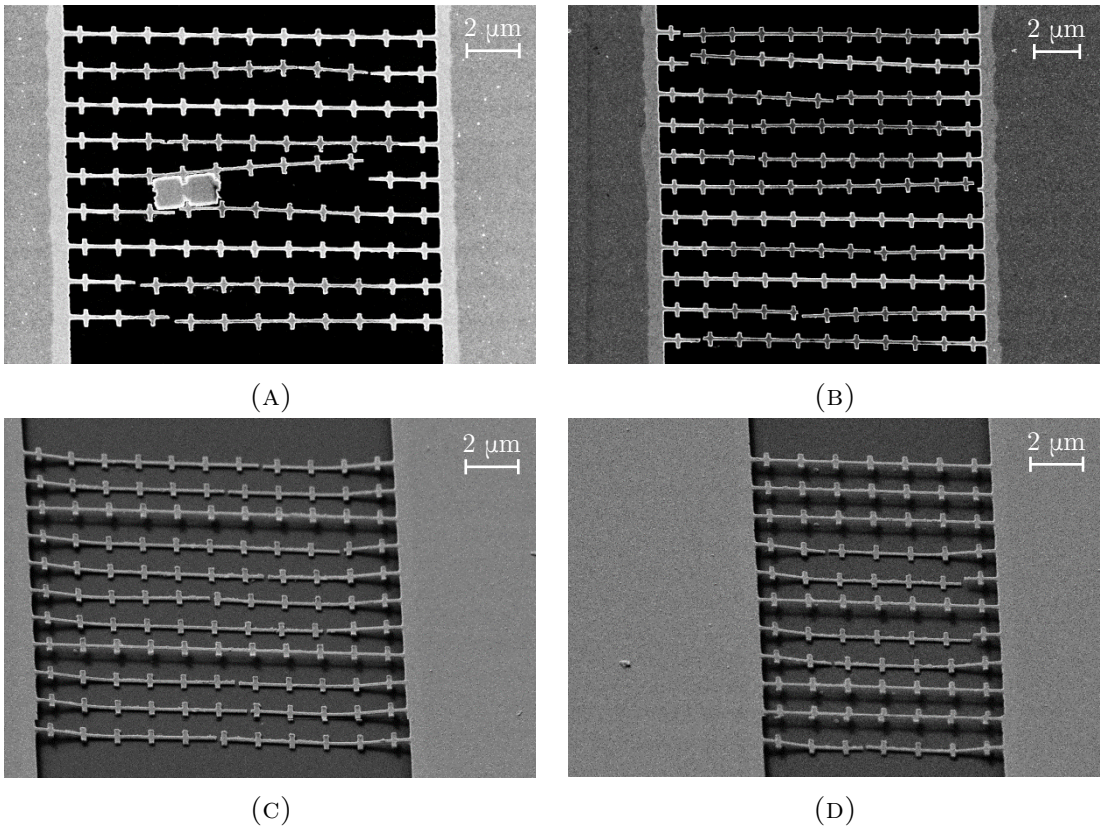

FIGURE 5.4: SEM images of several attempts to fabricate the OPACMEMS PoC device.

In chapter 4, and with the aim to study the behavior of the PoC device using the developed opto-thermo-mechanical model, the residual compressive stress and the imperfection level of the chromium layer were assumed. Both of these parameters can be experimentally extracted by measuring the static deflection profile of the fabricated devices. Nevertheless, such procedure can only be performed if the residual stress is compressive as long as a tensile stress would not deflect the clamped-clamped mechanical structure. If the characterized devices share the same structural layer, it can be considered that their residual compressive stress and imperfection level are approximately the same. An atomic force microscope (AFM) can be used to characterize the static deflection of several devices having different lengths. The value of the maximum deflection for each of the devices (which should be located at each of the beam's central point) can be fitted to equation (4.1) with the method of least squares, solving for the values of σ_r and δ_0 which minimize the error of the theoretical central point deflection as in [76].

However and as pointed out in section 5.2.1, the residual stress of the chromium layer seems to be tensile rather than compressive.

An AFM[10] working at a non-contact mode was used to study the topography of the fabricated PoC devices. Figure 5.5 shows the topography image of the set of three OPACMEMS unit devices shown in the top of figure 5.4d.

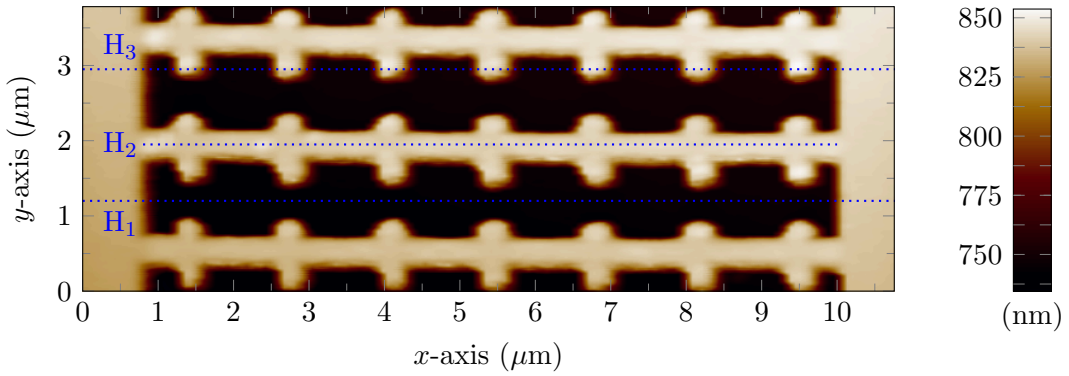

FIGURE 5.5: AFM image of a set of three OPACMEMS unit devices.

Figure 5.6 depicts the height profile along the horizontal H_1 line of figure 5.5. From this profile it can be seen that the sample was slightly tilted ($\sim 0.05\,^{o}$) during the AFM measurements. Furthermore, it can be seen that the thickness of the chromium layer plus the length of the gap is 93 nm when it should be 437.5 nm (from table 4.1, 387.5 nm + 50 nm). The growth of a too thin layer of SiO_2 and/or its partial etching are assumed to be the major cause(s) of such discrepancy, though further measurements should be performed in order to verify it.

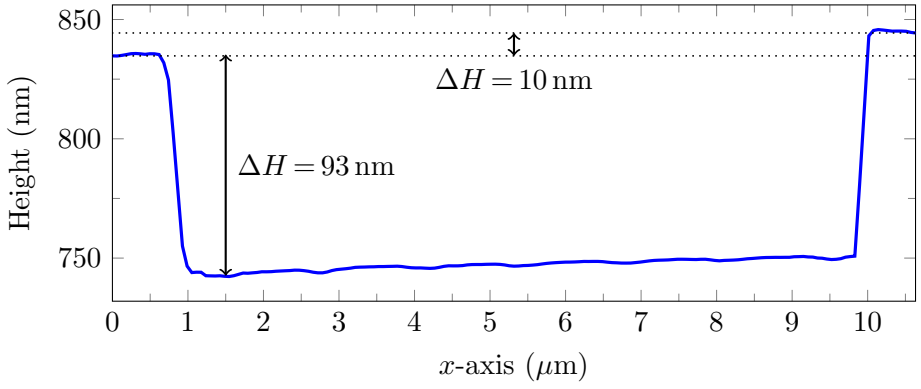

FIGURE 5.6: Height profile along the horizontal H_1 line of figure 5.5.

[10]The used atomic force microscope was a NT-MDT Solver Nano.

Figure 5.7 depicts the height profile along the horizontal H_3 line of figure 5.5 where the seven EM resonators are clearly distinguishable.

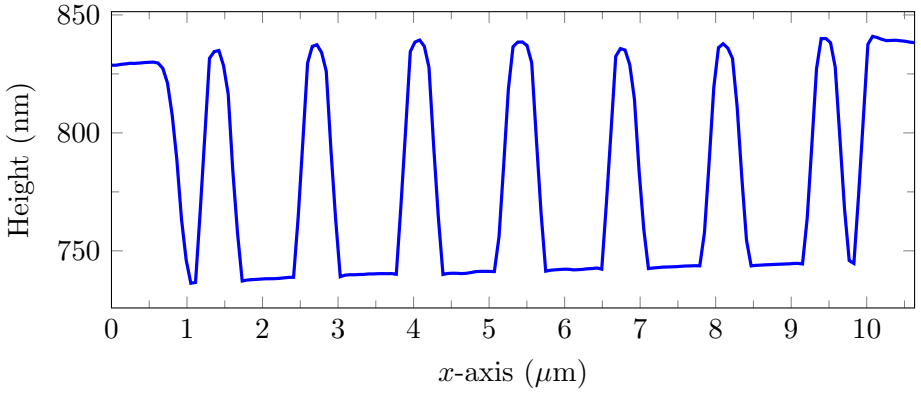

FIGURE 5.7: Height profile along the horizontal H_3 line of figure 5.5.

Figure 5.8 depicts the height profile along the horizontal H_2 line of figure 5.5, where rather than correct the sample's tilt a dashed line joining the first points of the unit device anchors has been added for comparison. Due to the roughness of the deposited chromium layer several peaks having a height of a few nanometers appear in the latter profile (characteristic that can be clearly grasp in the SEM image of figure 5.9). Comparing the measured profile along the beam's length with the dashed straight line it can be concluded that the beam is not deflected upwards. Such conclusion verifies the post-fabrication residual stress is tensile rather than compressive.

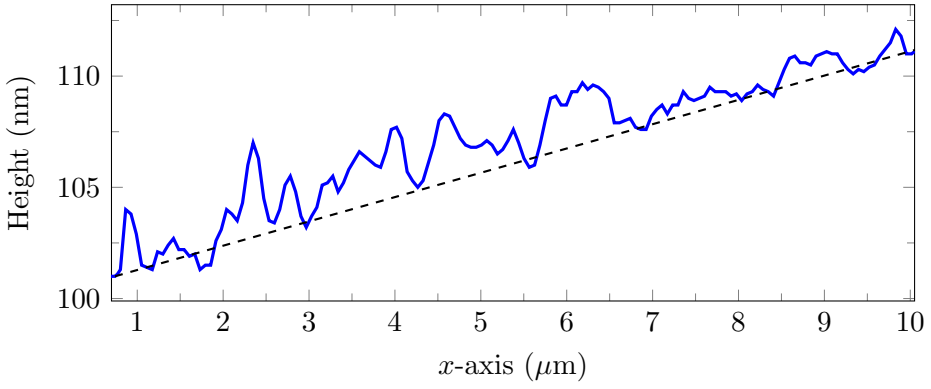

FIGURE 5.8: Height profile along the horizontal H_2 line of figure 5.5. The dashed line joins the first and the last points of the profile, points that correspond to the anchors of the unit device.

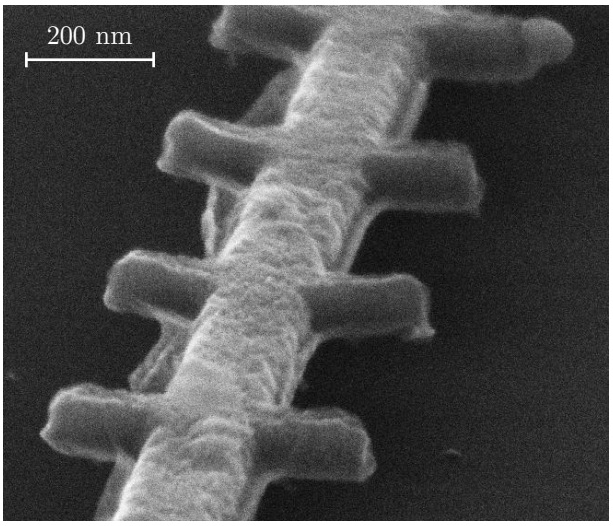

FIGURE 5.9: Detail of a unit device surface where the roughness of the chromium can be appreciated.

The conclusion that can be extracted from the fabricated samples is that the deposited chromium layer has a residual tensile stress. Consequently, the characterization process aimed to obtained the value the imperfection level of the fabricated OPACMEMES devices can not be applied. Such consequence does not imply that the fabricated devices can not auto-oscillate. However and from the modeling point of view, a clamped-clamped imperfect beam having a residual tensile stress would not start to deflect thanks to the thermo-mechanical coupling mechanism until the restraining compressive axial load (F_θ in (3.47)) compensates the axial load produced by the residual tensile stress ($\sigma_r A$ in (3.47)). Or in other words, when in equation (3.63) $P_0 = 0$ (i.e., when $\mathcal{C}_3 = -\mathcal{C}_4 \hat{T}_{l.e}$ being $\mathcal{C}_3 < 0$). Consequently, the absorbance value would be constant until this event happens; eliminating the possibility to establish any relationship between the irradiance and the deflection of the beam. Figure 5.10 depicts the evolution of the maximum equilibrium deflection of a clamped-clamped imperfect beam having a tensile residual stress with the irradiance. At $I_{rr} = I_{rr.c}$ the thermally induced compressive stress compensates the residual tensile stress and the thermo-mechanical coupling mechanism appears.

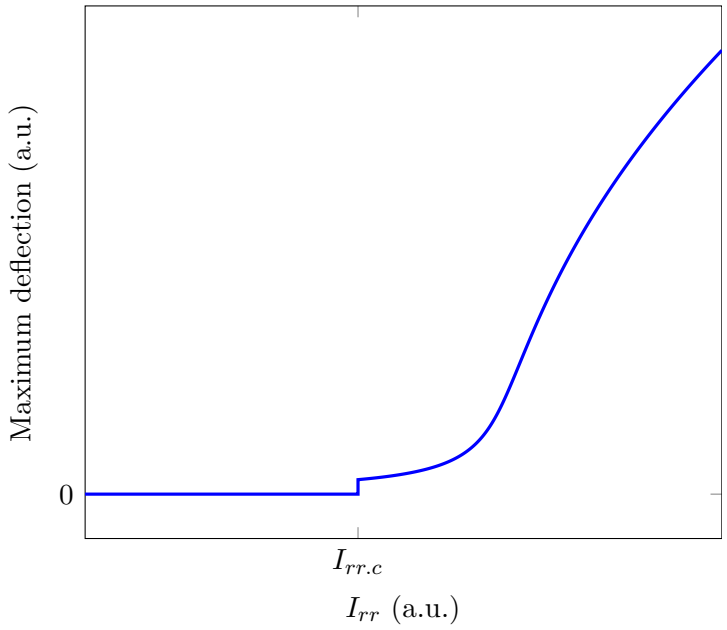

FIGURE 5.10: Bifurcation diagram: evolution of the maximum equilibrium deflection of a clamped-clamped imperfect beam having a residual tensils stress and an imperfection level $\delta_0 \neq 0$ with the irradiance.

5.3 Residual stress in thin films

Beneficial or not, almost all deposited thin films have a residual net stress σ_r as a consequence of either external or internal sources [80].

The most well-known and common extrinsic stress is due to the mismatch in the thermal expansion coefficient between the film and the substrate where it is begin deposited. A thermal stress is developed in a film/substrate composite structure when subjected to a uniform temperature change. The two different materials are going to suffer different amounts of either contraction or expansion due to this temperature variation. However and since the substrate is very thick compared to the film, it can be assumed that the thin film will suffer the same thermal contraction or expansion as the substrate. Thus and neglecting the Poisson effect, the thermal stress in the thin film can be expressed using linear thermoelasticity as the difference between the substrate stress and the stress that the beam would

suffer if it was not attached to the substrate,

$$\sigma_{r.th} = E\left(\alpha_{th.s} - \alpha_{th.f}\right)\Delta T \tag{5.1}$$

where E is the Young's modulus of the film, $\alpha_{th.s}$ the thermal expansion coefficient of the substrate, $\alpha_{th.s}$ the thermal expansion coefficient of the film and ΔT the temperature change. Since the thin film is deposited on the thick substrate at an elevated temperature and subsequently cooled at ambient temperature, the ΔT parameter will always be positive.

Following the stress sign convention adopted in chapter 3 (i.e., a positive stress is compressive and a negative stress is tensile) if $\alpha_{th.s} > \alpha_{th.f}$ a compressive stress will be developed in the thin film, on the contrary if $\alpha_{th.s} < \alpha_{th.f}$ it will be tensile. Therefore and taking into account the coefficients of thermal expansion included in table 4.2, it can be concluded that the thermal stress developed in the structural layer of the OPACMEMS devices will be always tensile.

On the other hand, intrinsic stress reflects the internal structure of a material during its deposition. Therefore, its value depends upon the deposition rate and temperature, the pressure in the deposition chamber, the incorporation of foreign atoms, the grain structure of the deposited film, etc. Intrinsic stresses are analytically difficult to model because they are less clearly understood than extrinsic stresses, that is why they are often studied by performing experimental measurements [81–83].

The net residual stress σ_r of a thin film is a result of both the extrinsic and intrinsic stresses. The fabrication of suspended clamped-clamped beams made directly out of a deposited thin film can be used to measure its local residual stress. As soon as the structures are released the stress will be relaxed. If the stress is compressive the beam will suffer a deflection which could be later measured (as explained in section 3.3.1, the beam can be deflected even though the residual stress is lower than the buckling stress. Notice that in this case the beam will be simply deflected, not buckled). In contrast, a tensile stress is more difficult to be relaxed and that is

why other structures must be used in order to measure their local post-fabrication stress [84, 85].

Measurements of the fabricated PoC OPACMEMS devices lead to the conclusion that a residual tensile stress had developed in the deposited chromium layer. However, the value of such stress can not be measured using the fabricated structures. Evaporated chromium films of about a few tens of nanometers have been measured to exhibit residual tensile stress of between 1 and 2 GPa [86]. Assuming that fabricated structures have a similar residual stress value, the equilibrium temperature at which the unit devices would have to be heated to compensate such stress can be compute using linear thermoelasticity as

$$T_e = \frac{\sigma_r}{E\alpha_{th}} \tag{5.2}$$

If the above equation is evaluated using the chromium properties (i.e., $E = 279\,\text{GPa}$ and $\alpha_{th} = 4.9{\cdot}10^{-6}\,\text{K}^{-1}$) and assuming that the residual stress is $\sigma_r = 1.5\,\text{GPa}$, it yields an equilibrium temperature of 1097 K (or 823.85 °C). Using equation (3.37) with the proper adimensionalization and assuming that the absorbance of the PoC devices is maximum (i.e., $\hat{\mathcal{A}} = 0.55$ as shown in figure 4.8), it can be computed that the irradiance needed to induce the previously computed equilibrium temperature would be $I_{rr.c,} = 3.74{\cdot}10^{7}\,W/m^2$. The experimental measurements presented in section 6.3.4 demonstrate that such irradiance can not be attained using the assembled characterization setup.

5.4 Summary

In this chapter the OPACMEMS devices fabrication process has been presented. Several unsuccessfully fabricated devices were used to point out and enhance some of the fabrication steps. Applying the necessary changes, various chips were processed with the aim to obtain the proof-of-concept devices designed and analyzed in chapter 4. One of the assumptions made in chapter 3 during the modeling of these devices was that their structural layer had a residual compressive stress.

However, in this chapter it has been found that the chromium layer had a residual tensile stress. Although such characteristic does not necessarily imply that the devices could not auto-oscillate, it though implies that the self-oscillation state would be harder to achieve. From the modeling point of view, the aforementioned characteristic introduces a discontinuity in the developed opto-thermo-mechanical model. Once the point of discontinuity has been achieved, the proposed model can be used to theoretically analyze the behavior of the devices.

Chapter 6

Optical characterization setup

In this chapter the optical setup assembled with the aim to characterize the designed OPACMEMS devices is presented. The various elements forming the system are described and their purpose explained. Finally, several experimental measurements that demonstrate the capabilities of the assembled setup are included and analyzed.

6.1 Setup description

The movement of the OPACMEMS devices is induced by the incidence of infrared light upon them. Given their micro/nano dimensions, detecting such movement represents a challenge that can be achieved by using capacitive, piezoresistive, piezoelectric or optical sensing techniques. While the latter technique can be implemented both inside and outside of the device's chip, the other ones must be partially implemented in the same chip. The particularities of an in-chip sensing technique must be taken into account during the device's fabrication. The PoC OPACMEMS devices fabrication process described in chapter 5 was designed without the aim to incorporate an in-chip sensing technique. Consequently, an optical detection scheme is the only option left to be able to characterize the fabricated devices.

The commercially available optical components can be classified by their working wavelength range (where their specifications are met). The visible (400-700 nm), near-infrared (NIR, 700-1100 nm) and infrared (IR, 1100-1600 nm) are the most used spectral regions for the design of optical characterization setups. Since the OPACMEMS devices must be perpendicularly illuminated with infrared light at $\lambda_0 = 1.55\,\mu$m, a laser source with this particular wavelength must be added in the setup's design. Given the above mentioned spectral regions, three schemes were contemplated during the design process of the whole optical setup. The differences between them lie in the detection technique:

- Two IR lasers scheme: the second laser is used to detect the motion of the device. Since both lasers shine light at the same spectral region, their optical path could be shared. A photodetector is used to capture the light reflected from the sample's surface.
  - Advantages: the setup only has one optical path and the light used to detect the motion has a different wavelength that the one used to excite it.
  - Disadvantages: two laser sources and their respectively controllers are needed. An undesired excitation of the device's EM resonators can also be produced by the second laser beam.
- One IR and one visible laser scheme: the visible laser (e.g., HeNe $\lambda_0 = 632.8$ nm) is used to detect the motion of the device by obliquely focusing its beam on the sample surface in the same way as in an AFM. A position sensing detector (PSD) would be used to capture the light reflected from the sample's surface.
  - Advantages: the light used to detect the motion has a different wavelength that the one used to excite it. The device's EM resonators can not be excited by the second laser beam. The detection technique is very well-known and widely used.

  - Disadvantages: the setup has two optical paths. Two laser sources and their respectively controllers are needed.

- One IR laser scheme: the same laser is used to excite the EM resonators and to read the motion of the device. A photodetector is used to capture the light reflected from the sample's surface.

  - Advantages: only one laser source is needed. The optical components can be specifically designed for light with $\lambda_0 = 1.55\,\mu$m.

  - Disadvantages: none a priori.

Given the pros and cons of the above mentioned schemes and the available budget, the third option was chosen. Figures 6.1 and 6.2 respectively show a diagram and a picture of the final designed and assembled setup. Details of the most important vacuum, optical and electrical components of the assembled setup can be find in appendix C.

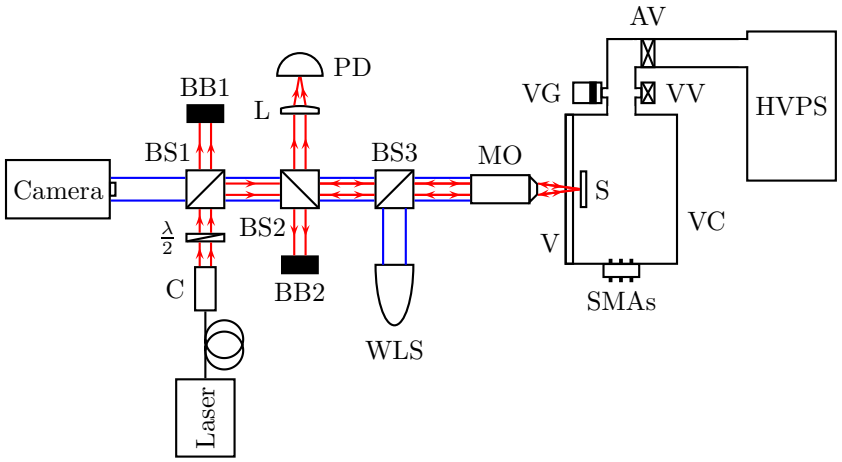

FIGURE 6.1: Diagram of the characterization setup including vacuum, optical and electrical components. Used terminology: BB = beam blocker, BS = beamsplitter, C = collimator, L = lens , PD = photodetector, MO = microscope objective, WLS = white light source, V = viewport, S = sample, VC = vacuum chamber, VG = vacuum gauge, VV = venting valve, AV = angle valve, HVPS = high vacuum pumping station and SMAs = SMA feedthroughs.

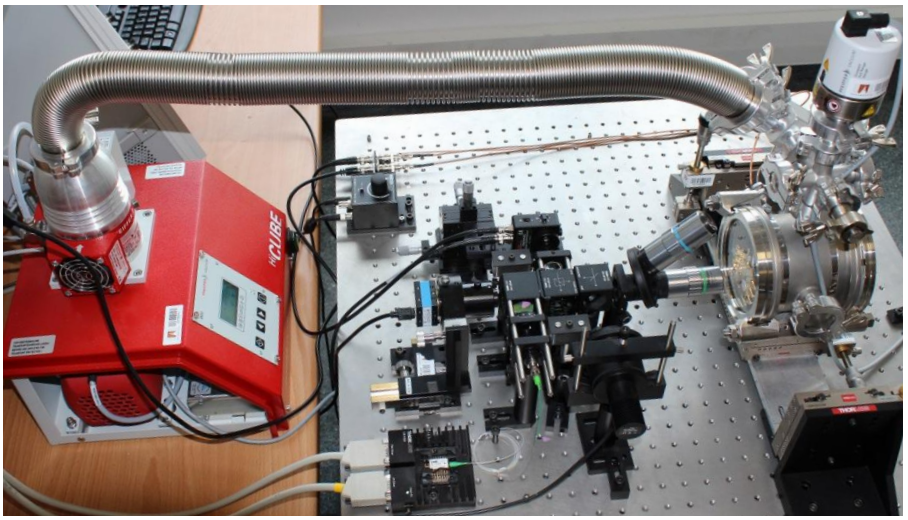

FIGURE 6.2: Picture of the characterization setup including vacuum, optical and electrical components.

6.1.1 Vacuum system

The sample chip (S) is placed in a vacuum chamber (VC) capable of being pumped to pressures below $1{\cdot}10^{-7}$ mbar. Such low pressure ensures that the motion of the to be measured nano/microdevices is not damped by the surrounding gases (i.e., the device dissipation is in the intrinsic regime, where the mechanical losses are due to other effects rather than because of the squeeze film damping effect [87]). The sample is situated near a viewport (V) through which it is illuminated. This optical window is round (diameter = 104 mm and thickness = 8 mm) and made of borosilicate glass, which has an ~82 % transmission at $\lambda_0 = 1.55\,\mu$m. The vacuum pressure is achieved using a high vacuum pumping station (HVPS) consisting of an air cooled turbomolecular pump backed by a dry diaphragm one, both operated through a control unit and connected to the chamber via a highly flexible corrugated hose. The pressure level is monitored using a vacuum gauge (VG) with two heads (Pirani and cold cathode) connected to the control unit. A venting valve (VV) is used to break the vacuum before opening the chamber. In order to isolate the pumping station from the rest of the vacuum elements an angle valve (AV) is mounted at the end of the corrugated hose. Electrical connectivity with the sample can be achieved by using the three female-female SMA feedthroughs

(SMAs) embedded into one of the lateral faces of the chamber. Since the position of the laser spot can not be modified, the vacuum chamber is mounted on top of a custom XYZ-axis translation platform that allows the positioning of the sample under characterization. Sub-micron resolution on the chamber displacements are achieved using the platform's manual fine micrometer drives.

6.1.2 Optical system

The laser illumination of the devices is performed by an infrared ($\lambda_0 = 1.55\,\mu$m) single-frequency laser diode operating with a continuous wave. The laser package contains an integrated thermoelectric cooler, a thermistor and an optical isolator with a polarization maintaining output fiber. While the isolator prevents unwanted feedback into the laser diode, the fiber preserves the linear polarization state of the generated laser beam. The diode's output optical power can be precisely adjusted by controlling the operating current and temperature (the maximum achievable power is obtained when the diode's forward voltage is 1.8 V). A triplet fiber collimator (C) is connected at the end of the laser's fiber to produce a nearly gaussian collimated beam. Since the EM response of the OPACMEMS devices depends on the polarization of the incident EMR, a zero-order half-wave plate ($\lambda_0/2$) is mounted right after the collimator and used to conveniently rotate the beam's polarization state. A 70:30 (reflection:transmission ratio) non-polarizing cube beamsplitter (BS1) is used to introduce a CMOS camera to the optical path while reflecting the laser beam towards the vacuum chamber. A beam blocker (BB1) safely absorbs the 30 % of the beam's power transmitted through this beamsplitter. A second non-polarizing cube beampslitter (BS2) with a ratio of 50:50 is mounted so that the device's reflected laser light reaches an InGaAs photodetector (PD) through a best form spherical lens (L). Another beam blocker (BB2) is used to absorb the unused laser beam's reflected energy. A pellicle beamsplitter (BS3) with a ratio of 8:92 is used to add a collimated white light beam from a LED source (WLS) to the optical path so that the camera can correctly acquire the sample's image. Finally, the direct beam is focused onto the sample using a long working distance

microscope objective (MO). Several objectives with different magnification and numerical aperture values can be mounted on a turret, hence being able to modify the spot's laser size and the magnification of the camera's image.

In order to reduce undesired reflections the collimator, the waveplate, the cube beamsplitters and the lens have an antireflective (AR) coating specially designed for wavelengths between 1.1 and 1.6 μm. In contrast, the pellicle beamsplitter is uncoated and the microscope objective is not optimized to work at infrared frequencies.

All the optical components are mounted in a 30 mm cage system for an easy alignment of the free-space optical components. In addition, the camera and the photodetector are mounted on an XYZ translation stage for their precise positioning. In order to reduce mechanical vibrations coming from the floor the entire characterization setup, except the pumping station, is mounted on an optical table with passive air isolators.

6.1.3 Instrumentation

Several electronic apparatus are connected to the optoelectronic devices of the assembled setup. The CMOS camera is connected to a computer through an USB port from which the digital image is processed by a specific software. The laser diode package is connected to a dual current/temperature controller. While the former is used to provide a precise and stable current to the diode, the latter integrates a PID controller which is linked to both the thermistor sensor and the thermoelectric cooler actuator. This dual controller is connected to the computer via USB in order to control it for unassisted measurements.

Finally, the instrument connected to the photodetector's output depends on how the device is being driven into motion:

- Case 1: the device vibrates without the need of an external excitation source. Then, the frequency content of the photodetector's output is analyzed on an

Agilent E4404B frequency spectrum analyzer and the sample is fixed in the vacuum chamber without any connection. Thus, the measured spectrum magnitude is directly proportional to the generated photocurrent.

- Case 2: the device's motion is forced by and external excitation source powered by an electric signal. In this case, the sample needs to be connected to that source through a SMA feedthrough. To be able to measure the device's response as a function of the electrical excitation the photodetector's output is analyzed on an Agilent E5100A or an Agilent E5061B network analyzer which tracking output is used to excite the device. With this measuring scheme, the magnitude and the phase of the mechanical response with respect to the exciting signal can be obtained.

Both the network and spectrum analyzers are connected to a computer through USB or GPIB with the aim to perform unassisted measurements and acquire the measured data.

6.2 Detection principles

The assembled optical setup was designed to characterize devices having dynamic out-of-plane deflections (i.e., parallel to the laser beam propagation direction). Moreover, it is also capable of measuring dynamic in-plane deflections (i.e., perpendicular to the laser beam propagation direction). The out-of-plane detection principle is based on the interference between a reference beam and a beam reflected on the moving device, whereas the in-plane one is based on the so-called knife-edge modulation of the laser's spot intensity. The ultimate consequence of both methods is the modulation of the EM power received by the photodetector as a function of the device's vibration.

The top section of figure 6.3 illustrates part of the diagram shown in figure 6.1, where the beamsplitter BS3 and the microscope objective MO have been omitted for clarity. Additionally, the bottom section illustrates the cross-sectional and

aerial views of a sample composed by a suspended micro/nanomechanical beam. The optical beams that play a key role on the interferometric detection principle of the time dependent out-of-plane vibration of the mechanical beam (represented by $w(t)$) are also sketched. The analysis of the knife-edge technique used to detect the in-plane vibration of the mechanical beam (represented by $v(t)$) require to take into account that the intensity of the optical beam has a Gaussian distribution.

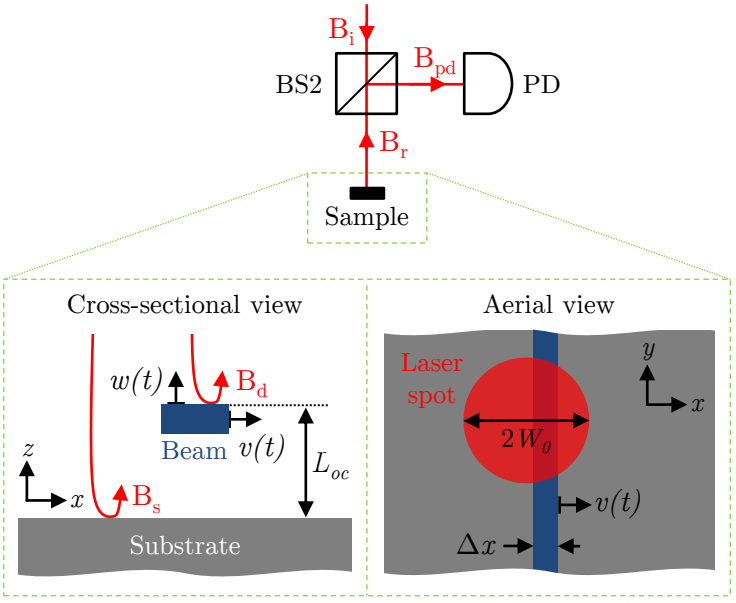

FIGURE 6.3: Cross-sectional and aerial views of a suspended M/NEMS beam in the sample position of the assembled setup.

Considering that the incident beam (B_i) is a linearly polarized EM plane wave whose wavefronts are infinite parallel planes of Gaussian amplitude E_{0ig}, the time-domain expression for the real value of its electric field can be described by[1]

$$\begin{aligned}\vec{\mathcal{E}}_i(x,y,z,t) &= \mathfrak{Re}\left\{\tilde{\vec{E}}_i(x,y,z)e^{j\omega t}\right\} = \hat{x}\,\mathfrak{Re}\Big\{E_{0ig}(x,y)e^{j\omega t+kz}\Big\} \\ &= \hat{x}\,\mathfrak{Re}\left\{E_{0i}e^{-\frac{x^2+y^2}{W_0^2}}e^{j(\omega t+kz)}\right\} : x\in(-\infty,\infty); y\in(-\infty,\infty)\end{aligned} \tag{6.1}$$

where ω and k are the angular frequency an wavenumber of the field, and W_0 is the spot radius of the Gaussian profile.

[1]Notice that equation (6.1) uses a simplification of the complex exponential form of the actual expression for the electric field of a Gaussian beam (D.7). Such simplification is considered to be valid if the distance between the M/NEMS and the substrate is smaller than the Rayleigh range of the incident Gaussian beam, see equation (D.10) for its definition.

Therefore and considering that the optical transmission through the mechanical beam can be neglected, the time-domain expressions for the real value of the electric field of the substrate (B_s) and device (B_d) beams towards the beamsplitter BS2 can be expressed as

$$\begin{aligned}\vec{\mathcal{E}}_s(x,y,z,t) &= \mathfrak{Re}\left\{\tilde{\vec{E}}_s(x,y,z)e^{j\omega t}\right\} = \hat{x}\,\mathfrak{Re}\Big\{E_{0sg}(x,y)e^{j(\omega t-kz)}\Big\} \\ &= \hat{x}\,\mathfrak{Re}\left\{E_{0s}e^{-\frac{x^2+y^2}{W_0^2}}e^{j(\omega t-kz)}\right\} \\ &: x \in \big(-\infty, x_1+v(t)\big)\cup\big(x_2+v(t),\infty\big); y\in(-\infty,\infty)\end{aligned} \tag{6.2}$$

$$\begin{aligned}\vec{\mathcal{E}}_d(x,y,z,t) &= \mathfrak{Re}\left\{\tilde{\vec{E}}_d(x,y,z)e^{j\omega t}\right\} = \hat{x}\,\mathfrak{Re}\Big\{E_{0dg}(x,y)e^{j(\omega t-kz)}\Big\} \\ &= \hat{x}\,\mathfrak{Re}\left\{E_{0d}e^{-\frac{x^2+y^2}{W_0^2}}e^{j(\omega t-kz)}\right\} \\ &: x \in \big[x_1+v(t), x_2+v(t)\big]; y\in(-\infty,\infty)\end{aligned} \tag{6.3}$$

where the x-axis static points (i.e., when $v(t)=0$) where the mechanical beam starts and ends are respectively denoted as x_1 and x_2 (thus, in figure 6.3: $\Delta x = x_2 - x_1$). It can be considered that $E_{0s}=\Gamma_s E_{0i}$ and $E_{0d}=\Gamma_d E_{0i}$, being Γ_s a proportionality factor that accounts for the reflectivity of the beamsplitter BS2, the scattering effects on the substrate, the transmittance of the substrate and the EM energy absorption of the substrate material; whereas Γ_s accounts for reflectivity of the beamsplitter BS2, the scattering effects on the device and the EM energy absorption of the device material.

The electric field of the reflected beam (B_r) at a certain point z_r along its propagation direction is the outcome of the superposition of (6.2) and (6.3); that is,

$$\begin{aligned}\vec{\mathcal{E}}_r(x,y,z=z_r,t) &= \mathfrak{Re}\left\{\tilde{\vec{E}}_r(x,y,z=z_r)e^{j\omega t}\right\} \\ &= \vec{\mathcal{E}}_s(z=z_s)+\vec{\mathcal{E}}_d\big[z=z_d-w\big] \\ &= \mathfrak{Re}\left\{\left(\tilde{\vec{E}}_s(z=z_s)+\tilde{\vec{E}}_d[z=z_d-w]\right)e^{j\omega t}\right\} \\ &= \hat{x}\,\mathfrak{Re}\left\{\left(E_{0sg}e^{-jkz_s}+E_{0dg}e^{-jk(z_d-2w)}\right)e^{j\omega t}\right\}\end{aligned} \tag{6.4}$$

where the static (i.e., when $w(t)=0$) optical path traveled by the substrate and

device beams at the point $z = z_r$ are respectively denoted as z_s and z_d. The cross-sectional view of figure 6.3 illustrates that $z_s = z_d + 2L_{oc}$, being L_{oc} the optical cavity length (which depends upon the out-of-plane vibration of the mechanical beam $w(t)$).

A photodetector measures light in terms of EM power over its active area. Such detectors can not measure the instantaneous oscillating power (to track the changes at a frequency of ω would require extremely fast responses), what they actually measure is the time-average electromagnetic energy flow of the incident EM field over many of its cycles. Therefore, the incident light can be seen as an irradiance being proportional to the square of the electric field amplitude (i.e, see (2.24)). The irradiance of the reflected beam is given by

$$\begin{aligned} I_{rr.r}(x,y,t) &= \frac{\tilde{\vec{E}}_r \tilde{\vec{E}}_r^*}{2\eta_0} = \frac{1}{2\eta_0}\left(\tilde{\vec{E}}_s + \tilde{\vec{E}}_d\right)\left(\tilde{\vec{E}}_s^* + \tilde{\vec{E}}_d^*\right) \\ &= \frac{1}{2\eta_0}\left(\tilde{\vec{E}}_s\tilde{\vec{E}}_s^* + \tilde{\vec{E}}_d\tilde{\vec{E}}_d^* + \tilde{\vec{E}}_s\tilde{\vec{E}}_d^* + \tilde{\vec{E}}_d\tilde{\vec{E}}_s^*\right) \\ &= \frac{1}{2\eta_0}\left\{E_{0sg}^2 + E_{0dg}^2 + 2E_{0sg}E_{0dg}\cos\left[k\left(\Delta z_{sd} + 2w\right)\right]\right\} \\ &= I_{rr.s} + I_{rr.d} + 2\sqrt{I_{rr.s}}\sqrt{I_{rr.d}}\cos\left[k\left(\Delta z_{sd} + 2w\right)\right]\Big\} \end{aligned} \tag{6.5}$$

, where $\Delta z_{sd} = (z_s - z_d)$ is the static optical path difference and

$$I_{rr.s}(x,y) = \frac{1}{2\eta_0}E_{0sg}^2 \tag{6.6}$$

$$I_{rr.d}(x,y) = \frac{1}{2\eta_0}E_{0dg}^2 \tag{6.7}$$

Equation (6.5) can also be expressed in terms of the total power over the involved areas at the xy-plane of the M/NEMS; that is,

$$P_{EM.r}\left[w(t), v(t)\right] = P_{EM.s} + P_{EM.d} + 2\sqrt{P_{EM.s}}\sqrt{P_{EM.d}}\cos\left[k\left(\Delta z_{sd} + 2w\right)\right] \tag{6.8}$$

where the total optical power carried by each beam is the integral of its irradiance,

$$\begin{aligned} P_{EM.s}\big[v(t)\big] &= \int_{-\infty}^{\infty}\int_{-\infty}^{x_1+v} I_{rr.s}\,dx\,dy + \int_{-\infty}^{\infty}\int_{x_2+v}^{\infty} I_{rr.s}\,dx\,dy \\ &= \frac{E_{0s}^2}{2\eta_0}\int_{-\infty}^{\infty} e^{\frac{-2y^2}{W_0^2}}\,dy\left(\int_{-\infty}^{x_1+v} e^{\frac{-2x^2}{W_0^2}}\,dx + \int_{x_2+v}^{\infty} e^{\frac{-2x^2}{W_0^2}}\,dx\right) \end{aligned} \tag{6.9}$$

$$P_{EM.d}\big[v(t)\big] = \int_{-\infty}^{\infty}\int_{x_1+v}^{x_2+v} I_{rr.d}\,dx\,dy = \frac{E_{0d}^2}{2\eta_0}\int_{-\infty}^{\infty} e^{\frac{-2y^2}{W_0^2}}\,dy\int_{x_1+v}^{x_2+v} e^{\frac{-2x^2}{W_0^2}}\,dx \tag{6.10}$$

Taking into account that

$$\int_{l_1}^{l_2} e^{\frac{-2x^2}{W_0^2}}\,dx = \sqrt{\frac{\pi}{8}}W_0\left[\operatorname{erf}\left(\frac{\sqrt{2}}{W_0}l_2\right) - \operatorname{erf}\left(\frac{\sqrt{2}}{W_0}l_1\right)\right] \tag{6.11}$$

, the integrals present in (6.9) and (6.10) can be explicitly computed or expressed using the error function

$$\int_{-\infty}^{\infty} e^{\frac{-2y^2}{W_0^2}}\,dy = \sqrt{\frac{\pi}{2}}W_0 \tag{6.12}$$

$$\int_{-\infty}^{x_1+v} e^{\frac{-2x^2}{W_0^2}}\,dx = \sqrt{\frac{\pi}{8}}W_0\left\{1 + \operatorname{erf}\left[\frac{\sqrt{2}(x_1+v)}{W_0}\right]\right\} \tag{6.13}$$

$$\int_{x_2+v}^{\infty} e^{\frac{-2x^2}{W_0^2}}\,dx = \sqrt{\frac{\pi}{8}}W_0\left\{1 - \operatorname{erf}\left[\frac{\sqrt{2}(x_2+v)}{W_0}\right]\right\} \tag{6.14}$$

$$\int_{x_1+v}^{x_2+v} e^{\frac{-2x^2}{W_0^2}}\,dx = \sqrt{\frac{\pi}{8}}W_0\left\{\operatorname{erf}\left[\frac{\sqrt{2}(x_2+v)}{W_0}\right] - \operatorname{erf}\left[\frac{\sqrt{2}(x_1+v)}{W_0}\right]\right\} \tag{6.15}$$

The xy-plane at the photodetector's position can be considered to be the same as the xy-plane at the sample position due to the effect of the microscope objective MO and the lens L (see figure 6.1). Taking into account that the photodetector's active area is big enough to capture all the light focalized by the lens L, its photocurrent can be expressed as

$$i_{pd}\big[w(t), v(t)\big] = \mathfrak{R}_{pd}\mathcal{R}_{BS2}P_{EM.r} \tag{6.16}$$

,where $\mathcal{R}_{BS2}$ is the reflectivity of the beamsplitter BS2 (i.e., $\mathcal{R}_{BS2} = 0.5$) and $\mathfrak{R}_{pd}$ the photodetector's responsitivity.

Since the photodetector's output current is proportional to the reflected beam's EM power the temporal evolution and the frequency content of this photocurrent will depend on both the in-plane and out-of-plane vibrations of the M/NEMS.

6.2.1 Study of the static reflected EM power

As an example, figure 6.4 shows the evolution of $P_{EM.r}$ for $L_{oc} = {}^{3\lambda_0}/_{8}$ (being λ_0 the wavelength of the laser) as the x-axis static position of the mechanical beam with respect to the laser spot center is swept. Both in-plane and out-of-plane vibrations are set to zero (i.e., $v = 0$ and $w = 0$).

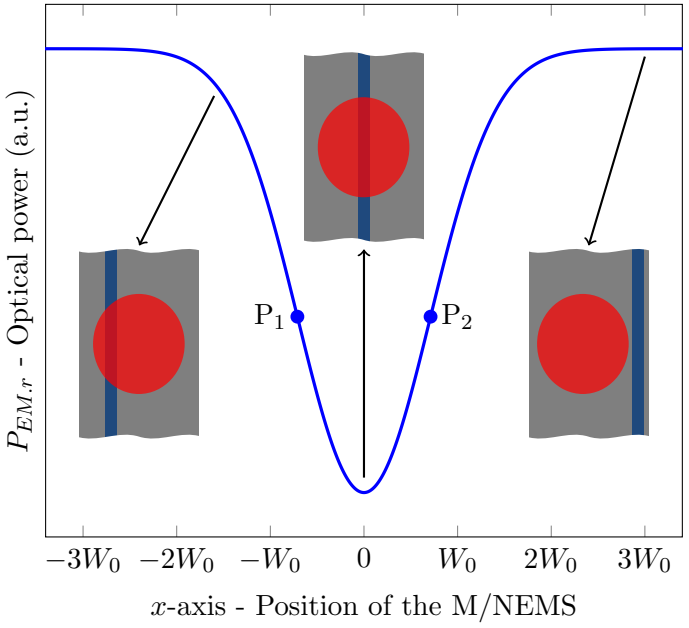

FIGURE 6.4: Reflected beam's EM power as a function of the mechanical beam's static position with respect to the laser spot center. The P_1 and P_2 circles represent the points where the second derivative is zero.

As an example, figure 6.5 shows the evolution of $P_{EM.r}$ when the x-axis static position of the mechanical beam with respect to the laser spot center is fixed at the point P_2 of figure 6.4 as the value of the optical cavity length L_{oc} is swept. Both in-plane and out-of-plane vibrations are set to zero (i.e., $w = 0$ and $w = 0$).

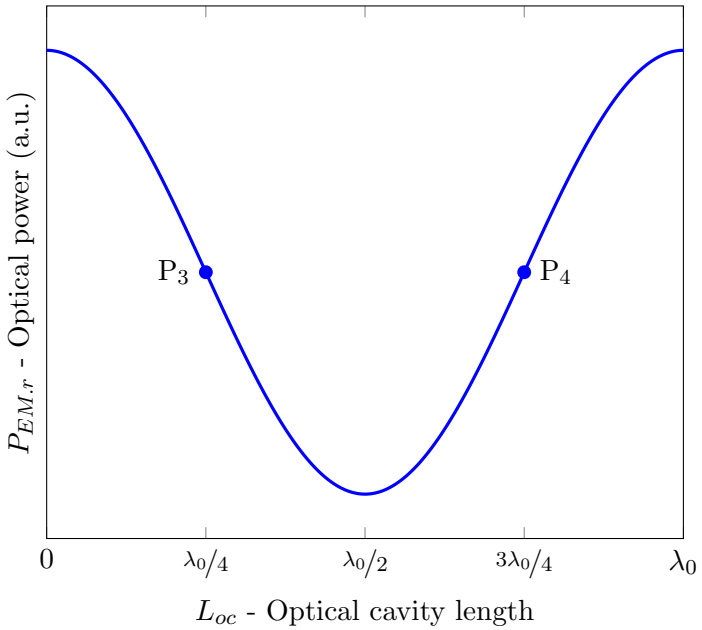

FIGURE 6.5: Reflected beam's EM power as a function of the optical cavity length for the P_2 mechanical beam's static position with respect to the laser spot center. The P_3 and P_4 circles represent the points where the second derivative is zero.

While the shape of figure 6.4 is due to the Gaussian distribution of the incident beam irradiance, the shape of figure 6.5 is due to the cosine interference term dependence of equation (6.8).

6.2.2 Study of the dynamic reflected EM power

Figure 6.6 shows the evolution of the peak-to-peak amplitude of the reflected beam's modulated EM power as the amplitude of the mechanical beam's in-plane sinusoidal vibration is swept (i.e., $v = A_v \sin(2\pi f_m t)$, where f_m is the frequency of oscillation). In the latter figure the static cavity length is $L_{oc} = 3\lambda_0/8$ and the x-axis static position of the mechanical beam is fixed at the same value for the point P_2 of figure 6.4 while the out-of-plane vibration is set to zero (i.e., $w = 0$).

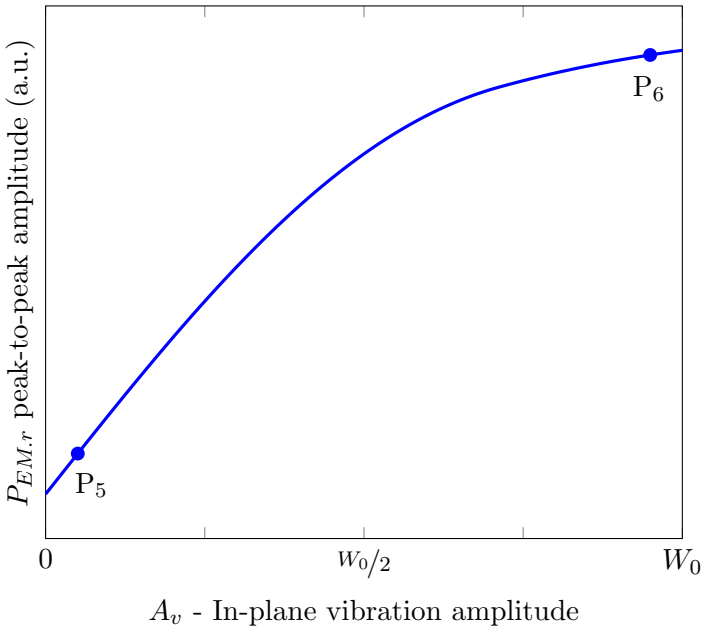

FIGURE 6.6: Peak-to-peak amplitude of the reflected beam's modulated EM power as a function mechanical beam's amplitude in-plane sinusoidal vibration.

In the above figure it can be graphically seen that the in-plane detection mechanism is inherently nonlinear. However, the response of the detection mechanism can be considered to be linear if the M/NEMS in-plane vibration amplitude is small enough and around the P_1 or P_2 static positions marked in figure 6.4. Figures 6.7 and 6.8 respectively show the temporal and frequency spectrum responses at the points P_5 and P_6 of figure 6.6. Notice that the DC component of depicted spectrums has been deleted for clarity. While the first figure represents an harmonic function, the second one is composed of several harmonics due to the nonlinearity of the in-plane vibration detection mechanism.

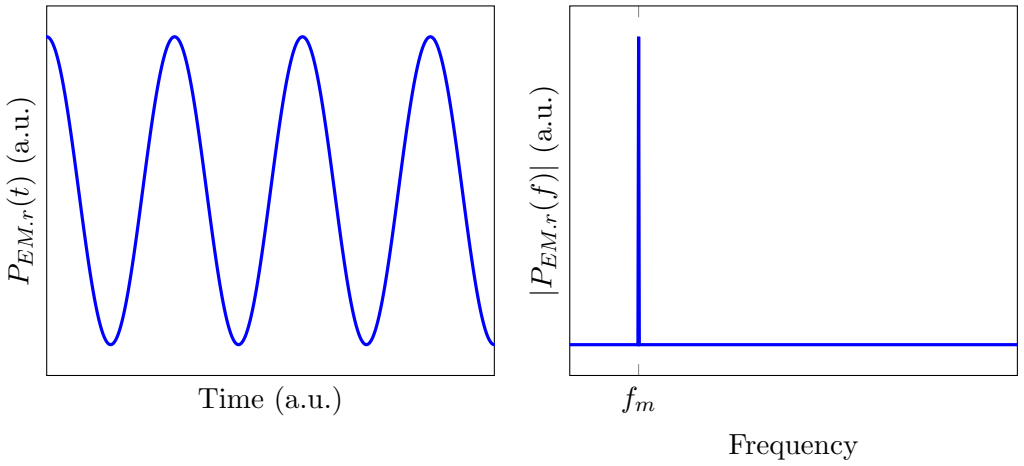

(A) Temporal response.

(B) Frequency spectrum of figure 6.7a.

FIGURE 6.7: Temporal response at the point P_5 of figure 6.6 and its frequency spectrum.

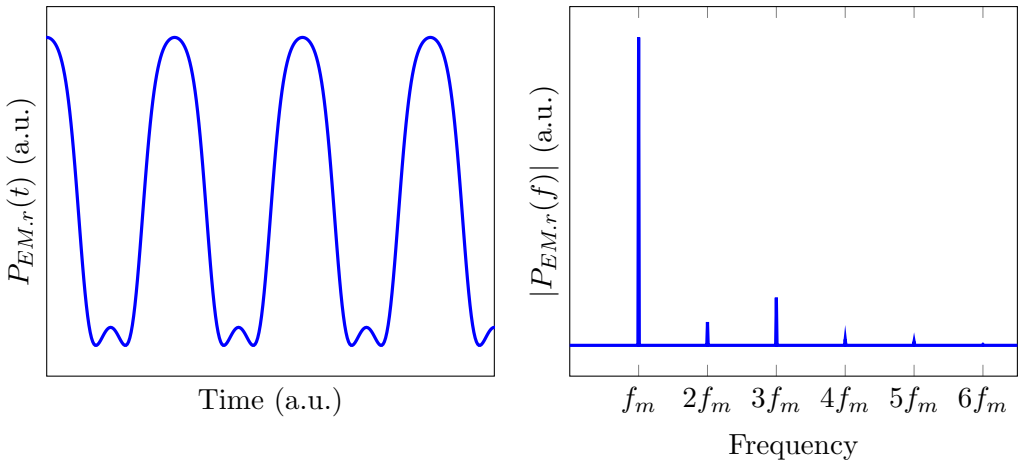

(A) Temporal response.

(B) Frequency spectrum of figure 6.8a.

FIGURE 6.8: Temporal response at the point P_6 of figure 6.6 and its frequency spectrum.

Figure 6.9 shows the evolution of the peak-to-peak amplitude of the reflected beam's modulated EM power as the amplitude of the mechanical beam's out-of-plane sinusoidal vibration is swept (i.e., $w = A_w \sin(2\pi f_m t)$, where f_m is the frequency of oscillation). In the latter figure the static cavity length is set at the point P_3 of figure 6.5 (i.e., $L_{oc} = \lambda_0/4$) and the x-axis static position of the mechanical beam is fixed at the point P_2 of figure 6.4 while the in-plane vibration is set to zero (i.e., $v = 0$).

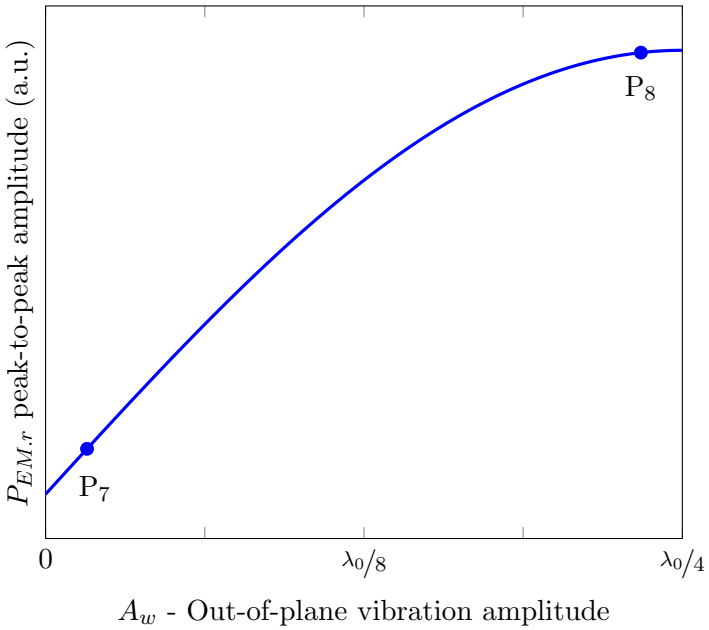

FIGURE 6.9: Peak-to-peak amplitude of the reflected beam's modulated EM power as a function of the mechanical beam's amplitude out-of-plane sinusoidal vibration. Static gap: $\lambda_0/4$.

In the above figure it can be graphically seen that the out-of-plane detection mechanism is inherently nonlinear. However, the response of the detection mechanism can be considered to be linear if the M/NEMS out-of-plane vibration amplitude is small enough and around the P_3 or P_4 static positions marked in figure 6.5. Figures 6.10 and 6.11 respectively show the temporal and frequency spectrum responses at the points P_7 and P_8 of figure 6.9. Notice that the DC component of depicted spectrums has been deleted for clarity. While the first figure represents an harmonic function, the second one is composed of several harmonics due to the nonlinearity of the out-of-plane vibration detection mechanism.

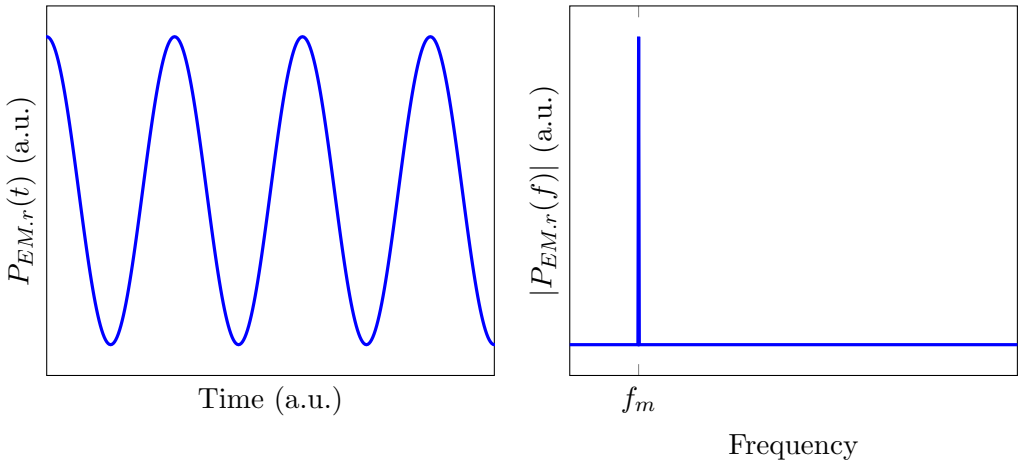

(A) Temporal response.

(B) Frequency spectrum of figure 6.10a.

FIGURE 6.10: Temporal response at the point P_7 of figure 6.9 and its frequency spectrum.

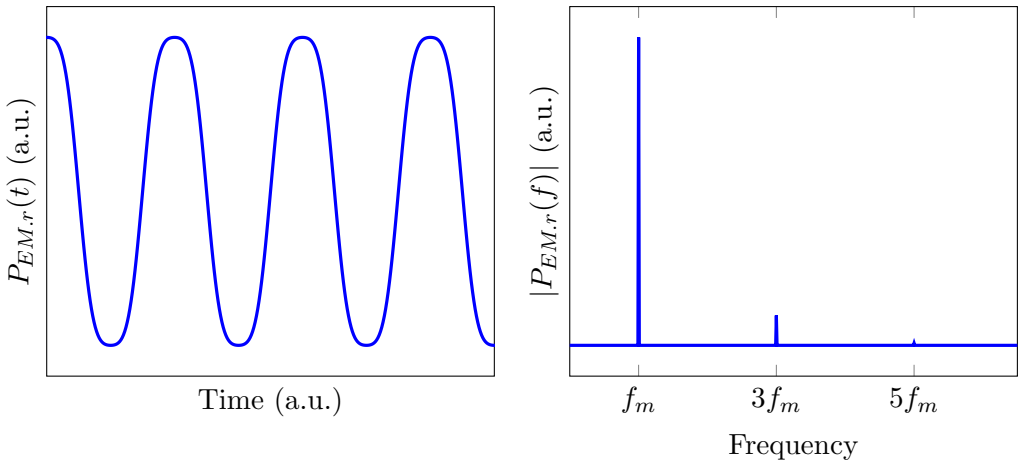

(A) Temporal response.

(B) Frequency spectrum of figure 6.11a.

FIGURE 6.11: Temporal response at the point P_8 of figure 6.9 and its frequency spectrum.

6.3 Experimental procedures

6.3.1 Laser beam alignment

Infrared light with a wavelength of 1.55 μm can not be directly seen by either the human eye or using common digital (CMOS or CCD) cameras. Therefore,

infrared fluorescing alignment disks are used to visualize the laser spot and help on its positioning. The alignment procedure is as follows:

- Step 1: a PCB containing both the sample and an IR fluorescing disk (⌀ 1.3 cm) is fixed in the vacuum chamber using a custom holder, see figure 6.12.

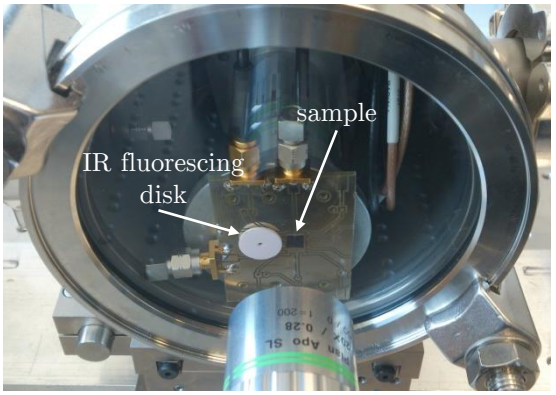

FIGURE 6.12: Picture of a PCB ready to perform the IR laser beam alignment.

- Step 2: the infrared laser is turned on and pointed to the alignment disk so its fluorescent light can be seen in the optical image acquired by the camera.
- Step 3: the camera's image is properly focused adjusting the vacuum chamber's Y-axis translation platform.
- Step 4: the camera's position is adjusted in order to locate the laser spot in the center of the image.
- Step 5: the position of the vacuum chamber is modified till the device under test (DUT) is at the center of the image.

After performing these steps the laser spot will be focused on the device and the characterization measurements can be carried out.

6.3.2 Setting the polarization state of the infrared beam

The EM response of the designed fishbone unit cell (see figure 4.1) depends on the polarization state of the illuminating light. The best EM response (i.e., the EM

resonance of the nanostrip) is obtained when the polarization is linear with the electric field vibrating along the long axis of the nanostrip. Taking into account the position of the sample within the characterization setup and that incidence of the laser beam is normal to the sample surface, the P and S polarization states are respectively defined as parallel and perpendicular to this plane as shown in figure 6.13. Consequently, fixing a device based on the fishbone unit cell with the long axis of the nanostrips parallel to the optical table imposes that the illuminating beam must have a P-polarization state in order to obtain the best device response.

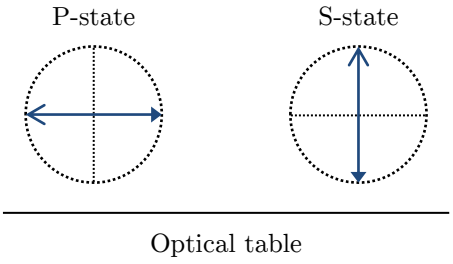

FIGURE 6.13: Representation of the P and S polarization states in the optical characterization setup. The lines with double ended arrows represent the linear oscillations of the infrared beam electric field.

The laser diode output beam polarization state is linear, characteristic that is preserved at the output after the polarization maintaining fiber. However, the angle of the transmitted beam polarization state can be modified by rotating the waveplate's fast axis. Since the rest of the optical elements of the optical path are non-polarizing, the beam that reaches the sample has the previously set polarization state.

The connector at the end of the laser fiber is aligned to the slow polarization axis, so the output light will be polarized perpendicular to the connector axis. Therefore, the collimator is mounted so that the fast polarization axis is set parallel to the optical table. Hence, setting the collimator output light as P-polarized. If the fast axis of the waveplate is set parallel to the optical table, the beam will maintain its P-polarized state without any phase change. Whereas if it is set perpendicular to the optical table, the beam's polarization state will suffer a 180 º

phase change. Nevertheless, both situations result in a transmitted beam with a P-polarized state. On the contrary, if the fast axis of the waveplate is rotated 45 ° counterclockwise from either of these two positions, the transmitted beam will suffer a 90 ° or a -90 ° change in its polarization state's angle. Thus, establishing the transmitted beam as S-polarized. Figure 6.14 shows a representation of the previously described polarization state cases. Rotating the waveplate's fast axis between 0 ° and 45 ° will consequently lead in a transmitted beam with a linear polarization state angle equal to two times this rotation.

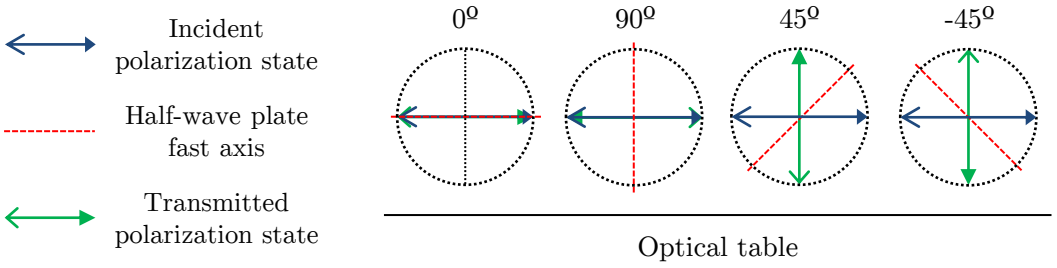

FIGURE 6.14: Representation of the incident and transmitted beam polarization state for four half-wave plate fast axis angles. The double ended arrows represents the linear oscillations of the infrared beam electric field.

6.3.3 Power of illumination

The laser beam reaches the sample with an optical power substantially attenuated due to the various optical elements in its path. A germanium power sensor (Thorlabs S122C & PM100USB) is used to quantitatively characterize the beam optical power. Figure 6.15 shows the measured power after the waveplate as a function of the laser diode forward current[2] for two polarization states. Whereas figure 6.16 shows the power values at the sample position for three different configurations of the microscope objective.

[2]For this configuration and due to the measurement range of the power sensor (50 nW - 50 mW), the maximum applicable current is 320 mA.

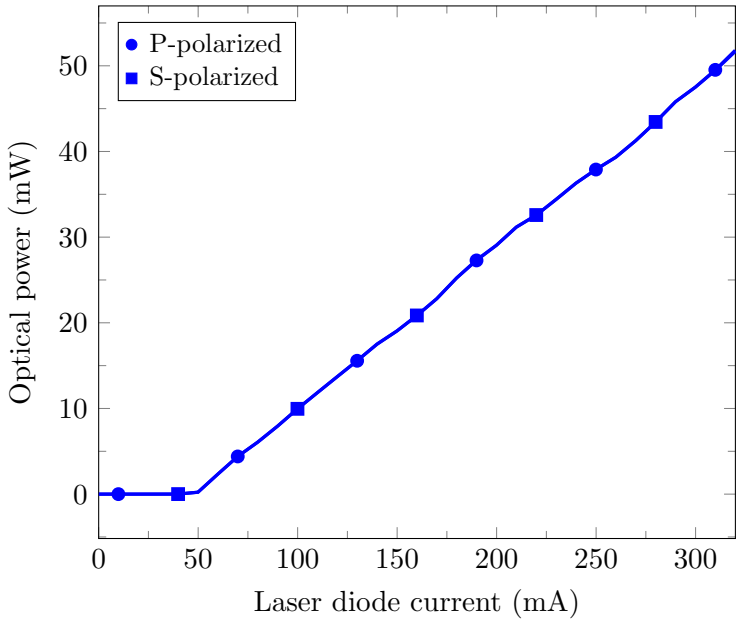

FIGURE 6.15: Optical power measured after the half-wave plate as a function of the laser diode current. Laser temperature = 26 °C.

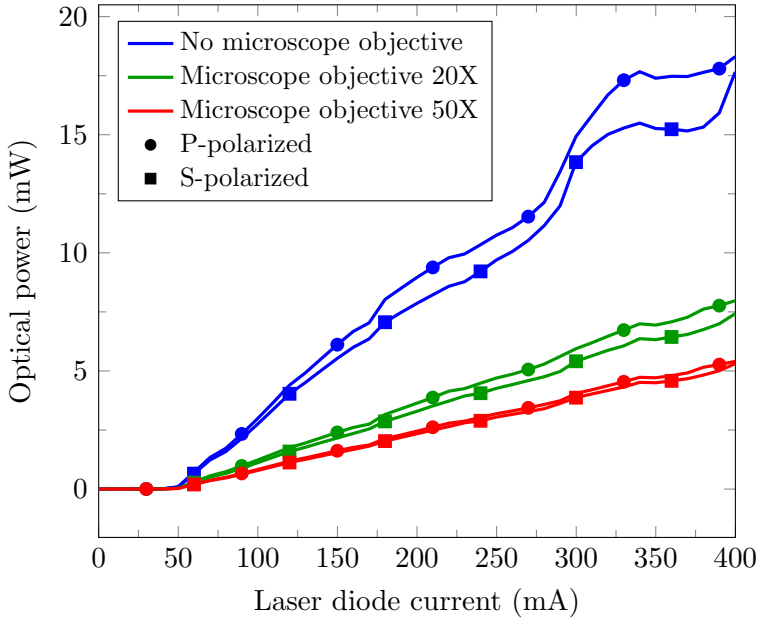

FIGURE 6.16: Optical power as a function of the laser diode current at the sample position. Laser temperature = 26 °C.

Observing figure 6.16 it can be seen that for the case of the P-polarization state the power values are always slightly higher than for the S case. When analyzing this observation for the case of no microscope objective, the power differences can be unequivocally associated with the polarization dependent transmission and

reflection coefficients of the used beamsplitters. Although being considered non-polarizing, their split ratios are lightly dependent on the polarization of the incident light (within 15 % depending on the wavelength). Incident P-polarized light at $\lambda_0 = 1.55\,\mu$m is reflected by BS1 and transmitted by BS2 and BS3 with greater ratios than when it is S-polarized.

When a microscope objective is included in the optical path the overall behavior of the optical components still benefits the P-polarized light besides the substantial attenuation of the optical power.

6.3.4 Laser beam irradiance

The area illuminated by the infrared laser is a key parameter of the assembled setup since the illumination of the OPACMEMS devices does not only provide a way to read their motion but also to excite it. If the illuminated area A_T and the power of a plane wavefront $P_{EM.T}$ are known, its irradiance can be computed as (see (2.25))

$$I_{rr} = \frac{P_{EM.T}}{A_T} \tag{6.17}$$

Assuming that the setup's infrared laser beam can be considered to have a plane wavefront at the beam waist location[3], the latter equation can be used if laser's illuminated area is somehow computed (as shown in figure 6.16, the EM power reaching the sample is a known parameter). One way to compute this area is by knowing the beam spot radius r_w at the sample, then it can be approached that

$$A_T \approx A_{spot} = \pi r_w^2 \tag{6.18}$$

Notice that when using equation (6.17) in combination with (6.18) the Gaussian profile of the beam intensity is neglected inasmuch as the EM power is assumed to be uniformly distributed over the spot area. Actually, the beam irradiance falling on the circle defined by the spot radius is about 86% of the total.

[3]The demonstration that such assumption is true can be found in section D.1.2 of appendix D.

The spot size of the laser beam was computed both theoretically and experimentally[4]. However, the theoretical results were found to be not accurate enough due to the fact that the used microscope objectives are designed and optimized to work with the visible frequency spectrum of light. Therefore, table 6.1 only reproduces the experimental results.

	r_w (μm)	A_{spot} (μm^2)
MO_{20X}	≈ 27.5	$2.376 \cdot 10^3$
MO_{50X}	≈ 14	$0.616 \cdot 10^3$

TABLE 6.1: Spot sizes measured experimentally and their corresponding areas for both microscope objectives used in the assembled setup.

The area values shown in table 6.1 need to be taken into account when designing the OPACMEMS devices inasmuch that all the unit devices (see figure 4.5) must be illuminated by the laser spot. Therefore, the designed devices must be fit in an area equal or lower than the corresponding A_{spot} value.

6.4 Setup validation: characterization of a microcantilever

In this section the characterization results of a microcantilever are presented with the aim to show the functionality of the assembled setup. Since this device do not include any EM resonators, the shined infrared light is only used to detect its motion.

The silicon cantilever beam with a rectangular cross section shown in the SEM image of figure 6.17 was designed to be electrostatically actuated (i.e., capacitive

[4]In appendix D the reader can find a description of both the theoretical background and the experimental procedure.

actuation) and read through its lateral electrodes. Three contact pads were fabricated for the necessary connections, one for each of the electrodes and another for the cantilever. In order to interconnect the device chip with a custom PCB with SMA connectors, the device pads were wedge bonded to the corresponding copper tracks. The PCB was then loaded into the setup's vacuum chamber where the SMA feedthroughs were used to have external electric access.

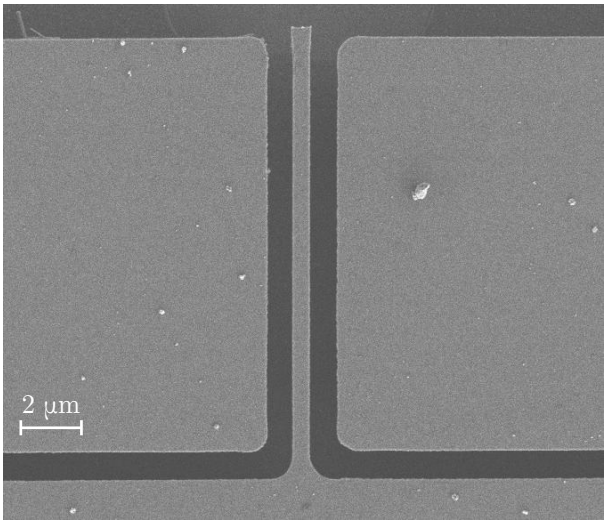

FIGURE 6.17: SEM image of the characterized cantilever with rectangular cross section. Dimensions (length × width × thickness): $15 \times 0.56 \times 1\,\mu\text{m}^3$. Gap beneath the microbeam: $1\,\mu\text{m} \approx 0.64\lambda_0$. Gap from the microbeam to each of the electrodes: 850 nm.

Figure 6.18 shows the cantilever's normalized frequency response when it is electrostatically actuated and optically measured. As it can be seen, two peaks corresponding to the first in-plane and out-of-plane resonances are measured. Figures 6.19 and 6.20 show a detail of these resonances. The measurements were performed using a network analyzer in order to compare the electrical excitation signal fed to the device and the photodetector's output signal.

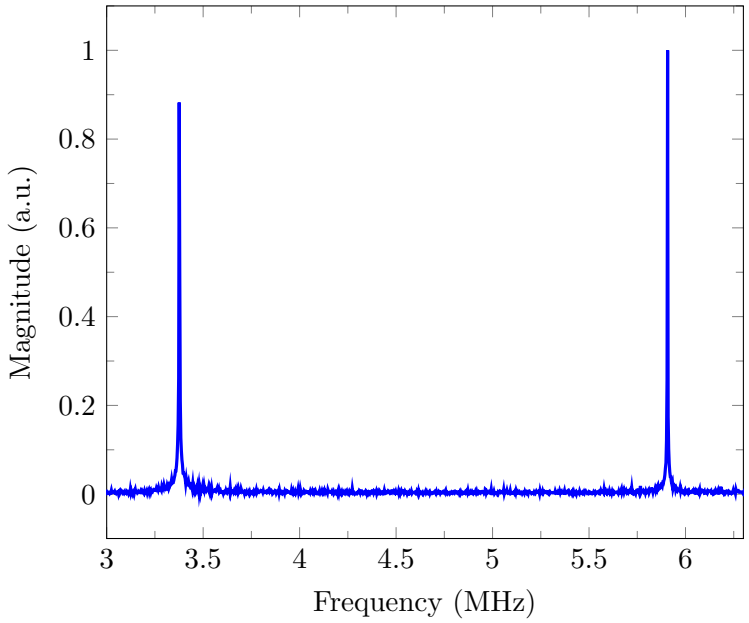

FIGURE 6.18: Mechanical response of an electrostatically driven μcantilever. No averaging performed. Pressure $= 4.6{\cdot}10^{-5}$ mbar.

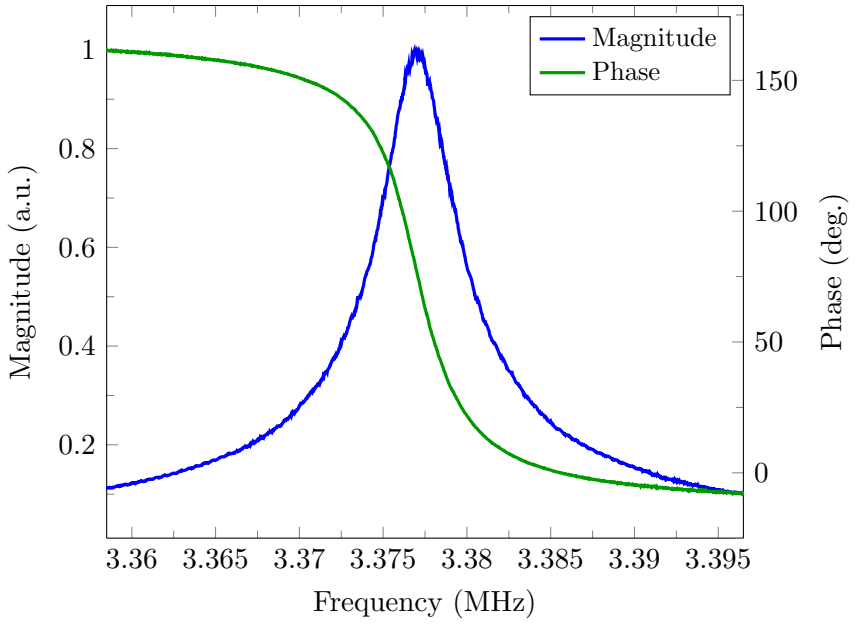

FIGURE 6.19: First in-plane resonance of an electrostatically driven μcantilever. No averaging performed. Pressure $= 4.6{\cdot}10^{-5}$ mbar.

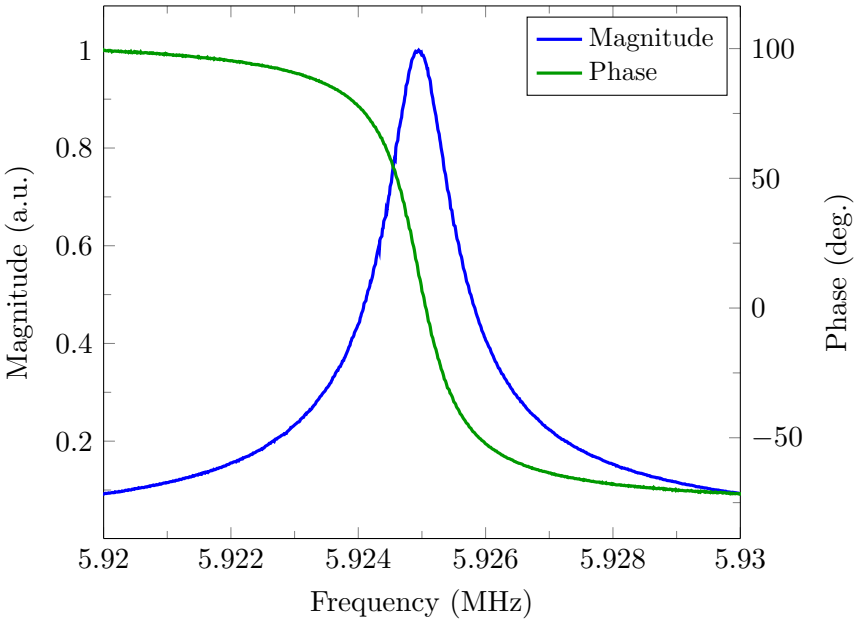

FIGURE 6.20: First out-of-plane resonance of an electrostatically driven μcantilever. No averaging performed. Pressure $= 4.6{\cdot}10^{-5}$ mbar.

In order to verify that the in-plane detection mechanism can be either linear or nonlinear (as theoretically analyzed in section 6.2) the μcantilever was excited[5] at its first in-plane resonance and the following temporal responses were acquired using an oscilloscope:

- The mechanical response shown in figure 6.21 demonstrates that the detection mechanism is linear (see figure 6.7 for comparison).
- Keeping the excitation signal constant (i.e., maintaining the vibration amplitude), the in-plane static position of the cantilever with respect to the laser spot center was modified till the measured signal was the one depicted in 6.22. Notice that rather than increasing the excitation signal (as done in figure 6.6) it is kept constant in order to avoid the combination of nonlinearities due to the mechanical vibration, the electrical actuation and the detection mechanism; hence it can be assured that the nonlinearity of figure 6.22 is due to the detection mechanism (see figure 6.8 for comparison).

[5]The excitation signal was kept at a value for which neither the mechanical nor the electrical nonlinearities were noticeable.

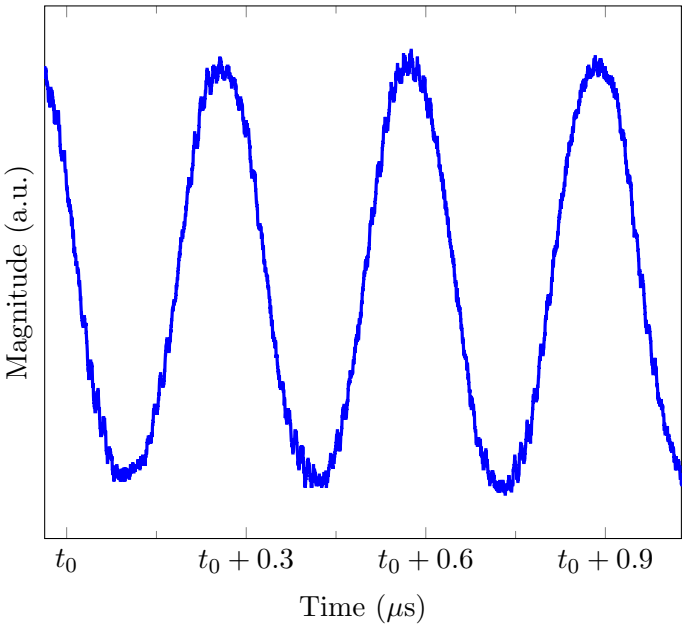

FIGURE 6.21: Temporal response of the μcantilever at its in-plane resonance frequency when the detection mechanism is linear.

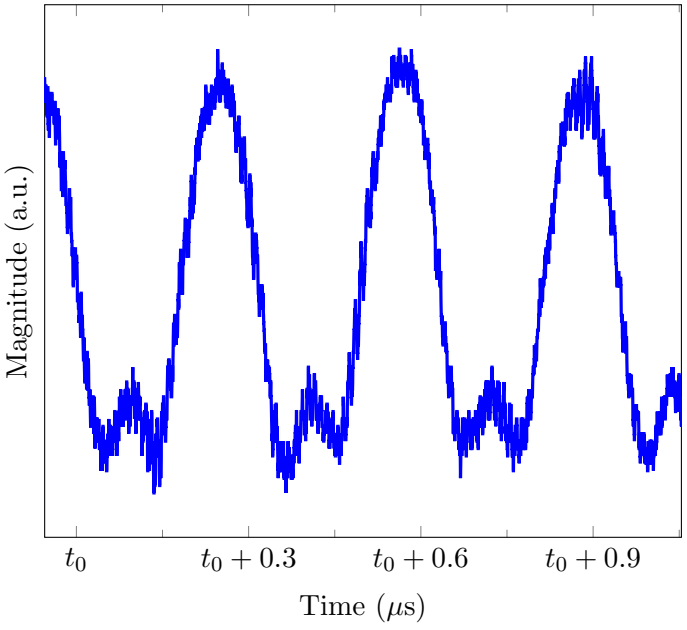

FIGURE 6.22: Temporal response of the μcantilever at its in-plane resonance frequency when the detection mechanism is nonlinear.

Since the gap length of the μcantilever device could not be modified, the nonlinearity of the out-of-plane detection mechanism could not be verified. However, figure 6.23 shows the temporal response of the μcantilever at its out-of-plane resonance frequency; from this data it can assumed that the detection mechanism is linear.

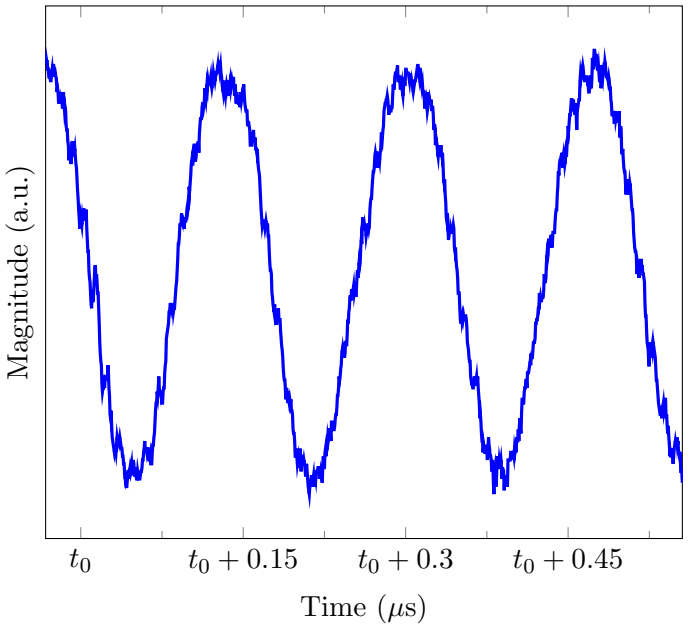

FIGURE 6.23: Temporal response of the μcantilever at its out-of-plane resonance frequency when the detection mechanism is linear.

The results presented in this section demonstrate that the assembled optical characterization setup can be used to measure forced frequency responses of μcantilevers.

6.4.1 Linearity of the detection mechanisms

In this section several measurements are analyzed with the aim to experimentally demonstrate that the optical detection mechanisms can be considered to be linear with the vibration amplitude of the characterized microcantilever. It has to be notice that the linearity of the detection mechanisms depend upon the geometric dimensions of the device. Therefore, the linearity should be studied individually for every different device.

In section 6.2 it was concluded that both out-of-plane and in-plane vibrations can be under certain conditions linearly converted to an electric signal by the photodetector; that is,

$$V_{pd}(t) \propto P_{EM.T}\, w \tag{6.19}$$

$$V_{pd}(t) \propto P_{EM.T}\, v \tag{6.20}$$

where $P_{EM.T}$ is the total EM power of the incident beam and V_{pd} the output voltage of the photodetector's transimpedance amplifier $\Big($i.e., $V_{pd} = i_{pd} G_t \frac{Z_{load}}{Z_{load}+Z_{pd}}$, being G_t the transimpedance gain and Z_{load} and Z_{pd} the impedances of the detection circuit and the photodetector $\Big)$.

Both out-of-plane and in-plane displacement amplitudes of the μcantilever at resonance can be considered to be linear with the amplitude of the applied electrostatic force $F_e(\omega_0)$ (till a certain point where mechanical and electrical nonlinearities will become noticeable) [88],

$$\left|\tilde{w}(\omega_0)\right| = \frac{\left|\tilde{F}_e(\omega_0)\right| Q_f}{m_{eff}\omega_0^2} \tag{6.21}$$

$$\left|\tilde{v}(\omega_0)\right| = \frac{\left|\tilde{F}_e(\omega_0)\right| Q_f}{m_{eff}\omega_0^2} \tag{6.22}$$

where Q_f and m_{eff} are the quality factor and effective mass at the resonance, ω_0.

The electrostatic force of a time harmonic capacitive actuation scheme with dc bias can be written as the sum of a static force $F_{e.dc}$ and time-varying force $F_{e.ac}$,

$$F_e(t) = F_{e.dc} + F_{e.ac}(t) \tag{6.23}$$

The dynamic force is proportional to the applied time-varying voltage [88],

$$F_{e.ac} \propto V_{AC} = V_{ac}\cos(\omega_0 t) \tag{6.24}$$

Therefore, the capacitive actuation ensures that the amplitude of the out-of-plane (6.21) and in-plane (6.22) vibrations are proportional to the amplitude of the applied ac voltage,

$$\left|w_0(\omega_0)\right| \propto V_{ac} \tag{6.25}$$

$$\left|w_0(\omega_0)\right| \propto V_{ac} \tag{6.26}$$

To demonstrate the linearity of the detection mechanisms two types of analysis can be performed using the μcantilever:

- Analysis 1 - Linearity between V_{pd} and the vibration amplitude: at a constant infrared optical power the amplitude of the electrostatic actuation force is gradually increased by changing the RF amplitude V_{ac} while the photodetector's voltage at the μcantilever resonant frequency is tracked.

- Analysis 2 - Linearity between V_{pd} and the optical power $P_{EM.T}$: at a constant vibration amplitude (accomplished by fixing the amplitude of the electrostatic actuation force) the infrared optical power is gradually increased by changing the laser diode current while the photodetector's voltage at the μcantilever resonant frequency is tracked.

All of the following measurements were done at atmospheric pressure.

Figure 6.24 shows several resonance curves of the μcantilever first out-of-plane mode for different RF excitation amplitudes when performing the linearity analysis 1. From figure 6.25 it can be seen that the photodetector signal amplitude peak increases linearly with the amplitude of the RF excitation signal, thereby establishing that for the applied out-of-plane vibrations $V_{pd} \propto w$.

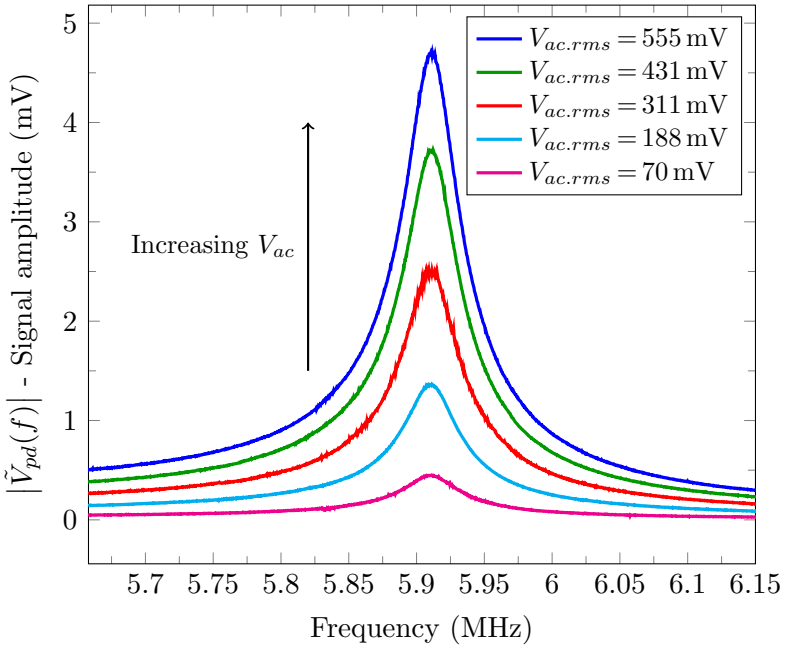

FIGURE 6.24: Several resonance curves of the μcantilever first out-of-plane mode for different RF excitation amplitudes.

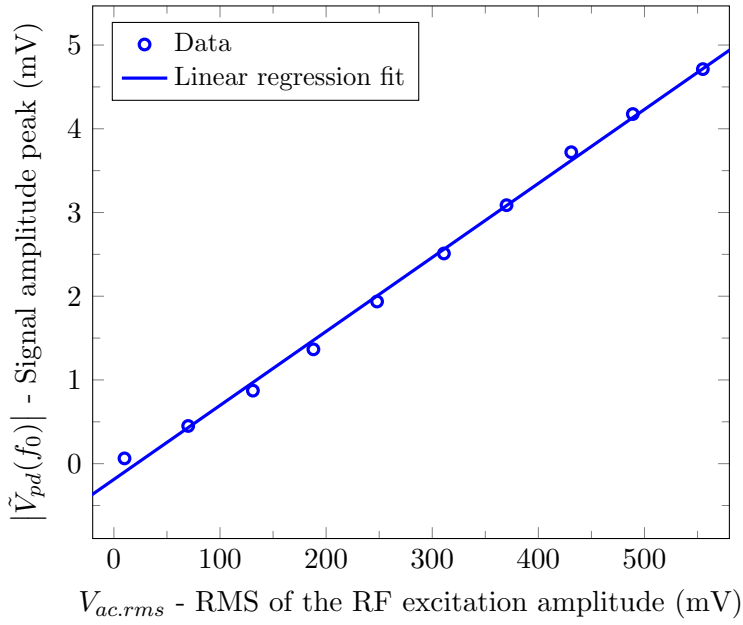

FIGURE 6.25: Photodetector signal amplitude peak vs. the amplitude of the RF excitation for the μcantilever first out-of-plane mode.

Figure 6.26 shows that when the linearity analysis 2 is performed the photodetector signal amplitude peak increases linearly with the infrared laser EM power, thereby establishing that for the applied out-of-plane vibrations $V_{pd} \propto P_{EM.T}$.

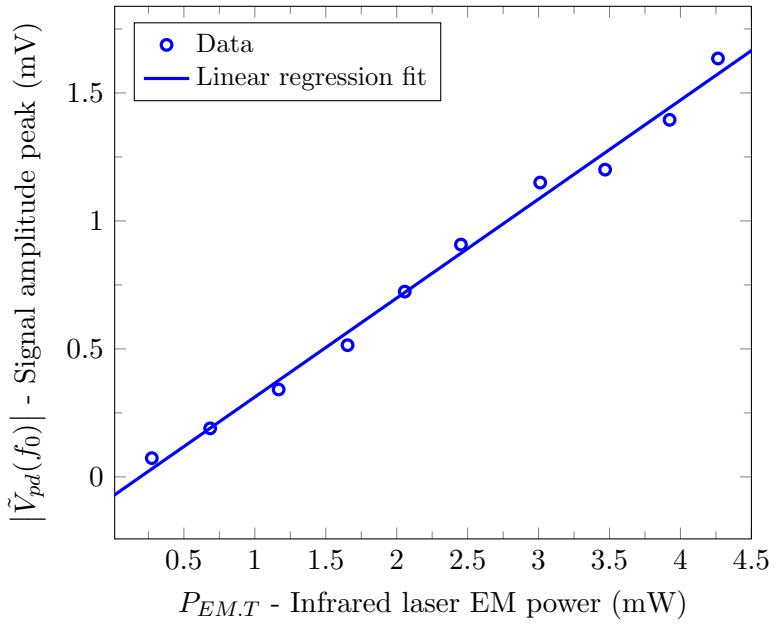

FIGURE 6.26: Photodetector signal amplitude peak vs. the infrared laser EM power for the μcantilever first out-of-plane mode.

Figure 6.27 shows that when the linearity analysis 1 is performed the photodetector signal amplitude peak increases linearly with the amplitude of the RF excitation signal, thereby establishing that for the applied in-plane vibrations $V_{pd} \propto v$.

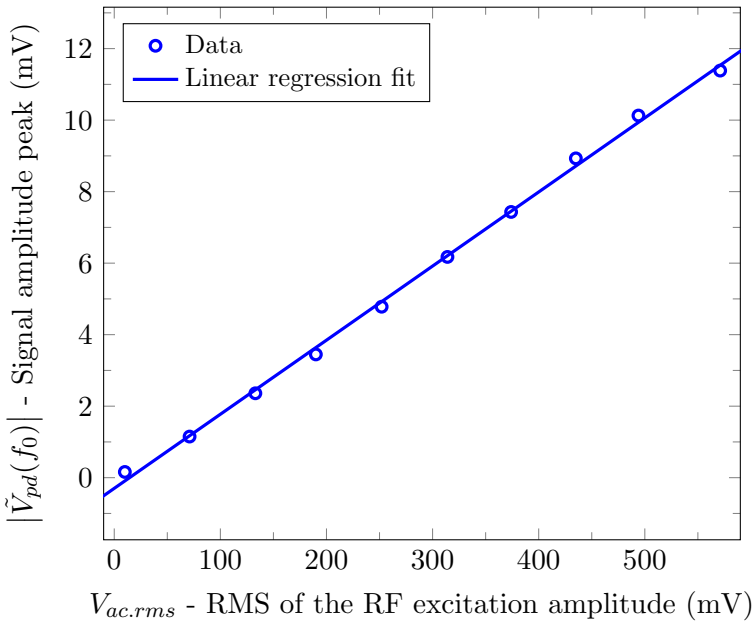

FIGURE 6.27: Photodetector signal amplitude peak vs. the amplitude of the RF excitation for the μcantilever first in-plane mode.

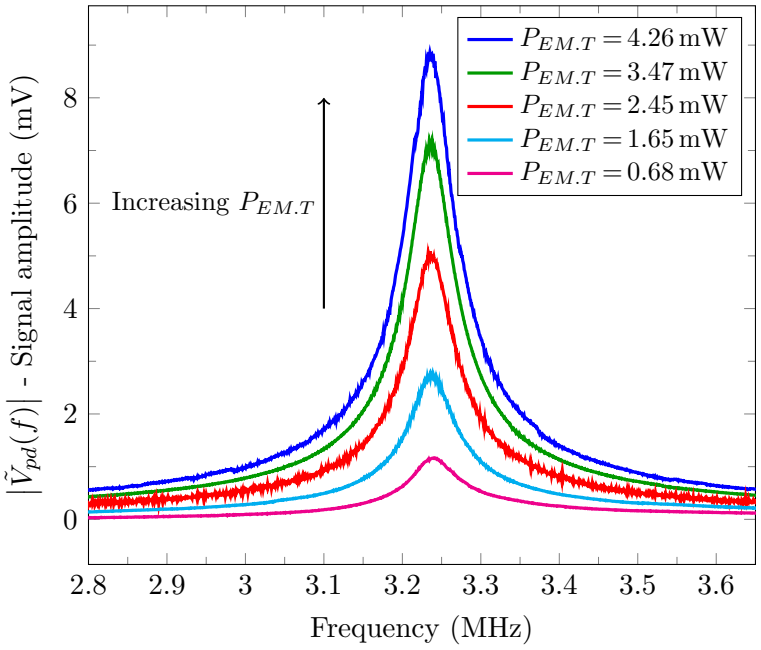

FIGURE 6.28: Several resonance curves of the μcantilever first in-plane mode for different infrared laser EM powers.

Figure 6.28 shows several resonance curves of the μcantilever first in-plane mode for different infrared laser EM power when performing the linearity analysis 2. From figure 6.29 it can be seen that the photodetector signal amplitude peak increases linearly with the infrared laser EM power, thereby establishing that for the applied in-plane vibrations $V_{pd} \propto P_{EM.T}$.

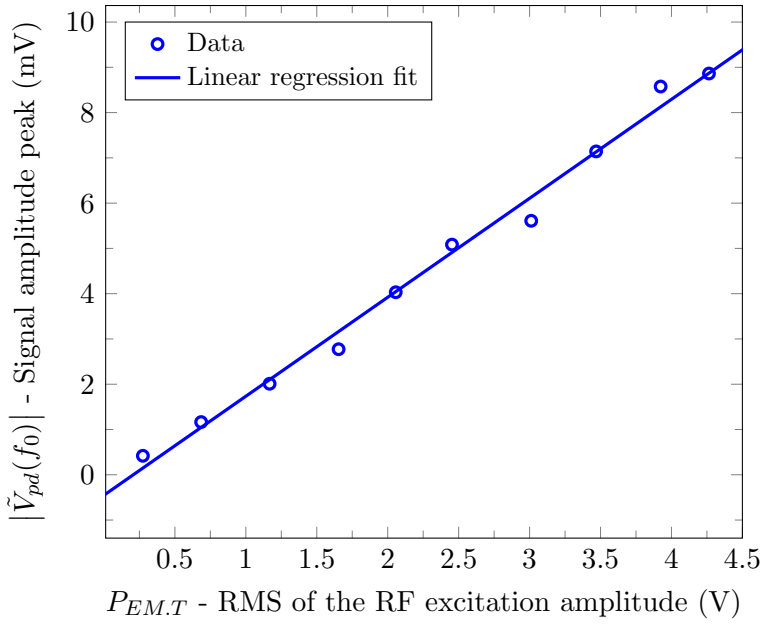

FIGURE 6.29: Photodetector signal amplitude peak vs. the infrared laser EM power for the μcantilever first in-plane mode.

6.5 Setup validation: characterization of a nanobridge

A set of nanobridges were fabricated [89] with the aim to determine if the characterization setup was able to measure the resonant frequency spectrum of NEMS devices, that is, electromechanical devices at the nanoscale. Figure 6.30 shows two SEM images of these structures.

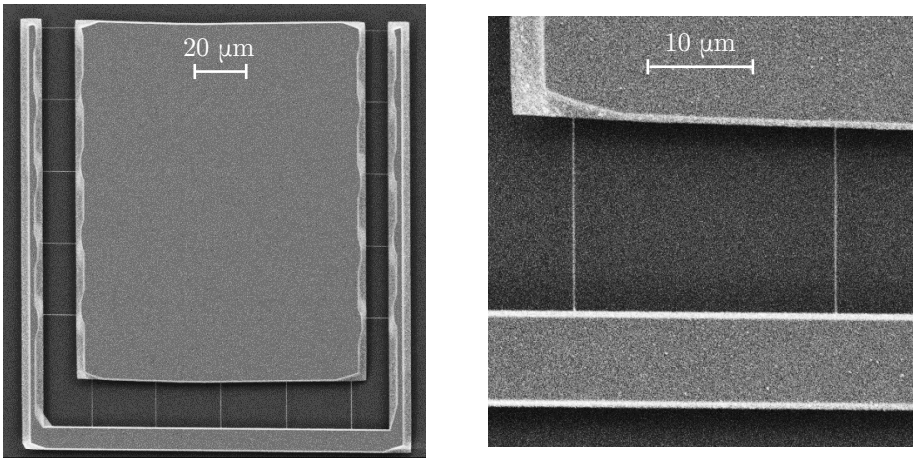

(A) SEM image of one of the fabricated samples.

(B) SEM image of two nanobridges ($20 \times 0.17 \times 0.04\,\mu m^3$).

FIGURE 6.30: SEM images of clamped-clamped nanobeams.

Figures 6.31 and 6.32 respectively show the normalized first out-of-plane and in-plane resonances of the left side nanobridge shown in figure 6.30b when it is driven by the thermomechanical noise fluctuations.

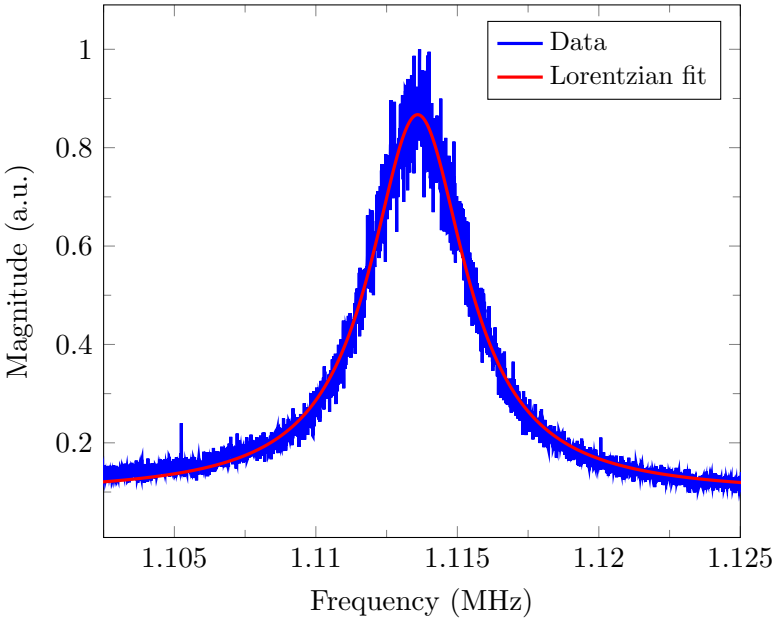

FIGURE 6.31: First thermomechanical out-of-plane resonance of a nanobridge. Plot of 50 averaged curves. Pressure $= 1.9 \cdot 10^{-5}$ mbar.

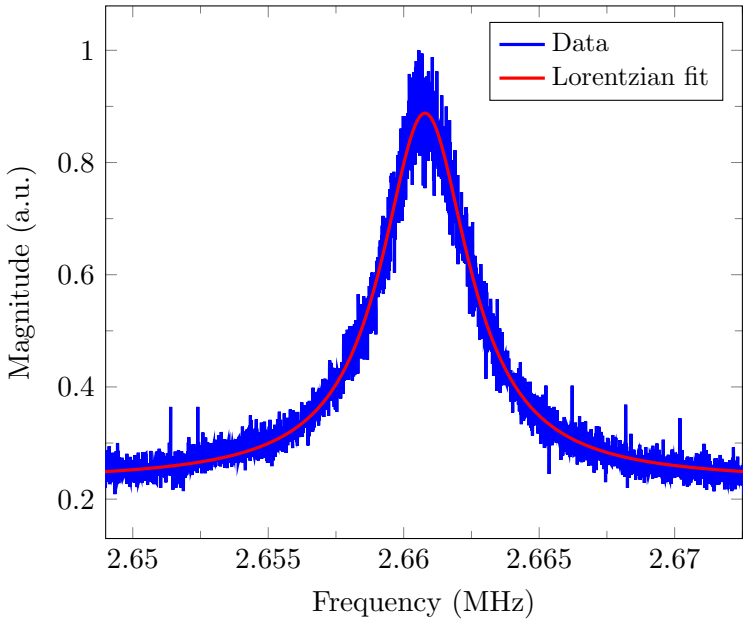

FIGURE 6.32: First thermomechanical in-plane resonance of a nanobridge. Plot of 50 averaged curves. Pressure = $1.9{\cdot}10^{-5}$ mbar.

To determine the in-plane and out-of-plane resonant frequencies the nanobridge was firstly electrostatically actuated and optically measured using a network analyzer (FEM simulations were also performed but due to the inevitable fabrication tolerances the obtained results differ from the measured ones). Once the frequencies were found, the device was disconnected from the external excitation source and left unconnected inside the vacuum chamber. Then a frequency spectrum analyzer was used to analyze the frequency content of the photodetector's output. The represented data is the outcome of such analysis.

6.5.1 Analysis of the thermomechanical noise

The thermally driven random motion experienced by a mechanical resonator when it is not subjected to an external driving force can be treated as a classical Brownian motion. The equipartition theorem is used to analyze these vibrations, yielding that the energy associated at each resonator's vibration mode is [90]

$$\frac{1}{2}m\omega_0^2\left\langle w_{th}^2\right\rangle = \frac{1}{2}k_B T_{th} \tag{6.27}$$

where k_B is the Boltzmann constant ($1.3806488{\cdot}10^{-23}\,{}^{J}/_{K}$) and the rest of terms are characteristics of the resonator: m is its mass, ω_0 its resonant frequency, $\langle w_{th}^2 \rangle$ its mean square displacement and T_{th} its absolute temperature.

The latter analysis gives the following expression for the resonator's thermomechanical root mean square displacement

$$w_{th-rms} = \sqrt{\langle w_{th}^2 \rangle} = \sqrt{\frac{k_B T_{th}}{m\omega_0^2}} \tag{6.28}$$

The continuous system that a clamped-clamped beam represents can be modeled as a mass-spring-dashpot single degree of freedom system [91]. When such model is adopted, equation (6.28) must be rewritten as

$$w_{th-rms} = \sqrt{\langle w_{th}^2 \rangle}\varphi_n(x = x_p) = \sqrt{\frac{k_B T_{th}}{m_{eff}\omega_0^2}}\varphi_n(x = x_p) \tag{6.29}$$

where m_{eff} is the effective mass of the beam (i.e., $m_{eff} = \rho BH \int_0^L \varphi_n^2 dx$, being L, B and H respectively the length, width and thickness of the beam) and $\varphi_n(x = x_p)$ is the n_{th} spatial function used as the trial function in the space discretization method performed during the modeling (e.g., the Galerkin method) evaluated at the x_p point along the beam's length. Since for the fundamental mode (i.e., $n = 1$) the point of maximum displacement is the bridge's central point, $x_p = {}^{L}/_{2}$.

When the spatial functions are normalized such that $\int_0^L \varphi_n^2 dx = L$, the effective mass of the beam for the fundamental mode becomes its total mass. Assuming a silicon density of $2330\,{}^{kg}/_{m^3}$ the mass of the characterized nanobridge is $m_{eff} = 3.17{\cdot}10^{-16}$ kg. The linear undamped mode shapes of a clamped-clamped beam are normally used as the trial functions of the space discretization method [92]. As a consequence, for the fundamental mode: $\varphi_1(x = {}^{L}/_{2}) \approx 1.588$.

Extracting the resonant frequency from the data shown in figures 6.31 and 6.32 and assuming that the device is at room temperature (i.e., $T_{th} = 300$ K), equation (6.29) yields the table 6.2 root mean square displacement values due to the thermomechanical noise for the two cases.

Case	Resonant frequency (MHz)	w_{th-rms} (pm)
Out-of-plane	*1.114*	*820.6*
In-plane	*2.661*	*343.4*

TABLE 6.2: Resonant frequency and root mean square displacement values for each measured thermomechanical resonance.

The previous calculations had been done as an example to give an idea about the displacements which the assembled setup is capable of measuring. In order to compute the sensitivity of the optical setup a deep analysis on the electrical noise sources of the setup must be carried out (see for example [93] for the in-plane modes and [94, 95] for the out-of-plane ones). Notice that such analysis becomes crucial when the optical characterization setup is designed to detect displacement as small as possible.

The results presented in this section demonstrate that the assembled optical characterization setup can be used to measure frequency responses of both in-plane and out-of-plane resonant modes of nanobridges driven by thermomechanical noise fluctuations. Such results suggest that the setup might be capable of measuring the vibrations of the designed PoC OPACMEMS device given the fact that its dimensions (see table 4.1) are similar to the characterized nanobridge.

6.6 Summary and discussion

In this chapter the optical setup based on both an interferometric technique and a knife-edge technique was theoretically studied, designed, assembled and used to experimentally characterize micro and nano devices; demonstrating that both in-plane and out-of-planes modes can be measured and used to study the linearity of the corresponding detection mechanism. A clamped-clamped beam having a width of 170 nm and a vibration amplitude as lower as 343.4 pm could be measured using the assembled setup. All of the obtained results indicate that system should

be capable to characterize the proof-of-concept devices designed and analyzed in chapter 4. However, no results of such characterization were presented in this chapter. Regardless of the incomplete devices obtained during the fabrication of the PoC devices, the following discussion analyzes if the assembled setup could actually induce and measure the auto-oscillations of a device having a residual tensile stress of 1.5 GPa.

As computed in chapter 4, a residual tensile stress of 1.5 GPa could be compensated by the compressive stress induced when a PoC device is illuminated with an infrared irradiance of $3.74{\cdot}10^7\ {}^{mW}/_{m^2}$. The total EM power that the laser must shine in order to generate such irradiance can be computed if the illuminated area is known. Using the spot area values listed in table 6.1 it can be computed that if the 50x microscope objective is used, an optical power of 23 mW must arrive at the sample position. The same computation can be done for the 20x microscope ojective, yielding an EM power of 88.85 mW. Nevertheless, the data plotted in figure 6.16 reveals that neither of the latter optical powers can be achieved using the available infrared laser.

Chapter 7

Conclusions and future directions

7.1 Conclusions

The main objective of this thesis was the design and analysis of a device that merges optical antennas with micro/nano-mechanical structures. The most important results found during the described work can be summarized by the following conclusions:

- In terms of the thermal power per unit volume, a FSS-based absorber shows a better performance than a multilayer absorber.
- To correctly account for the effect of a temperature field in a clamped-clamped beam, an initial predeformation must be added to the Euler-Bernoulli equation governing the transverse vibrations of the beam. Such modeling develops into a thermo-mechanical coupling mechanism.
- The opto-themo-mechanical coupling mechanism was demonstrated to lead to the auto-oscillation of a proof-of-concept device at an irradiance of $210\,{}^{mW}/_{m^2}$.
- The gap thickness and the quality factor were shown to play a key role on the auto-oscillation state of the proposed devices.

- The theoretical optimization of the transition point where a mechanical device coupled to EM resonators starts to self-oscillate is almost impossible due to the intrinsic nature of a Hopf bifurcation.

- A chromium layer deposited on top of silicon dioxide by common electron beam evaporation techniques develops a tensile residual stress. Such stress difficults the self-oscillation of the proposed OPACMEMS devices.

- An optical setup with one single optical probe can be designed to linearly measure both in-plane and out-of-plane vibration modes of M/NEMS devices. The setup described in this manuscript was able to characterize a clamped-clamped beam having a width of 170 nm and a thickness of 40 nm vibrating at its first out-of-plane mode with an amplitude of 343.4 pm.

7.2 Future directions

Although not being mentioned, several experimental measurements and theoretical models reported in the literature [56, 57, 59, 61] describe that the M/NEMS exhibiting self-oscillations have an hysteresis cycle. Meaning that once the laser power reaches the value for which the auto-oscillations begin, the device will continue to oscillate as the laser power is reduced until a power lower than the aforementioned one is reached. Such behavior is due to the existence of a saddle node bifurcation of cycles, where two limit cycles coalesce or divide [77]. However, the model described in chapter 3 is not able to track this type of bifurcation (it only detects Hopf bifurcations). As a future line of work, the model should be enhanced by introducing the capability to detect saddle node bifurcations.

Due to the lack of time and to the fact that the fabrication process was not fully controlled by the author, this thesis only reports semi-final fabricated OPACMEMS devices. Therefore, a big effort should be made to obtain devices which can be characterized using the assembled setup. A deep study of the metal deposition techniques should be performed with the aim to find a metal that once

deposited its residual stress does not suppose the invalidation of its characterization. It must also be taken into account that post-deposition techniques can be used to reduce a residual tensile stress (e.g., ion bombardment of the sample [96]).

7.3 Scientific contributions of the author

7.3.1 Publications

G. Abadal, J. Alda, and **J. Agustí**, "Electromagnetic radiation energy harvesting - The rectenna based approach," Book: *ICT-Energy - Nanoscale Energy Management Concepts Towards Zero-Power Information and Communication Technology*, Intech Open Science, pp. 79–106, 2014.

J. Agustí, A. Cuadrado, M. López-Suárez, J. Alda, and G. Abadal, "The opto-thermo-mechanical conversion mechanism in a MEMS with integrated nanoantennas for energy harvesting from infrared radiation," *Nanoenergy Letters*, no. 6, pp. 45–46, 2013.

A. Cuadrado, **J. Agustí**, G. Abadal, and J. Alda, "Diffractive characterization of the vibrational state of an array of micro-cantilevers," *Optical Engineering*, vol. 52, no. 9, pp. 091717-1–091717-6, 2013.

J. Agustí, A. Cuadrado, J. C. Martínez-Antón, J. Alda, and G. Abadal, "An analytical model for the opto-thermo-mechanical conversion mechanisms in a MOEMS-based energy harvester," *SPIE proceedings in Nanoengineering: Fabrication, Properties, Optics, and Devices IX*, vol. 8463, pp. 846313-1–846313-9, 2012.

A. Cuadrado, F. J. González, **J. Agustí** and J. Alda, "Material dependence of the distributed bolometric effect in resonant metallic nanostructures," *SPIE proceedings in Plasmonics: Metallic Nanostructures and Their Optical Properties X*, vol. 8457, pp. 845724-1–845724-10, 2012.

I. Pellejero, **J. Agustí**, M. A. Urbiztondo, J. Sesé, M. P. Pina, J. Santamaría, and G. Abadal, "Nanoporous silicalite-only cantilevers as micromechanical sensors: fabrication, resonance response and VOCs sensing performance," *Sensors and Actuators B: Chemical*, vol. 168, pp. 74–82, 2012.

A. Cuadrado, **J. Agustí**, M. López-Suárez, G. Murillo, G. Abadal, and J. Alda, "Measurement of the vibration state of an array of micro cantilevers by diffractional methods," *Óptica Pura y Aplicada*, vol. 45, no. 2, pp. 105–111, 2012.

G. Murillo, H. Campanella, **J. Agustí**, J. Esteve, and G. Abadal, "Integration of piezoelectric energy scavengers with FBAR resonators for the miniaturization of autonomous wireless sensors nodes," *Proceedings of IEEE International Conference on Micro Electro Mechanical Systems*, pp. 1253–1256, 2012.

G. Murillo, **J. Agustí**, M. López-Suárez and G. Abadal, "Heterogeneous integration of autonomous systems in package for wireless sensor networks," *Procedia Engineering*, vol. 25, pp. 88–91, 2011.

J. Agustí, I. Pellejero, G. Abadal, G. Murillo, M. A. Urbiztondo, J. Sesé, M. Villarroya-Gaudó, M. P. Pina, J. Santamaría, and N. Barniol, "Optical vibrometer for mechanical properties characterization of silicalite-only cantilever based sensors," *Microelectronic Engineering*, vol. 87, no. 5, pp. 1207–1209, 2010.

G. Murillo, Z. J. Davis, S. Keller, G. Abadal, **J. Agustí**, A. Cagliani, N. Noeth, A. Boisen, and N. Barniol, "Novel SU-8 based vacuum wafer-level packaging for MEMS devices," *Microelectronic Engineering*, vol. 87, no. 5, pp. 1173–1176, 2010.

7.3.2 Conference contributions

G. Vidal-Álvarez, **J. Agustí**, F. Torres, G. Abadal, N. Barniol, J. Llobet, M. Sansa, M. Fernández-Regúlez, F. Pérez-Murano and Á. San Paulo, "Top-down silicon microcantilever with coupled bottom-up silicon nanowire for enhanced mass resolution," *Workshop on nanomechanical sensing (NMC)*, 30 April - 2 May 2014, Madrid (Spain). Poster.

F. Torres, O. Súchil, P. Bramon, M. López, **J. Agustí** and G. Abadal, "Vibrational energy harvesting and mechanical storage," *NanotechItaly*, 27-29 November 2013, Venice (Italy). Poster.

J. Agustí, A. Cuadrado, M. López-Suárez, J. Alda and G. Abadal, "MOEMS characterization through CW infrared laser excitation and read-out," *Conference on micro and nano engineering (MNE)*, 16-19 September 2013, London (United Kingdom). Poster.

M. López-Suárez, **J. Agustí**, F. Torres, R. Rurali and G. Abadal, "Electret based bistable MEMS for energy harvesting," *Conference on micro and nano engineering (MNE)*, 16-19 September 2013, London (United Kingdom). Poster.

G. Abadal, M. López-Suárez, P. Bramon, **J. Agustí**, R. Rurali and F. Torres, "NEMS for energy harvesting. Towards hybrid solutions to improve conversion efficiency in multisource scenarios," *Energy materials nanotechnology (EMN)*, 7-10 September 2013. Beijing (China). Oral.

F. Torres, O. Súchil, P. Bramon, M. López, **J. Agustí** and G. Abadal, "Multisource nanoenergy harvesting and storage in the mechanical domain," *Trends in nanotechnology (TNT)*, 9-13 September 2013, Sevilla (Spain). Poster.

J. Agustí, A. Cuadrado, M. López-Suárez, J. Alda and G. Abadal, "The opto-thermo-mechanical conversion mechanism in a MEMS with integrated nanoantennas for energy harvesting from infrared radiation," *Nanoenergy*, 10-13 July 2013, Perugia (Italy). Oral.

G.Abadal, **J.Agustí**, M. López-Suárez, F.Torres, P. Bramon, R. Rurali, A. Cuadrado and J. Alda, "Energy harvesting from ambient mechanical vibrations and electromagnetic radiations based on MEMS and NEMS devices," *Imagine-nano. Trends in nano applications energy*, 23-26 April 2013, Bilbao (Spain). Oral.

J. Agustí, A. Cuadrado, J. Alda and G. Abadal, "Analytical model for the opto-thermo-mechanical conversion mechanisms in a MOEMS," *Zeropower workshop*, 16-18 October 2012, Barcelona (Spain). Oral.

J. Agustí, A. Cuadrado, G. Abadal, J. C. Martínez-Antón and J. Alda, "An analytical model for the opto-thermo-mechanical conversion mechanisms in a NOEMS-based energy harvester," *SPIE nanoscience + engineering*, 12-16 August 2012, San Diego (United States of America). Oral.

A. Cuadrado, F. J. González, **J. Agustí** and J. Alda, "Material dependence of the distributed bolometric effect in resonant metallic nanostructures," *SPIE nanoscience + engineering*, 12-16 August 2012, San Diego (United States of America). Poster.

M. López-Suárez, **J. Agustí**, F. Torres, G. Murillo, R. Rurali and G. Abadal, "MEMS based wide-band energy harvesting: a non linear approach," *NiPS summer school workshop. Energy harvesting: models and applications*, 26-27 July 2012, Erice (Italia). Oral.

G. Abadal, G. Murillo, **J. Agustí**, M. López-Suárez and F. Torres, "Energy harvesting based on micro and nano-optoelectromechanical systems," *Zeropower workshop*, 3-4 July 2012, Glasgow (United Kingdom). Oral.

G. Murillo, H. Campanella, **J. Agustí**, J. Esteve and G. Abadal, "Integration of piezoelectric energy scavengers with FBAR resonators for the miniaturization of autonomous wireless sensors nodes," *IEEE conference on micro electro mechanical systems (MEMS)*, 29 January - 2 February 2012, Paris (France). Poster.

G. Murillo, **J. Agustí** and G. Abadal, "Zeropower solutions based on integrated M/NOEMS resonators," *Workshop on nanoscale materials and engineering for energy-efficient electronics*, 26-27 October 2011, Cork (Ireland). Oral.

G. Murillo, **J. Agustí**, M. López-Suárez and G. Abadal, "Heterogeneous integration of autonomous systems in package for wireless sensor networks," *Eurosensors*, 4-7 September 2011, Athens (Greece). Oral.

G. Abadal, G. Murillo, **J. Agustí**, M. López-Suárez, F.Torres and M. Placidi, "Zeropower solutions based on integrated vibrational MEMS energy harvesters,"

Workshop on energy efficient electronic technologies and systems, 18-19 July 2011, Barcelona (Spain). Oral.

A. Cuadrado, **J. Agustí**, M. López-Suárez, G. Murillo, G. Abadal and J. Alda, "Measurement of the vibration state of an array of micro cantilevers by diffractional methods," *Reunión española de optoelectrónica (OPTOEL)*, 30 June - 1 July 2011, Santander (Spain). Poster.

G. Murillo, **J. Agustí**, M. López-Suárez and G. Abadal, "N/MEMS-based energy scavenging for enabling autonomous WSN shrinkage," *Third nanonetworking summit*, 22-23 June 2011, Barcelona (Spain). Oral.

G. Murillo, **J. Agustí**, M. López-Suárez and G. Abadal, "Microscale energy harvester driven by a built-in permanent magnet for self-powered nodes in appliance power cables", *PowerMEMS*, 30 November - 3 December 2010, Leuven (Belgium). Poster.

J. Agustí, G. Murillo, M. López-Suárez and G. Abadal, "RF energy harvester based on MEMS," *NiPS workshop: noise in dynamical systems at the micro and nanoscale*, 6-8 August 2010, Avigliano Umbro (Italy). Oral.

M. López-Suárez, G. Murillo, **J. Agustí**, H. Vocca, L. Gammaitoni and G. Abadal, "Efficient non-linear NEMS based energy harvesting from thermomechanical noise," *Conference on statistical mechanics. Energy conversion: from nanomachines to renewable sources*, 7-11 June 2010, Sitges (Spain). Poster.

J. L. Muñoz-Gamarra, E. Marigó, **J. Agustí**, J. Giner, A. Uranga, F. Torres and N.Barniol, "Characterization of CMOS-NENS resonators by pulsed mode electrostatic actuation," *IEEE frequency control symposium (FCS)*, 2-4 June 2014, Newport Beach (United States of America). Poster.

G. Murillo, **J. Agustí**, G.Abadal, F.Torres, J. Giner, E, Marigó, A.Uranga and N.Barniol, "Integration of an improved harvester-on-chip core dice on commercial SOI-based MEMS technology," *PowerMEMS*, 1-4 December 2009, Washington DC (United States of America). Poster.

J. Agustí, I. Pellejero, G. Abadal, G. Murillo, M.A. Urbiztondo, J. Sesé, M. Villarroya-Gaudó, M. P. Pina, J. Santamaría and N. Barniol, "Mechanical properties characterization of silicalite-only cantilever based sensors for explosives early detection," *Conference on micro and nano engineering (MNE)*, 28 September - 1 October 2009, Ghent (Belgium). Poster.

G. Murillo, Z. Davis, S. Keller, G. Abadal, **J. Agustí**, A. Cagliani, N. Noeth, A. Boisen and N. Barniol, "Novel SU-8 based vacuum wafer-level packaging for MEMS devices," *Conference on micro and nano engineering (MNE)*, 28 September - 1 October 2009, Ghent (Belgium). Poster.

I. Pellejero, M. Urbiztondo, M. P. Pina, J. Sesé, **J. Agustí**, G. Abadal, J. Santamaría, M. Villarroya-Gaudó and N. Barniol, "Silicalite as structural layers for MEMS applications to chemical sensors," *Workshop on micromachining, micro mechanics and micro systems (MME)*, 20-22 September 2009, Toulouse (France). Poster.

Appendix A

Mathematics of the opto-thermo-mechanical model

A.1 Temperature field mode profiles - Mathematical steps

The mathematical steps followed in order to solve the homogeneous partial differential equation (A.1) (or (3.22)) are shown in this section.

$$\dot{\hat{\theta}} - \mathcal{C}_1 \hat{\theta}^{II} = 0 \tag{A.1}$$

Using the separation of variables technique, the temperature field of the beam can be split into a position and a time dependent components as

$$\hat{\theta}(\hat{x}, \hat{t}) = \psi(\hat{x})\hat{G}(\hat{t}) \quad \begin{cases} \dot{\hat{\theta}} & = \psi \dot{\hat{G}} \\ \hat{\theta}^{II} & = \psi^{II} \hat{G} \end{cases} \tag{A.2}$$

where dots and roman numerals denote respectively the partial differentiation with respect to $\hat{t}$ and to $\hat{x}$.

Taking the separation of variables into account, (A.1) can be rewritten as

$$\psi\dot{\hat{G}} = \mathcal{C}_1\psi^{II}\hat{G} \quad \rightarrow \quad \frac{\dot{\hat{G}}}{\hat{G}} = \mathcal{C}_1\frac{\psi^{II}}{\psi} \tag{A.3}$$

From (A.3), τ_m and κ_m are defined as

$$\frac{\dot{\hat{G}}_m}{\hat{G}_m} = -\frac{1}{\tau_m} \quad \rightarrow \quad \dot{\hat{G}}_m + \frac{1}{\tau_m}\hat{G}_m = 0 \tag{A.4}$$

$$\frac{\psi_m^{II}}{\psi_m} = -\frac{1}{\mathcal{C}_1\tau_m} = -\kappa_m^2 \quad \rightarrow \quad \psi_m^{II} + \kappa_m^2\psi_m = 0 \tag{A.5}$$

where m is the number of the temperature mode, $m = 1, 2, \ldots, M$.

The solution for $\hat{G}_m$ has the following form

$$\hat{G}_m = A_m e^{-\hat{t}/\tau_m} \tag{A.6}$$

where A_m is determined by the initial temporal conditions and τ_m is the mth dimensionless time constant.

The roots of the homogeneous ordinary differential equation (A.5) when solving for $\psi_m = e^{r_m\hat{x}}$ are

$$r_{m.1} = j\kappa_m\,, \quad r_{m.2} = -j\kappa_m \tag{A.7}$$

Hence, the solution of (A.5) can be written as

$$\psi_m = D_m e^{j\kappa_m\hat{x}} + E_m e^{-j\kappa_m\hat{x}} \tag{A.8}$$

Using the Euler's formulas

$$\begin{aligned} e^{j\hat{x}} &= \cos(\hat{x}) + j\sin(\hat{x}) \\ e^{-j\hat{x}} &= \cos(\hat{x}) - j\sin(\hat{x}) \end{aligned} \tag{A.9}$$

, (A.8) can be rewritten as

$$\psi_m = B_m\sin(\kappa_m\hat{x}) + C_m\cos(\kappa_m\hat{x}) \tag{A.10}$$

where $B_m = j\,(D_m - E_m)$ and $C_m = D_m + E_m$.

The Dirichlet boundary conditions for the case of the modeled clamped-clamped beam are isothermal temperature field at the clamped ends (see the seventh assumption made in section 3.2),

$$\psi_m = 0 \;\text{ at }\; \hat{x} = 0 \;\text{ and }\; 1 \tag{A.11}$$

The following relations are found by applying the above boundary conditions to (A.10),

$$C_m = 0 \tag{A.12}$$

$$B_m \sin(\kappa_m) = 0 \tag{A.13}$$

Therefore,

$$\kappa_m = m\pi \tag{A.14}$$

$$\tau_m = \frac{1}{\mathcal{C}_1 m^2 \pi^2} \tag{A.15}$$

Table A.1 shows the value of κ_m for the first three temperature modes.

Mode	1st	2nd	3rd
κ_m	π	2π	3π

TABLE A.1: Value of κ_m for the first three temperature modes.

Taking into account (A.12), (A.10) can be rewritten as

$$\psi_m = B_m \sin(\kappa_m \hat{x}) \tag{A.16}$$

where B_m remains as an undetermined value.

The first three temperature mode profiles are plotted in figure A.1. In order to give a value to B_m, the eigenfunctions ψ_m have been normalized so that

$$\int_0^1 \psi_m^2 \, d\hat{x} = 1 \tag{A.17}$$

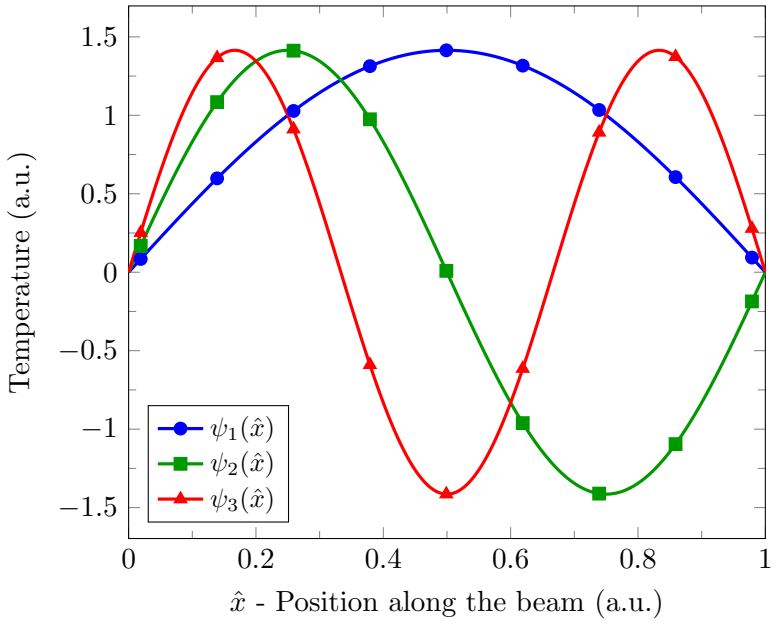

FIGURE A.1: First three temperature mode profiles of the modeled clamped-clamped beam.

A.2 Lumped thermal model - Mathematical steps

The mathematical steps followed in order to solve the partial differential equation (A.18) (or (3.19)) are shown in this section.

$$\mathscr{F}\left[\hat{\theta}(\hat{x},\hat{t})\right] = \dot{\hat{\theta}} - \mathcal{C}_1\hat{\theta}^{II} - \hat{Q} = 0 \tag{A.18}$$

Since $\mathscr{F}\left[\hat{\theta}\right] = 0$ can not be solved exactly, the Galerkin space discretization procedure based on the temperature field mode profiles is used to eliminate the spatial dependence of $\hat{\theta}$. With this method the solution is represented in terms of a linearly independent set of basis or trial functions. Where each one of them satisfies the boundary conditions of the problem (see (3.21)),

$$\hat{\theta}(\hat{x},\hat{t}) = \sum_{m=1}^{M} \hat{g}_m(\hat{t})\psi_m(\hat{x}) \tag{A.19}$$

$$\psi_m = 0 \;\text{ at }\; \hat{x} = 0 \;\text{ and }\; 1 \tag{A.20}$$

In (A.19), $\hat{g}_m$ is the mth generalized temperature and ψ_m is the mth temperature field mode profile (see (A.16)) normalized such that

$$\int_0^1 \psi_m \psi_i \, d\hat{x} = \delta_{mi} \tag{A.21}$$

where $\delta_{mj} = 0$ if $m \neq j$ and $\delta_{mj} = 1$ if $m = j$, the Kronecker delta.

This modal decomposition method has an associated error,

$$\text{error} = \text{e} = \mathscr{F}\left[\sum_{m=1}^{M} \hat{g}_m \psi_m\right] - \mathscr{F}\left[\hat{\theta}\right] = \mathscr{F}\left[\sum_{m=1}^{M} \hat{g}_m \psi_m\right] \tag{A.22}$$

The Galerkin method requires this error to be orthogonal to each of the basis functions, meaning that the error is a residual that cannot be expressed in terms of the given finite set of basis functions,

$$\int_0^1 e \, \psi_i \, d\hat{x} = 0 \,, \quad i = 1, 2, \ldots, M. \tag{A.23}$$

The reduced-order model is generated by substituting (A.22) into (A.23), using (A.5) to eliminate the ψ_m^{II} term and taking into account the orthogonality condition of the basis functions or modes (A.21). Thus, the modal decomposition can be expressed as a multiple degree-of-freedom system consisting of ordinary differential equations in the dimensionless time where $i = 1, 2, \ldots, M$

$$\sum_{m=1}^{M} \dot{\hat{g}}_m \delta_{mi} + \mathcal{C}_1 \sum_{m=1}^{M} \hat{g}_m \kappa_m^2 \delta_{mi} = \hat{Q} \int_0^1 \psi_i \, d\hat{x} \tag{A.24}$$

A.3 Buckling mode shapes of and ideal clamped-clamped beam

When a critical compressive axial load $S_{c.o}$ is applied to an ideal clamped-clamped beam, its static bending shape takes the form of a buckling mode shape $\vartheta_o(x)$. In order to study these shapes the static Euler-Bernoulli equation for an ideal beam

is used; that is,

$$EI\frac{\partial^4\vartheta_o}{\partial x^4}+S_{c.o}\frac{\partial^2\vartheta_o}{\partial x^2}=0 \tag{A.25}$$

where o is the number of the buckling mode, $o=1,2,\ldots,O$.

The following spatial variables are defined when normalizing the longitudinal coordinate by the beam length and the static beam deflection by a wavelength

$$\hat{x}=\frac{x}{L}\,,\quad \hat{\vartheta}_o=\frac{\vartheta_o}{\lambda_w} \tag{A.26}$$

Rescaling (A.25) using these new variables yields the following nondimensional equation

$$\hat{\vartheta}_o^{IV}+\hat{S}_{c.o}\hat{\vartheta}_o^{II}=0 \tag{A.27}$$

where $\hat{S}_{c.o}=\frac{S_{c.o}L^2}{EI}$.

The roots of the homogeneous ordinary differential equation (A.27) when solving for $\hat{\vartheta}_o=e^{r_o\hat{x}}$ are

$$r_{o.1}=0\,,\quad r_{o.2}=0\,,\quad r_{o.3}=j\sqrt{\hat{S}_{c.o}}\,,\quad r_{o.4}=-j\sqrt{\hat{S}_{c.o}} \tag{A.28}$$

Taking into account that $r=0$ is a root of multiplicity 2, the solution of (A.27) can be written in the form of a sum of exponential functions as

$$\hat{\vartheta}_o=A_oe^0+B_o\hat{x}e^0+E_oe^{j\sqrt{\hat{S}_{c.o}}\hat{x}}+F_oe^{-j\sqrt{\hat{S}_{c.o}}\hat{x}} \tag{A.29}$$

Using the Euler's formulas (A.9), (A.29) can be rewritten as

$$\hat{\vartheta}_o=A_o+B_o\hat{x}+C_o\sin\left(\sqrt{\hat{S}_{c.o}}\hat{x}\right)+D_o\cos\left(\sqrt{\hat{S}_{c.o}}\hat{x}\right) \tag{A.30}$$

where $C_o=j\,(E_o-F_o)$ and $D_o=E_o+F_o$.

The Dirichlet boundary conditions for a clamped-clamped beam are zero deflection and slope at the fixed ends,

$$\hat{\vartheta}_o=0\ \text{ and }\ \hat{\vartheta}_o^I=0\ \text{ at }\ \hat{x}=0\ \text{ and }\ 1 \tag{A.31}$$

The following relations are found by applying the above boundary conditions to (A.30) ,

$$\begin{aligned} A_o + D_o &= 0 \\ B_o + C_o\sqrt{\hat{S}_{c.o}} &= 0 \\ A_o + B_o + C_o \sin\left(\sqrt{\hat{S}_{c.o}}\hat{x}\right) + D_o \cos\left(\sqrt{\hat{S}_{c.o}}\hat{x}\right) &= 0 \\ B_o + C_o\sqrt{\hat{S}_{c.o}} \cos\left(\sqrt{\hat{S}_{c.o}}\hat{x}\right) - D_o\sqrt{\hat{S}_{c.o}} \sin\left(\sqrt{\hat{S}_{c.o}}\hat{x}\right) &= 0 \end{aligned} \tag{A.32}$$

The linear system formed by collecting the equations in (A.32) can be expressed as

$$\mathbf{N} \cdot \begin{pmatrix} A_o \\ B_o \\ C_o \\ D_o \end{pmatrix} = \begin{pmatrix} 0 \\ 0 \\ 0 \\ 0 \end{pmatrix} \tag{A.33}$$

where

$$\mathbf{N} = \begin{pmatrix} 1 & 0 & 0 & 1 \\ 0 & 1 & \sqrt{\hat{S}_{c.o}} & 0 \\ 1 & 1 & \sin\left(\sqrt{\hat{S}_{c.o}}\hat{x}\right) & \cos\left(\sqrt{\hat{S}_{c.o}}\hat{x}\right) \\ 0 & 1 & \sqrt{\hat{S}_{c.o}} \cos\left(\sqrt{\hat{S}_{c.o}}\hat{x}\right) & -\sqrt{\hat{S}_{c.o}} \sin\left(\sqrt{\hat{S}_{c.o}}\hat{x}\right) \end{pmatrix} \tag{A.34}$$

The eigenvalues or the values of $\sqrt{\hat{S}_{c.o}}$ of the eigenvalue problem are found when solving the transcendental characteristic equation obtained by equaling to zero the determinant of the coefficient matrix (A.34); that is,

$$\det(\mathbf{N}) = 2\left(\cos\left(\sqrt{\hat{S}_{c.o}}\right) - 1\right) + \sqrt{\hat{S}_{c.o}} \sin\left(\sqrt{\hat{S}_{c.o}}\right) = 0 \tag{A.35}$$

The double-angle trigonometric formulas are used to recognize that

$$\sin\left(\sqrt{\hat{S}_{c.o}}\right) = 2\sin\left(\frac{\sqrt{\hat{S}_{c.o}}}{2}\right)\cos\left(\frac{\sqrt{\hat{S}_{c.o}}}{2}\right) \tag{A.36}$$

$$\cos\left(\sqrt{\hat{S}_{c.o}}\right) = 1 - 2\sin^2\left(\frac{\sqrt{\hat{S}_{c.o}}}{2}\right) \tag{A.37}$$

Therefore (A.35) becomes

$$\sin\left(\frac{\sqrt{\hat{S}_{c.o}}}{2}\right)\left[\frac{\sqrt{\hat{S}_{c.o}}}{2}\cos\left(\frac{\sqrt{\hat{S}_{c.o}}}{2}\right)-\sin\left(\frac{\sqrt{\hat{S}_{c.o}}}{2}\right)\right]=0 \tag{A.38}$$

For the symmetric mode shapes, the only valid solutions of (A.38) are the ones which satisfy that

$$\sin\left(\frac{\sqrt{\hat{S}_{c.o}}}{2}\right)=0 \tag{A.39}$$

Therefore,

$$\sqrt{\hat{S}_{c.o}}=\pm 2o\pi \quad \rightarrow \quad \hat{S}_{c.o}=4o^2\pi^2 \tag{A.40}$$

Table A.2 shows the value of $\hat{S}_{c.o}$ for the first three symmetric buckling modes.

Mode	1st	2nd	3rd
$\hat{S}_{c.o}$	$4\pi^2$	$16\pi^2$	$36\pi^2$

TABLE A.2: Value of $\hat{S}_{c.o}$ for the first three symmetric buckling modes.

The following relations are found when applying the $\hat{S}_{c.o}$ solutions to the equations in (A.32),

$$B_o=0\,,\;\; C_o=0\,,\;\; A_o+D_o=0 \tag{A.41}$$

Therefore, (A.30) can be rewritten as

$$\hat{\vartheta}_o=A_o\left[1-\cos\left(\sqrt{\hat{S}_{c.o}}\hat{x}\right)\right] \tag{A.42}$$

where A_o, the buckling amplitude, remains as an undetermined value.

The first three buckling mode shapes are plotted in figure A.2. In order to give a value to A_o, the eigenfunctions ϑ_o have been normalized so that

$$\int_0^1 \hat{\vartheta}_o^2\, d\hat{x}=1 \tag{A.43}$$

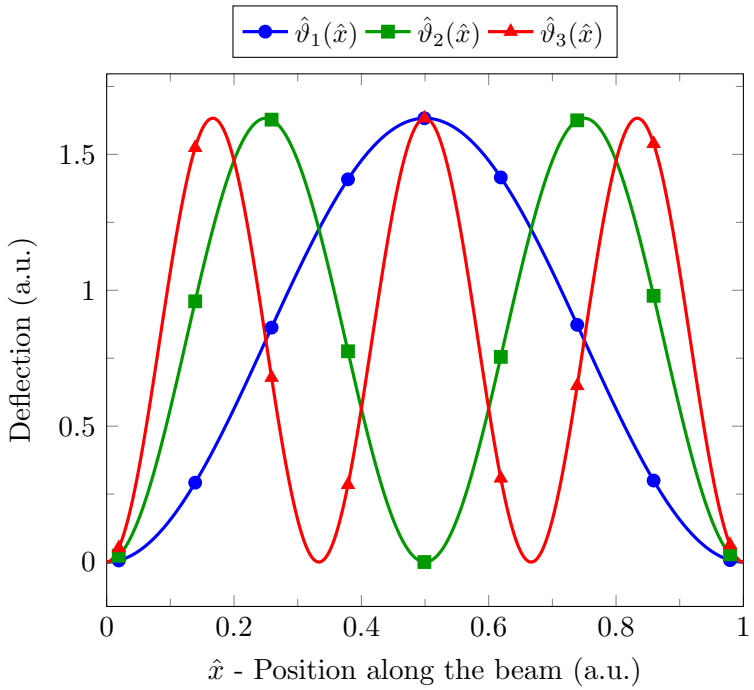

FIGURE A.2: First three symmetric buckling mode shapes of a clamped-clamped beam.

A.4 The nonlinear equilibrium deflection - Mathematical steps

The mathematical steps followed in order to solve the nonhomogeneous differential equation (A.44) (or (3.64)) are shown in this section.

$$\hat{w}_e^{IV} + \lambda^2 \hat{w}_e^{II} = \hat{w}_0^{IV} \tag{A.44}$$

The sum of an homogeneous solution and a particular one forms the general solution of (A.44),

$$\hat{w}_e = \hat{w}_{e.h}(\hat{x}) + \hat{w}_{e.p}\big[\hat{w}_0(\hat{x})\big] \tag{A.45}$$

Equation (A.46) must be solve in order to get the homogeneous solution of (A.44).

$$\hat{w}_{e.h}^{IV} + \lambda^2 \hat{w}_{e.h}^{II} = 0 \tag{A.46}$$

Since the above equation has the same form as (A.27), its solving process is the same as the one developed in section A.3. Hence, its homogeneous solution can be written as

$$\hat{w}_{e.h} = A + B\hat{x} + C\sin(\lambda\hat{x}) + D\cos(\lambda\hat{x}) \tag{A.47}$$

Equation (A.48) must be solve in order to get the particular solution of (A.44).

$$\hat{w}_{e.p}^{IV} + \lambda^2\hat{w}_{e.p}^{II} = \hat{w}_0^{IV} \tag{A.48}$$

Considering that the static predeformation can be described by (3.62), the term $\hat{w}_0^{IV}$ of (A.48) becomes

$$\hat{w}_0^{IV} = -8\pi^4\delta_0\frac{L}{\lambda_w}\cos(2\pi\hat{x}) \tag{A.49}$$

Given $\hat{w}_0^{IV}$, $\hat{w}_{e.p}$ can be assumed to have the following form

$$\hat{w}_{e.p} = E\cos(2\pi\hat{x}) \tag{A.50}$$

Then (A.48) can be solved for E, yielding that

$$E = \frac{2\pi^2\delta_0 L}{\lambda_w\left(\lambda^2 - 4\pi^2\right)} \tag{A.51}$$

Therefore, the general solution of (A.44) is given by

$$\hat{w}_e = \hat{w}_{e.h} + \hat{w}_{e.p} = A + B\hat{x} + C\sin(\lambda\hat{x}) + D\cos(\lambda\hat{x}) + \frac{2\pi^2\delta_0 L}{\lambda_w\left(\lambda^2 - 4\pi^2\right)}\cos(2\pi\hat{x}) \tag{A.52}$$

The boundary conditions of (A.44) are (see (3.60))

$$\hat{w}_e = 0 \;\text{ and }\; \hat{w}_e^I = 0 \;\text{ at }\; \hat{x} = 0 \;\text{ and }\; 1 \tag{A.53}$$

The following relations are found when applying the above boundary conditions to (A.52),

$$A = \frac{2\pi^2\delta_0 L}{\lambda_w\left(4\pi^2 - \lambda^2\right)}\,,\quad B = 0\,,\quad C = 0\,,\quad D = 0 \tag{A.54}$$

As a consequence, the expression for the general solution of (A.44) can be written as

$$\hat{w}_e = \frac{2\pi^2 \delta_0 L}{\lambda_w \left(4\pi^2 - \lambda^2\right)} \left[1 - \cos(2\pi\hat{x})\right] \tag{A.55}$$

A.5 Nonlinear equilibrium deflection ranges

Figure A.3 shows the qualitative nonlinear equilibrium deflection behavior of the modeled clamped-clamped beam for various δ_0 values (as seen in figure 3.7). Embedded in this figure the different equilibrium ranges have been depicted. Solid lines are stable solutions, while the dashed ones are unstable.

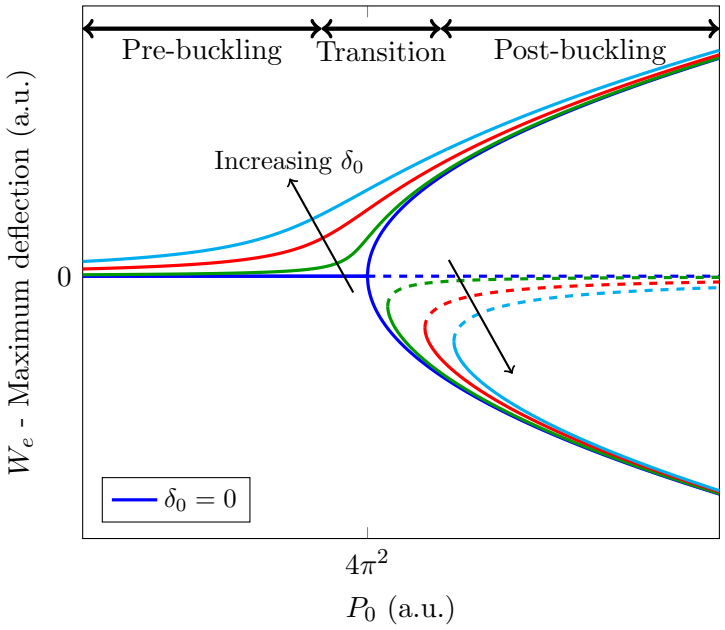

FIGURE A.3: Bifurcation diagram: variation of the maximum equilibrium deflection W_e with the P_0 load for various δ_0 values. Solutions: stable (solid lines) and unstable (dashed lines).

From the point of view of a nonlinear analysis, the qualitative change that takes place during the transition range is a bifurcation.

When $\delta_0 = 0$ the pre-buckling range ends when $P_0 = P_{buckling} = 4\pi^2$. After this point the post-buckling range starts. Hence, and only for this particular case, the transition range is nonexistent and the beam go from being straight to buckled

in an abrupt way. This type of bifurcation is called a supercritical pitchfork bifurcation.

When $\delta_0 \neq 0$ the equilibrium behavior between the pre and post-buckling ranges shows a transition range, where the beam suffers a smooth transition towards buckling. This type of bifurcation is called a saddle-node bifurcation.

A.6 Natural frequencies and linear undamped mode shapes around the nonlinear equilibrium - Mathematical steps

The mathematical steps followed in order to resolve the natural frequencies and the associated mode shapes of (A.56) (or (3.73)) are shown in this section.

$$\ddot{\hat{w}}_{d.lu} + \hat{w}^{IV}_{d.lu} + K\hat{w}^{II}_{d.lu} - 2\mathcal{C}_5\hat{w}^{II}_e \int_0^1 \hat{w}^I_e \hat{w}^I_{d.lu} d\hat{x} = 0 \tag{A.56}$$

$$K = P_0 - \mathcal{C}_5 \int_0^1 \left[\left(\hat{w}^I_e\right)^2 - \left(\hat{w}^I_0\right)^2 \right] d\hat{x} \tag{A.57}$$

With the aim to resolve the natural frequencies ω_n and the associated mode shapes $\varphi_n(\hat{x})$, $\hat{w}_{d.lu}$ is replaced by $e^{j\omega_n \hat{t}}\varphi_n$. Thus, equation (A.56) turns into

$$\varphi^{IV}_n + K\varphi^{II}_n - \omega^2_n \varphi_n = 2\mathcal{C}_5 \Gamma \hat{w}^{II}_e \tag{A.58}$$

where $\Gamma = \int_0^1 \varphi^I_n \hat{w}^I_e d\hat{x}$, which is a constant for a given φ_n and $\hat{w}_e$, and n is the number of the mode, $n = 1, 2, \ldots, N$.

The sum of an homogeneous solution and a particular one forms the general solution of (A.58),

$$\varphi_n = \varphi_{n.h}(\hat{x}) + \varphi_{n.p}\left[\hat{w}_e(\hat{x})\right] \tag{A.59}$$

Equation (A.60) must be solve in order to get the homogeneous solution of (A.58).

$$\varphi_{n.h}^{IV} + K\varphi_{n.h}^{II} - \omega_n^2\varphi_{n.h} = 0 \tag{A.60}$$

The roots of the homogeneous ordinary differential equation (A.60) when solving for $\varphi_{n.h} = e^{r_n\hat{x}}$ are

$$\begin{aligned} r_{n.1} &= \sqrt{-\frac{K}{2} + \sqrt{\omega_n^2 + \frac{K^2}{4}}}\,, \quad r_{n.2} = \sqrt{-\frac{K}{2} - \sqrt{\omega_n^2 + \frac{K^2}{4}}}\,, \\ r_{n.3} &= -\sqrt{-\frac{K}{2} + \sqrt{\omega_n^2 + \frac{K^2}{4}}}\,, \quad r_{n.4} = -\sqrt{-\frac{K}{2} - \sqrt{\omega_n^2 + \frac{K^2}{4}}} \end{aligned} \tag{A.61}$$

These roots can also be expressed as

$$r_{n.1} = \sqrt{-\frac{K}{2} + \sqrt{\omega_n^2 + \frac{K^2}{4}}}\,, \quad r_{n.2} = jr_{n.5}\,, \quad r_{n.3} = -r_{n.1}\,, \quad r_{n.4} = -jr_{n.5} \tag{A.62}$$

where $r_{n.5}$ has been defined as $r_{n.5} = j\sqrt{\frac{K}{2} + \sqrt{\omega_n^2 + \frac{K^2}{4}}}$.

Hence, the solution of (A.60) can be written as

$$\varphi_{n.h} = E_n e^{r_{n.1}\hat{x}} + F_n e^{jr_{n.5}\hat{x}} + G_n e^{-r_{n.1}\hat{x}} + H_n e^{-jr_{n.5}\hat{x}} \tag{A.63}$$

Using the complex exponential function formula relations with the sinh and cosh

$$\begin{aligned} e^{\hat{x}} &= \cosh(\hat{x}) + \sinh(\hat{x}) \\ e^{-\hat{x}} &= \cosh(\hat{x}) - \sinh(\hat{x}) \end{aligned} \tag{A.64}$$

, and the Euler's formula (A.9), (A.63) can be rewritten as

$$\varphi_{n.h} = A_n \sin(r_{n.5}\hat{x}) + B_n \cos(r_{n.5}\hat{x}) + C_n \sinh(r_{n.1}\hat{x}) + D_n \cosh(r_{n.1}\hat{x}) \tag{A.65}$$

where $A_n = j\,(F_n - H_n)\,,\ B_n = F_n + H_n,\ C_n = E_n - G_n$ and $D_n = E_n + G_n$.

Equation (A.66) must be solved in order to get the particular solution of (A.58).

$$\varphi_{n.p}^{IV} + K\varphi_{n.p}^{II} - \omega_n^2\varphi_{n.p} = 2\mathcal{C}_5\Gamma\hat{w}_e^{II} \tag{A.66}$$

Considering that the equilibrium can be described by (3.66), the term $\hat{w}_e^{II}$ of (A.66) becomes

$$\hat{w}_e^{II} = 2\pi^2 W_e \cos(2\pi\hat{x}) \tag{A.67}$$

Given $\hat{w}_e^{II}$, $\varphi_{n.p}$ can be assumed to have the following form

$$\varphi_{n.p} = E_n \cos(2\pi\hat{x}) \tag{A.68}$$

Therefore, the general solution of (A.58) is given by

$$\begin{aligned}\varphi_n = \varphi_{n.h} + \varphi_{n.p} =& A_n \sin(r_{n.5}\hat{x}) + B_n \cos(r_{n.5}\hat{x}) + C_n \sinh(r_{n.1}\hat{x}) \\ &+ D_n \cosh(r_{n.1}\hat{x}) + E_n \cos(2\pi\hat{x})\end{aligned} \tag{A.69}$$

Considering that the static predeformation can be described by (3.62), the parameter P_0 from K (see (A.57)) can be isolated from (3.67), yielding

$$P_0 = \pi^2 \frac{\mathcal{C}_5\lambda_w^2 W_e^3 + W_e\left(8\lambda_w^2 - \mathcal{C}_5\delta_0^2 L^2\right) - 8L\lambda_w\delta_0}{2\lambda_w^2 W_e} \tag{A.70}$$

Therefore, (A.57) becomes

$$K = 4\pi^2\left(1 - \frac{\delta_0 L}{W_e\lambda_w}\right) \tag{A.71}$$

Given the expression of K and the forms of $\varphi_{n.p}$ and $\hat{w}_e$, the parameter Γ of (A.58) can also be isolated from (A.66). Doing so, it results on

$$\Gamma = E_n \frac{16\pi^4 \frac{\delta_0 L}{W_e\lambda_w} - \omega_n^2}{4\pi^2 W_e \mathcal{C}_5} \tag{A.72}$$

The boundary conditions of (A.56) are (see (3.74))

$$\hat{w}_{d.lu} = 0 \;\text{ and }\; \hat{w}_{d.lu}^I = 0 \;\text{ at }\; \hat{x} = 0 \;\text{ and }\; 1 \tag{A.73}$$

The following relations are found by applying the above boundary conditions to (A.69)

$$\begin{aligned} B_n + D_n + E_n &= 0 \\ A_n r_5 + C_n r_1 &= 0 \\ A_n \sin(r_5) + B_n \cos(r_5) + C_n \sinh(r_1) + D_n \cosh(r_1) + E_n &= 0 \\ A_n r_5 \cos(r_5) - B_n r_5 \sin(r_5) + C_n r_1 \cosh(r_1) + D_n r_1 \sinh(r_1) &= 0 \end{aligned} \tag{A.74}$$

Two more equations are needed to particularly obtain the values of A_n, B_n, C_n, D_n and E_n. The fifth equation is obtained using the definition of the parameter Γ,

$$\int_0^1 \varphi_n^I \hat{w}_e^I \, d\hat{x} - \Gamma = 0 \tag{A.75}$$

Since Γ is given by (A.72), (A.75) develops into

$$\begin{aligned} -A_n r_5 \frac{\cos(r_5) - 1}{4\pi^2 - r_5^2} + B_n r_5 \frac{\sin(r_5)}{4\pi^2 - r_5^2} - C_n r_1 \frac{\cosh(r_1) - 1}{4\pi^2 + r_1^2} \\ - D_n r_1 \frac{\sinh(r_1)}{4\pi^2 + r_1^2} - E_n \left(\frac{1}{2} + \frac{16\pi^4 \frac{\delta_0 L}{W_e \lambda_w} - \omega_n^2}{8\pi^4 \mathcal{C}_4 W_e^2} \right) = 0 \end{aligned} \tag{A.76}$$

The sixth equation is obtained by imposing the following normalization to φ_n

$$\int_0^1 \varphi_n^2 \, d\hat{x} = 1 \tag{A.77}$$

Therefore, the value of A_n, B_n, C_n, D_n and E_n is found by solving the system of equations formed by collecting equations (A.74), (A.76) and (A.77). With these values the eigenvectors or mode shapes φ_n of the eigenvalue problem are particularized.

The linear system formed by collecting equations (A.74) and (A.76) can be expressed as

$$\mathbf{M} \cdot \begin{pmatrix} A_n \\ B_n \\ C_n \\ D_n \\ E_n \end{pmatrix} = \begin{pmatrix} 0 \\ 0 \\ 0 \\ 0 \\ 0 \end{pmatrix} \tag{A.78}$$

where

$$\mathbf{M}=\begin{pmatrix} 0 & 1 & 0 & 1 & 1 \\ r_5 & 0 & r_1 & 0 & 0 \\ \sin(r_5) & \cos(r_5) & \sinh(r_1) & \cosh(r_1) & 1 \\ r_5\cos(r_5) & -r_5\sin(r_5) & r_1\cosh(r_1) & r_1\sinh(r_1) & 0 \\ -r_5\frac{\cos(r_5)-1}{4\pi^2-r_5^2} & r_5\frac{\sin(r_5)}{4\pi^2-r_5^2} & -r_1\frac{\cosh(r_1)-1}{4\pi^2+r_1^2} & -r_1\frac{\sinh(r_1)}{4\pi^2+r_1^2} & -\left(\frac{1}{2}+\frac{16\pi^4\frac{\delta_0 L}{W_e\lambda_w}-\omega_n^2}{8\pi^4\mathcal{C}_4 W_e^2}\right) \end{pmatrix} \tag{A.79}$$

The eigenvalues or natural frequencies ω_n of the eigenvalue problem are found when solving the transcendental characteristic equation obtained by equaling to zero the determinant of the coefficient matrix (A.79); that is,

$$\det(\mathbf{M})=0 \tag{A.80}$$

A.7 Dynamic lumped mechanical model - Mathematical steps

The mathematical steps followed in order to solve the partial differential equation (A.81) (or (3.78)) are shown in this section.

$$\begin{aligned} \mathscr{L}\left[\hat{w}_d(\hat{x},\hat{t})\right] &= \ddot{\hat{w}}_d+\mathcal{C}_2\dot{\hat{w}}_d+\hat{w}_d^{IV}+\Big\{\mathcal{C}_3+\mathcal{C}_4\hat{T}_l \\ -\mathcal{C}_5\int_0^1\left[\left(\hat{w}_e^I\right)^2-\left(\hat{w}_0^I\right)^2\right]d\hat{x}\Big\}\hat{w}_d^{II}&-\mathcal{C}_5\hat{w}_d^{II}\int_0^1\left[\left(\hat{w}_d^I\right)^2+2\hat{w}_e^I\hat{w}_d^I\right]d\hat{x} \\ &-\mathcal{C}_5\hat{w}_e^{II}\int_0^1\left[\left(\hat{w}_d^I\right)^2+2\hat{w}_e^I\hat{w}_d^I\right]d\hat{x}+\mathcal{C}_4\hat{w}_e^{II}\hat{T}_{l.d}=0 \end{aligned} \tag{A.81}$$

Since $\mathscr{L}\left[\hat{w}_d\right]=0$ can not be solved exactly, the Galerkin space discretization procedure based on the linear undamped mode shapes computed in section A.6 is used to eliminate the spatial dependence of $\hat{w}_d$. With this method the solution is represented in terms of a linearly independent set of basis or trial functions. Where

each one of them satisfies the boundary conditions of the problem (see (3.61)),

$$\hat{w}_d(\hat{x},\hat{t}) = \sum_{n=1}^{N} \hat{q}_n(\hat{t})\varphi_n(\hat{x}) \tag{A.82}$$

$$\varphi_n = 0 \;\text{ and }\; \varphi_n^I = 0 \;\text{ at }\; \hat{x} = 0 \;\text{ and }\; 1 \tag{A.83}$$

In (A.82), $\hat{q}_n$ is the nth generalized coordinate and φ_n is the nth linear undamped mode shape (see (A.69)) normalized such that

$$\int_0^1 \varphi_n \varphi_i \, d\hat{x} = \delta_{ni} \tag{A.84}$$

where $\delta_{ni} = 0$ if $n \neq i$ and $\delta_{ni} = 1$ if $n = i$, the Kronecker delta.

This modal decomposition method has an associated error,

$$\text{error} = \text{e} = \mathscr{L}\left[\sum_{n=1}^{N} \hat{q}_n\varphi_n\right] - \mathscr{L}\left[\hat{w}_d\right] = \mathscr{L}\left[\sum_{n=1}^{N} \hat{q}_n\varphi_n\right] \tag{A.85}$$

The Galerkin method requires this error to be orthogonal to each of the basis functions, meaning that the error is a residual that cannot be expressed in terms of the given finite set of basis functions,

$$\int_0^1 e\,\varphi_i \, d\hat{x} = 0\,, \;\; i = 1, 2, \ldots, N. \tag{A.86}$$

The reduced-order model is generated by substituting (A.85) into (A.86) and taking into account the orthogonality condition of the basis functions or linear undamped mode shapes (A.84). Thus, the modal decomposition can be expressed as a multiple degree-of-freedom system consisting of ordinary differential equations in the dimensionless time where $i = 1, 2, \ldots, N$

$$\begin{aligned}
&\sum_{n=1}^{N}\ddot{\hat{q}}_n\delta_{ni}+\mathcal{C}_2\sum_{n=1}^{N}\dot{\hat{q}}_n\delta_{ni}+\sum_{n=1}^{N}\hat{q}_n\int_0^1\varphi_n^{IV}\varphi_i\,d\hat{x}\\
&+\left[\mathcal{C}_3+\mathcal{C}_4\hat{T}_l-\mathcal{C}_5\int_0^1\left(\left(\hat{w}_e^I\right)^2-\left(\hat{w}_0^I\right)^2\right)d\hat{x}\right]\sum_{n=1}^{N}\hat{q}_n\int_0^1\varphi_n^{II}\varphi_i\,d\hat{x}\\
&-\mathcal{C}_5\sum_{n=1}^{N}\hat{q}_n\int_0^1\varphi_n^{II}\varphi_i\,d\hat{x}\left(\sum_{l=1}^{N}\sum_{o=1}^{N}\hat{q}_l\hat{q}_o\int_0^1\varphi_l^I\varphi_o^I\,d\hat{x}+2\sum_{l=1}^{N}\hat{q}_l\int_0^1\hat{w}_e^I\varphi_l^I\,d\hat{x}\right)\\
&-\mathcal{C}_5\int_0^1\hat{w}_e^{II}\varphi_i\,d\hat{x}\left(\sum_{n=1}^{N}\sum_{l=1}^{N}\hat{q}_n\hat{q}_l\int_0^1\varphi_n^I\varphi_l^I\,d\hat{x}+2\sum_{n=1}^{N}\hat{q}_n\int_0^1\hat{w}_e^I\varphi_n^I\,d\hat{x}\right)\\
&+\mathcal{C}_4\hat{T}_{l.d}\int_0^1\hat{w}_e^{II}\varphi_i\,d\hat{x}=0
\end{aligned}\tag{A.87}$$

A.8 Relation between the distributed damping D and the quality factor Q_f

The relation between the distributed damping D and the quality factor Q_f for a given resonant mode is [97]

$$D=\frac{\omega_0 m_T}{Q_f L}\tag{A.88}$$

where ω_0 is the resonant frequency, m_T the total mass of the beam, Q_f its quality factor and L its length.

The dimensionless distributed damping $\mathcal{C}_2$ is defined in (3.59); that is,

$$\mathcal{C}_2=\frac{D}{\rho A\omega_s}\tag{A.89}$$

Using (A.88), this parameter can be rewritten as

$$\mathcal{C}_2=\frac{\omega}{\omega_s Q_f}\tag{A.90}$$

The next appendix section explains how to extract the quality factor from the frequency spectrum response of a resonator (e.g., a clamped-clamped beam in its n^{th} resonant mode).

A.9 Computing the quality factor of a resonator

Experimentally, the quality factor of a resonator can be extracted from the frequency spectrum of its resonance by using the following ratio

$$Q_f = \frac{f_0}{BW} \tag{A.91}$$

where f_0 is the resonant frequency (or the frequency at which the measured magnitude is maximum) and BW is the bandwidth of the resonance. The latter term is renamed as BW_{3dB} when the magnitude of the measured spectrum is in dB units and represents the half-power, or -3 dB, bandwidth of the measured peak. If the magnitude of the measured spectrum is in volts or amps, the BW parameter represents the bandwidth down by a factor of $1/\sqrt{2}$.

Notice that each resonant mode of a mechanical structure will have its own characteristic resonant frequency and quality factor. Table A.3 summarizes the parameters illustrated in figure A.4 as an example the extraction of the quality factor of a resonance (the experimental data is the dimensional version of the data shown in figure 6.32).

f_0 (MHz)	BW (MHz)	Q_f
2.661	*0.0032*	*832*

TABLE A.3: Parameters and Q_f value of the resonant peak in figure A.4.

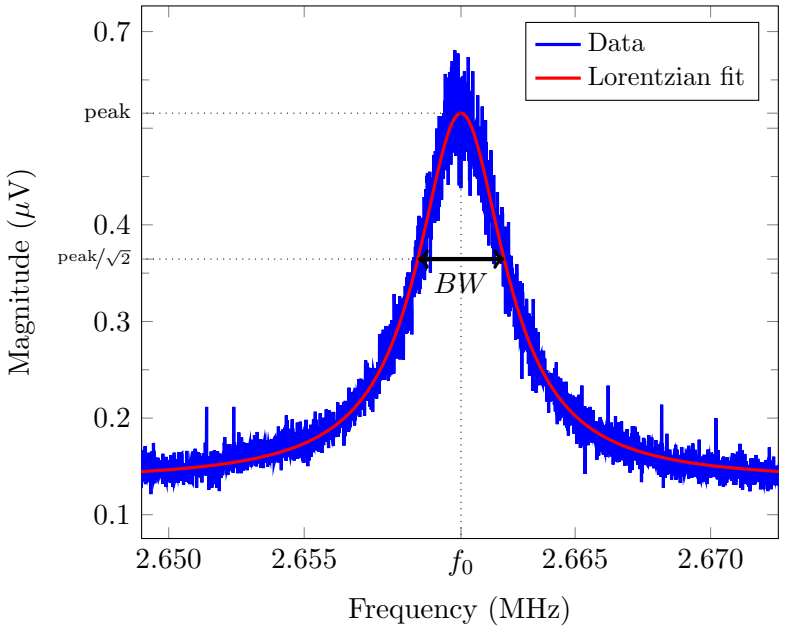

FIGURE A.4: Resonance curve example and its parameters used to compute Q_f.

Appendix B

Analysis of the irradiance dependent opto-thermo-mechanical model parameters

Figures B.1, B.2 and B.3 show the evolution of the irradiance dependent model parameters for different imperfection levels when the residual stress is set to zero. The characteristics and properties needed to computed these graphs are took from the proof-of-concept device analyzed in chapter 4.

The graphs included in figure B.1 correspond to a clamped-clamped perfect beam (i.e., $\delta_0 = 0$). In contrast, the graphs included in figures B.2 and B.3 correspond to clamped-clamped imperfect beams (i.e., $\delta_0 \neq 0$). As it can be seen, the general evolution of the analyzed parameters are similar. Therefore, a few general comments are written concerning the evolution of the most intuitive parameters:

- As expected, the evolution of the beam's central point lumped equilibrium deflection $W_{l.e}$ follows the analysis performed in section 3.3.3.

- The evolution of all the irradiance dependent parameters is closely related with the irradiance value that buckles the mechanical structure (i.e., when $P_0 = P_b$).

- The first out-of-plane resonant frequency decreases monotonically before the buckling load is reached. At $P_0 = P_b$ the resonant frequency is zero and then it increases monotonically with the irradiance.

- Increasing the imperfection level δ_0 value smooths the abrupt changes that take place when $P_0 = P_b$ with $\delta_0 = 0$.

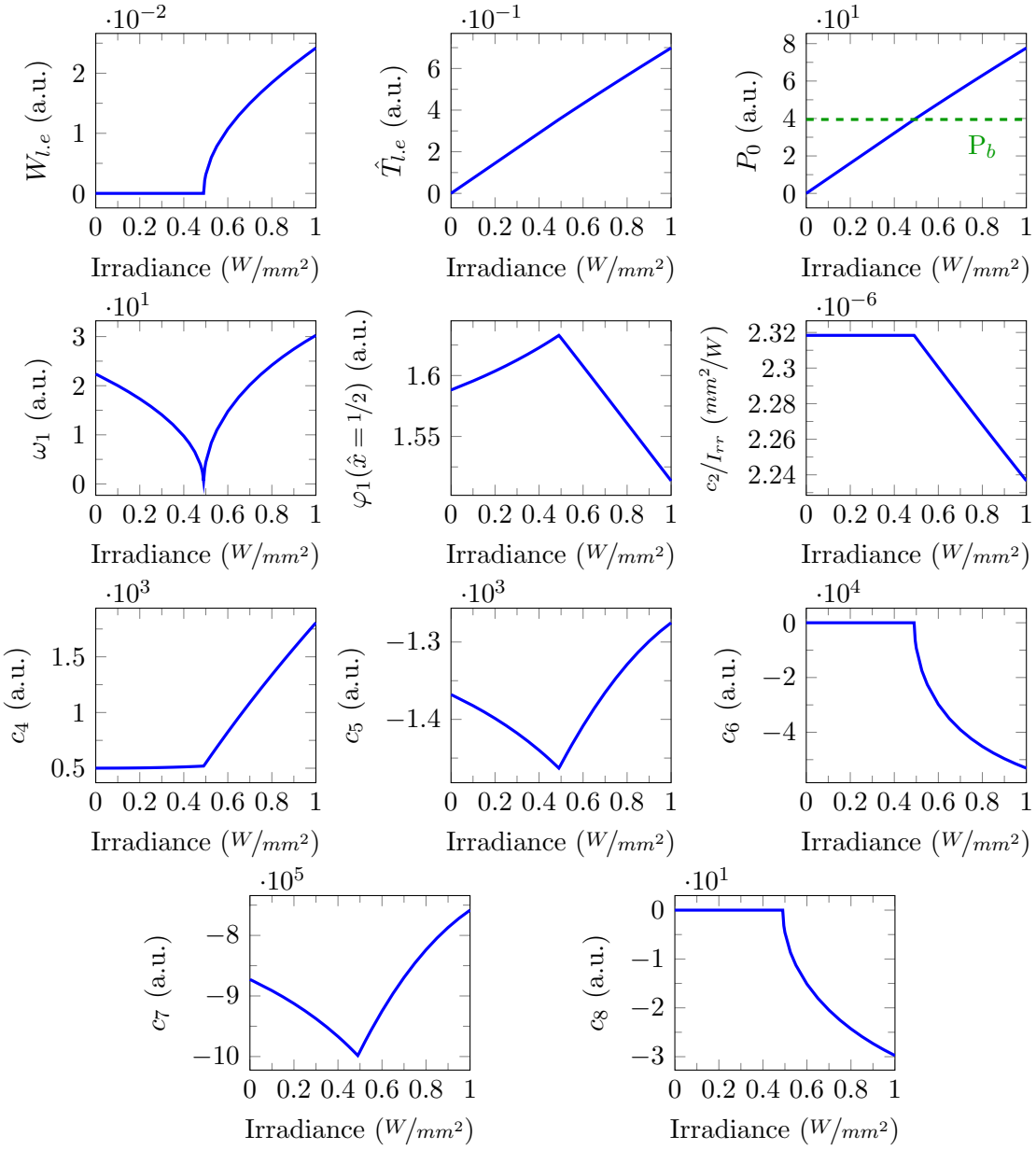

FIGURE B.1: Evolution of the opto-thermo-mechanical model parameters for $\sigma_r = 0$ and $\delta_0 = 0$.

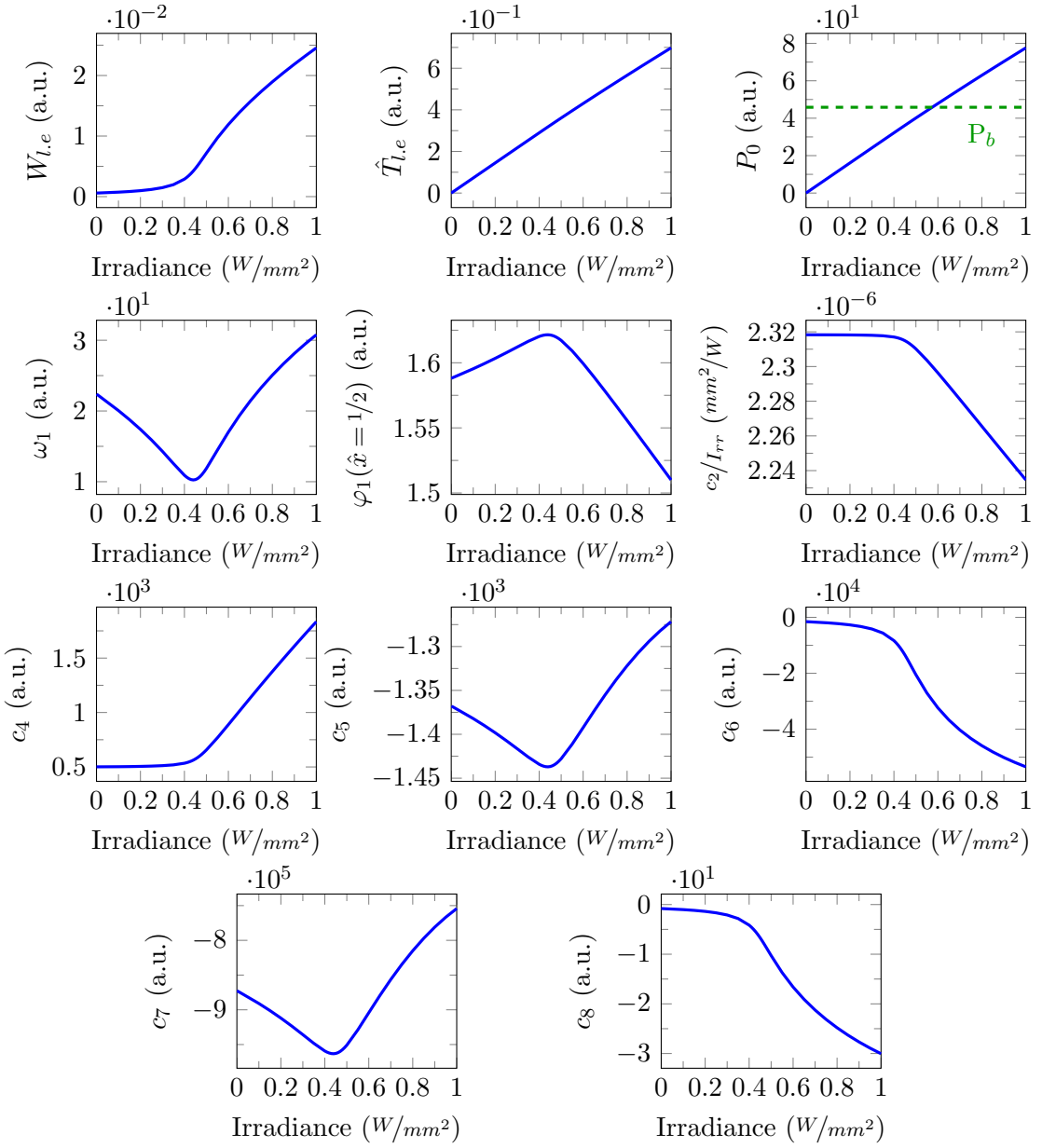

FIGURE B.2: Evolution of the opto-thermo-mechanical model parameters for $\sigma_r = 0$ and $\delta_0 = 1 \cdot 10^{-4}$.

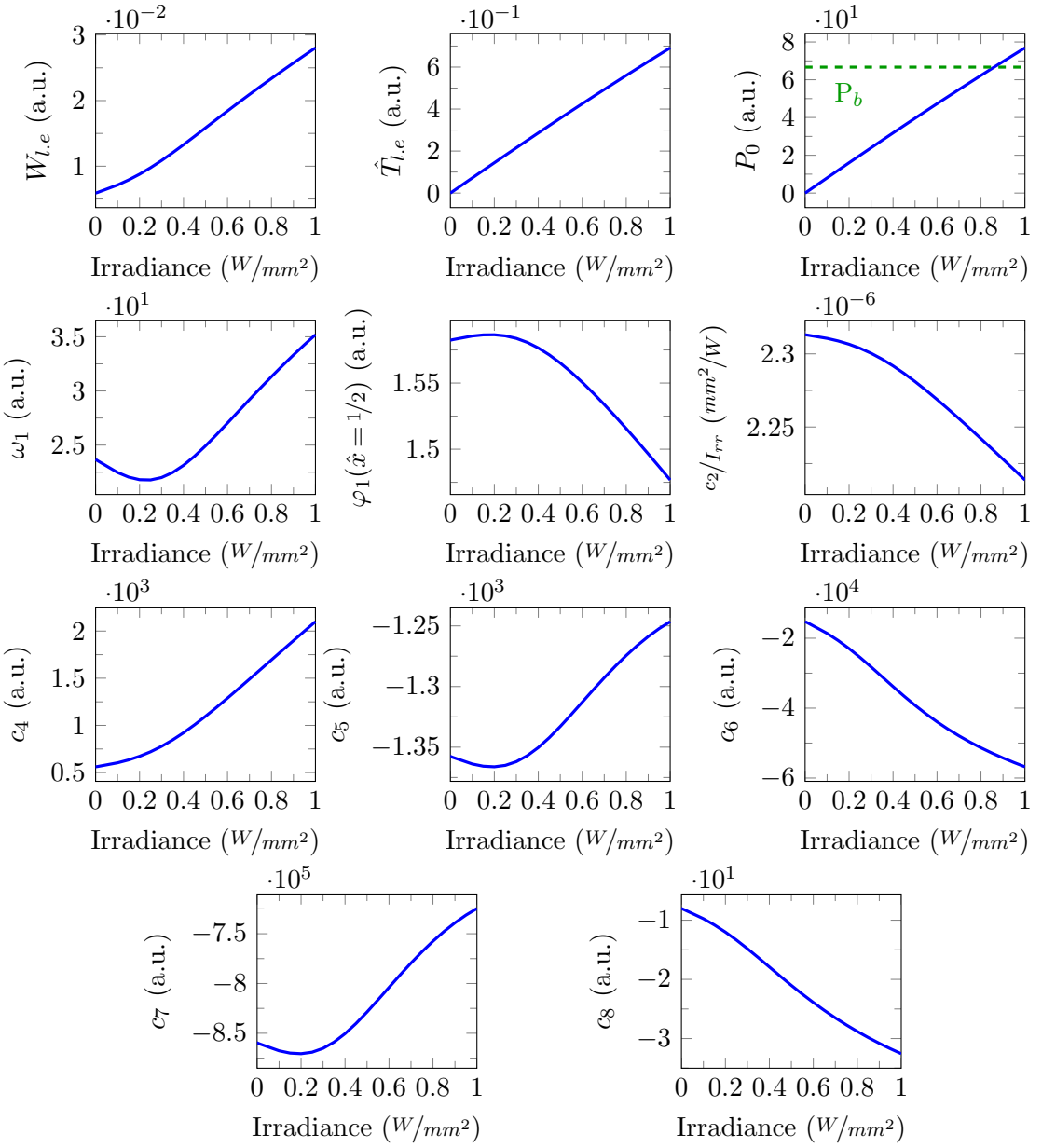

FIGURE B.3: Evolution of the opto-thermo-mechanical model parameters for $\sigma_r = 0$ and $\delta_0 = 1 \cdot 10^{-3}$.

Appendix C

Components of the assembled characterization setup

Tables C.1, C.2, C.3, C.4 and C.5 respectively summarize the most important vacuum, electrical, mechanical, optical and electro-optical components of the assembled setup and their relevant characteristics.

Element	**Reference**	**Relevant characteristics**
Pumping station (HVPS)	Pfeiffer PM S03 557 (HiCube Eco 80)	Ultimate pressure: $1{\cdot}10^{-7}$ mbar Flange: DN 40 ISO-KF Air-cooled
Angle valve (AV)	VAT 26424-KA01	Flange: DN 16 ISO-KF
Vacuum gauge (VG)	Pfeiffer PKR 251 (PT R26 000)	Measurement range: $5{\cdot}10^{-9}$ - 1000 mbar Gauge heads: Pirani and cold cathode Flange: DN 25 ISO-KF
Venting valve (VV)	Pfeiffer FVB 010 HX	Flange: DN 10 ISO-KF
Vacuum chamber (VC)	Pfeiffer 320RKM100	2 × DN 100 ISO-K flanges 1 × DN 40 ISO-KF flange 1 × DN 25 ISO-KF flange 1 × DN 16 ISO-KF flange
Viewport (V)	Pfeiffer 322GSG100	Glass: borosilicate Flange: DN 100 ISO-K

TABLE C.1: Vacuum components of the assembled setup.

Element	**Reference**	**Relevant characteristics**
Current/temperature controller (laser package controller)	Thorlabs ITC4001	Current control range: 0 - 1 A TEC stability: 0.002 °C TEC control: PID
WLS driver	Thorlabs LEDD1B	LED current: up to 1.2 A Manual control knob
Power sensor meter	Thorlabs PM100USB	PC interface: USB
Spectrum analyzer	Agilent E4404B	Freq. range: 9 kHz - 6.7 GHz
Network analyzer 1	Agilent E5100A	Freq. range: 10 kHz - 300 MHz
Network analyzer 2	Agilent E5061B	Freq. range: 5 Hz - 3 GHz
Oscilloscope	Agilent DSO-X 3054A	Bandwidth: 500 MHz

Table C.2: Electrical components of the assembled setup.

Element	**Reference**	**Relevant characteristics**
Beam blocker (BB1) & (BB2)	Thorlabs LB1/M	Absorption: up to 10 W CW
Laser diode mount	Thorlabs LM14S2	Supported package: 14-pin butterfly Socket: zero insertion force (ZIF)
Translation stage (used to position the VC)	Thorlabs LNR50DD/M	Configuration: XYZ orientations Travel: 50 mm Horizontal load capacity: 30 kg Vertical load capacity: 10 kg Drive resolution: up to 1 μm
Translation stage (used to position the PD)	Thorlabs LMT3/M	Configuration: XYZ orientations Travel: 13 mm Horizontal load capacity: 41 kg Vertical load capacity: 9 kg Drive resolution: 10 μm
Optical breadboard	Thorlabs PBI51511	Dimensions (l $\times$ w $\times$ t): 90 $\times$ 75,$\times$ 6 cm^3 Threads: M6 tapped holes Spacing between holes: 25 mm
Breadboard frame	Thorlabs PFH52505	Isolators: passive air-mounted Max. load capacity: 700 kg

Table C.3: Mechanical components of the assembled setup.

Element	**Reference**	**Relevant characteristics**
Fiber collimator (C)	Thorlabs TC12APC-1550	Type: triplet lenses AR coating: 1.05 - 1.65 μm Alignment at: $\lambda_0 = 1.55\,\mu$m Focal length: 12.56 mm
Waveplate ($\lambda_0/2$)	Thorlabs WPH05M-1550	Type: half-wave Order: zero AR coating: 1.55 μm
Bamsplitter (BS1)	Thorlabs BS024	Type: non-polarizing cube R:T ratio: 70:30 AR coating: 1.1 - 1.6 μm Substrate: N-BK7 Size: 25.4 mm
Beamsplitter (BS2)	Thorlabs CM1-BS015	Type: non-polarizing cube R:T ratio: 50:50 AR coating: 1.1 - 1.6 μm Substrate: N-BK7 Size: 25.4 mm
Beamsplitter (BS3)	Thorlabs CM1-BP108	Type: pellicle R:T ratio: 8:92 AR coating: uncoated
Microscope objective (MO_{20x})	Mitutoyo M Plan Apo SL20X	Magnification: 20X Focal length: 10 mm Working distance: 30.5 mm Numerical aperture: 0.28
Microscope objective (MO_{50x})	Mitutoyo M Plan Apo SL50X	Magnification: 50X Focal length: 4 mm Working distance: 20.5 mm Numerical aperture: 0.42
Camera lens	Thorlabs MVL10A	Magnification: 1X
IR detector card	Thorlabs VRC4 and VRC4D05	Absorption bands: 790 - 840 nm, 0.87 - 1.07 μm and 1.5 - 1.59 μm. Emission band: 520 - 580 nm
Laser safety glasses	Thorlabs LG11	Visible light transmission: 75% 0.945 - 2.3 μm transmission: 0.001%

TABLE C.4: Optical components of the assembled setup.

Element	**Reference**	**Relevant characteristics**
Camera	The Imaging Source DFK 72AUC02	Resolution: 5 Mpixel Interface: USB
Laser	Thorlabs SFL1550P	Wavelength: 1.55 μm Typ. operating voltage: 1.5 V Typ. output power: 40 mW (Typ. values at $T_{diode} = 25\,^{\circ}\mathrm{C}$) Max. operating voltage: 1.8 V
	Optical fiber	Type: polarization-maintaining Mode field diameter: $10.5 \pm 1.0\,\mu$m
White light source (WLS)	Thorlabs MCWHL2-C2	Color: cold white Total beam power: 150 mW Max. current: 1.6 A
Photodetector 1 (PD)	Thorlabs PDA10CS-EC	Detector: InGaAs PiN Wavelength range: 0.7 - 1.8 μm Bandwidth range: DC - 17 MHz Peak wavelength: 1.55 μm (Typ.) Peak response: 0.95 $^{A}/_{W}$ (Typ.) Active area: $\varnothing$1 mm (0.8 mm^2) Gain: 0 - 70 dB (8×10 dB steps) NEP: $2{\cdot}10^{-12}$ - $6{\cdot}10^{-11}$ $^{W}/_{\sqrt{Hz}}$
Photodetector 2 (PD)	Thorlabs PDA10CF-EC	Detector: InGaAs PiN Wavelength range: 0.7 - 1.8 μm Bandwidth range: DC - 150 MHz Peak wavelength: 1.55 μm (Typ.) Peak response: 0.95 $^{A}/_{W}$ (Typ.) Active area: $\varnothing$0.5 mm (0.2 mm^2) Transimpedance gain: $5{\cdot}10^{3}$ $^{V}/_{A}$ NEP: $1.2{\cdot}10^{-11}$ $^{W}/_{\sqrt{Hz}}$
Power sensor	Thorlabs S122C	Detector type: Ge photodiode Wavelength range: 0.7 - 1.8 μm Measurement range: 50 nW - 50 mW Resolution: 2 nW Response time: $< 1\,\mu$s Input aperture: $\varnothing$9.5 mm

TABLE C.5: Electro-optical components of the assembled setup.

Appendix D

Laser spot characterization

In the following sections a method for the theoretical characterization of the laser's spot is presented and applied for the case of the assembled setup. The next section introduces an experimental method to determine the size of the laser's spot.

D.1 Theoretically: $ABCD$ law for Gaussian beams

D.1.1 $ABCD$ matrix and $ABCD$ law

The $ABCD$ matrix analysis provides a way to describe the propagation of optical rays through an optical system within the paraxial regime [98]. The following calculation can be done to trace the propagation of a spherical wave represented as a fan of rays (see figure D.1) through an optical system represented by its $ABCD$ matrix,

$$\begin{pmatrix} r_{out} \\ r'_{out} \end{pmatrix} = \begin{pmatrix} A & B \\ C & D \end{pmatrix}_T \begin{pmatrix} r_{in} \\ r'_{in} \end{pmatrix} \tag{D.1}$$

where the r vectors represent the input/output ray's trajectory height and slope with respect to the optical axis of the system. Figure D.2 shows an scheme of the operation described by equation (D.1).

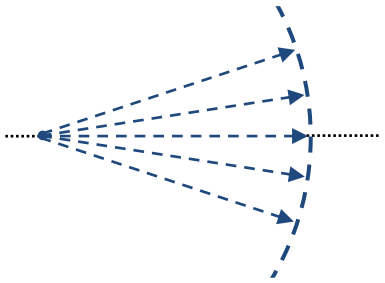

FIGURE D.1: Spherical wave represented as a fan of rays.

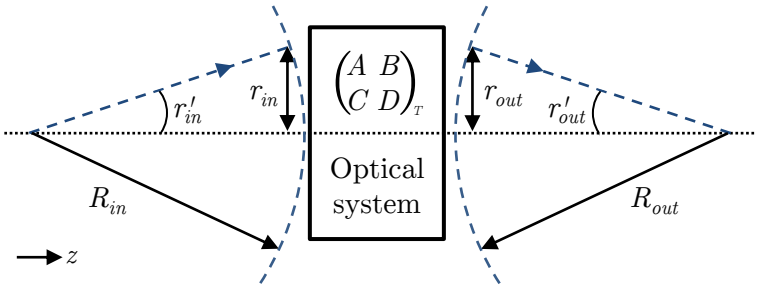

FIGURE D.2: Ray trajectory through an optical system represented by its $ABCD$ matrix.

In figure D.2 the distances labeled as R describe the radius of curvature of the input/output spherical wave. These distances coincide with the following definition

$$r'(z) = \frac{dr(z)}{dz} = \frac{r(z)}{R(z)} \rightarrow R \equiv \frac{r}{r'} \tag{D.2}$$

Using equation (D.1), the output radius of figure D.2 can be obtained using the so-called $ABCD$ law

$$R_{out} \equiv \frac{r_{out}}{r'_{out}} = \frac{Ar_{in} + Br'_{in}}{Cr_{in} + Dr'_{in}} = \frac{AR_{in} + B}{CR_{in} + D} \tag{D.3}$$

Each of the system components are represented by an $ABCD$ matrix. The $ABCD$ matrix of an optical system composed by a cascade of m optical elements is obtained by multiplying all the components matrices,

$$\begin{pmatrix} A & B \\ C & D \end{pmatrix}_T = \begin{pmatrix} A_m & B_m \\ C_m & D_m \end{pmatrix} \ldots \begin{pmatrix} A_2 & B_2 \\ C_2 & D_2 \end{pmatrix} \begin{pmatrix} A_1 & B_1 \\ C_1 & D_1 \end{pmatrix} \tag{D.4}$$

Equation (D.5) is the matrix representation of the free space region with a distance d and a refractive index n shown in figure D.3. Whereas equation (D.6) represents the lens with a focal length f of figure D.4.

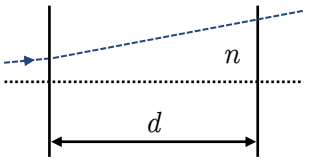

FIGURE D.3: Space region.

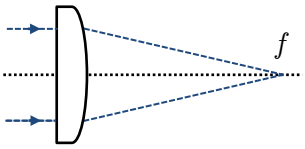

FIGURE D.4: Lens.

$$\begin{pmatrix} A & B \\ C & D \end{pmatrix} = \begin{pmatrix} 1 & {}^{d}/_{n} \\ 0 & 1 \end{pmatrix} \qquad \text{(D.5)} \qquad \begin{pmatrix} A & B \\ C & D \end{pmatrix} = \begin{pmatrix} 1 & 0 \\ {}^{-1}/_{f} & 1 \end{pmatrix} \qquad \text{(D.6)}$$

D.1.2 Propagation of Gaussian beams

The complex exponential form expression for the electric field of a Gaussian beam having rotational symmetry and traveling in vacuum can be obtained from the direct solution of the paraxial Helmholtz wave equation [69]

$$\tilde{\vec{E}}(x,y,z,t) = \tilde{\vec{E}}_0 \frac{W_0}{W(z)} e^{-\frac{x^2+y^2}{(W(z))^2}} e^{-jkz - jk\frac{x^2+y^2}{2R(z)} + j\phi(z)} e^{j\omega t} \qquad \text{(D.7)}$$

where $\tilde{\vec{E}}_0$ is a constant complex vector (thus, it is assumed that the polarization is uniform throughout the xy-plane), W the beam spot radius along the propagation direction z, W_0 the beam waist size, $k = \frac{2\pi}{\lambda_m}$ the wavenumber (being λ_m the wavelength in the propagation medium, which for vacuum $\lambda_m = \lambda_0$), R the wavefront radius of curvature along the propagation direction z, ω the angular frequency of the electric field and $\phi = \tan^{-1}\left(\frac{\lambda_m z}{\pi W_0^2}\right)$ is the Guoy phase shift.

The intensity or irradiance profile of the electric field (D.7) is (see (2.24))

$$I(x,y,z) = I_0 \frac{W_0^2}{W^2} e^{-2\frac{x^2+y^2}{W^2}} \qquad \text{(D.8)}$$

where $I_0 = \frac{1}{2}\frac{|\tilde{\vec{E}}_0|^2}{\eta_0}$.

The beam spot radius W is defined as the evolution of the points along the propagation direction having an irradiance decrease of $1/e^2 = 13.5\,\%$ with respect to the amplitude at the propagation axis $\big((x, y, z) = (0, 0, z)\big)$. Its dependence with z is as follows

$$W = W_0\sqrt{1 + \frac{z\lambda_m}{\pi W_0^2}} \tag{D.9}$$

where the beam waist size $W_0 = W(z = 0)$ is the minimum spot radius. Therefore, the parameter I_0 of equation (D.8) is the irradiance on axis of the beam at its waist.

Figure D.5 illustrates the propagation of a Gaussian beam emitted by a laser. Where the increase of the beam spot radius with z can be graphically seen.

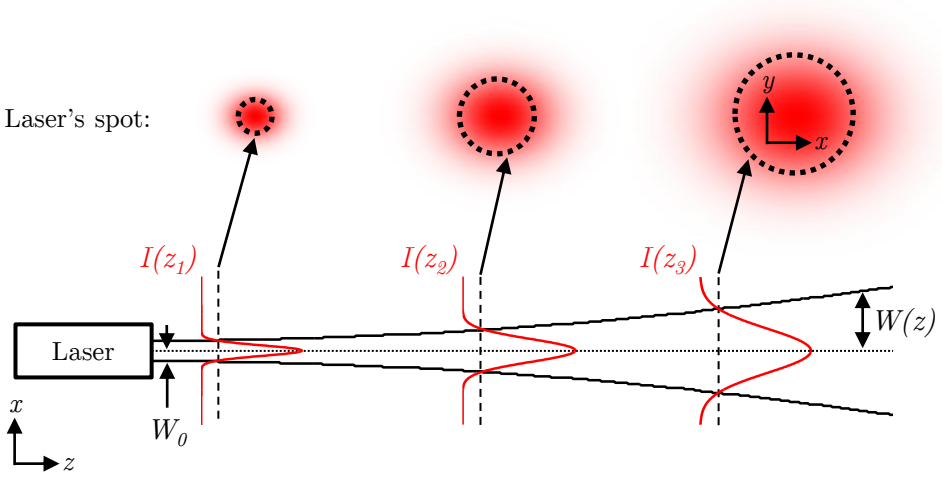

FIGURE D.5: Propagation of a Gaussian beam emitted by a laser.

The function that describes the wavefront radius of curvature of a Gaussian beam is

$$R = z\left[1 + \left(\frac{z_r}{z}\right)^2\right] \tag{D.10}$$

where $z_r = \frac{\pi W_0^2}{\lambda_m}$ is the Rayleigh range.

Notice that at the beam waist the radius of curvature becomes

$$R(z = 0) = \infty \tag{D.11}$$

, meaning that the wavefront is plane (i.e., with constant phase) at the corresponding xy-plane.

The complex radius of curvature $q(z)$ relates both the spot radius and the wavefront radius of curvature,

$$\frac{1}{q} = \frac{1}{R} - j\frac{\lambda_m}{\pi W^2} \tag{D.12}$$

Taking into account equations (D.9) and (D.10), $q(z)$ develops into

$$q = z + j\frac{\pi W_0^2}{\lambda_m} \tag{D.13}$$

Given the complex radius of curvature q, the $ABCD$ law (D.3) can be applied when computing the output parameters of a Gaussian beam transmitted through an arbitrary optical system [99]. This analysis provides the $ABCD$ law for Gaussian beams,

$$q_{out} = \frac{Aq_{in} + B}{Cq_{in} + D} \tag{D.14}$$

D.1.3 Computing the setup's laser spot size

The optical path followed by the laser's beam towards the sample is represented in figure D.6. Comparing the latter diagram with the one shown in figure 6.1 it can be seen that the half-wave plate, the beamsplitter 3 and the vacuum chamber's viewport have been removed from the optical path. The reason of that is because the expected beam modification produced by these elements are assumed to be negligible due to their small thicknesses.

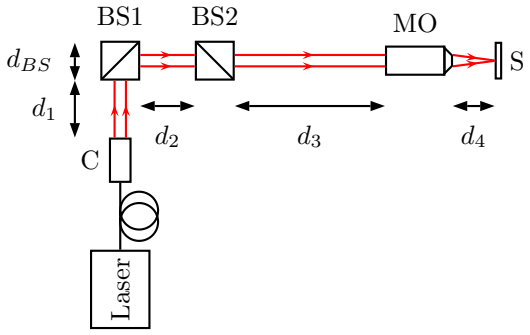

FIGURE D.6: Diagram of the optical path.

Analyzing the optical components of figure D.6 the $ABCD$ matrix of the whole optical system is given by

$$\begin{pmatrix} A & B \\ C & D \end{pmatrix}_T = \begin{pmatrix} 1 & d_4 \\ 0 & 1 \end{pmatrix} \begin{pmatrix} 1 & 0 \\ -1/f_{MO} & 1 \end{pmatrix} \begin{pmatrix} 1 & d_3 \\ 0 & 1 \end{pmatrix} \begin{pmatrix} 1 & d_{BS}/n_{BS} \\ 0 & 1 \end{pmatrix} \cdots \begin{pmatrix} 1 & d_2 \\ 0 & 1 \end{pmatrix} \begin{pmatrix} 1 & d_{BS}/n_{BS} \\ 0 & 1 \end{pmatrix} \begin{pmatrix} 1 & d_1 \\ 0 & 1 \end{pmatrix} \begin{pmatrix} 1 & 0 \\ -1/f_C & 1 \end{pmatrix} \begin{pmatrix} 1 & d_C \\ 0 & 1 \end{pmatrix} \tag{D.15}$$

where the distances d_1, d_2, d_3 and d_{BS} are sketched in figure D.6, d_C is the distance between the fiber tip and the first lens surface of the collimator, the value of d_4 remains as an unknown parameter since it is the distance of the output beam waist size, the focal length of the lens components are named as f and n_{BS} is the refractive index of the cube beamsplitters material (i.e., N-BK7 glass) at $\lambda_0 = 1.55\,\mu$m. Notice that the refractive index of the air has been assumed to be $n_{air} = 1$ and that the last matrix accounts for the distance traveled by the beam from the output of the fiber to the first lens surface of the collimator.

Table D.1 summarizes all the values of the variables present in (D.15) for the assembled setup.

d_1 (mm)	*62*	d_{BS} (mm)	*25.4*	f_C (mm)	*12.56*
d_2 (mm)	*12*	n_{BS} (mm)	*1.5*	$f_{MO_{20X}}$ (mm)	*10*
d_3 (mm)	*100*	d_C (mm)	*6.979*	$f_{MO_{50X}}$ (mm)	*4*

TABLE D.1: Setup parameters for the spot size characterization.

The complex radius of curvature of the beam at the sample surface can be computed using the $ABCD$ law for Gaussian beams (D.14), where the input complex radius of curvature is

$$q_{in} = j\frac{\pi}{\lambda_m}\left(\frac{M_{FD}}{2}\right)^2 \tag{D.16}$$

being M_{FD} the mode field diameter of the fiber (i.e., two times the waist size of the fiber's output beam).

The distance d_4 must be computed assuming that the sample is allocated at $z=0$ (i.e., where $W=W_0$ and $R=\infty$). Consequently, q_{out} is purely imaginary. Once d_4 is determined, the spot size can be found using equation (D.13),

$$W_0 = \sqrt{\frac{q_{out}\lambda_m}{j\pi}} \tag{D.17}$$

Table D.2 summarizes the theoretical values of the beam spot size at the sample surface for the different microscope objectives.

	Spot radius (μm)
MO_{20X}	*0.553*
MO_{50X}	*0.215*

TABLE D.2: Theoretical spot sizes.

Prior to the experimental validation of the theoretically computed values of table D.2, it has to be noticed that the diffraction, the blur and the aberrations introduced by the microscope objective are not being taken into account when computing the spot radius with the latter theoretical procedure. Since the used microscope objectives are designed and optimized to work in the visible spectral range, outside this region the behavior might differ significantly. In order to account for all these phenomena, which might be translated into a bigger spot size, the point spread function (PSF) of the microscope objective must be known. However, the procedure to do such computation is out of the scope of this appendix.

D.2 Experimentally: knife-edge technique

To experimentally determine the size of the laser's spot the knife-edge scanning technique is used [100]. The KOH etched lateral edge of an AFM cantilever's support chip is used as the reflective surface of the measurement procedure. A 30 nm

thin layer of aluminum is used as the reflective coating. The chip is mounted inside the vacuum chamber positioned away from the beam and brought towards it by manually rotating the sub-micron resolution drive of the corresponding translation stage. Figure D.7 shows a scheme of such setup.

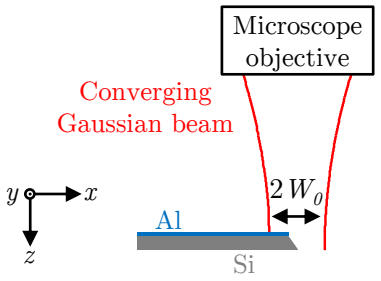

FIGURE D.7: Schematic of the knife-edge technique used to measure the laser's spot size.

Considering that the knife-edge is positioned at the waist of the Gaussian beam, the irradiance of the beam at such propagation direction point is (see (D.8))

$$I(x,y) = I_0\, e^{-2\frac{x^2+y^2}{W_0^2}} \tag{D.18}$$

where I_0 is related with the total EM power of the beam through

$$P_{EM.T} = \int_{-\infty}^{\infty}\int_{-\infty}^{\infty} I\,dx\,dy = \frac{\pi}{2} I_0 W_0^2 \tag{D.19}$$

During the scanning process the power of the partially reflected incident beam is collected by a power sensor mounted in the photodetector's position (see figure 6.1). Therefore, the output of the experimental measurement is the sensor's incident power $P_s(x)$ as a a function of the transverse position of the chip acting as a knife-edge,

$$P_s = \int_{-\infty}^{\infty}\int_{-\infty}^{x} I\,dx\,dy \tag{D.20}$$

Introducing (D.18) into (D.20) yields

$$P_s = I_0 \int_{-\infty}^{\infty} e^{-2\frac{y^2}{W_0^2}}\,dy \int_{-\infty}^{x} e^{-2\frac{x^2}{W_0^2}}\,dx = \frac{P_{EM.T}}{2} + \sqrt{\frac{\pi}{2}} I_0 W_0 \int_0^x e^{-2\frac{x^2}{W_0^2}}\,dx \tag{D.21}$$

Figure D.8 shows the P_s experimental data obtained by performing the scanning procedure when the 20X microscope objective is used.

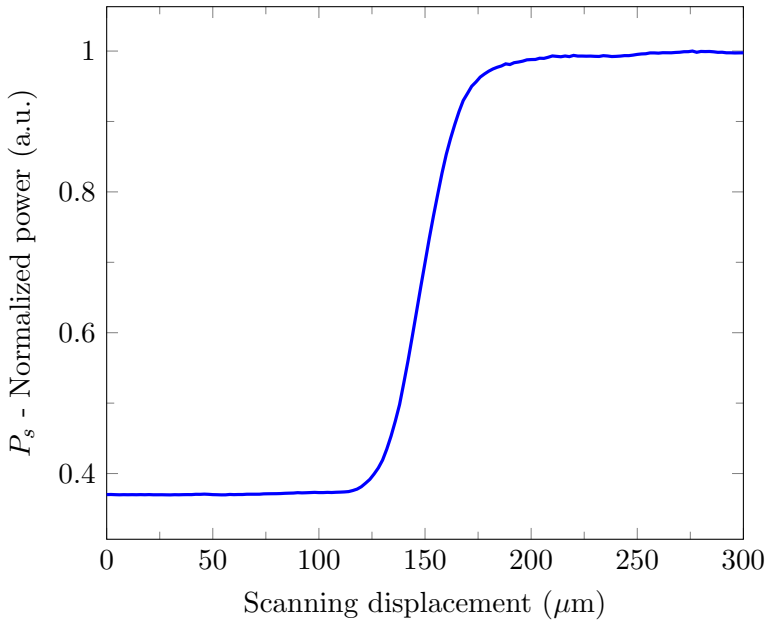

FIGURE D.8: Normalized power received by the sensor as a function of the scanning displacement when using the 20X microscope objective.

The derivative of (D.21) with respect to x is given by

$$\frac{dP_s}{dx} = \sqrt{\frac{\pi}{2}} I_0 W_0 \, e^{-2\frac{(x-x_0)^2}{W_0^2}} \tag{D.22}$$

When the latter derivative is obtained by numerically differentiating the experimental P_s discrete values, the result can be fitted to the following Gaussian function

$$P_{s.fit}(x) = a_1 e^{-\frac{(x-b_1)^2}{c_1^2}} \tag{D.23}$$

where $a_1 = \sqrt{\frac{\pi}{2}} I_0 W_0$, $b_1 = x_0$ and $c_1 = \frac{W_0}{\sqrt{2}}$.

When using the Gaussian fit, the corresponding spot radius can be computed as

$$W_0 = c_1 \sqrt{2} \tag{D.24}$$

Figure D.9 shows the numerical differentiation of figure D.8 and its corresponding Gaussian fit.

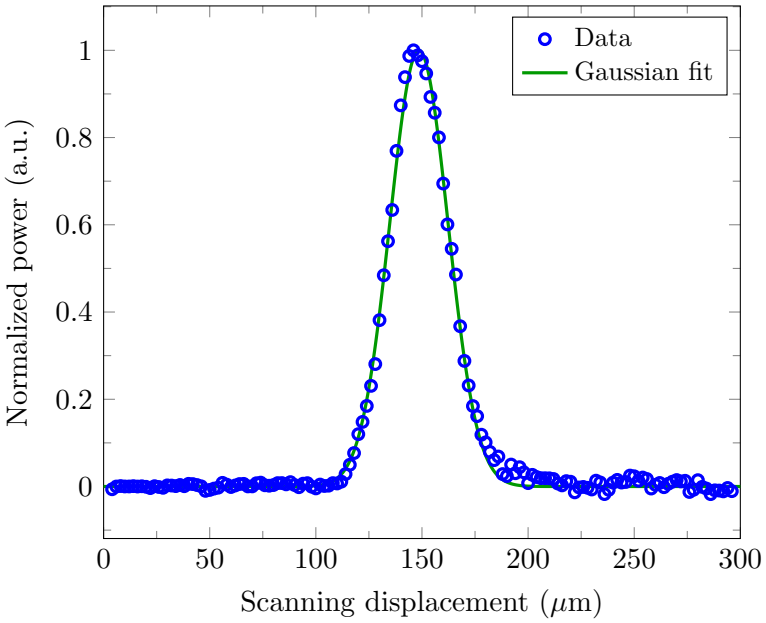

FIGURE D.9: Power distribution of the laser spot profile when using the 20X microscope objective.

Table D.3 summarizes the obtained values of the beam spot size at the sample surface for the different microscope objectives when following the explained procedure.

	Spot radius (μm)
MO_{20X}	≈ 27.5
MO_{50X}	≈ 14

TABLE D.3: Experimental spot sizes.

Bibliography

[1] R. P. Feynman, "There's plenty of room at the bottom," *Engineering and Science*, vol. 23, no. 5, pp. 22–36, 1960.

[2] H. C. Nathanson, W. E. Newell, R. A. Wickstrom, and J. R. Davis Jr., "The resonant gate transistor," *IEEE Transactions on Electron Devices*, vol. 14, no. 3, pp. 117–133, 1967.

[3] International Roadmap Committee, *International technology roadmap for semiconductors: micro-electro-mechanical systems report*, 2013.

[4] S. Priya and D. J. Inman, *Energy harvesting technologies*. Springer, 2009, vol. 21.

[5] A. Harb, "Energy harvesting: state-of-the-art," *Renewable Energy*, vol. 36, no. 10, pp. 2641–2654, 2011.

[6] S. Roundy, "On the effectiveness of vibration-based energy harvesting," *Journal of Intelligent Material Systems and Structures*, vol. 16, no. 10, pp. 809–823, 2005.

[7] H. D. Akaydin, N. Elvin, and Y. Andreopoulos, "Energy harvesting from highly unsteady fluid flows using piezoelectric materials," *Journal of Intelligent Material Systems and Structures*, vol. 21, no. 13, pp. 1263–1278, 2010.

[8] H. A. Sodano, G. E. Simmers, R. Dereux, and D. J. Inman, "Recharging batteries using energy harvested from thermal gradients," *Journal of Intelligent Material Systems and Structures*, vol. 18, no. 1, pp. 3–10, 2007.

[9] J. A. Hagerty, F. B. Helmbrecht, W. H. McCalpin, R. Zane, and Z. B. Popovic, "Recycling ambient microwave energy with broad-band rectenna arrays," *IEEE Transactions on Microwave Theory and Techniques*, vol. 52, no. 3, pp. 1014–1024, 2004.

[10] R. Duggirala, A. Lal, R. G. Polcawich, and M. Dubey, "CMOS compatible multiple power-output MEMS radioisotope μ-power generator," in *International Electron Devices Meeting*. IEEE, 2006, pp. 1–4.

[11] E. Lefeuvre, A. Badel, C. Richard, L. Petit, and D. Guyomar, "A comparison between several vibration-powered piezoelectric generators for standalone systems," *Sensors and Actuators A: Physical*, vol. 126, no. 2, pp. 405–416, 2006.

[12] S. Meninger, J. O. Mur-Miranda, R. Amirtharajah, A. P. Chandrakasan, and J. H. Lang, "Vibration-to-electric energy conversion," *IEEE Transactions on Very Large Scale Integration Systems*, vol. 9, no. 1, pp. 64–76, 2001.

[13] S. P. Beeby, R. N. Torah, M. J. Tudor, P. Glynne-Jones, T. O'Donnell, C. R. Saha, and S. Roy, "A micro electromagnetic generator for vibration energy harvesting," *Journal of Micromechanics and Microengineering*, vol. 17, no. 7, p. 1257, 2007.

[14] J. P. Carmo, L. M. Gonçalves, and J. H. Correia, "Thermoelectric microconverter for energy harvesting systems," *IEEE Transactions on Industrial Electronics*, vol. 57, no. 3, pp. 861–867, 2010.

[15] N. J. Guilar, T. J. Kleeburg, A. Chen, D. R. Yankelevich, and R. Amirtharajah, "Integrated solar energy harvesting and storage," *IEEE Transactions on Very Large Scale Integration Systems*, vol. 17, no. 5, pp. 627–637, 2009.

[16] G. Sebald, E. Lefeuvre, and D. Guyomar, "Pyroelectric energy conversion: optimization principles," *IEEE Transactions on Ultrasonics, Ferroelectrics and Frequency Control*, vol. 55, no. 3, pp. 538–551, 2008.

[17] U. Mizutani, *Introduction to the electron theory of metals.* Cambridge University Press, 2001.

[18] P. Bharadwaj, B. Deutsch, and L. Novotny, "Optical antennas," *Advances in Optics and Photonics*, vol. 1, no. 3, pp. 438–483, 2009.

[19] W. C. Brown, "The history of power transmission by radio waves," *IEEE Transactions on Microwave Theory and Techniques*, vol. 32, no. 9, pp. 1230–1242, 1984.

[20] R. L. Bailey, "A proposed new concept for a solar-energy converter," *Journal of Engineering for Gas Turbines and Power*, vol. 94, no. 2, pp. 73–77, 1972.

[21] B. J. Eliasson, "Metal-insulator-metal diodes for solar energy conversion," Ph.D. dissertation, University of Colorado, 2001.

[22] R. Corkish, M. A. Green, and T. Puzzer, "Solar energy collection by antennas," *Solar Energy*, vol. 73, no. 6, pp. 395–401, 2002.

[23] S. Grover and G. Moddel, "Applicability of metal/insulator/metal (MIM) diodes to solar rectennas," *IEEE Journal of Photovoltaics*, vol. 1, no. 1, pp. 78–83, 2011.

[24] H. Mashaal and J. M. Gordon, "Fundamental bounds for antenna harvesting of sunlight," *Optics Letters*, vol. 36, no. 6, pp. 900–902, 2011.

[25] G. S. Agarwal, G. Gbur, and E. Wolf, "Coherence properties of sunlight," *Optics Letters*, vol. 29, no. 5, pp. 459–461, 2004.

[26] H. Mashaal, A. Goldstein, D. Feuermann, and J. M. Gordon, "First direct measurement of the spatial coherence of sunlight," *Optics Letters*, vol. 37, no. 17, pp. 3516–3518, 2012.

[27] Z. Gong, T.-W. Lee, and L. Que, "Design and modeling of a MEMS-based tunable optical nanoantenna," in *International Mixed-Signals, Sensors, and Systems Test Workshop.* IEEE, 2008, pp. 1–6.

[28] B. D. Sosnowchik, P. J. Schuck, J. Chang, and L. Lin, "Tunable optical enhancement from a MEMS-integrated TiO_2 nanosword plasmonic antenna," in *Conference on Micro Electro Mechanical Systems*. IEEE, 2009, pp. 128–131.

[29] K. Iwami, T. Ono, and M. Esashi, "Optical near-field probe integrated with self-aligned bow-tie antenna and electrostatic actuator for local field enhancement," *Journal of Microelectromechanical Systems*, vol. 15, no. 5, pp. 1201–1208, 2006.

[30] F. Yi, H. Zhu, J. C. Reed, and E. Cubukcu, "Plasmonically enhanced thermomechanical detection of infrared radiation," *Nano Letters*, vol. 13, no. 4, pp. 1638–1643, 2013.

[31] C. A. Balanis, *Antenna theory: analysis and design*. John Wiley & Sons, 2012.

[32] K. B. Crozier, A. Sundaramurthy, G. S. Kino, and C. F. Quate, "Optical antennas: Resonators for local field enhancement," *Journal of Applied Physics*, vol. 94, no. 7, pp. 4632–4642, 2003.

[33] L. Novotny, "Effective wavelength scaling for optical antennas," *Physical Review Letters*, vol. 98, no. 26, p. 266802, 2007.

[34] B. A. Munk, *Frequency selective surfaces: theory and design*. John Wiley & Sons, 2005.

[35] B. Monacelli, J. B. Pryor, B. A. Munk, D. Kotter, and G. D. Boreman, "Infrared frequency selective surface based on circuit-analog square loop design," *IEEE Transactions on Antennas and Propagation*, vol. 53, no. 2, pp. 745–752, 2005.

[36] J. S. Tharp, J. M. Lopez-Alonso, J. C. Ginn, C. F. Middleton, B. A. Lail, B. A. Munk, and G. D. Boreman, "Demonstration of a single-layer meanderline phase retarder at infrared," *Optics Letters*, vol. 31, no. 18, pp. 2687–2689, 2006.

[37] J. Ginn, B. Lail, J. Alda, and G. Boreman, "Planar infrared binary phase reflectarray," *Optics Letters*, vol. 33, no. 8, pp. 779–781, 2008.

[38] H. Zhu, F. Yi, and E. Cubukcu, "Nanoantenna absorbers for thermal detectors," *Photonics Technology Letters*, vol. 24, no. 14, pp. 1194–1196, 2012.

[39] K. L. Ekinci, X. M. H. Huang, and M. L. Roukes, "Ultrasensitive nanoelectromechanical mass detection," *Applied Physics Letters*, vol. 84, no. 22, pp. 4469–4471, 2004.

[40] A. M. Shkel, C. Acar, and C. Painter, "Two types of micromachined vibratory gyroscopes," in *Sensors*. IEEE, 2005, pp. 6–pp.

[41] C. T.-C. Nguyen, "MEMS technology for timing and frequency control," *IEEE Transactions on Ultrasonics, Ferroelectrics and Frequency Control*, vol. 54, no. 2, pp. 251–270, 2007.

[42] J. L. Lopez, J. Verd, J. Teva, G. Murillo, J. Giner, F. Torres, A. Uranga, G. Abadal, and N. Barniol, "Integration of RF-MEMS resonators on submicrometric commercial CMOS technologies," *Journal of Micromechanics and Microengineering*, vol. 19, no. 1, p. 015002, 2009.

[43] H.-C. Lee, J.-Y. Park, and J.-U. Bu, "Piezoelectrically actuated RF MEMS DC contact switches with low voltage operation," *Microwave and Wireless Components Letters*, vol. 15, no. 4, pp. 202–204, 2005.

[44] R. B. Reichenbach, M. K. Zalaludinov, K. L. Aubin, D. A. Czaplewski, B. Ilic, B. H. Houston, H. G. Craighead, and J. M. Parpia, "Resistively actuated micromechanical dome resonators," in *Micromachining and Microfabrication*. International Society for Optics and Photonics, 2004, pp. 51–58.

[45] J. W. Judy and R. S. Muller, "Magnetically actuated, addressable microstructures," *Journal of Microelectromechanical Systems*, vol. 6, no. 3, pp. 249–256, 1997.

[46] B. R. Ilic, S. Krylov, M. Kondratovich, and H. G. Craighead, "Optically actuated nanoelectromechanical oscillators," *IEEE Journal of Selected Topics in Quantum Electronics*, vol. 13, no. 2, pp. 392–399, 2007.

[47] R. M. Langdon and D. L. Dowe, "Photoacoustic oscillator sensors," in *Hague International Symposium*. International Society for Optics and Photonics, 1987, pp. 86–93.

[48] H. Rokhsari, T. Kippenberg, T. Carmon, and K. J. Vahala, "Radiation-pressure-driven micro-mechanical oscillator," *Optics Express*, vol. 13, no. 14, pp. 5293–5301, 2005.

[49] O. Arcizet, P.-F. Cohadon, T. Briant, M. Pinard, and A. Heidmann, "Radiation-pressure cooling and optomechanical instability of a micromirror," *Nature*, vol. 444, no. 7115, pp. 71–74, 2006.

[50] F. Marquardt, J. G. E. Harris, and S. M. Girvin, "Dynamical multistability induced by radiation pressure in high-finesse micromechanical optical cavities," *Physical Review Letters*, vol. 96, no. 10, p. 103901, 2006.

[51] D. M. Weld and A. Kapitulnik, "Feedback control and characterization of a microcantilever using optical radiation pressure," *Applied Physics Letters*, vol. 89, no. 16, p. 164102, 2006.

[52] L. M. Zhang, D. Uttamchandani, and B. Culshaw, "Stabilisation of optically excited self-oscillation," *Electronics Letters*, vol. 25, no. 18, pp. 1235–1236, 1989.

[53] N. A. D. Stokes, R. M. A. Fatah, and S. Venkatesh, "Self-excitation in fiber-optic microresonator sensors," *Sensors and Actuators*, vol. A21–A23, pp. 369–372, 1990.

[54] Y. J. Rao and B. Culshaw, "Continuously stable selfoscillation of silicon cantilever microresonators," *Electronics Letters*, vol. 27, no. 19, pp. 1697–1699, 1991.

[55] J. D. Zook, D. W. Burns, W. R. Herb, H. Guckel, J.-W. Kang, and Y. Ahn, "Optically excited self-resonant microbeams," *Sensors and Actuators A: Physical*, vol. 52, no. 1, pp. 92–98, 1996.

[56] K. Hane and K. Suzuki, "Self-excited vibration of a self-supporting thin film caused by laser irradiation," *Sensors and Actuators A: Physical*, vol. 51, no. 2, pp. 179–182, 1996.

[57] E. Hollander and O. Gottlieb, "Self-excited chaotic dynamics of a nonlinear thermo-visco-elastic system that is subject to laser irradiation," *Applied Physics Letters*, vol. 101, no. 13, p. 133507, 2012.

[58] M. Zalalutdinov, J. Parpia, K. Aubin, H. Craighead, T. Alan, A. Zehnder, and R. Rand, "Hopf bifurcation in a disk-shaped NEMS," in *ASME 2003 International Design Engineering Technical Conferences and Computers and Information in Engineering Conference*. American Society of Mechanical Engineers, 2003, pp. 1759–1769.

[59] K. Aubin, M. Zalalutdinov, T. Alan, R. B. Reichenbach, R. Rand, A. Zehnder, J. Parpia, and H. Craighead, "Limit cycle oscillations in CW laser-driven NEMS," *Journal of Microelectromechanical Systems*, vol. 13, no. 6, pp. 1018–1026, 2004.

[60] C. Metzger, M. Ludwig, C. Neuenhahn, A. Ortlieb, I. Favero, K. Karrai, and F. Marquardt, "Self-induced oscillations in an optomechanical system driven by bolometric backaction," *Physical Review Letters*, vol. 101, no. 13, p. 133903, 2008.

[61] D. Blocher, A. T. Zehnder, R. H. Rand, and S. Mukerji, "Anchor deformations drive limit cycle oscillations in interferometrically transduced MEMS beams," *Finite Elements in Analysis and Design*, vol. 49, no. 1, pp. 52–57, 2012.

[62] M. W. Pruessner, T. H. Stievater, J. B. Khurgin, and W. S. Rabinovich, "Integrated waveguide-DBR microcavity opto-mechanical system," *Optics Express*, vol. 19, no. 22, pp. 21 904–21 918, 2011.

[63] J. A. Dunnmon, S. C. Stanton, B. P. Mann, and E. H. Dowell, "Power extraction from aeroelastic limit cycle oscillations," *Journal of Fluids and Structures*, vol. 27, no. 8, pp. 1182–1198, 2011.

[64] V. C. Sousa, M. de M Anicézio, C. De Marqui Jr, and A. Erturk, "Enhanced aeroelastic energy harvesting by exploiting combined nonlinearities: theory and experiment," *Smart Materials and Structures*, vol. 20, no. 9, p. 094007, 2011.

[65] M. Bryant and E. Garcia, "Modeling and testing of a novel aeroelastic flutter energy harvester," *Journal of Vibration and Acoustics*, vol. 133, no. 1, p. 011010, 2011.

[66] G. N. Nielson, J. Wittwer, L. Phinney, D. Epp, U. Krishnamoorthy, V. Gupta, and P. Resnick, "MEMS solar energy harvesting," Sandia National Laboratories, Tech. Rep., 2007.

[67] D. M. Pozar, *Microwave engineering*. John Wiley & Sons, 2009.

[68] E. D. Palik, *Handbook of optical constants of solids*. Academic Press Inc. (Elsevier), 1998, vol. 3.

[69] M. C. Teich and B. Saleh, *Fundamentals of photonics*. John Wiley & Sons, 1991.

[70] F. D. Otín, D. A. García, J. R. Martos, A. C. Tejero, and F. C. Bienzobal, *Campos electromagnéticos*. Edicions UPC, 1998.

[71] M. Born and E. Wolf, *Principles of optics: electromagnetic theory of propagation, interference and diffraction of light*. CUP Archive, 1999.

[72] G. Dhatt, E. Lefrançois, and G. Touzot, *Finite element method*. John Wiley & Sons, 2012.

[73] J. Jin, *The finite element method in electromagnetics*. Wiley-IEEE, 2002.

[74] COMSOL, "Model manual: Optical scattering off of a gold nanosphere," 2013.

[75] L. D. Landau and E. M. Lifshitz, *Theory of elasticity*. Elsevier, 1986.

[76] W. Fang and J. A. Wickert, "Post buckling of micromachined beams," *Journal of Micromechanics and Microengineering*, vol. 4, no. 3, p. 116, 1994.

[77] S. H. Strogatz, *Nonlinear dynamics and chaos: with applications to physics, biology and chemistry*. Perseus Books Publishing, 1994.

[78] COMSOL, "Material library," 2014.

[79] MathWorks. MATLAB. Accessed: 15/09/2014. [Online]. Available: http://www.mathworks.com/products/matlab/

[80] M. J. Madou, *Fundamentals of microfabrication: the science of miniaturization*. CRC Press, 2002.

[81] E. Klokholm and B. S. Berry, "Intrinsic stress in evaporated metal films," *Journal of the Electrochemical Society*, vol. 115, no. 8, pp. 823–826, 1968.

[82] J. A. Thornton and D. W. Hoffman, "Stress-related effects in thin films," *Thin Solid Films*, vol. 171, no. 1, pp. 5–31, 1989.

[83] R. Abermann, "Measurements of the intrinsic stress in thin metal films," *Vacuum*, vol. 41, no. 4, pp. 1279–1282, 1990.

[84] H. Guckel, D. Burns, C. Rutigliano, E. Lovell, and B. Choi, "Diagnostic microstructures for the measurement of intrinsic strain in thin films," *Journal of Micromechanics and Microengineering*, vol. 2, no. 2, p. 86, 1992.

[85] Y. F. Lau, *MEMS structures for stress measurements for thin films deposited using CVD*. Massachusetts Institute of Technology, 2001.

[86] R. Berger and H. K. Pulker, "Mechanical stresses on evaporated chromium films," in *1983 International Techincal Conference/Europe*. International Society for Optics and Photonics, 1983, pp. 69–73.

[87] W. E. Newell, "Miniaturization of tuning forks," *Science*, vol. 161, no. 3848, pp. 1320–1326, 1968.

[88] V. Kaajakari, *Practical MEMS*. Las Vegas, NV: Small Gear Publishing, 2009.

[89] J. Llobet, M. Sansa, M. Gerbolés, N. Mestres, J. Arbiol, X. Borrisé, and F. Pérez-Murano, "Enabling electromechanical transduction in silicon nanowire mechanical resonators fabricated by focused ion beam implantation," *Nanotechnology*, vol. 25, no. 13, p. 135302, 2014.

[90] C. V. Heer, *Statistical mechanics, kinetic theory, and stochastic processes*. Academic Press Inc. (Elsevier), 1972.

[91] R. R. Craig and A. J. Kurdila, *Fundamentals of structural dynamics*. John Wiley & Sons, 2006.

[92] N. Kacem, S. Baguet, S. Hentz, and R. Dufour, "Computational and quasi-analytical models for non-linear vibrations of resonant MEMS and NEMS sensors," *International Journal of Non-Linear Mechanics*, vol. 46, no. 3, pp. 532–542, 2011.

[93] D. Karabacak, T. Kouh, C. C. Huang, and K. L. Ekinci, "Optical knife-edge technique for nanomechanical displacement detection," *Applied Physics Letters*, vol. 88, no. 19, p. 193122, 2006.

[94] D. Karabacak, T. Kouh, and K. L. Ekinci, "Analysis of optical interferometric displacement detection in nanoelectromechanical systems," *Journal of Applied Physics*, vol. 98, no. 12, p. 124309, 2005.

[95] N. O. Azak, M. Y. Shagam, D. M. Karabacak, K. L. Ekinci, D. H. Kim, and D. Y. Jang, "Nanomechanical displacement detection using fiber-optic interferometry," *Applied Physics Letters*, vol. 91, no. 9, p. 093112, 2007.

[96] D. W. Hoffman and M. R. Gaerttner, "Modification of evaporated chromium by concurrent ion bombardment," *Journal of Vacuum Science and Technology*, vol. 17, no. 1, pp. 425–428, 1980.

[97] A. S. Nowick and B. S. Berry, *Anelastic relaxation in crystalline solids*. Academic Press Inc. (Elsevier), 1972, vol. 1.

[98] A. E. Siegman, *Lasers*. University Science Books, 1986.

[99] S. Wang and D. Zhao, *Matrix optics*. Springer-Verlag, 2000.

[100] A. H. Firester, M. E. Heller, and P. Sheng, "Knife-edge scanning measurements of subwavelength focused light beams," *Applied Optics*, vol. 16, no. 7, pp. 1971–1974, 1977.